Freie Universität Berlin

Amphibious Magnetotellurics at the South-Central Chilean Continental Margin

Dissertation zur Erlangung des Doktorgrades im Fachbereich Geowissenschaften an der Freien Universität Berlin

Gerhard Kapinos

Fachrichtung Geophysik
Berlin, 2011

Erstgutachter: Prof. Dr. Shapiro
Zweitgutachter: Prof. Dr. Kaufmann

Tag der Disputation: 12.07.2011

Erklärung

Hiermit versichere ich, daß ich die vorliegende Arbeit selbständig verfaßt und keine anderen als die angegebenen Hilfsmittel benutzt habe. Die Stellen der Arbeit, die anderen Werken wörtlich oder inhaltlich entnommen sind, wurden durch entsprechende Angaben der Quellen kenntlich gemacht. Diese Arbeit hat in gleicher oder ähnlicher Form noch keiner Prüfungsbehörde vorgelegen.

A part of this work entered into this publication:

Brasse, H., Kapinos, G., Li, Y., Mütschard, L., Soyer, W. and Eydam, D. (2009). *Structural electrical anisotropy in the crust at the South-Central Chilean continental margin as inferred from geomagnetic transfer functions.* Physics of the Earth and Planetary Interiors, 173, 7-16, doi:10.1016/j.pepi.2008.10.017.
http://dx.doi.org/10.1016/j.pepi.2008.10.017

Contents

1. Introduction **1**

2. Methodological basis **4**
2.1. Base equations of magneteotellurics 4
2.1.1. The magnetotelluric impedance tensor 7
2.1.2. Magnetic transfer functions 12
2.1.3. Dimensionality analysis 13

3. Presentation of the study area **18**
3.1. Geological setting - the evolution and tectono-magmatic history of South-Central Andes 18
3.1.1. Pre-Andean evolution 19
3.1.2. "Andean tectonic cycle" 20
3.2. Previous and present electromagnetic studies 24
3.3. Other geophysical investigations 27

4. Analysis of the onshore data **31**
4.1. Onshore instruments and deployment 31
4.2. Magnetotelluric transfer functions in South Chile 32
4.3. GDS transfer functions 36
4.4. Dimensionality analysis and geological strike estimation 38

5. Magnetotellurics in marine environments **44**
5.1. Electromagnetic oceanic effects 44
5.1.1. Electromagnetic fields induced by oceanic motion 45
5.1.2. Electromagnetic fields induced in the ocean by external sources . . 46
5.2. Decay of fields in the ocean 46
5.3. Offshore magnetotelluric and magnetic transfer functions in the presence of bathymetry 53
5.3.1. Kramers-Kronig dispersion relations 56
5.4. Marine measurements 69
5.4.1. Offshore instrumentation 69
5.4.2. Marine data 71

6. The standard isotropic modeling **78**
6.1. Basics of inverse problem 78
6.1.1. Formulation of the nonlinear inverse problem 78

6.1.2. The Gauss-Newton algorithm 79
6.1.3. Steepest descent and conjugate gradient methods 85
6.2. 2-D isotropic inversion and conductivity distribution below the South-Central Chilean continental margin 89
6.2.1. Inversion settings 89
6.2.2. Starting models 91
6.3. Isotropic 3-D forward modeling at Villarrica volcano 102
6.3.1. Measurements and data 103
6.3.2. Model discretization 104
6.3.3. Results from 3-D forward modeling 105

7. Anisotropic 2-D forward modelling **110**
7.1. 3-D modeling attempts to explain induction vectors 110
7.2. 2-D models with anisotropy: some principal considerations 113
7.3. Anisotropic models for the Chilean margin 117

8. Discussion and outlook **123**
8.1. Isotropic models 123
8.2. Anisotropic models 127

9. Summary **133**

10. Zusammenfassung **136**

Bibliography **138**

A. Appendix **152**
A.1. Influence of the inversion parameters, model discretization and a priori informations on the model 152
A.2. Data and inversion responses 154

1. Introduction

Active continental margins, as collision zones between convergent tectonic plates, are marked by high earthquake activity, volcanoes and mountain belts. Such tectonically active zones serve as a natural laboratory, and are an ideal place to study the dynamics of the Earth, and particularly the mechanisms in the Earth's interior controlling the subduction processes, and are therefore the focus of diverse geophysical investigations. One of the most prominent convergent continental margins is the Andean subduction zone, where the oceanic Nazca Plate slides beneath the less dense continental South American Plate with a relatively high convergence rate of $\sim$6.5 cm/yr (Klotz et al., 2006). On May 22th, 1960, the southern part of the Andean subduction system suffered the largest ever recorded earthquake, with a moment magnitude M_w=9.5 (Cifuentes, 1989). In order to understand the processes causing seismicity, and ultimately, to improve the hazard assessment strategies at convergent margins, the South-Central Chilean continental margin was made the subject of the multidisciplinary project **TIPTEQ** (from **T**he **I**ncoming **P**late to mega-**T**hrust **E**arth**Q**uake processes).

This project involved many partner institutions from Chile and Germany, and incorporated several geological subprojects and geophysical methods. It aimed to image the plate interface, and to quantify the relation between the evolution of seismic ruptures occurring in the seismogenic coupling zone and the resulting deformations on the surface. Fluids are among the controlling factors in this rupturing process which is associated with the genesis and nucleations of earthquakes; water triggers partial melting reactions and acts as the driving force for the arc-volcanism (Peacock, 1990). The presence of water in a subduction zone is related to enhanced electrical conductivity, and thus a direct connection between a magnetotelluric target and the seismogenic coupling zone may exist. The detection and imaging of fluids considered to be a trigger and controlling factor of seismicity and volcanism in the subduction process was the major objective of a joint offshore-onshore magnetotelluric (MT) experiment (Fig. 1.1).

Magnetotellurics is a passive method which is applied to determine the conductivity distribution in the Earth by using the phenomenon of electromagnetic induction in the subsurface caused by natural fluctuations of the Earth's external magnetic field. Since the induced electric currents flow preferentially in conductive rock, MT is primarily sensitive to conductive material, and thus appropriate to resolve predominantly conductive structures in a resistive environment. In a fractured rock matrix occurring in a subduction zone, an interconnected network of cracks and ruptures, filled by electrolytic water or partial melts, serves as a pathway for electrical charges and currents, and provides an enhanced conductivity. Furthermore, the temperature also may contribute to increased electrical conductivity. Thus, there exists a close relationship between the electrical parameters and the rheological (mechanical) conditions in the underground.

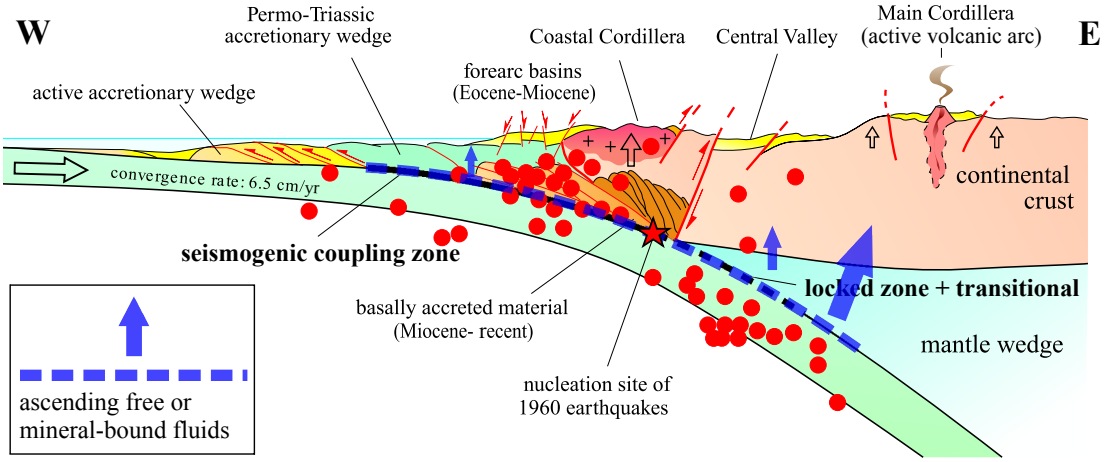

Figure 1.1.: Schematic cross section through the South-Central Chilean continental margin, illustrating tectonic and geologic features, as well as fluid transport and release in the subduction zone (after H. Echtler, pers. comm.).

Magnetotellurics enables to quantify this relation, and to assess the fluid budget and the temperature in the Earth's interior by estimating the electrical conductivity, and thus is an appropriate approach for investigating subduction zones.

At the South Andean continental margin, where a considerable amount of water is transported into the subduction zone by both water saturated marine sediments, which are abundant on the oceanic plate, particularly in the trench, as well as by the oceanic lithosphere, which is infiltrated by water due to bending-related faulting, zones of enhanced conductivity associated with fluid accumulations can be expected on the landward side of the trench and above the subducting plate. In the front of the subduction zone (forearc), the dehydration of the downgoing plate occurs at shallow depths, and is thus governed by low-temperature and low-pressure conditions. Here, the water is primarily expelled due to compaction and lithification of the marine sediments. Whereas in the volcanic arc and backarc, partial melts, triggered by liberated water due to a further increase in temperature and pressure with the depth, may instead account for possible increases in conductivity.

However, a complete image of the conductivity distribution, allowing to draw conclusions about the accumulation of fluids in the entire subduction zone, can only be realized if the data are acquired along an amphibious (on- and offshore) magnetotelluric transect across the trench. Evans et al. (2002) show that in particular, data acquired on the seaward side of the trench are sensitive to the geometry and magnitude of the electrical connection between the ocean and the mantle, which is provided by a conductive slab; such data enable to asses amount of, an pathways taken by migrating water.

Whilst onshore MT is an established method for imaging electrical conductivity structures, the acquisition of data in marine environments is still associated with some challenges. Problems related to offshore electromagnetic exploration, as well as the presentation of data recorded on the ocean floor, are the subject of chapter 4 of this work.

Although the theory behind electromagnetic induction, and the basic MT relations are generally valid for both the terrestrial and marine electromagnetics (EM), a simple transference of the standard terrestrial approaches to a marine environment is not possible. Apart from logistical challenges, high technical demands on the instruments, and financial aspects, particular attention has to be paid to the special physical conditions on the seafloor; these differ from those on land due to the fact that the fields are not recorded on the surface, but beneath a conductive layer of sea water. As a consequence thereof, the usable period spectrum is considerably limited on the seafloor. At long periods, the primary field is contaminated by motion-induced secondary electromagnetic fields; and at short periods, the source field is attenuated by the overlying highly conductive ocean layer. Additional complications emerge near the coast, where the bathymetric changes affect the distribution of electric currents, and massively distort the electromagnetic fields, and thus also the magntetotelluric responses at the seafloor.

However, the physics of the magnetotelluric method, based on electromagnetic induction, is generally applicable for both offshore and onshore MT studies, and follows the principles of Maxwell's equations. Starting with these fundamental relations, the theoretical background, including derivation of the impedance tensor and the magnetic transfer functions, as well as some aspects of dimensionality analysis, will be outlined at the beginning of this work in chapter 1. After this, the study area is presented in chapter 2, firstly from a geological point of view, with an emphasis on the evolution of the tectono-magmatic activity, and then from a geophysical point of view, with a brief overview of previous investigations in South Chile; in particular, results obtained from active and passive seismic and magnetotelluric studies. Chapter 3 focuses on the analysis of the onshore data: the magnetotelluric and magnetic transfer functions, as well as the results of dimensionality analysis and the estimation of the electrical strike. After the aforementioned outline of MT responses on the seafloor in chapter 4, chapter 5 treats isotropic modeling. The first part of this chapter provides an insight into the principle and the theory of the inversion problem; in the second part, the isotropic 2-D inversion and 3-D forward modeling approaches are applied. In search of an acceptable solution, i.e., a geologically reasonable model which is able to fit the data within a reasonable RMS error, several preliminary experiments are required in order to select optimal inversion settings and a proper mesh design, as well as to appraise existing a priori constraints, and evaluate their effects on the solution. Finally, the relevance of the modeled structures must be evaluated. The resulting 2-D conductivity distribution along all profiles across the South Chilean continental margin, and a 3-D model of Villarrica volcano are presented and discussed in terms of their geological meaning. The analysis of the magnetic transfer functions, in chapter 3, reveals an obvious anisotropy signature. Chapter 6 addresses the search for a 2-D anisotropic model which is able to reproduce the observed transfer functions, and, together with the isotropic model, provides a more complete image of the South-Chilean subduction zone. The interpretation and discussion of the isotropic and anisotropic models in the context of active and passive seismic results, and a comparison with magnetotelluric models from other subduction zones is given in Chapter 7.

2. Methodological basis

Magnetotellurics (MT) is a passive geophysical method that uses the phenomenon of electromagnetic induction to investigate the electrical conductivity distribution in the Earth. The theory of MT is based on Maxwell's equations, and was first presented by Tikhonov (1950), and in more detail by Cagniard (1953). As a signal source the technique utilizes variations of the natural, external electromagnetic field caused by diverse extraterrestrial processes, and encompasses a broad spectrum of frequencies. In terms of MT, the field variations can generally be classified as: *solar daily variations (Sq variations)*, *magnetic storms*, *pulsations*, and *spherics*. The spectra of these variations cover periods ranging from $\sim 10^{-3}$ to $\sim 10^{5}\,s$, and are generated by the interaction between the solar wind and the Earth's magnetosphere and ionosphere. Perhaps the best known signal source are *spherics*, which occur as discharges during thunderstorms. Induced magnetic fields of interest in long period MT have periods longer than 1 s. A relationship between the applicative signal's period and the penetration depth, connected by the *skin effect*, allows, with a sufficiently broad frequency band, a wide range of depths, up to several hundred kilometers, to be penetrated and imaged by electromagnetic waves. A description of the sources of the electromagnetic field and its properties can be found in many articles and books (e.g., Parker, 1958; Rokityansky, 1982; Vozoff, 1987; Onwumechili, 1997).

2.1. Base equations of magneteotellurics

The time varying external magnetic field in the Ionosphere induces in the Earth's interior, according to Faraday's law, an electric field which in turn induces a secondary internal magnetic field (Ampère's law). The induction process in a homogeneous isotropic medium (constant conductivity σ in $[S/m]$, magnetic permeability μ_r in $\left[\frac{Vs}{Am}\right]$ and dielectric permittivity ε_r in $\left[\frac{C}{Vm}\right]$) is governed by the Maxwell's equations:

$$\nabla \times \vec{H} = \vec{j} + \frac{\partial \vec{D}}{\partial t} \qquad \textit{(Ampère's law)} \tag{2.1}$$

$$\nabla \times \vec{E} = -\mu_0 \mu_r \frac{\partial \vec{H}}{\partial t} \qquad \textit{(Faraday's law)} \tag{2.2}$$

$$\nabla \cdot \vec{B} = 0 \tag{2.3}$$

$$\nabla \cdot \vec{D} = q \tag{2.4}$$

where $\vec{B}$ is the magnetic field in $[T]$, $\vec{E}$ the electric field in $\left[\frac{V}{m}\right]$, $\vec{D}$ the displacement field or electric flux density in $\left[\frac{C}{m}\right]$, $\vec{j}$ the current density in $\left[\frac{A}{m^2}\right]$, q the charge density in $\left[\frac{C}{m^3}\right]$, μ_0 is the magnetic permeability in free space. Using the material equations

$\vec{B} = \mu_0\mu_r\vec{H}$, $\vec{D} = \varepsilon_0\varepsilon_r\vec{E}$, $\vec{j} = \sigma\vec{E}$, the Maxwell's equations can be rewritten as

$$\nabla \times \vec{B} = \mu\sigma\vec{E} + \mu\varepsilon\frac{\partial\vec{E}}{\partial t} \tag{2.5}$$

$$\nabla \times \vec{E} = -\frac{\partial\vec{B}}{\partial t} \tag{2.6}$$

$$\nabla \cdot \vec{B} = 0 \tag{2.7}$$

$$\nabla \cdot \vec{E} = \frac{q}{\varepsilon} \tag{2.8}$$

where ε_0 is the dielectric permittivity of free space in $\left[\frac{As}{Vm}\right]$, $\mu = \mu_0\mu_r$ and $\varepsilon = \varepsilon_0\varepsilon_r$. Some approximations are adopted regarding electromagnetic induction in the Earth. First, the electromagnetic fields generated by distant large-scale magnetospheric currents are treated as plane-polarized waves vertically incident on the surface of the conductive Earth. Second, the Earth is treated as having horizontal layers of differing resistivity. By applying the curl operator ($\nabla\times$) equations 2.5 and 2.6 can be coupled and an equation for damped propagation of an electromagnetic field into the Earth may be derived. With the vector identity $\nabla \times (\nabla \times \vec{F}) = \nabla(\underbrace{\nabla \cdot \vec{F}}_{0}) - \nabla^2\vec{F}$ where $\vec{F}$ may either represent $\vec{E}-$ or $\vec{B}-$field, equations 2.5 and 2.6 lead to:

$$\left[\left(\nabla^2 - \mu\varepsilon\frac{\partial^2}{\partial t^2}\right) - \mu\sigma\frac{\partial}{\partial t}\right]\vec{F} = 0 \tag{2.9}$$

The term $\nabla\cdot\vec{F}$ in the vector identity can be omitted because, in accordance with equation 2.3, no magnetic monopoles exist ($\nabla \cdot \vec{B} = 0$), and, as subsequently shown no free charge can accumulate in a medium of uniform conductivity ($\nabla\sigma = 0$); i.e. $\nabla \cdot \vec{D} = 0$ and $\nabla \cdot \vec{E} = 0$. This so-called *telegrapher's equation* is a common type of wave equation. It describes the propagation of a time-varying electromagnetic field trough the Earth. The first term contains the conductivity and describes a diffusion process. The second term depicts wave propagation of the field.

Using the harmonic time dependency of the excitation field, $e^{i\omega t}$, some of these relationships are commonly transformed from the time to the frequency domain ($\vec{f}(\vec{r},t) \rightarrow \vec{F}(\vec{r},\omega)$) via the Fourier transform pair:

$$\vec{F}(\vec{r},\omega) = \int_{-\infty}^{\infty}\vec{f}(\vec{r},t)e^{-i\omega t}dt \tag{2.10}$$

$$\vec{f}(\vec{r},t) = \frac{1}{2\pi}\int_{-\infty}^{\infty}\vec{F}(\vec{r},\omega)e^{-i\omega t}d\omega \tag{2.11}$$

where $\omega = \frac{2\pi}{T}$ is the angular frequency with period T. Thus the time derivative $\frac{\partial}{\partial t}$ in the time domain is replaced by $i\omega$ in the frequency domain and it becomes clearer that relation 2.9 describes harmonic time variations of the electromagnetic field ($\vec{E}, \vec{B} \sim e^{i\omega t}$). Thus, *Ampère's law* and *Faraday's law* can be rewritten as:

$$\nabla \times \vec{B} = \mu\sigma\vec{E} + i\omega\mu\varepsilon\vec{E} \tag{2.12}$$

$$\nabla \times \vec{E} = -i\omega\vec{B} \tag{2.13}$$

and the *telegrapher's equation* can be rearranged into the *Helmholtz equation*:

$$\nabla^2 \vec{F} = i\mu\sigma\omega\vec{F} - \mu\varepsilon\omega^2\vec{F} = \gamma^2\vec{F} \tag{2.14}$$

with:

$$\gamma^2 = i\mu\sigma\omega - \mu\varepsilon\omega^2 \tag{2.15}$$

where γ is the (complex) wavenumber. Equations 2.9 and 2.14 are second order partial differential equations, and can be satisfied by a variety of solutions. An appropriate general solution is a periodic function of the form:

$$\vec{F} = \vec{F}_1 e^{i\omega t - kz} + \vec{F}_2 e^{i\omega t + kz}. \tag{2.16}$$

The exponent γ can also be evaluated by substituting the solution in equation 2.9.

Further conclusions follow from the consideration of the *equation of continuity*, which indicates that the time varying charge rate is a source of conduction currents. It is derived by taking the divergence of equation 2.1 and substituting equation 2.4

$$\nabla \cdot \vec{j} = -\frac{\partial q}{\partial t} \tag{2.17}$$

which can be rewritten in turn, with the material equation ($\vec{j} = \sigma\vec{E}$) as:

$$\sigma\nabla \cdot \vec{E} + (\nabla\sigma) \cdot \vec{E} = -\frac{\partial q}{\partial t} \tag{2.18}$$

Combined with 2.8, this gives an expression for the exponential charge decay:

$$\frac{\partial q}{\partial t} = -\frac{\sigma q}{\epsilon} \tag{2.19}$$

which may be integrated to obtain

$$q(\vec{x}, t) = q(\vec{x}, 0)e^{-\frac{\sigma}{\epsilon}t} \tag{2.20}$$

The charge decays exponentially with a *relaxation time* $\frac{\epsilon}{\sigma}$, which depends on the conductivity σ, but not on the time variations of the electromagnetic field. For realistic values of conductivity for Earth materials charges disperse instantaneously to regions of non-vanishing conductivity gradient ($\nabla\sigma$); so that inside a uniform conductor practically no charges remain (Ward and Hohmann, 1988; Weaver, 1994). This result implies that the electric charges can only accumulate in regions of non-uniform conductivity, as at boundaries between regions of uniform conductivity. Accordingly, in homogeneous regions of uniform conductivity where no charge sources exist equations 2.4 and 2.8 simplify to $\nabla \cdot \vec{E} = 0$, as previously assumed. Substituting this into equation 2.18 gives $\frac{\partial q}{\partial t} = 0$ and $\nabla \cdot \vec{j} = 0$. These statements correspond to stationary conditions in the magnetostatic field and lead to the *quasi-stationary approximation* of the Maxwell's equations. Combining these statements with equation 2.8, the volume charge density dissipated to the boundary of a conductive medium can be estimated from equation 2.18 to:

$$q = -\frac{\epsilon}{\sigma}(\nabla\sigma) \cdot \vec{E} \tag{2.21}$$

The *quasi-stationary approximation* requires that we neglect the displacement currents in Ampère's law. The significane of the displacement $i\varepsilon\omega\vec{F}$ in comparison to the conduction currents $\sigma\vec{F}$ can be evaluated from equation 2.14 in terms of the *relaxation time*. Indeed, for Earth materials with resistivity $\rho < 10^4\,\Omega$m and for frequencies $f < 10^5$ Hz commonly used in MT, $\varepsilon\omega \ll \sigma$, which means that the average decay time of free electric charges in an observed volume is small compared to the oscillation period, and the displacement currents can be omitted. It shows that the electromagnetic fields propagate in the Earth diffusively. Equation 2.14 reduces to:

$$\nabla^2\vec{F} = i\mu\sigma\omega\vec{F} = k^2\vec{F} \tag{2.22}$$

with a propagation constant, or complex wavenumber k:

$$k = \sqrt{i\mu\sigma\omega}. \tag{2.23}$$

It describes the induction of currents; its meaning becomes clear after splitting into real and imaginary parts:

$$k = \sqrt{i\mu\sigma\omega} = (1+i)\sqrt{\frac{\omega\sigma\mu}{2}} = \sqrt{\frac{\omega\sigma\mu}{2}} + i\sqrt{\frac{\omega\sigma\mu}{2}}. \tag{2.24}$$

where both parts are identical real quantities if displacement currents are negligible. Whereas the latter indicates the oscillatory nature of the wave with time, the first one describes an exponential attenuation of the amplitude along the penetration path. The inverse of the real part of k is defined as the *skin depth* or *penetration depth*, δ, i.e. the depth at which the electromagnetic field amplitude has dropped to $\frac{1}{e}$ of the surface value:

$$\delta = \frac{1}{\Re(k)} = \sqrt{\frac{2}{\omega\sigma\mu}} \tag{2.25}$$

This equation shows that the penetration depth is a function of underground resistivity and wave period. That means that the induction currents migrate into deeper structures with increasing wave period and resistivity. The relation to the *complex penetration depth* called also the *magnetotelluric response function* and defined by (Weidelt, 1972; Schmucker, 1973) as the inverse of k is given by:

$$c(\omega) = \frac{1}{k} = \frac{\delta}{2} - \frac{i\delta}{2} \tag{2.26}$$

2.1.1. The magnetotelluric impedance tensor

2.1.1.1. 1-D case

In a **one-dimensional** N-layered half space without lateral variability $\frac{\partial\sigma}{\partial x} = \frac{\partial\sigma}{\partial y} = 0$, the conductivity depends only on depth $\sigma = \sigma(z)$. A suitable choice of coordinate system with an in $x-y-$plane polarized and vertically propagating plane wave, and assuming that there are no vertical currents across the air-Earth boundary, currents and electric

fields in z-direction can be eliminated, and the *diffusion equation* 2.22 for the $x-$ and $y-$components of the electric and magnetic fields simplifies to:

$$\frac{\partial^2 \vec{F}}{\partial z^2} = k^2 \vec{F} \tag{2.27}$$

where $\vec{F}$ may be taken to be either $\vec{E} = (E_x, E_y, 0)$ and $\vec{B} = (B_x, B_y, 0)$, as before. The solution for the $x-$component of the electric field in an $n-$ layer medium can be written as:

$$E_{n,x} = E_{1n} e^{i\omega t - k_n z} + E_{2n} e^{i\omega t + k_n z} \tag{2.28}$$

where the solution represents both waves traveling from above downward, and from the layer interface below upward (Cagniard, 1953; Keller and Frischknecht, 1966; Zhdanov and Keller, 1994). From the frequency-domain *Ampère's* and *Faraday's laws* (equations 2.12, 2.13) the following holds for the 1-D case:

$$\frac{\partial B_x}{\partial z} = \mu\sigma E_y \qquad \frac{\partial E_y}{\partial z} = i\omega B_x \tag{2.29}$$

$$\frac{\partial E_x}{\partial z} = -i\omega B_y \qquad \frac{\partial B_y}{\partial z} = -\mu\sigma E_x \tag{2.30}$$

Combining the solution for $E_{n,x}$ (2.28) with the corresponding expression of *Faraday's law*, the $y-$component of the magnetic field becomes:

$$B_{n,y} = \frac{k_n}{i\omega} \left(E_{1n} e^{i\omega t - k_n z} - E_{2n} e^{i\omega t + k_n z} \right) \tag{2.31}$$

The ratio of orthogonal electric and magnetic fields is defined as the *magnetotelluric impedance* $\overleftrightarrow{Z}$. In an $N-$layered Earth the *magnetotelluric impedance* Z_n within each layer n can be expressed as:

$$Z_{n,xy} = \frac{E_{n,x}(z)}{B_{n,y}(z)} = \frac{i\omega}{k_n} \frac{E_{1n} e^{i\omega t - k_n z} + E_{2n} e^{i\omega t + k_n z}}{E_{1n} e^{i\omega t - k_n z} - E_{2n} e^{i\omega t + k_n z}} \tag{2.32}$$

Particularly with regard to the ultimate substratum considered as a homogeneous half space with infinite downward extent, the penetrating and diffusing electromagnetic field attenuates and decays according to the *skin depth*. It disappears at infinite depth, without any reflection at transitions, so that only the first term in the solution of the *diffusion equation* must be kept. The *magnetotelluric impedance* Z_N thus corresponds to the condition of a homogeneous half space and becomes simply:

$$Z_{N,xy} = i\omega c_N = \frac{E_{N,x}(z)}{B_{N,y}(z)} = \frac{i\omega}{k_N} = \sqrt{\frac{\omega}{\mu\sigma_N}} \sqrt{i} \tag{2.33}$$

Based on the transfer function of a half space, Wait (1954) showed that the impedance observed at the surface can be expressed in terms of the transfer functions in each of the

lower layers. Conversely a relation for the *wave impedance* at the top of the lowermost layer N, defined as a homogeneous half space can be tied progressively in a recursion from layer to layer until the surface.

$$Z_{xy} = \frac{E_x(z)}{B_y(z)} = -\frac{i\omega}{k_1} \coth\left\{k_1 h_1 + \coth^{-1}\left[\frac{k_1}{k_2}\coth(k_2 h_2 + \cdots + \coth^{-1}\frac{k_{n-1}}{k_n})\right]\right\} \quad (2.34)$$

The expansion can be found with the aid of boundary conditions that ensure continuity of the tangential components of the electric and magnetic field across the boundaries between layers, which means that the wave impedance at the bottom of the first layer must equal the wave impedance at the top of the second layer (Keller and Frischknecht, 1966; Zhdanov and Keller, 1994). In the most basic case of a homogeneous half space ($\sigma = const.$), the second term in the solution of the *diffusion equation* 2.28 can be neglected, since the electromagnetic field doesn't reflect from the interface below and attenuates with depth due to *skin effect* ($E_x(z) \to 0$ as $z \to \infty$). The relation 2.34 reduces to equation 2.33 and depends only on the electrical properties of the medium and on the frequency. Because of the symmetry of the problem it can be easy verified that $Z_{xy} = -Z_{yx}$ and $Z_{xx} = Z_{yy} = 0$. In matrix form the coupling between horizontal $\vec{E}$ and $\vec{B}$ is expressed as:

$$\vec{E} = \begin{pmatrix} E_x \\ E_y \end{pmatrix} = \begin{pmatrix} 0 & Z_{xy} \\ Z_{yx} & 0 \end{pmatrix} \begin{pmatrix} B_x \\ B_y \end{pmatrix} = \overleftrightarrow{Z}\vec{B} \quad (2.35)$$

where $\overleftrightarrow{Z}(\omega)$ is termed the *impedance tensor*. The complex *impedance* written in exponential form as $\overleftrightarrow{Z} = |Z|\, e^{i\phi}$ has phase $\phi = \arg(Z)$ and magnitude $|Z| = \sqrt{\frac{\omega}{\mu\sigma_N}}$ that can be solved for the electrical resistivity:

$$\rho_{a_{ij}}(\omega) = \frac{\mu_0}{\omega}\,|Z_{ij}(\omega)|^2 \quad \text{equivalently,} \quad \rho_{a_{ij}}(T) = 0.2T\,|Z_{ij}(T|^2 \quad (2.36)$$

where $i, j = x, y$. Formula 2.36 gives an exact value for resistivity in the case of a homogeneous Earth, and a volumetric average value called the *apparent resistivity* ρ_a that is loosely related to the actual resistivity distribution, in the case of a heterogeneous Earth. The argument of the complex *impedance* corresponds to the phase shift between the electric and magnetic fields:

$$\phi_{ij}(T) = \arg(Z_{ij}(T)) = \arctan\left(\frac{\Im Z_{ij}(T)}{\Re Z_{ij}(T)}\right). \quad (2.37)$$

In a homogeneous half space, where $\phi_{ij}(T) = \frac{\pi}{4} = 45°$ since $\arg(Z) = \sqrt{i} = e^{i\frac{\pi}{4}}$ (eq. 2.33), the electric field precedes the magnetic field by this amount. Note that $\phi_{ji}(T) = -\sqrt{i} = -135°$. $\rho_{a_{ij}}(T)$ and $\phi_{ij}(T)$ are linked via a *dispersion relationship* or *Kramers-Kronig relationship* (Weidelt, 1972):

$$\phi(\omega) = \frac{\pi}{4} - \frac{\omega}{\pi}\int_0^\infty \log\frac{\rho_a(x)}{\rho_0}\frac{dx}{x^2 - \omega^2}. \quad (2.38)$$

2.1.1.2. 2-D case

In an idealized **two-dimensional** Earth the conductivity varies only in a vertical $y-z$ plane ($\sigma = \sigma(y,z)$) remaining constant along an infinitely extending geological strike in $x-$direction ($\frac{\partial\sigma}{\partial x} = 0$). In this case, the *Maxwell's equations* decouple into two classes of relations: one referred to as the *tangential electric* or *TE mode* with induced currents flowing parallel to the strike and where B_y, B_z and their derivatives are related to E_x; the other is referred to as the *tangential magnetic* or *TM mode*, with currents flowing perpendicular to the strike, with E_y, E_z and their derivatives are related to B_x (Cantwell, 1960; Vozoff, 1987; McNeill and Labson, 1987):

TE-mode:			**TM-mode:**		
$\frac{\partial B_z}{\partial y} - \frac{\partial B_y}{\partial z}$	$=$	$\mu_0\sigma E_x$	$\frac{\partial E_z}{\partial y} - \frac{\partial E_y}{\partial z}$	$=$	$-i\omega B_x$
$\frac{\partial E_x}{\partial z}$	$=$	$-\omega B_y$	$\frac{\partial B_x}{\partial z}$	$=$	$\mu_0\sigma E_y$
$\frac{\partial E_x}{\partial y}$	$=$	$-\omega B_z$	$\frac{\partial B_x}{\partial y}$	$=$	$-\mu_0\sigma E_z$

(2.39)

In this special geometry, called as *principal coordinate system*, two different *impedances* for the *TE mode* and the *TM mode* can be derived from relationship 2.39, depending on whether the currents flow parallel or perpendicular to strike

$$Z_{TE} = Z_{xy} = \frac{E_x}{B_y} \qquad \text{and} \qquad Z_{TM} = Z_{yx} = \frac{E_y}{B_x}, \tag{2.40}$$

where $Z_{xx} = Z_{yy} = 0$, as in one-dimensional case but $Z_{xy} \neq -Z_{yx}$. This, together with equations 2.36 and 2.37 leads to different apparent resistivities $\rho_{a_{xy}}$, $\rho_{a_{yx}}$ and phases ϕ_{xy}, ϕ_{yx}. The differences in the behavior of the modes along a 2-D structure are governed by boundary conditions (Ward and Hohmann, 1988).

In the *TE mode* $\vec{E} = (E_x, 0, 0)$ is continuous, whereas the density of surface currents $\vec{j_s} = \sigma\vec{E}$ changes abruptly across the conductivity interface, with obviously higher intensity in the conductive than the resistive medium. However, the jump is not a reduction of the total current, since this remains constant. It implies rather an extension or partial shift of current downwards due to increased *skin depth* in the less conductive material. Indeed, on the resistive side, away from the transition zone, the current density near the surface drops, but the induction depth rises; the decrease in density at the surface is quasi-compensated for greater depth. Additionally, the fields interact in the immediate vicinity of the contact, so that the resulting horizontal magnetic field, likewise the electric field, and the impedance in the *TE mode* (here associated with Z_{xy}) vary smoothly across the transition.

In the *TM mode* the boundary conditions require that currents across a discontinuity must be conserved. In order to satisfy *Ohm's laws* ($j_y = \sigma E_y$), the electric field E_y must be discontinuous. The degree of discontinuity becomes amplified by the secondary

electric field, which is generated by charges accumulated at the contact between two materials of different resistivity; similar to a charging process in a parallel plate capacitor. Consequently, the impedance associated with the *TM mode* (here Z_{yx}) and ρ_a will abruptly jump across the interface. This distortion in the curves is exactly that which qualifies the *TM mode* to resolve lateral inhomogeneity more accurately than the *TE mode* does.

Distortions of impedance caused by free charges accumulating on superficial and small scale conductivity discontinuities, i.e. on anomalies having depth and dimension less than the *skin depth* of the shortest applied period are undesirable. These impedance distortions results from undersampling in both time and space. The electrostatic charge on such inhomogeneities has a non-inductive effect, in accordance with the assumption that $\nabla \cdot \vec{E} = 0$, used in the derivation of the *telegrapher's equation*. However, the charge conservation distorts the electric field and the impedance magnitude and shifts the *apparent resistivity* curve by a constant factor over its entire period range without modifying its shape. Particularly, *TM mode* currents polarized in the $y-$direction are susceptible to distortion. Since the impedance phase is unaffected and the phenomenon is period-independent, this is referred to as the *static shift effect* (Vozoff, 1987).

Although or rather since the modes reveal different sensitivity to discontinuities, due to the different governing boundary conditions and current flow directions they supply complementary views of heterogeneous structure. Berdichevsky et al. (1998) outline the practical attributes of both modes. While the *TM mode* is more sensitive to near-surface structures, including small scale anomalies that cause the *static shift effect*, and more robust to 3-D effects induced by conductive structures, the *TE mode* is more suitable to resolve deep structure; thus less susceptible to *static shift effects*.

2.1.1.3. 3-D case

In a true world the conductivity distribution is always **three-dimensional** ($\sigma = \sigma(x, y, z)$) and the impedance tensor is a fully occupied matrix with unequal elements, in all coordinate systems

$$\overleftrightarrow{Z} = \begin{pmatrix} Z_{xx} & Z_{xy} \\ Z_{yx} & Z_{yy} \end{pmatrix}. \tag{2.41}$$

Until recently 3-D analysis was only rarely applied because of significantly higher computational costs compared to 1-D or 2-D investigations irrespective of the fact that 3-D analysis requires an area-covering data set which is also associated with higher survey costs. Usually, data of a "slightly" three dimensional underground are approached as two dimensional, provided that certain criterion are satisfied. However, with the increasing computational speed and memory capability accompanied by the continuous development of reliable 3-D algorithms the 3-D investigations attract more and more attention.

In the case when the conductivity exhibits different values when measured along different axis, the rock is referred to as *anisotropic* and the scalar quantity σ in Ohm's law

becomes a second rank 3-D tensor $\overleftrightarrow{\sigma}$:

$$\overleftrightarrow{\sigma} = \begin{pmatrix} \sigma_{xx} & \sigma_{xy} & \sigma_{xz} \\ \sigma_{yx} & \sigma_{yy} & \sigma_{yz} \\ \sigma_{zx} & \sigma_{zy} & \sigma_{zz} \end{pmatrix}. \tag{2.42}$$

2.1.2. Magnetic transfer functions

The *TE mode* is associated with a magnetic field whose vertical component is linearly related to the horizontal components via complex-valued magnetic transfer functions: T_x and T_y

$$B_z = T_x B_x + T_y B_y. \tag{2.43}$$

$\vec{T} = (T_x, T_y)$ is sometimes called *tipper* because it is accompanied by tipping $\vec{H}$ out of the horizontal plane. The vertical magnetic field is only present above structures with lateral conductivity gradients and lateral conductivity boundaries. Its magnitude depends directly on the intensity of the different currents that are induced by the primary magnetic field in the heterogeneous Earth and polarized in the strike direction, i.e. along interfaces between the conductive layers. Hence B_z is determined fully by the magnitude of the conductivity gradient, or the conductivity contrast. Consequently, it can help resolve ambiguity in strike, and furthermore can be used to image the distribution of conductivity in the Earth; and particularly to show where good conductors are located. In a homogeneous or layered 1-D half space, $B_z = 0$ and $T_x = T_y = 0$ as well. The information inherent in the vertical magnetic field about the conductivity distribution can be visualized by *induction arrows* and plotted on a map. For this the *induction arrows* are commonly separated into real and imaginary parts:

$$\vec{P} = \Re(T_x)\vec{x} + \Re(T_y)\vec{y}, \qquad \vec{Q} = \Im(T_x)\vec{x} + \Im(T_y)\vec{y} \tag{2.44}$$

with the real magnitude M_r and phase shift ϕ_r

$$M_r = \sqrt{\Re(T_x)^2 + \Re(T_y)^2}, \qquad \phi_r = \arctan\left(\frac{\Re(T_y)}{\Re(T_x)}\right) \tag{2.45}$$

and imaginary magnitude M_i and phase shift ϕ_i

$$M_i = \sqrt{\Im(T_x)^2 + \Im(T_y)^2}, \qquad \phi_i = \arctan\left(\frac{\Im(T_y)}{\Im(T_x)}\right). \tag{2.46}$$

In the perfect 2-D case presented above with strike in $x-$direction, $T_x = 0$ and equation 2.43 simplifies to:

$$B_z = T_y B_y. \tag{2.47}$$

If only a single two-dimensional conductivity anomaly is present, a plot of the real arrows will point away from regions of enhanced conductivity due to Wiese convection (Wiese, 1962), while imaginary vectors change sign at a period where the real parts are maximal. The length of the real arrow reflects the gradient or conductivity contrast. The magnitude is largest at periods where the anomaly has the biggest induction effect.

2.1.3. Dimensionality analysis

Recall that in the pure 2-D case the impedance tensor in equation 2.35 has zero elements on the diagonal ($Z_{xx} = Z_{yy} = 0$), and non-zero on the off-diagonal ($Z_{xy} \neq Z_{yx} \neq 0$) if the mensural alignment corresponds to the *principal coordinate system*. However, in practice the measurement arrangement are oriented to magnetic north, irrespective of geological strike, and does not coincide with the *principal coordinate system*. Nevertheless, the systems are simply coupled by a rotation through the angle α from the mensural coordinates to the new *principal coordinate system* via the rotation matrix, $\overleftrightarrow{R}$:

$$\overleftrightarrow{R} = \begin{pmatrix} \cos\alpha & \sin\alpha \\ -\sin\alpha & \cos\alpha \end{pmatrix}. \tag{2.48}$$

Thus, the fields $\vec{E}$, $\vec{B}$ in a mensural system can be linearly transformed to $\vec{E}'$, $\vec{B}'$ in a new *principal coordinate system* by matrix multiplication of the measured fields:

$$\vec{E}' = \overleftrightarrow{R}\vec{E} \qquad \vec{B}' = \overleftrightarrow{R}\vec{B}. \tag{2.49}$$

Thus, the new tensor expressed in the *principal coordinate system* is diagonal. The new impedance tensor and the relationship between $\vec{E}$ and $\vec{B}$ in terms of the original measured values can be expressed in terms of a similarity transform:

$$\overleftrightarrow{Z}' = \overleftrightarrow{R}\overleftrightarrow{Z}\overleftrightarrow{R}^T \qquad \vec{E} = \overleftrightarrow{R}\overleftrightarrow{Z}\overleftrightarrow{R}^T\vec{B}. \tag{2.50}$$

This operation obviously modifies the individual values, but certain combinations of terms remain constant, independent of the rotation angle and initial reference frame. These relations, well-known as *rotational invariants* characterize a (non-symmetric) second-rank, 2-D tensor, and are referred by e.g. Bibby (1986); Szarka and Menvielle (1997); Weaver et al. (2000); Vozoff (1987):

- $I_1 = Z_{xy} - Z_{yx}$
- trace $tr(\overleftrightarrow{Z}) = I_2 = Z_{xx} + Z_{yy}$
- determinant $det(\overleftrightarrow{Z}) = I_3 = Z_{xx}Z_{yy} - Z_{xy}Z_{yx}$.

One of several ways to determine the angle α between the strike and the measurement's alignment is minimizing the principal diagonal elements of the impedance tensor $|Z_{xx}(\alpha)|^2 + |Z_{yy}(\alpha)|^2 = min$ by satisfying the condition:

$$\frac{\partial}{\partial\alpha}(|\,Z_{xx}(\alpha)\,|^2 + |\,Z_{yy}(\alpha)\,|^2) \;=\; 0 \tag{2.51}$$

with a solution for α derived for instance by Swift (1967):

$$\alpha_{Swift} = \frac{1}{4}\arctan\left(\frac{2\Re[(Z_{xx} - Z_{yy})\,(Z_{xy} + Z_{yx})]}{|Z_{xx} - Z_{yy}|^2 - |Z_{xy} + Z_{yx}|^2}\right) \pm \frac{n\pi}{2}, \quad n = 0, 1, 2, ... \tag{2.52}$$

The diagonalization of $\overleftrightarrow{Z}$ should be understood simply as an approximation to a pure 2-D structure, which does not exist in the real world. A practical and widely used method to estimate the real dimensionality of the impedance tensor is to calculate the *skewness* or *skew* S defined by Swift (1967) as ratio of the absolute values of the previously mentioned rotational invariants:

$$S = \frac{|I_2|}{|I_1|} = \frac{|Z_{xx} + Z_{yy}|}{|Z_{xy} - Z_{yx}|}. \tag{2.53}$$

S disappears for a pure 1- or 2-D case (numerator = 0), whereas a value between 0.3 and 0.6 is usually interpreted, subject to the judgment of the observer, as an indicator of 3-D structure. Similarly, a relation between the rotated off-diagonal impedances, defined as the *anisotropy* A, is used as a tool to distinguish between 1- and 2-D structures:

$$A = \frac{\left|Z'_{xy}\right|}{\left|Z'_{yx}\right|}. \tag{2.54}$$

If the impedance tensor is distorted by non-inductive effects caused by small scale, 3-D heterogeneities, the skew and strike proposed by Swift will mostly lead to unsatisfactory results. The remedy is the *phase-sensistive skew* of Bahr (1988), η_{Bahr} that is rotationally invariant and focuses on the phases of the impedance tensor beeing unsusceptible for galvanic distortions:

$$\eta_{Bahr} = \frac{\sqrt{|[D_1, S_2] - [I_2, I_1]|}}{|I_1|} \tag{2.55}$$

where $[D_1, S_2] = \Re(D_1)\Im(S_2) - \Im(D_1)\Re(S_2) = \Im(S_2 D_1^*)$, $D_1 = Z_{xx} - Z_{yy}$, $S_2 = Z_{xy} - Z_{yx}$ and * denotes complex conjugate. Using the Bahr model, the angle, α_{Bahr} of the *phase-sensitive strike* is found from:

$$\alpha_{Bahr} = \frac{1}{2} \arctan \left(\frac{\Im\left(S_2 I_2^*\right) - \Im\left(I_1 D_1^*\right)}{\Im\left(D_1 I_2^*\right) + \Im\left(I_1 S_2^*\right)} \right). \tag{2.56}$$

2.1.3.1. Phase tensor

In order to interpret the MT data, techniques have been developed that try to recover undistorted transfer functions from the regional conductivity distribution in deeper levels, removing near-surface distortions. In general, these methods are based on decomposition of the impedance tensor, and use the assumption of a simple regional 2-D conductivity structure superposed by local multi-dimensional heterogeneities which produce *galvanically* distorted, i.e. non-inductive, responses (Bahr, 1988; Groom and Bailey, 1989; Jiracek, 1990). Caldwell et al. (2004) and Bibby et al. (2005) present a method to analyze magnetotelluric data where the phase relationship between the horizontal components of electric and magnetic fields can be directly derived from the observed and *galvanically* affected impedance tensor without any assumptions or foreknowledge of dimensionality of the underlying regional structure. The approach provides to determine

the dimension of the impedance tensor, and, in the 2-D case, the strike direction. This method is based on phase relationships which can be generalized to a real second rank *phase tensor* $\overleftrightarrow{\Phi}$ defined as product of the inverse real $\overleftrightarrow{X}^{-1}$ and imaginary $\overleftrightarrow{Y}$ part of the complex impedance tensor $\overleftrightarrow{Z} = \overleftrightarrow{X} + i\overleftrightarrow{Y}$

$$\overleftrightarrow{\Phi} = \overleftrightarrow{X}^{-1}\overleftrightarrow{Y}. \tag{2.57}$$

Caldwell et al. (2004) show that the observed *phase tensor* is produced by underlaying regional structure and unsusceptible to any local galvanic distortions. The initial point is that an electric observed field $\vec{E}$ distorted by a local inhomogeneity can be expressed in terms of a distortion matrix $\overleftrightarrow{D}$ as

$$\vec{E} = \overleftrightarrow{D}\vec{E}_R, \tag{2.58}$$

where $\vec{E}_R$ is the undistorted regional electric field. Whereas no distortion (to a good approximation) is expected in the observed magnetic field $\vec{B}$, so that it may be taken to equal the regional magnetic field $\vec{B}_R$ (Groom and Bahr, 1992; Singer, 1992; Chave and Smith, 1994). These conditions modify the observed impedance $\overleftrightarrow{Z}$ as follows:

$$\overleftrightarrow{Z} = \frac{\vec{E}}{\vec{B}} = \frac{\overleftrightarrow{D}\vec{E}_R}{\vec{B}_R} = \overleftrightarrow{D}\overleftrightarrow{Z}_R, \tag{2.59}$$

with the regional impedance tensor $\overleftrightarrow{Z}_R$. As complex quantities, the observed impedance tensors can be separated into real ($\overleftrightarrow{X}$) and imaginary ($\overleftrightarrow{Y}$) parts:

$$\overleftrightarrow{Z} = \overleftrightarrow{X} + i\overleftrightarrow{Y} \qquad \overleftrightarrow{Z}_R = \overleftrightarrow{X}_R + i\overleftrightarrow{Y}_R. \tag{2.60}$$

which in turn can be written using equation 2.59 as:

$$\overleftrightarrow{X} = \overleftrightarrow{D}\overleftrightarrow{X}_R \qquad \overleftrightarrow{Y} = \overleftrightarrow{D}\overleftrightarrow{Y}_R. \tag{2.61}$$

By applying these relationships to the phase tensor equation 2.57 it becomes clear, that the measured phase tensor is identical with the regional one and thus not affected by local galvanic distortions

$$\overleftrightarrow{\Phi} = \overleftrightarrow{X}^{-1}\overleftrightarrow{Y} = (\overleftrightarrow{D}\overleftrightarrow{X}_R)^{-1}\overleftrightarrow{D}\overleftrightarrow{Y}_R) = \overleftrightarrow{X}_R{}^{-1}\overleftrightarrow{D}^{-1}\overleftrightarrow{D}\overleftrightarrow{Y}_R = \overleftrightarrow{X}_R^{-1}\overleftrightarrow{Y}_R = \overleftrightarrow{\Phi}_R. \tag{2.62}$$

The tensor elements Φ_{ij} are in general different from the phases calculated from the corresponding impedance tensor components $\phi_{ij}(T) = \arg(Z_{ij}(T))$, i.e. $(\Phi_{ij} \neq \phi_{ij})$ which becomes more clear by rewriting the tensor in matrix form:

$$\begin{pmatrix} \Phi_{xx} & \Phi_{xy} \\ \Phi_{yx} & \Phi_{yy} \end{pmatrix} = \frac{1}{\det(\overleftrightarrow{X})} \begin{pmatrix} X_{yy}Y_{xx} - X_{xy}Y_{yx} & X_{yy}Y_{xy} - X_{xy}Y_{yy} \\ X_{xx}Y_{yx} - X_{yx}Y_{xx} & X_{xx}Y_{yy} - X_{yx}Y_{xy} \end{pmatrix} \tag{2.63}$$

with $\det(\overleftrightarrow{X}) = X_{xx}X_{yy} - X_{yx}X_{xy}$. Any symmetric tensor of rank 2 can be represented as a diagonal matrix with non-zero elements on the main diagonal and zero entries

outside, by applying the principal axis transformation. This transformation converts the tensor into a mutually rotated coordinate system without altering its properties. Mathematically, it is equivalent to a classical eigenvalue problem. The principal axis represent a new, "individual" or "own" (eigen) coordinate system that is associated with the diagonal matrix representation of the tensor and determined by the orientation of the eigenvectors. The eigenvectors compose a rotation matrix which transforms the tensor matrix into diagonal form. In the preferred orientation the magnitude of the eigenvectors correspond to the eigenvalues of the diagonal matrix. These relationships are valid only for an idealized two-dimensional structure. In the general case, with three-dimensional and non-symmetric structure the maximum and minimum magnitudes don't correspond to the eigenvalues but rather they are defined by principal or singular values. In particular it is not possible to determine the principal axis via solution of an eigenvalue problem. Graphically, any tensor of second rank can be represented as an ellipse (Fig. 2.1). Its equation, especially the orientation and lengths of the major and minor axes,

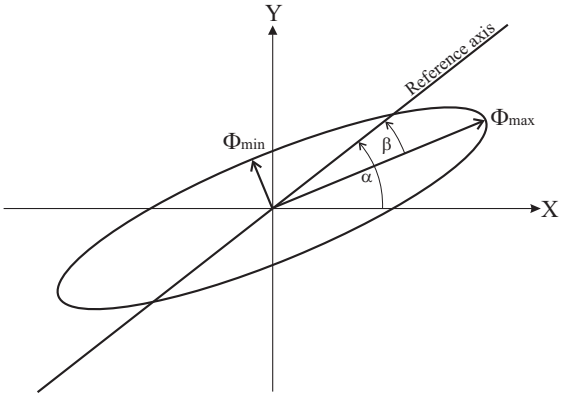

Figure 2.1.: Ellipse as a graphical representation of the phase tensor after (Caldwell et al., 2004). In the symmetric case, its shape and position can be completely determined by two *rotationally invariant* Φ_{max}, Φ_{min}; which are the singular values of the diagonal tensor matrix, and describe the major and minor axes of the ellipse, respectively; and by the angle α, which reflects the orientation of the symmetric tensor in the coordinate system. In the non-symmetric case the orientation of the ellipse is rotated away from its symmetric position by the *skew angle* β.

corresponds to the principal axes, and the singular values of the tensor matrix can be estimated by singular value decomposition (SVD). In terms of *rotational invariants*, which are free of distortions caused by near-surface inhomogeneities, the phase tensor can be formulated as:

$$\overleftrightarrow{\Phi} = \overleftrightarrow{R}^T(\alpha - \beta) \begin{pmatrix} \Phi_{max} & 0 \\ 0 & \Phi_{min} \end{pmatrix} \overleftrightarrow{R}(\alpha + \beta) \tag{2.64}$$

where $\overleftrightarrow{R}(\alpha + \beta)$ is a rotation matrix, and $\overleftrightarrow{R}^T(\alpha - \beta)$ the transpose of a rotation matrix. Φ_{min} and Φ_{max} are the minimum and maximum singular values of $\overleftrightarrow{\Phi}$ and can be expressed

as functions of the invariants of the impedance tensor $\overleftrightarrow{Z}$:

$$\Phi_{max} = \frac{1}{2}\left[\left(tr(\overleftrightarrow{\Phi})\right)^2 + \left(sk(\overleftrightarrow{\Phi})\right)^2\right]^{\frac{1}{2}} + \frac{1}{2}\left[\left(tr(\overleftrightarrow{\Phi})\right)^2 + \left(sk(\overleftrightarrow{\Phi})\right)^2 - 4det(\overleftrightarrow{\Phi})\right]^{\frac{1}{2}} \quad (2.65)$$

$$\Phi_{min} = \frac{1}{2}\left[\left(tr(\overleftrightarrow{\Phi})\right)^2 + \left(sk(\overleftrightarrow{\Phi})\right)^2\right]^{\frac{1}{2}} - \frac{1}{2}\left[\left(tr(\overleftrightarrow{\Phi})\right)^2 + \left(sk(\overleftrightarrow{\Phi})\right)^2 - 4det(\overleftrightarrow{\Phi})\right]^{\frac{1}{2}}, \quad (2.66)$$

where $tr(\overleftrightarrow{\Phi}) = \Phi_{xx} + \Phi_{yy}$, $sk(\overleftrightarrow{\Phi}) = \Phi_{xy} - \Phi_{yx}$ and $det(\overleftrightarrow{\Phi}) = \Phi_{xx}\Phi_{yy} - \Phi_{xy}\Phi_{yx}$. The angles α and β describe the orientation of the phase tensor ellipse. The non-invariant α reflects the position of a reference axis relative to the coordinate system and is defined as:

$$\alpha = \frac{1}{2}\arctan\left(\frac{\Phi_{xy} + \Phi_{yx}}{\Phi_{xx} - \Phi_{yy}}\right). \quad (2.67)$$

An additional *rotational invariant*, the *skew angle* β has to be introduced to describe the rotation of the ellipse axis away from an ellipse represented by a symmetrical tensor, i.e. away from the 2-D case:

$$\beta = \frac{1}{2}\arctan\left(\frac{\Phi_{xy} - \Phi_{yx}}{\Phi_{xx} + \Phi_{yy}}\right) = \frac{1}{2}\arctan\left(\frac{sk(\overleftrightarrow{\Phi})}{tr(\overleftrightarrow{\Phi})}\right). \quad (2.68)$$

The value of β is a measure of the degree of asymmetry caused by the non-symmetric 3-D background. In an approximate 2-D case ($\beta \approx 0$), the tensor becomes symmetric and the singular values coincide with the eigenvalues (Bibby, 1986; Bibby et al., 2005; Caldwell et al., 2004; Heise et al., 2006).

3. Presentation of the study area

The history of magmatism at the Chilean margin extends into the late Paleozoic ∼305 Ma ago, when oceanic plate subduction along the Chilean segment of Gondwana began. However, the Andean tectono-magmatic cycles associated with the formation of N-S running magmatic arc systems - approximately similar to what can be seen nowadays - started in the Jurassic, and were initiated by the break-up of Gondwana and the opening of the South Atlantic Ocean (Glodny et al., 2006). A mountain chain which ranges over 7000 km and forms the western margin of the South American Continent is the most recognizable result of the plate collision and subduction of the Nazca beneath the South American plate. Its relief reaches from 8000 m depth in the oceanic trench to nearly 7000 m in the Main Cordillera of the Northern and Central Andes; and 4000 m depth to 3000 m altitude for the Southern Andes (see Fig. 3.1). This chapter focuses on the Andean evolution in South-Central Chile, between latitudes 38°S and 41°S, where 1960 the most powerful earthquake ever recorded (moment magnitude $M_w = 9.5$) occurred (Cifuentes, 1989) as well as on previous geophysical investigations in this area.

3.1. Geological setting - the evolution and tectono-magmatic history of South-Central Andes

The study area is located in the northernmost Patagonian (Neuquén) Andes, and can be subdivided into several main morphotectonic units (Melnick et al., 2006a) which consist of (see Fig. 3.2):

- a narrow Coastal Platform, comprising uplifted Tertiary marine and coastal sequences;
- the Coastal Cordillera, with elevation ranging from 1500 m to only a few hundred meters, formed by a Permo-Triassic accretionary complex, the Western Series and a late Palaeozoic magmatic arc, the Eastern Series (Hervé, 1988; Glodny et al., 2006; Hackney et al., 2006);
- the Longitudinal Valley, also called Central Depression or Central Valley, a basin filled with up to 2 km thick Oligocene-Miocene sedimentary and volcanic rocks, covered by Pliocene-Quaternary sediments;
- the Main Cordillera, formed by the modern magmatic arc and intra-arc volcano-sedimentary basins;
- the Loncopué Trough, an extensional basin east of the Main Cordillera associated with abundant mafic volcanism (e.g., Folguera et al., 2006);

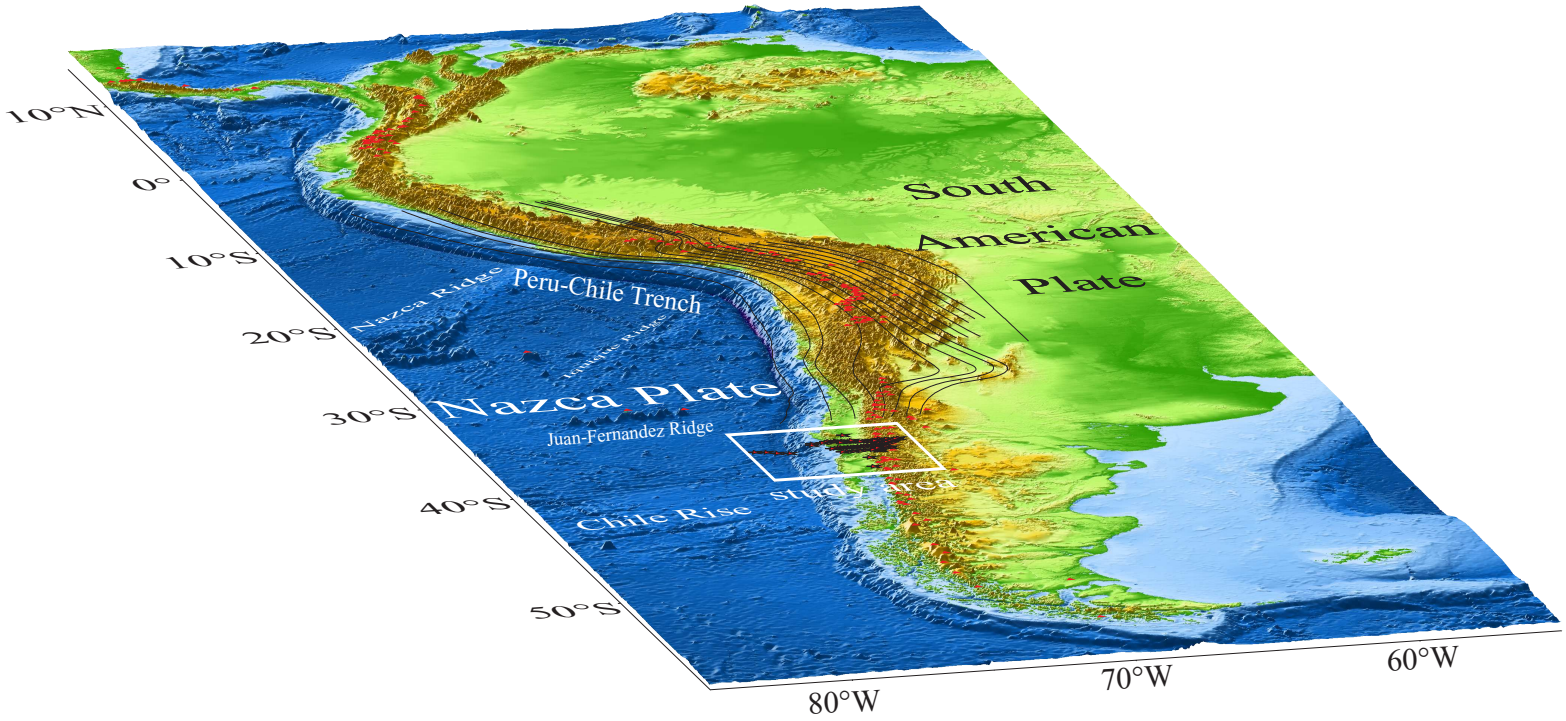

Figure 3.1.: Relief around South America based on ETOPO2 data. Depth contours (from left to right: 50 km to 350 km at 25 km intervals) delimit the Wadati-Beniof zone between $8°S$ and $36°S$ imaged by hypocenter locations from globally registered earthquakes (Isacks, 1988). The oceanic Nazca plate converges toward the continental South American plate at a rate of 65 mm/yr and an angle of $N77°E$ (Klotz et al., 2006). Red triangles mark Holocene volcanoes (catalogue from Smithsonian Institution, Global Volcanism Program). The white frame indicates the location of the magnetotelluric study area.

- the southern extension of the Agrio fold-and-thrust belt and
- the Mesozoic Neuquén Basin and the Cretaceous-Tertiary foreland basin to the east.

3.1.1. Pre-Andean evolution

Since the earliest beginnings of tectonic and magmatic activity in the late Paleozoic, the Chilean margin has passed through several evolutionary stages, generating a variety of geological features. They reflect distinct magmatic events, which are in turn related to changes in ocean-floor geodynamics and changes in both the velocity and the obliqueness of the subducting plate. Periods of intense eruptive activity were followed by magmatic and tectonically quiescent intervals in which erosion and sedimentary processes prevailed. Unsurprisingly, the former Paleozoic Andean history was obliterated and overprinted by younger tectonic cycles. Nevertheless, some orogenic features (like the magmatic

arc and the accretionary wedge) provide evidence for a tectonically active margin and subduction-related magmatism in the Paleozoic.

Eastern and Western Series Another Paleozoic relic is the forearc fold and thrust belt, consisting of two metamorphic units, the *Eastern* and *Western Series*, which are disrupted, and slipped along a major crustal discontinuity - the Lanalhue Fault Zone. The *Eastern Series* is presumably formed by thrusting and frontal accretion of rocks with turbiditic and sedimentary origins. The signatures of meta-sedimentary or meta-turbiditic sequences in the *Western Series* are interpreted as an exposed basal-accretionary wedge fed with oceanic lithology and turbidites via a subduction channel (Glodny et al., 2006, 2008; Hervé et al., 2007).

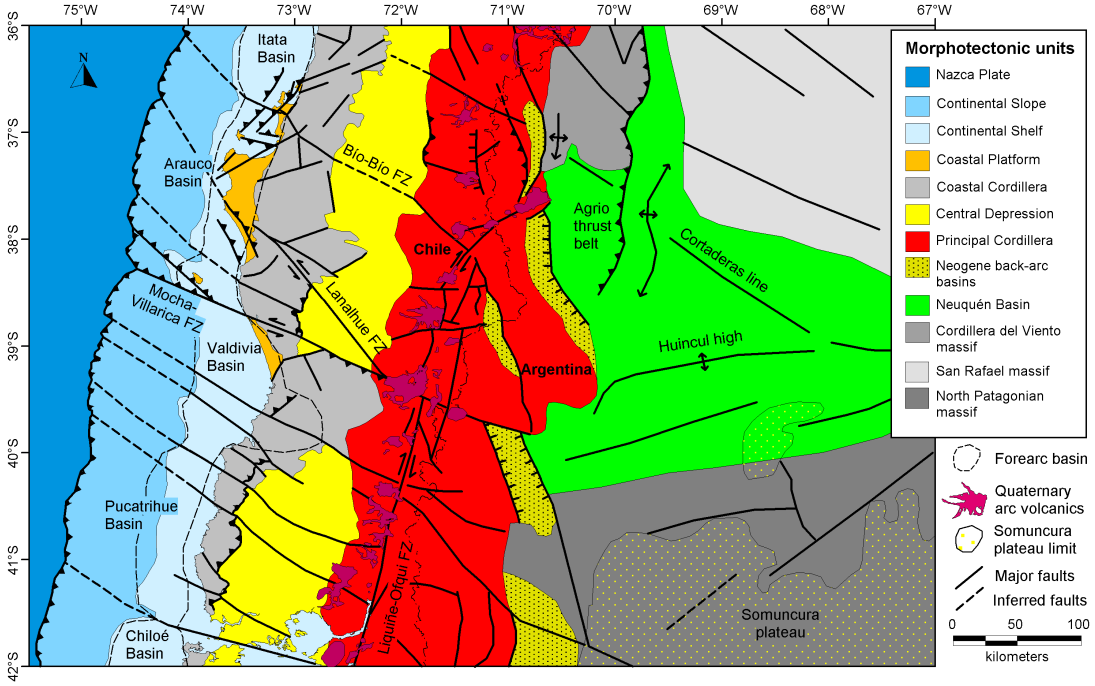

Figure 3.2.: Morphotectonical overview with major faults of the South Chilean continental margin after Melnick (2007).

3.1.2. "Andean tectonic cycle"

The second subduction-related tectonic cycle referred to as the "Andean cycle", began with tectonic and magmatic activity in the Jurassic along the entire Pacific margin, and continues to imprint the Andean evolution to the present day. In the early phase the magmatism was dominated by mantle melts, and concentrated in the Main Cordillera and backarc (Glodny et al., 2006; Pankhurst, 1990). It has generated a magmatic arc

close to its present location and the North Patagonian Batholith, which forms a north-south trending belt in the Main Cordillera of mostly granitoid origin. On the northern flank, the extensions of the continuous block pass into unsystematically distributed outcrops. North of 38°S, the batholith complex, generated in the Carboniferous to Permian, is displaced to the west and forms the Coastal Batholith belt along the margin; a few patches of this occur south of 38°S (Hervé et al., 1988, 2007; Parada et al., 2007).

3.1.2.1. Plutonism in the Cretaceous

A period of voluminous plutonism in the Cretaceous is exemplified by large outcrops of granitoid intrusions within the North Patagonian Batholith, and even in the Coastal Cordillera south of 39°S. The intense magmatic activity, particularly in the forearc, was probably triggered by reorganization on the Phoenix plate in the mid to late Cretaceous (Glodny et al., 2006).

3.1.2.2. Magmatic activity in the Oligocene-Miocene

After marginal tectonic and volcanic activity in the Palaeocene and Eocene, major changes in the subduction geometry followed in the Oligocene to Miocene, as the the Farallon plate broke up and split into the Cocos and the Nazca plates. This event initiated probably an increase in convergence rate from <4 cm/yr to >10 cm/yr, as well as a less oblique convergence angle between the Nazca and South American plates (Muñoz et al., 2000). A higher convergence rate is in turn associated with a steeper subduction angle of the descending slab and a migration of the volcanic front 80-100 km westwards towards the Coastal Cordillera (Fig. 3.3) (Parada et al., 2007).

Hints of this migration are provided by outcrops in the Longitudinal Valley and the Coastal Cordillera, which include late Oligocene and early Miocene volcanic complexes. The lava generated by effusive eruptions overlie a Palaeozoic-Triassic basement and underlie, cover, or are interbedded with late Oligocene to early Miocene continental and marine sedimentary sequences. These facts suggest that the Longitudinal Valley and Coastal Cordillera were covered at that time with ocean, and thus the volcanic belt was formed in a marine environment, perhaps as an island arc built on the Paleozoic-Triassic continental crust. Moreover, they mean that the extension-related Oligocene-early Miocene magmatic activity partially overlapped with the opening or subsidence of the forearc and intra-arc sedimentary basin and the initiation of the evolution of the present-day Longitudinal Valley (Muñoz et al., 2000; Parada et al., 2007). Some authors, referring to the composition of the mid-Tertiary Coastal Magmatic Belt magmas, ascribe the trigger for the transistory volcanic activity in the Coastal Cordillera to an asthenospheric mantle upwelling through a slab window which opened between the young, fast, and steeply descending Nazca plate and the old, slow, and flattened subducting Farallon plate rather than simple slab dehydration (Muñoz et al., 2000; Stern et al., 1990; Parada et al., 2007).

This forearc magmatism was accompanied by contemporaneous volcanic activity in the intra-arc and backarc (Glodny et al., 2006) since the changes in the plate movement

and subduction geometry caused crustal extension and thinning, which in turn favored the ascent of asthenospheric melts from the upwelling mantle into the crust. Released volcanic eruptions formed volcanic belts in the Longitudinal Valley, the Main Cordillera, and the backarc, which resulted in broadening of the volcanic system culminating in a maximum of activity between 15-9 Ma.

This period of widespread magmatism concluded in the mid-Miocene, as the subducting slab flattened and closed the slab window, causing the magmatic chain to be re-established as a narrow structure, and returned to the Main Cordillera (Muñoz et al., 2000; Glodny et al., 2006). An assemblage of marine sediments interbedded with igneous rocks of a thickness up to 2 km indicates that during the extension and broadening of volcanic activity into the forearc, the emerging Longitudinal Valley was used in the Oligocene-Miocene as a depocenter for detritus, mainly derived from the eroded Coastal Cordillera (Parada et al., 2007; Glodny et al., 2006). Furthermore, the extension reactivated pre-existing, major fault structures like the Lanalhue Fault Zone, a sinistral strike-slip fault, which is interpreted as the former divergent contact zone between the Western and Eastern Series (Glodny et al., 2006, 2008).

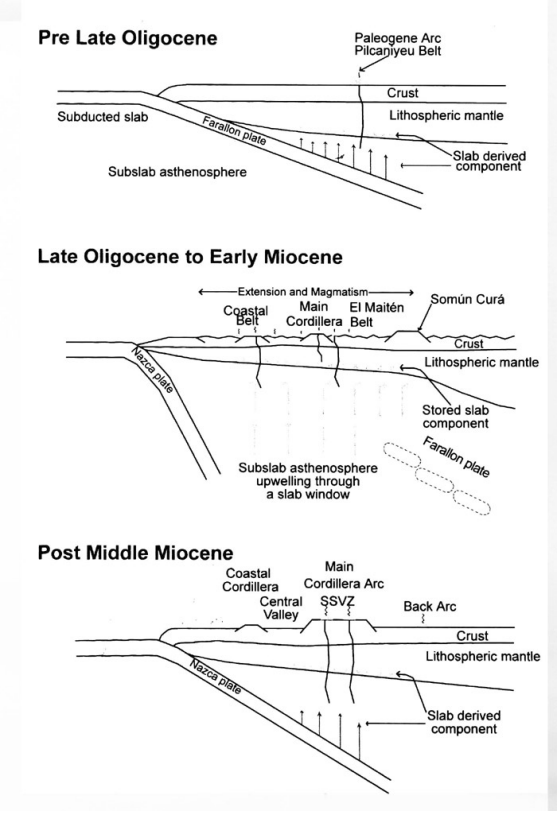

Figure 3.3.: Schematic tectonic section showing the evolution of the South Chilean margin from the pre-Oligocene to the post-Miocene (from Muñoz et al. (2000)). Changes in slab dip and convergence rates resulted in westward migration of the volcanic front and extension across the continental margin during late Oligocene to early Miocene.

3.1.2.3. Plio-Pleistocene to Holocene Evolution

Since the Miocene, no significant changes occurred in the subduction geometry or tectonic regime. A revival of a transient episode of intense volcanism in the Pliocene and Pleistocene in the arc-backarc system manifested itself mostly in enhanced production and geochemical variations of magma. In fact, geochemical and geochronological signatures indicate a broad magmatic arc reaching up to the Loncopué Trough in the east (retroarc). A decrease in the convergence rate and moderate steepening of the subducted slab in the early Pleistocene caused a westward narrowing of the arc, as well. In contrast to previous Oligocene-Miocene events, the magmatic arc front did not migrate westwards; it remained largely stable in its current position ∼250 km east of the trench (Glodny et al., 2006; Lara and Folguera, 2006; Ramos and Kay, 2006). Seismic and gravimetric studies suggest a thinned crust in the western retroarc which can be related to the minor steepening of the subducting oceanic plate and extensional deformation of the crust (Yuan et al., 2006; Folguera et al., 2006). Particularly sensitive to the attenuation of the crust are ancient lithospheric structures so that the extensional deformation may results in a reactivation of partly pre-Andean discontinuities and lithospheric boundaries. The intersection of the Loncopué Trough and Huincul ridge in the South Andean retroarc corresponds to such crustal attenuation and an extended astenospheric wedge, and is considered to be a reactivated ancient suture between the Patagonia terrane and the Gondwana margin. This zone, associated with an asthenospheric ascent or anomaly, is marked at the surface by a particular concentration of late Pliocene to Quaternary calderas and volcanic centers. They are distributed along fractures and extensional faults, which offer pathways for rising magmas (Folguera et al., 2007).

In the Longitudinal Valley up to 2 km of Pliocene-Quaternary deposits have accumulated, covering Oligocene-Miocene sequences. The marine sedimentation has been focused into the Peru-Chile Trench, which is filled with up to 2 km of continental material. The continental shelf contains at least several hundred meters of deposits. Both the on- and offshore sedimentation rate and pattern were affected by climate variations, like glaciation, during the Pleistocene. In particular, during the interglacial period the continental shelf acted as a depocenter for terrestrial material, whereas during the glacial periods, the accumulation in the trench supplied by turbiditic currents increased (Völker et al., 2006; Melnick and Echtler, 2006a,b; Bangs and Cande, 1997; Blumberg et al., 2008; Glodny et al., 2006).

3.1.2.4. LOFZ

The recent volcanism is apparently controlled by one of the most conspicuous tectonic features of southern Chile: a mega-shear zone trending trench-parallel in N10°E direction, at a distance of ∼280 km east of the trench, extending for over 1 000 km from the triple junction of the Antarctic, South American, and Nazca plates to ∼38°S: the Liquiñe-Ofqui Fault Zone (LOFZ) (Cembrano et al., 1996, 2000, 2007). The LOFZ system is characterized by a series of N-S to NNE-SSW lineaments along the magmatic arc, regional-scale faults, horse-tails, graben, fault bend and pull-apart basins, fault splays,

tension gashes, and crop-scale faults with volcanic dikes, and marked by a chain of stratovolcanoes with some of the most active volcanoes in South America, e.g., Villarrica, Llaima, and Lonquimay. Most of the volcanoes are established either directly over the LOFZ, or along secondary structures running parallel to the arc (Lavenu and Cembrano, 1999; Rosenau et al., 2006; Melnick et al., 2006a,b; Melnick, 2007; Gonzáles-Ferrán, 1994). However, independent of this approximately NNE-SSW distribution of the large stratovolcanoes, several minor eruptive centers, parasitic vents, and flank craters are rather aligned NE-SW as well as NW-SE, and thus obliquely to the LOF. Nakamura (1977) and López-Escobar et al. (1995) have related the arc-oblique, N50-70°E trending lineaments to the maximum horizontal stress S_H in the arc region, and have postulated a system of crustal fractures and tension gashes that enable the ascent of molten or partially molten material to the surface and generate crustal feeder dikes.

The LOF-oblique, NW-SE orientated fault system crosses the arc and forearc, and is closely connected to the major eruption in the Cordón Caulle volcanic complex immediately after the largest ever recorded earthquake with moment magnitude M_w = 9.5, that occurred on 22 May 1960 (Lara et al., 2004). At the western border of the Longitudinal Valley, the fault system continues with strikes of N30°E to N40°E (Lavenu and Cembrano, 1999). In particular, the Lanalhue Fault which also runs obliquely to the main morpho-structural units, is regarded as an inherited, continuously reactivated, pre-Andean structure associated with deep-reaching seismicity (Yuan et al., 2006). This fault has been active since the Mesozoic, and is thus a long-living structure which is reactivated repeatedly as a response to changes in subduction geometry.

Modified subduction conditions due to reorganization in the subducting plate affect the stress field and are reflected in the partitioning of deformation and the kinematics of the faults: both the Lanalhue, as well as the Liquiñe-Ofqui Fault. In this way the right-oblique subduction in the Eocene-Miocene (48-26 Ma) initiated or reactivated dextral slip at the LOFZ with a transtensional tectonic regime. After a phase in the Miocene with orthogonal convergence, owing to the break-up of the Farallon plate, the subduction became right-oblique again at 20 Ma leading to transpression and dextral slip at the LOFZ (Rosenau, 2004; Cembrano et al., 1996, 2000).

Nowadays, the subduction again occurs obliquely, with an angle of ∼25° with respect to the plate margin (i.e. N77°E), and with a current velocity of ∼6.5 cm/yr (Klotz et al., 2006). The current dextral slip along the LOFZ may be promoted by the oblique convergence and a strong interplate coupling, resulting from the subduction of young and buoyant oceanic lithosphere as well as the collision of the Chile Ridge with the overriding South American Plate (Cembrano et al., 1996, 2000).

3.2. Previous and present electromagnetic studies

Several previous geological and geophysical investigations in the region have been performed by the present day in order to obtain a better understanding of the subduction mechanism, and to provide an insight into the Earth's interior beneath the Andes. The aim of the electromagnetic measurements at the South Chilean margin is imaging of the

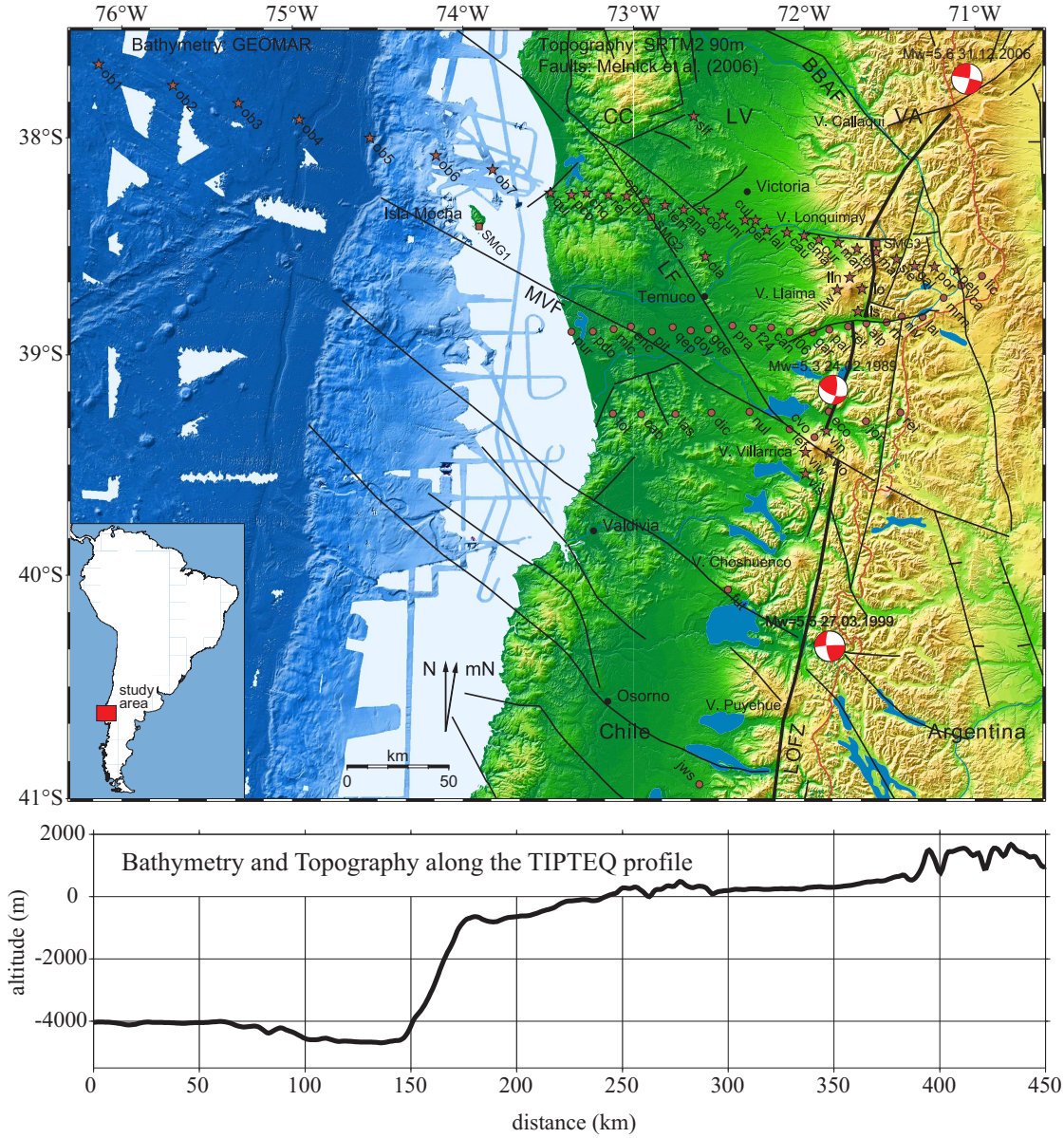

Figure 3.4.: a) Shaded relief map of the study area at the South Chilean margin. Topography is based on SRTM (NASA), swath bathymetry is from various cruises of RV Sonne (Scherwath et al., 2006), fault traces (black lines) are modified from Melnick et al. (2006a). Faults mentioned in the text: LOF Liquiñe-Ofqui, LF Lanalhue, MVF Mocha-Villarrica and BBAF Bío-Bío-Aluminé Fault, respectively. CC denotes Coastal Cordillera, LV Longitudinal Valley, VA volcanic arc; mN is magnetic north with a declination of $10°E$ from geographic N. Stars indicate sites from the recent TIPTEQ expedition 2004/2005, circles from 2000; SMG1-3 are monitoring sites operated by GFZ Potsdam. b) profile showing bathymetry/ topography along the TIPTEQ track.

electrical conductivity structure in the subduction zone. Since an enhanced conductivity in the Earth is usually associated with fluids or high temperatures due to melting Earth material, the electromagnetic method, and especially magnetotellurics, is a suitable tool for investigation of subduction zones where fluids and molten rocks are expected.

The first magnetotelluric deep sounding experiment in South Chile was carried out in the 80's by Muñoz et al. (1990) at the active Villarrica volcano. The 1-D modelling of the short (AMT) and long (MT) period data yielded a model of a conducting zone with a resistivity of 20-60 Ωm at a depth between 35-50 km. This is supported by preliminary 2-D models showing that the zone of poor resistivity, whose upper boundary is at 45-60 km depth, is surrounded by highly resistive material (Muñoz et al., 1990).

This pilot experiment was followed in 2000 by the initiation of a project run by the Free University of Berlin in the framework of the collaborative research center SFB 267, *Deformation Processes in the Andes*. 34 long period MT stations were established, primarily along two profiles, with a separation of approx. 10 and 15 km, respectively, running perpendicularly to the well known geological structures, like the volcanic arc and the trench from the coast to the Argentinian border (Fig. 3.4).

An early modeling approach, which inverted only impedance data, shown in Fig 3.5, revealed a modest high conductivity zone (HCZ) in the lower crust, beneath and east of the active volcanic arc, presumably controlled by the Liquiñe-Ofqui Fault; and an additional HCZ beneath the Central Depression, associated with the Lanalhue Fault in the forearc. Another finding was based on the anomalous behavior of geomagnetic induction vectors, which point consistently NE throughout the whole study area, instead of the expected east direction, due to the presence of the highly conductive Pacific Ocean. This spectacular effect could only be explained by an anisotropic structure in the crust (Brasse and Soyer, 2001; Soyer, 2002; Brasse et al., 2009).

To corroborate these unexpected results, and especially to investigate the role of fluids and melts in the subduction process and to image fluids in the interface between the downgoing Nazca and the overriding South American plate, further electromagnetic experiments were conducted. The area became the subject of an amphibious electromagnetic investigation as part of the multi-disciplinary **TIPTEQ** (from **T**he **I**ncoming **P**late to mega-**T**hrust **E**arth**Q**uake processes) project from December 2004 to the end of February 2005. During the campaign a total of 33 long-period magnetotelluric stations were deployed between latitudes 37.5° - 41°S, along a line running perpendicularly to main geological structures such as the trench and the volcanic arc, in order to measure the variation of the magnetic and electric fields. It extended over 400 km: from the incoming plate to the Argentinian border north of the previous profile, and encompassed on land the areas of the Coastal Cordillera, the Longitudinal Valley and the Principal Cordillera. The TIPTEQ track with 23 stations on the land side, established with a separation of approximately 10 km, was additionally extended with an offshore component on the sea side comprising 7 sea-bottom stations from the Woods Hole Oceanographic Institution (WHOI), deployed across the Peru-Chile Trench towards the Pacific Ocean at intervals of 30-35 km, during RV Sonne leg SO-181 (Fig. 3.4). The survey is part of a large-scale magnetotelluric network, including 3 profiles in this area, several connecting sites and small, auxiliary networks of stations around the active volcanoes Villarrica

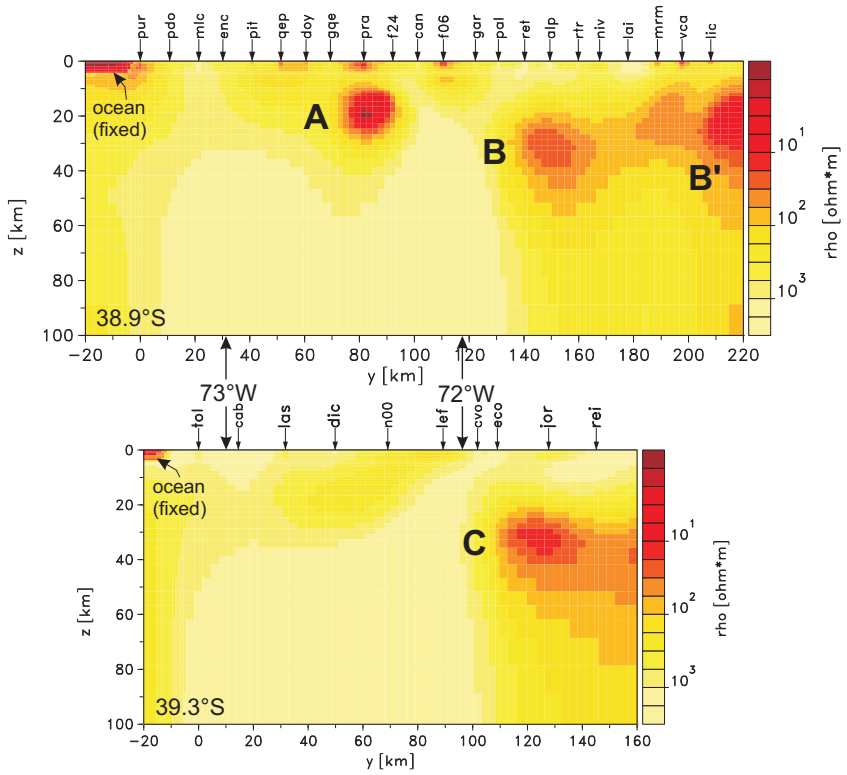

Figure 3.5.: Resistivity models from 2-D inversion of the impedances along both profiles surveyed in 2000 (Brasse and Soyer, 2001). High conductivity zones (HCZ) are marked with letters.

and Llaima, intended as auxiliary to the profiles in order to study the conductivity distribution beneath the volcanic arc. For monitoring of temporary variability in the geomagnetic transfer function, 3 stations from the GeoForschungsZentrum Potsdam (GFZ) have been operated out close to the profile and on Isla Mocha for a time period of 3 years (O. Ritter, pers. comm.). During the two campaigns, a network with a total number of 72 stations was deployed, yielding electromagnetic (MT and GDS) transfer functions in the period range between 10 s – 20000 s.

The analysis of the data from the recent electromagnetic survey in the Southern Andes and comparison with the previous results in order to complete the image of the conductivity distribution in the South Chilean subduction zone, is the subject of this study.

3.3. Other geophysical investigations

The structural image of the South Chilean subduction zone like the geometry of the downgoing plate, the plate interface, and Moho depths may be inferred from a large number of recent seismic experiments (Bohm et al., 2002; Lueth and Wigger, 2003;

Rietbrock et al., 2005; Haberland et al., 2006; Krawczyk et al., 2006; Yuan et al., 2006; Groß et al., 2008). The first seismic investigations in the area between latitudes 36° and 40°S, where the great earthquake of 1960 occurred, were carried out in framework of the **ISSA 2000** project (Integrated Seismological experiment in the Southern Andes) and comprise a temporary seismological network and a refraction seismic profile. The study revealed an east dipping band with a continuous seismicity down to 120 km depth, which can be associated with the Wadati-Benioff zone and the subducted Nazca Plate, and two maxima of seismicity at 20 - 30 km and 60 km depth (Bohm et al., 2002). While the first maximum is caused by the seismic coupling between the downgoing and overriding plates the cluster of earthquakes at 60 km depth is supposed to be related to dehydration processes in the oceanic plate, probable dehydration embrittlement. A further region of seismicity, associated with crustal seismicity, is located in the forearc in the upper plate and coincides with Bío-Bío and Lanalhue Faults. The latter seems to be a lithospheric-scale discontinuity, which has been imaged by a swarm of earthquakes in the entire upper plate down to the plate boundary (Yuan et al., 2006).

The depth of the continental Moho calculated via the receiver function method reveals spatial variations across the section, and correlates with topographic features. The lower boundary of the lower crust reaches ∼40 km beneath the Main Cordillera, and shallows eastwards to ∼35 km below the Neuquén Basin, and to ∼30 km beneath the Loncopué Trough, probably owing to backarc spreading and thinning of the crust in the Pliocene-Pleistocene. Beneath the Longitudinal Valley the position of the Moho is derived from refraction seismic data, and is at 25-30 km depth. The receiver functions derived image of the crust is also in accordance with the two-dimensional velocity model of the refraction seismic profile along 39°S, which corresponds to the middle MT profile (Fig. 3.6) (Yuan et al., 2006; Bohm et al., 2002; Krawczyk et al., 2006).

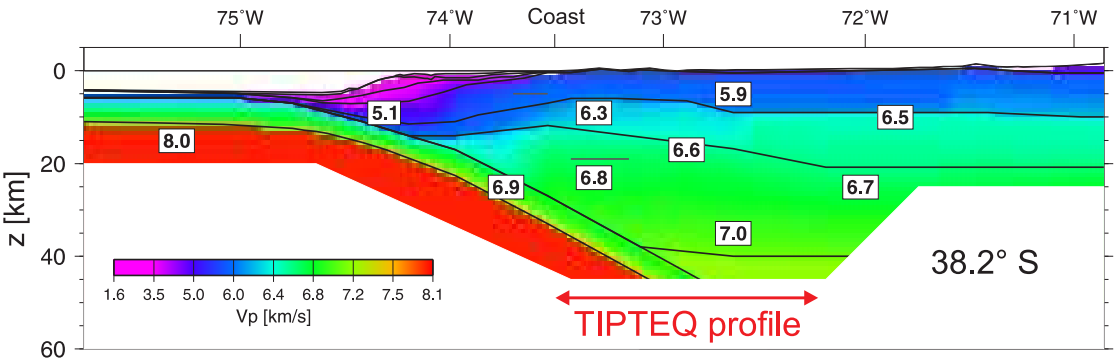

Figure 3.6.: Wide angle P-wave velocity model from the SPOC-study along a profile at 38.2°S, showing the geometry of the subducted plate and the velocity structure (Krawczyk and the SPOC Team, 2003; Groß et al., 2008).

In autumn 2001, the region between 36° and 40°S, became the subject of amphibious investigations in order to study tectonophysical features in the seismogenic coupling zone and the forearc. The study, including a wider spectrum of methods, such

as combined offshore-onshore, reflection and refraction seismic, passive seismic, gravity, as well as magnetotellurics, were performed within the multidisciplinary project **SPOC** (Subduction Processes Off Chile). The onshore reflection seismic experiment, focusing particularly on the seismogenic plate interface, provides a high resolution of the internal structures in the Permo-Triassic accretionary wedge, with several reflective bands between 5 and 25 km, which are interpreted as meta-basitic and meta-ophiolitic structures (Krawczyk and the SPOC Team, 2003; Krawczyk et al., 2006; Sick et al., 2006). The offshore study detected up to 2-3 km thick terrigenous sedimentary deposits (turbidites) in the trench, and a maximum 150 m thick layer of pelagic sediments, covering an approximately 6-7 km thick, faulted oceanic crust. The oceanic Moho is observed in the offshore seismic data at about 10 km beneath the ocean, and at approximately 40 km under the Coastal Cordillera.

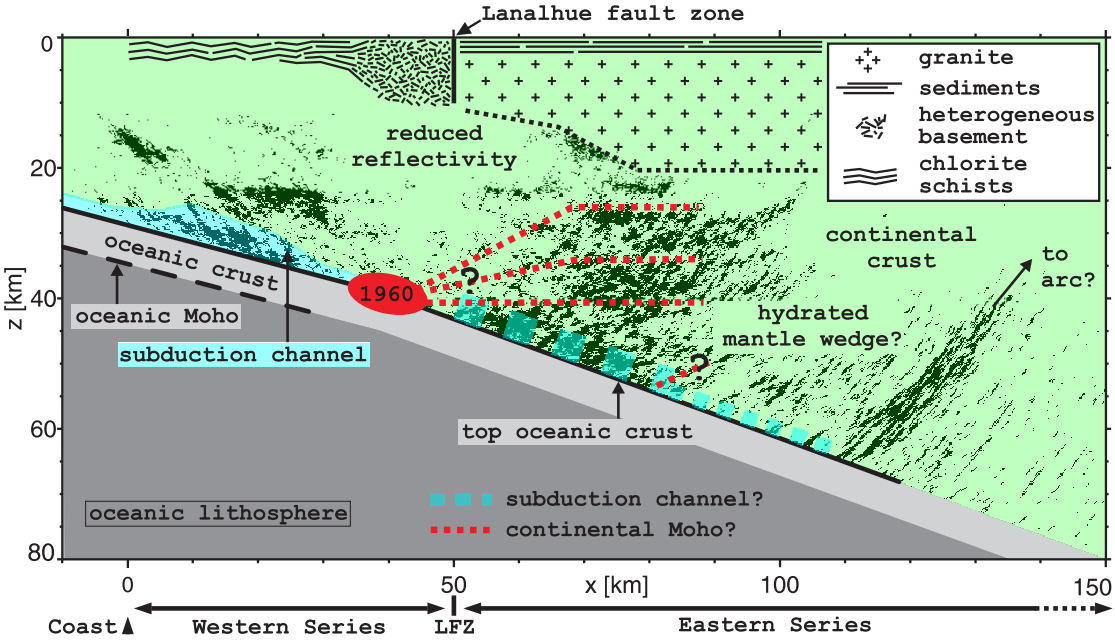

Figure 3.7.: Preliminary interpreted seismic section along the TIPTEQ profile at 38.2°S kindly provided by (Groß et al., 2008). 1960 marks the hypocenter of the largest ever recorded earthquake.

Based on the seismic results of the very latest amphibious and multi-disciplinary study of the TIPTEQ program, the reflective band interpreted as the top of the downgoing Nazca plate can be prolongated to 50 km depth below the Central Valley. Thus, it is in accordance with the results of the SPOC 2001 study. The 2 - 5 km thick reflectivity band at the plate interface at 24 - 36 km below the coastal region is attributed to water saturated and downwardly transported material, and it continues, analogously to observations in the Cascadia subduction zone, eastwards to 40 - 55 km depth in the mantle wedge. Groß et al. (2008) and Krawczyk et al. (2006) interpret this as a signature of

a fluid filled subduction channel. According to a common theory, the subduction channel represents a zone consisting of water-saturated upper oceanic crust, and sediments derived from the trench and oceanic plate (Fig. 3.7). It differs from the surroundings due to the strong impedance contrast. A similar effect may be caused by dehydration processes from downward transport of water-saturated material and migration of fluids into the continental crust. In this manner, some high reflectivity can be attributed to the presence of fluids above the oceanic lithosphere. The same dewatering processes, on the other hand, reduce the velocity contrast between the continental crust and mantle, and consequently prevent a seismic image of the continental Moho.

The plate interface is also evidently marked by an easterly dipping, high-seismicity zone in the coastal wedge between 20 and 40 km depth. This earthquake cluster is related to an inhomogeneous stress distribution in the coupling zone, and presumable accounts for the forearc fragmentation and faulting. An analysis of the ratio of seismic P- and S-wave velocities (ν_p/ν_s) suggests the presence of fluids in the marine forearc; these were probably expelled from fluid-saturated sediments, as well as from within the coupling zone of the plate interface (subduction channel) (Haberland et al., 2006, 2009).

4. Analysis of the onshore data

4.1. Onshore instruments and deployment

Magnetotelluric equipment generally consists of electric and magnetic field sensors and a data-acquisition system (datalogger) to sense fluctuations of natural electric and magnetic fields. The temporal variation of the electric field were calculated by measuring the potential difference between pairs of unpolarizable Ag-KCl electrodes, manufactured by GFZ Potsdam, after a design of Filloux (1973). The electrodes were connected via cables as dipoles of usually 100 m length, buffered with wet bentonite, and buried below the surface to ensure good electrical contact between electrodes and the ground and eliminate any temperature variations. To detect the fluctuations of the three magnetic field components a fluxgate magnetometer from MAGSON, consisting of a vector-compensated ring-core sensor, was used. Both electrodes and magnetometer were aligned with a geomagnetic reference frame which deviates due to magnetic declination from the geographic system in the measurement area in the time of the survey by approximately 7°. The magnetic declination changes with time and with position; it is calculated by the International Geomagnetic Reference Field Model (IRGF) and has to be considered in estimation of the electrical strike direction. The RAP (RAM-Apparatur) datalogger developed at the University of Göttingen by Steveling (1996) was used to sample the electromagnetic signals with a 2 s sampling rate. A recording time of at least two weeks from several, mostly simultaneously operating, instruments was targeted in order to perform remote reference processing; this is usually adequate to obtain data of satisfactory quality in the period band from 10 s-10000 s. The offshore instruments and their deployment are depicted in chapter 5.

The recorded data were converted to electromagnetic field units, and plotted over time, then visually checked for runtime, and any irregularities. Next, the time series were Fourier transformed, filtered and cleaned of outliers by employing the well-known processing scheme of Egbert (1997). This robust remote-reference algorithm yielded mostly high-quality magnetotelluric (MT) and geomagnetic transfer functions (referred to as GDS; Geomagnetic Depth Sounding) in the period range 10-10000 s. The former, known as impedances, are the ratio between the horizontal electric and magnetic field; the latter, known also as "tipper", express the ratio of the horizontal to vertical magnetic field.

4.2. Magnetotelluric transfer functions in South Chile

An overview of transfer functions, as they were used for subsequent modeling, is shown in Fig. 4.1. The images display a clear indication of static shift effects that displace the apparent resistivities relative to each other along the resistivity axes, and leave the phases unaffected. The shift is caused by near-surface and small scale anomalies, and, as expected, appears stronger in TM than in TE mode.

Data quality was generally satisfactory though regional differences can be observed. While in the Coastal Cordillera, Volcanic Arc, and backarc regions, the transfer functions in the 10-10000 s range are characterized by predominantly smoothly varying shape, apparent resistivities and phases in the Longitudinal Valley scatter strongly at periods over 1000 s, particularly in the Z_{xy} component. This corresponds to a NS oriented electric field, and thus to currents flowing along the Longitudinal Valley, and can be confirmed by inspecting the time series. It is thus apparent that the electric field, in particular, recorded in the densely populated Longitudinal Valley is strongly contaminated by cultural electrical noise. In contrast, the magnetic field seems not to be affected, inasmuch the magnetic transfer functions are not disturbed. Besides the anthropogenic noise that interferes with the induced electric field and biases the main- and off-diagonal impedances in the Longitudinal Valley, minor perturbations in the Z_{xy} component at periods mostly above 2000 s can also be observed in the transfer functions at other sites in the region. The scattering of impedance values, and rough curves are assumed to be the result of diminished signal-to-noise ratio due to the coast effect, which leads to damped magnitude in the E_x component of the electric field on the land side. These noise sources affecting the electric field limit the data usability at long periods, and cannot be eliminated by remote-reference processing, as can be applied to stabilize the transfer function at short periods.

All onshore transfer functions seem to indicate a multidimensional underground. A distribution of magnetotelluric transfer functions along a profile for the period of 744 s is presented in Fig. 4.2. Generally, the apparent resistivities in both modes jump from station to station for almost all periods. While the TM mode is generally sensitive to strike-aligned heterogeneous structures, and such discontinuities in ρ_a and more gentle also in ϕ across a conductivity contact are not surprising, and, even useful to resolve a transition zone between two adjacent inhomogeneities, in TE mode a rather more continuous conductivity distribution, and smoothly varying transfer functions are expected (see chapter 2). Particularly, any changes of apparent resistivity caused by induction should be accompanied, according to eq. 2.38, by corresponding variations in the phase. However, in the calculated transfer functions this is not the case. Especially in TM mode the phase values form a smooth curve as shown exemplarily for a period of 744 s in Fig. 4.2. Jumping phase values in TE mode can be classified as outliers due to worser data quality, as can be concluded from the relative large error bars. Thus the observed scattering transfer function in TM and TE modes along the profile are rather due to non-inductive galvanic effects than to huge and sudden conductivity discontinuities in the underground.

Prior to starting the modeling, inspection of apparent resistivities and induction vec-

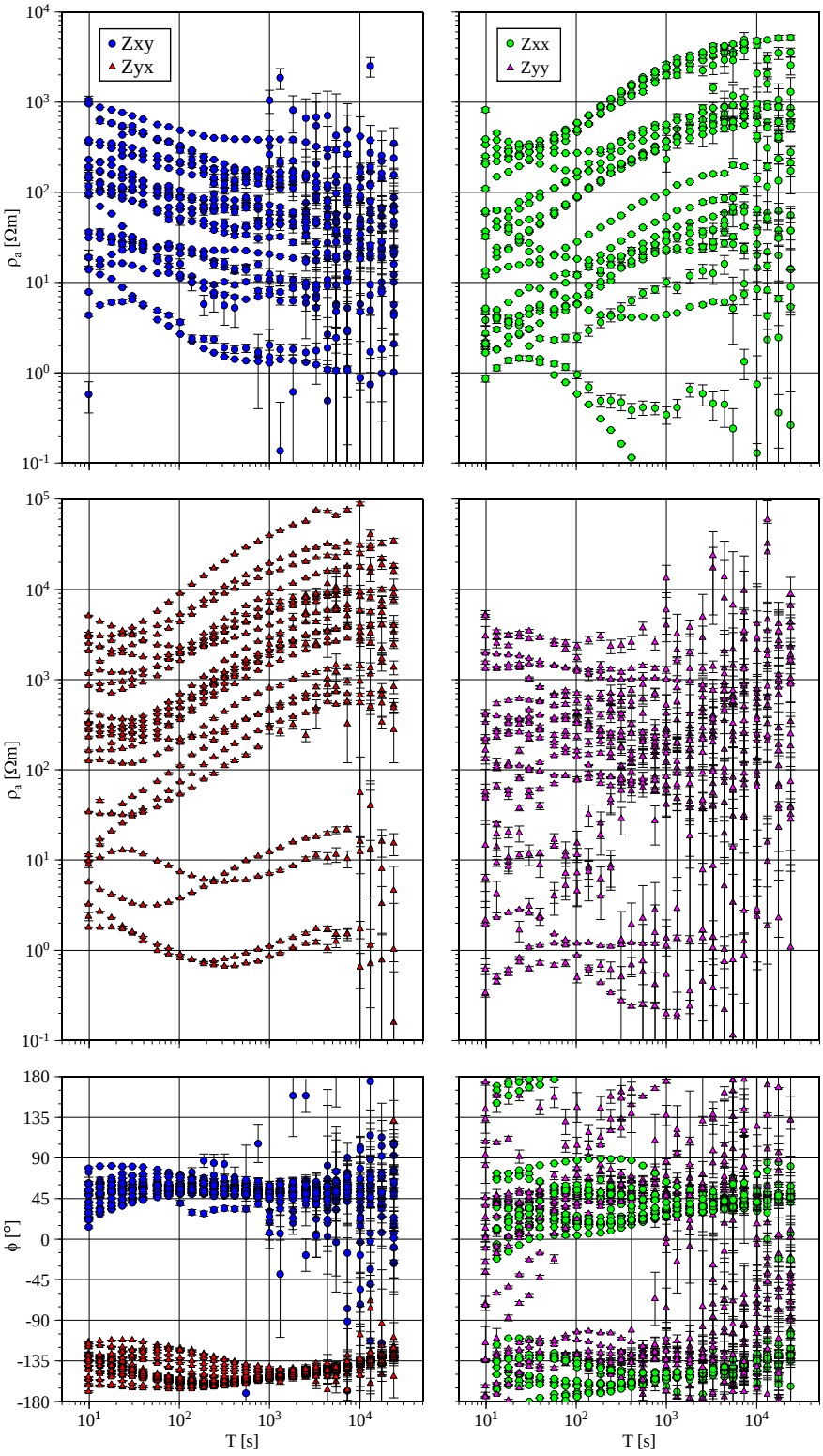

Figure 4.1.: Apparent resistivities and phases of all stations along the onshore TIPTEQ profile derived, from the off-diagonal (left) and on-diagonal (right) elements of the impedance tensor.

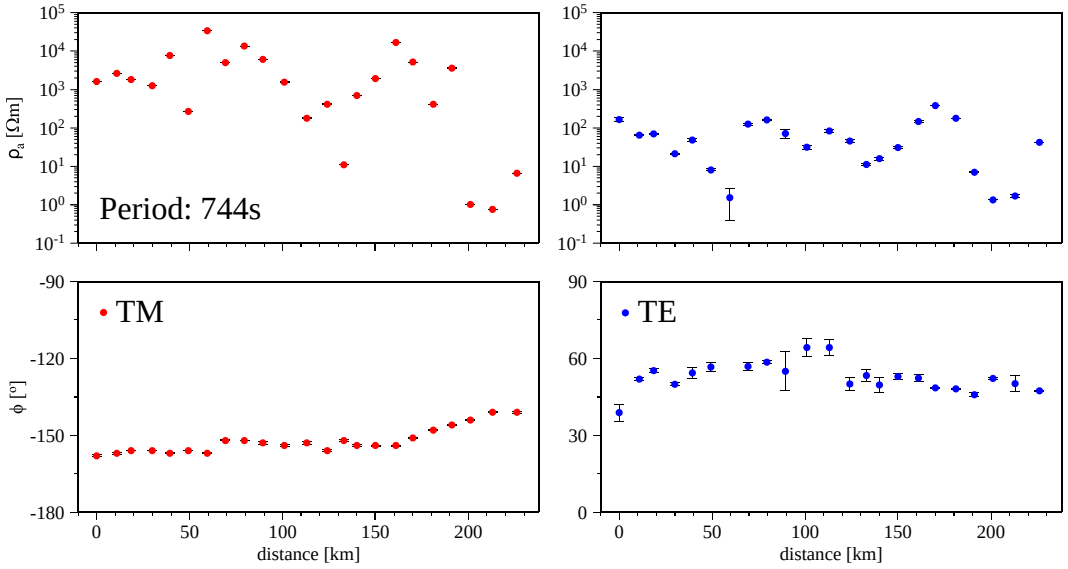

Figure 4.2.: An example of apparent resistivities and phases of TM and TE modes along the TIPTEQ profile at a period of 744 s.

tors at short periods, at the eastern end of the profile, indicate to enhanced conductivity in the lower crust, east of the active volcanic arc, and in the backarc.

Fig. 4.3 presents multi-site and multi-frequency magnetotelluric transfer functions, as pseudosections, for TE and TM modes. The pseudosection images reveal that the apparent resitivity distribution in TE mode is more moderate and smoother than that of TM mode. Certainly, this fact is related to the focus of the modes and their different sensitivity to strike-parallel or -perpendicular structures. While the TE mode better resolves the vertical structures, for lateral resolution, the TM mode is preferred. However, the strong lateral variations of apparent resistivities in the TM mode, accompanied by relatively smooth phases, suggest, that the transfer function in TM mode is strongly affected by static shift, as argued above. In the TE mode this effect is less pronounced, but still evident in a few transfer functions. Particularly in the eastern profile, a conductive structure evidenced over whole period range in apparent resistivity, is not accordingly reflected in the respective phases and thus this feature is probably caused by near surface sediments of the Bío-Bío Valley. These images are compatible with features in Fig. 4.1 and Fig. 4.2, and encourage stronger weighting of the phases than the apparent resistivities in modeling.

Due to static shift problem, the static shift-unbiased phase tensor is more appropriate to investigate trends in conductivity distribution. The phase tensor can be graphically represented as an ellipse whose colors are linked to the geometric mean of the tensor principal values, and indicate the vertical conductivity gradient. Plotted for all profile stations and against increasing period the phase tensors provide an overview of conductivity distribution versus depth, as shown in Fig. 4.4. Note that the range of the color scale is slightly modified compared to that of the scale in Fig. 4.3. Although the image

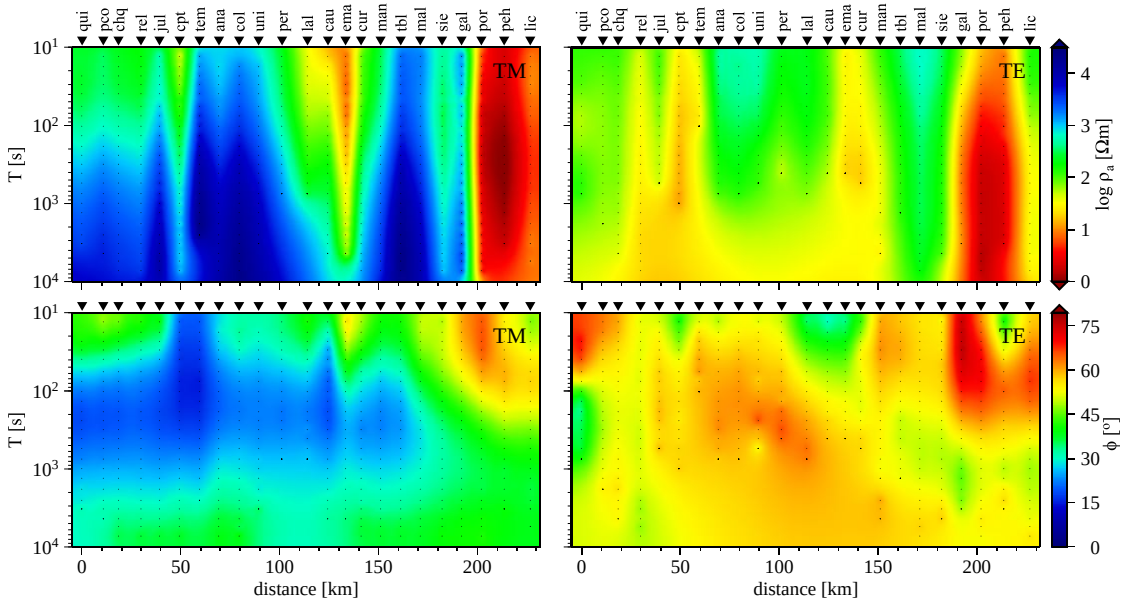

Figure 4.3.: Pseudosections of apparent resistivities and phases of TM and TE modes for TIPTEQ profile.

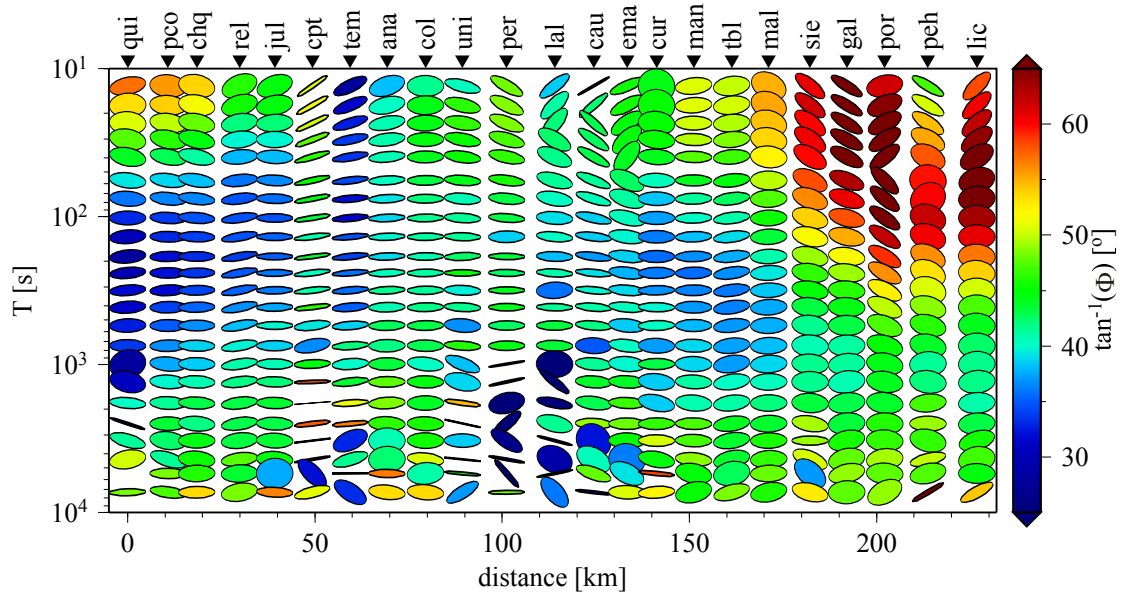

Figure 4.4.: Phase tensor ellipse map for the TIPTEQ profile. The minor axes of the ellipses correspond to the strike direction. The colors of the phase tensor ellipses are the geometric mean of the maximum and minimum phases.

is a composite of both modes, and thus involves the main features of both, a direct comparison with the pseudosections in Fig. 4.3 can mislead one to conclude that the phase tensor can reproduce the phases of TM mode better than that of the TE. This impression may arise because in TM mode, the phase pseudosections present a more heterogeneous image, with a pronounced low phase feature ($< 25°$) and thus are more amplified than the rather homogeneous image with moderate phase values ($\approx 55°$) in TE mode. However, the most striking feature in the eastern part of the profile, with geometric mean values exceeding 45°, corresponds to conductive features in Fig. 4.3, and can be interpreted as an indicator of enhanced conductivity below the backarc.

4.3. GDS transfer functions

In addition to magnetotelluric impedances displayed as apparent resistivities and phases, the geomagnetic transfer function (tipper) derived from vertical and horizontal magnetic fields, may be also used to image the electrical conductivity in the Earth. The tipper, as well as the impedance, is a complex quantity and can be divided into real and imaginary parts which are commonly represented in the form of real and imaginary induction arrows or vectors. The commonly used term "vector" should be used with care when several induction anomalies are coupled (Siemon, 1997). In "Wiese convention", used here, the real vectors point, in unrotated coordinates, away from internal current concentration, and thus away from regions of enhanced conductivity, while imaginary vectors change sign at a period where the real parts are maximal (Wiese, 1962).

At an ocean margin, induction vectors point commonly away from the ocean and perpendicularly to the coastline, due to the high conductivity of seawater (in the range of $\sigma = 3\,\mathrm{S/m}$). This behavior, known as "coast effect" may be observable far inland, dependent on the resistivity of the continent. Accordingly, it was expected that in the Chilean margin the highly conductive ocean, with the average N10°E trend of the trench, and the similar overall course of the volcanic chain, would dominate the orientation of the real parts of the induction vectors giving them a general WE tendency. This is, however, not the case. Instead, at long periods (3277 s), all real induction vectors point systematically NE for all sites in the measurement area, regardless of which geological unit data were collected from (Fig. 4.5, right). Note that there is not a single site in the study area where this observation is contradicted. Thus, flow of anomalous currents in the continent – itself induced by magnetic field of coast parallel currents in the ocean – is not NS as would be the case for a simple 2-D distribution of conductivity, but obliquely deflected on a large lateral scale. On the other hand, this effect is not observed at shorter periods (Fig. 4.5, left): The coast effect is "normal", and vectors in the Coastal Cordillera point roughly perpendicularly away from the shoreline (not necessarily perpendicular to the trench, since local bathymetry is dominant at short periods). This also rules out an instrumental effect, which was initially suspected (and which gave rise to a later extensive test program of stations near the Niemegk geomagnetic observatory close to Berlin). Source effects should not play a significant role either, because the study area is located in mid-latitudes and far from both polar and equatorial electrojets. Except for the

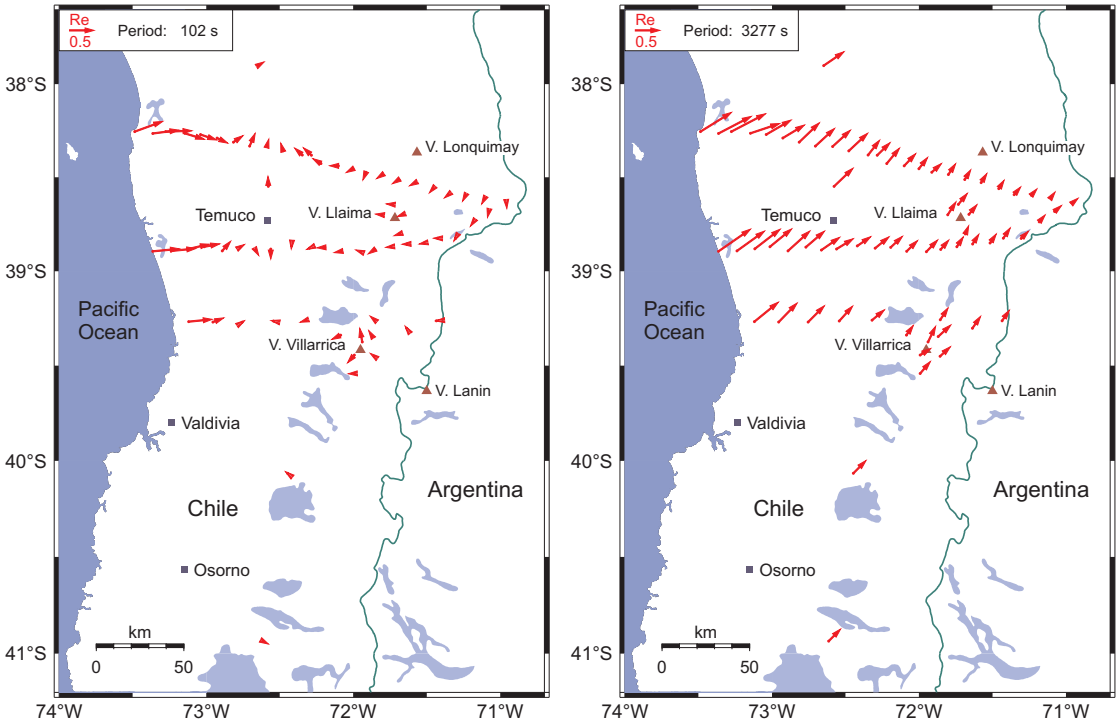

Figure 4.5.: Real induction vectors in South Chile from two campaigns in 2000 and 2004/2005. Left: at 102 s they display the coast effect near the Pacific Ocean and several local anomalies, particularly around Villarrica volcano; in contrast, Llaima volcano does not show an effect (the latter data were obtained in early 2005). Right: deflection of vectors at a period of 3277 s from the expected W-E direction over the entire study area.

westernmost stations, where the inductive influence of the Pacific ocean becomes visible in long vectors, all other vectors at 102 s are short and indicate no major conductivity contrast. In the eastern part of the area they point towards the west and turn east, indicating increasing conductivities below the volcanic arc. An interesting effect is visible around the highly active volcanoes Villarrica (altitude 2 847 m) and Llaima (3 125 m, latest eruption on January 1, 2008), where a small network of sites was established. Especially around Villarrica volcano, induction vectors at 100-200 s point away from the center of the volcano at the closest sites. Although all volcanic edifices themselves lead to a topographic effect at their slopes, this cannot be the reason for the direction and magnitude of vectors at Villarrica. Considering that the slope of Villarrica is only on the order of 25-30°, effects in MT transfer functions caused by topography are rather expected at short periods (<10 s) and only a static shift-like effect remains in apparent resistivities, as was shown by 2-D and 3-D modeling of topographic effects in the central Andes (Eydam, 2008; Brasse and Eydam, 2008). Moreover, arrows pointing away from volcano are not observed at the Llaima, and accordingly, this pattern is probably caused by enhanced conductivities in the upper crust, which produce these induction vectors,

rather than topography. It can be inferred that deeper in the crust beneath Villarrica, a large-scale magma deposit might exist – note that the crater at the top of Villarrica is filled with a lava lake (Calder et al., 2004). A more detailed statement about conductivity distribution at depth below the volcano requires a 3-D modeling approach (see chapter 6).

The magnitudes of the real part of tipper present an image consisting of a zone with magnitude values below 0.2 in the east and a zone with values up to 0.85 in the west, divided by a diagonal running interface (Fig. 4.6 left). This image clearly shows the effect of the ocean, which becomes particularly noticeable at stations close to the ocean (large magnitudes) for the entire observed period range, and continues smoothly with increasing periods landwards to the east. However, the ocean effect is limited to a relatively small part of the the onshore induction space, allowing one to regard the onshore stations in the eastern part of the profile as being largely free of any perturbations due to the ocean. The problem is discussed in detail in chapter 5. The phase shift ϕ_r, calculated according to 2.45, and representing the deviation of the arrows from north, is shown on the right. While for short and intermediate periods ($< 1000\,\mathrm{s}$) the tipper rotates along the profile by almost 360° due to crustal and near-surface conductors, it is approximately stable for long periods, or varies only slightly between 75° close to the ocean and 30° east of the Coastal Cordillera. Note that the turbulently oscillating induction arrows along the profile at short periods become quite abruptly stable at long periods. In Fig. 4.6 this transition is marked by a sharp bounded zone at intermediate periods.

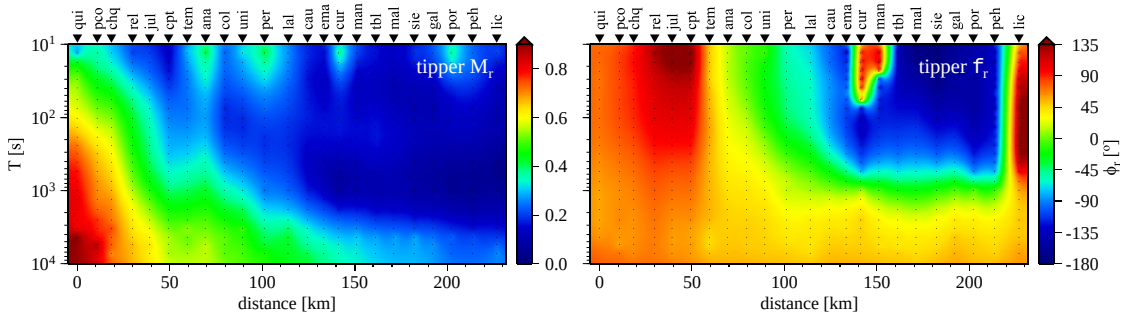

Figure 4.6.: Maps showing the magnitude of the real part of tipper (right) and its phase shift (left). The sensitivity of the transfer functions to the ocean effect strongly depends on period, specially the longer the period, the wider-reaching the effect. The broad spectrum of ϕ_r at short periods suggests that the real induction vectors change due to crustal anomalies along the profile orientation several times, whereas at long periods their orientations remains relatively constant.

4.4. Dimensionality analysis and geological strike estimation

A crucial and fundamental task in the analysis of magnetotelluric data and their interpretation is the investigation of the dimensionality of the underground. The target of

this investigation is to determine, if the transfer functions reflect a two-dimensional (2-D) background, so that two-dimensional modeling is sufficient, or if three-dimensional (3-D) structures are required by the data. In the 2-D case, i.e. if the conductivity structure can be approximated via a rotation through an appropriate angle to a 2-D geometry, Maxwell's equations decouple into two systems of equations associated with the TE and TM modes. In this case the electric currents can be referred to a geoelectrical strike and flow either parallel or perpendicular to this geological feature. In other words, the determination of the strike direction is equivalent to estimation of an angle by which the measured impedance tensor must be rotated in order to minimize the sum of its on-diagonal elements, and, subsequently to assign the off-diagonal elements to TE or TM modes. There are several techniques to estimate the dimensionality of the impedance tensor, and thus the regional strike.

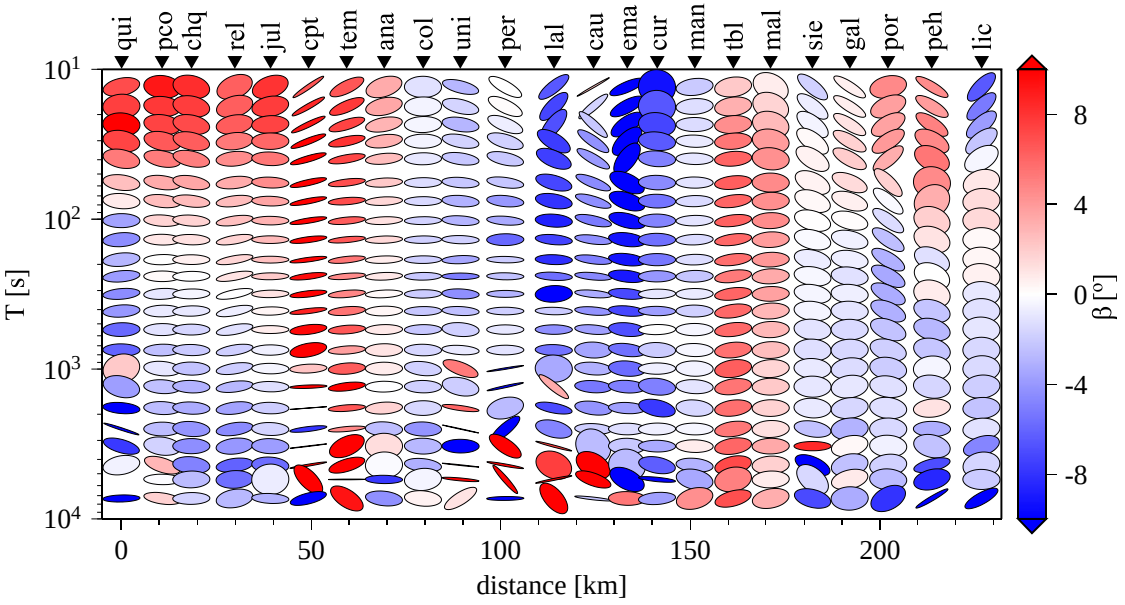

Figure 4.7.: Phase tensor ellipse map showing the dimensionality for the onshore TIPTEQ profile. The minor axes of the ellipses correspond to the strike direction. The colors of the ellipses express the skew angle β, which is a measure of asymmetry produced by 3-D structures.

Useful information about subsurface dimensionality can be extracted from the phase tensor that is represented as an ellipse whose major and minor axes correspond to the strike direction of the conductivity contrast. If the conductivity distribution is one dimensional, the regional currents do not have any preferred flow direction and the phase tensor is represented by a unit circle. The flow direction of the induced currents in the background of a survey area can be visualized by plotting of the phase tensor ellipses along the profile and against period. Such multi-site and multi-frequency maps provide an overview of dimensionality and conductivity distribution versus depth, as shown

already in Fig. 4.4. Fig. 4.7 shows a pseudosection of phase tensor ellipses surveyed along the profile for the period range between 10 – 10000 s, with the predominantly uniform EW orientated major ellipse axis. The colors of the ellipses express the skew angle β, which is a measure of asymmetry produced by 3-D structures. Thus it reflects the rotation of the ellipses axis away from its symmetric form, that in the 2-D case corresponds to the strike direction α (see Fig.2.1). Regarding the 90° ambiguity, the EW orientation of the major ellipse axis is aligned perpendicularly to the main morphological and geological structures, like the approximately NS striking trench, the similar overall course of the volcanic chain, and LOFZ. Thus the minor axis of the ellipses coincide with these features and with the NS striking normal of the conductivity gradient, as has been revealed by the strike angle analysis presented in Fig. 4.10 at the end of the chapter. Some deviations from uniform orientation occur at the shortest (< 40 s) and at long (> 1000 s) periods. Especially for the latter, in the middle of the profile, a wedge of randomly orientated ellipses is noticeable in Fig. 4.7, and can be attributed to poor data quality at periods above 1000 s in the Longitudinal Valley.

3-D effects observed at certain stations and periods in the Volcanic Arc, Longitudinal Valley, and Coastal Cordillera correspond to the results of dimensionality analysis of Bahr (1988) and to a lesser extent to Swift (1967) as shown in Fig. 4.8. As expected,

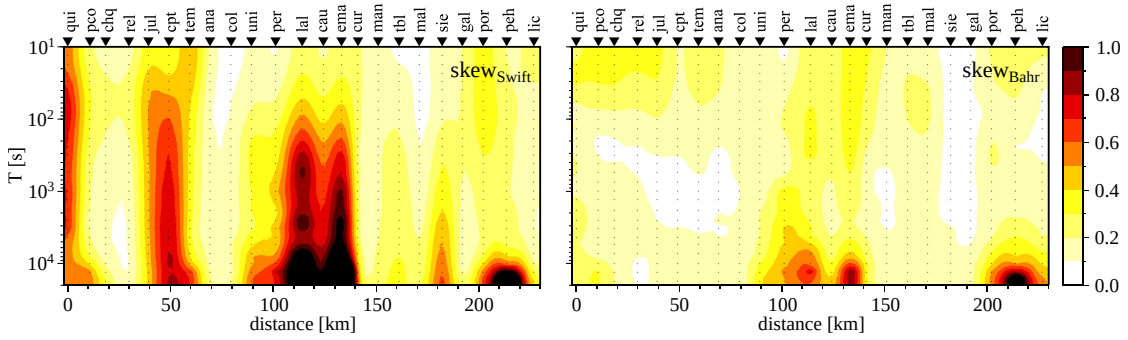

Figure 4.8.: Dimensionality maps calculated from the impedance tensor after Swift's method (left) and using the phase-sensitive and and for galvanic distortions unsusceptible Bahr model (right).

the phase-sensitive skew, estimated using the tensor decomposition approach of Bahr (1988), that separates local heterogeneities from regional underlaying 2-D structure, is less affected by galvanic distortion caused by small three-dimensional and non-inductive anomalies or current channeling, and yields a more stable and smooth image. Skew values around 0.3 are commonly regarded as the tentative threshold between 2-D and 3-D structure. These were observed at short periods in the coastal region, and correspond very well with high β values in Fig. 4.7, and can probably be related to effects produced by the ocean or bathymetric changes at the continental margin. High skew values at long periods in the Longitudinal Valley are caused by anthropogenic distortion of the electric field, previously observed in the discussion of time series and magnetotelluric

transfer functions, and corresponds with high β values and arbitrarily orientated ellipses in Fig. 4.7. Higher β values in the eastern Coastal Cordillera correspond roughly with high skew values shown by the Swift approach, but can't be confirmed by Bahr's method. However, the Swift skew estimated directly from the impedances can be distorted by near surface structures, like the highly conductive sediments in the Central Depression and the Bío-Bío Valley, producing higher skew values over a wide period range, so that care is required in the interpretation. In general, the skew is in the most part of the image below the value 0.3, so that an approach to model the data two-dimensionally might be adequate and 2-D interpretation of the target area seems to be justified.

The resulting strikes recovered using the Swift and Bahr methods are shown in Fig. 4.9 as multi-site and multi-frequency image for period range between 10 - 10000 s. Note that the strike obtained by the Swift model varies predominantly along the profile (in horizontal direction), from station to station and only marginally depends on period. This is because the impedances used in the Swift model are not free of static shift, which affects the entire period range. The phase-sensitive and galvanically less distorted Bahr model yields a more heterogeneous image with lateral and vertical variations. However, the magnitude of these variations is evidently smaller and the contrast weaker than in the Swift model so that the image is generally smoother, at least over most of the induction space. For this nearly homogeneous range the assumption of an approximately uniform regional strike is justified. Some deviations with stronger scattering values appear in the short-period band, and can be associated with diverse anomalies in the upper crust. The strike deviation of the overall trend below the volcanic arc and backarc at short and middle periods is also conspicuous.

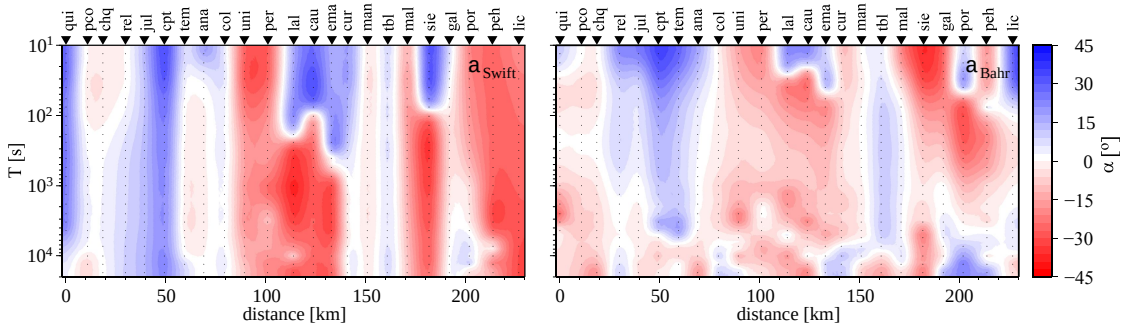

Figure 4.9.: Map with electrical strike recovered using the Swift method (left) and the phase-focused Bahr method (right).

Fig. 4.10 shows electrical strike directions estimated after an alternative multi-site and multi-frequency approach of Smith (1997), in the form of rose diagrams. It is a widely utilized way to clearly present the results of strike analysis. Since the strike direction can change depending on period, as well as different geological or tectonic conditions, the data were split into three period bands (short, intermediate, and long), and, separately, three profile sections in order to investigate the strike as a function of depth, and spatial

variations. Although the strike angles vary at the single stations, both the profile seg-

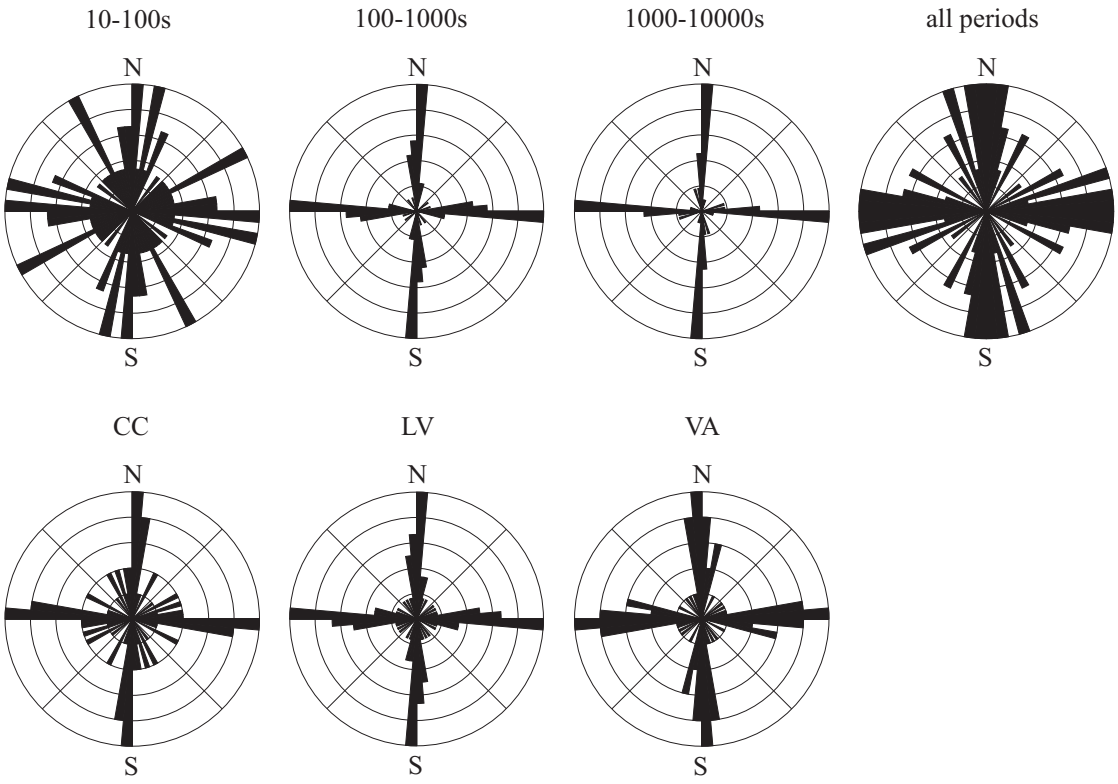

Figure 4.10.: Electrical strike of the onshore TIPTEQ profile calculated by algorithm of Smith (1997) and shown as circular histograms for short, intermediate, long period bands, and for the entire period range (top) and for three profile segments representing the main morphotectonic units in the survey area (CC: Coastal Cordillera, LV: Longitudinal Valley, VA: Volcanic Arc or Main Cordillera) for period range of 100-10000 s (bottom).

ments and the frequency bands exhibit a consistent and obvious approximate NS trend. Because of the 90° ambiguity inherent to impedances, the decision as to the true strike must be made by taking geological information into account. Regarding the extension of morphological structures like the trench and the volcanic chain, the strike runs approximately NS. The scattering of strike angles at short periods (10-100 s), where the influence of near-surface anomalies is dominant, is unsurprising. This effect continuous toward long periods, and masks any deeper lineaments, as becomes evident by plotting the strike for all periods together. Additionally the algorithm allows one to determine one "best" strike direction for all requested periods and stations, which yielded in this case a strike of N4°E. Note that the strike analysis was performed in a geomagnetic reference system and taking into account the magnetic declination of approximately N7°E in this area during the measurement time, the "best" strike of N4°E is equivalent to N11°E in a geographic frame, and is roughly perpendicular to the the survey profile. These

results confirm the strike direction estimated by the Bahr method presented in Fig. 4.9, and moreover the findings from dimensionality and strike analyses match previous results of the two southern profiles in the South Chilean margin performed by Brasse and Soyer (2001). On the basis of this results, rotation of the impedances for 2-D modeling was deemed unnecessary.

5. Magnetotellurics in marine environments

Offshore magnetotellurics is a useful method for exploration of the conductivity structure beneath the seafloor, particularly at ocean-continent subduction zones, where fluids and melts are known to control the subduction process. Evans et al. (2002) show that a combined on- and offshore magnetotelluric transect across a subduction zone may be able to resolve highly conductive structures associated with dehydration processes, water migration and melts.

Whilst the onshore magnetotelluric method is well established for imaging electrical conductivity structures deep in the Earth's interior, electromagnetic investigation in marine environments has attracted much less attention until recently, although the oceans cover most of the Earth's surface. Besides logistical challenges, high technical demands on the instruments and consequent higher costs, in particular physical conditions in marine environments restrict a direct application of the terrestrial approach to marine environments. The acquisition, analysis, and interpretation of offshore data require that the special conditions on the ocean bottom are taken into consideration, and thus can be more complicated than for onshore data. The ionospheric and magnetospheric primary source field recorded on the ocean bottom is, at short periods, strongly attenuated by the overlying highly conductive ocean layer, and, at long periods, is contaminated by motion-induced secondary electromagnetic fields. Thus, the broad period range of usable signals utilized in terrestrial MT is significantly reduced on the seafloor.

Additionally, care and attention has to be paid to the seafloor relief, which plays a far more important role in marine electromagnetic exploration than the land relief in onshore studies, and greatly affects the magnetic field, particularly at surveys at the continental shelf. The combination of both the changing seafloor shape and the covering highly conductive ocean layer induce a strong anomalous magnetic field directly above the sensing points, which radically distorts the source field and is reflected in the data by anomalous effects.

5.1. Electromagnetic oceanic effects

The electromagnetic fields and currents in the ocean can be divided into fields induced by external sources, and fields induced by motion of high-conductivity water masses through the Earth's main magnetic field (Maus, 2007). The mixture of the induction processes limits the application of MT in deep ocean at very long periods.

5.1.1. Electromagnetic fields induced by oceanic motion

The types of water motion in the ocean can be primarily classified as: gravity waves (surface and internal waves), turbulences, and tides. On the temporal scale, they cover a broad spectrum of periods, ranging from seconds to years; and on the spatial scale, wavelengths from centimeters to thousands of kilometers. Electrical charge carriers, q, moving with the oceanic flow with velocity $\vec{v}$, interact with the stationary magnetic or main field of the Earth, $\vec{B}_{main}$, and experience the Lorentz force $q\vec{v} \times \vec{B}_{main}$. This force, related to the frame of oceanic flow, is proportional to the electric field $\vec{E}_{ocean}$ induced in this system. The local current density $\vec{j}$ in the moving ocean water of conductivity σ generated by $\vec{E}_{ocean}$ is given by Ohm's law (Chave, 1984; Maus, 2007):

$$\vec{j} = \sigma\vec{E}_{ocean} = \sigma(\vec{E} + \vec{v} \times \vec{B}_{main}), \tag{5.1}$$

with the motional electric field:

$$\vec{E}_m = \vec{v} \times \vec{B}_{main} = \begin{vmatrix} \hat{x} & \hat{y} & \hat{z} \\ v_x & v_y & v_z \\ B_x & B_y & B_z \end{vmatrix}. \tag{5.2}$$

Assuming that the vertical velocity v_z is negligible compared to the horizontal components, and an $x-z$-plane polarized magnetic field Filloux (1987), the motional electric field simplifies to:

$$\vec{E}_m = \begin{vmatrix} \hat{x} & \hat{y} & \hat{z} \\ v_x & v_y & 0 \\ B_x & 0 & B_z \end{vmatrix} = (v_y\hat{x} - v_x\hat{y})B_z - v_yB_x\hat{z}. \tag{5.3}$$

Thus, the electric field in the sea includes both a horizontal component, and also a vertical component associated with vertical electric currents. The current density generated by the resulting electric field induces a secondary magnetic field in the ocean:

$$\vec{j} = \frac{1}{\mu}\nabla \times \vec{B}_{ocean} \tag{5.4}$$

So in a stationary reference frame, i.e fixed to the seafloor, the electric field is given by combining eqs. 5.1 and 5.4:

$$\vec{E} = \frac{1}{\mu\sigma}\nabla \times \vec{B}_{ocean} - \vec{v} \times \vec{B}_{main}. \tag{5.5}$$

Using Faraday's law of induction:

$$\frac{\partial\vec{B}_{ocean}}{\partial t} = -\nabla \times \vec{E} \tag{5.6}$$

the induction in a moving ocean related to the Earth's main field can be written as:

$$\frac{\partial\vec{B}_{ocean}}{\partial t} = \nabla \times (\vec{v} \times \vec{B}_{main} - \frac{1}{\mu\sigma}\nabla \times \vec{B}_{ocean}). \tag{5.7}$$

5.1.2. Electromagnetic fields induced in the ocean by external sources

The external time varying magnetic field $\frac{\partial \vec{B}}{\partial t}$ generated in the ionosphere and magnetosphere induces in the ocean an electric field $\vec{E}$ according Faraday's law:

$$\frac{\partial \vec{B}}{\partial t} = -\nabla \times \vec{E}. \tag{5.8}$$

The electric field generates electric currents $\vec{j} = \sigma \vec{E}$, which in turn induce a secondary magnetic field:

$$\mu \vec{j} = \nabla \times \vec{B}_{induced}. \tag{5.9}$$

The primary and secondary magnetic field are related via:

$$\frac{\partial \vec{B}}{\partial t} = -\nabla \times \frac{1}{\mu\sigma} \nabla \times \vec{B}_{induced}. \tag{5.10}$$

5.2. Decay of fields in the ocean

The behavior of electromagnetic fields in the ocean has been analyzed by several authors, and the present review is based on the studies performed by Brasse (2009) and McNeill and Labson (1987).

The broad usable period range of terrestrial MT is strongly reduced on the seafloor by contamination with oceanic noise at long periods, and attenuation of the primary field at short periods. The decay of the electromagnetic field in a highly conductive homogeneous half space, like ocean water ($\rho = 0.3\,\Omega$m), and a less conductive medium, like earth ($\rho = 100\,\Omega$m), is shown in Fig. 5.1. This behavior, governed by the simple relation

$$\vec{F} \;=\; \vec{F}_0 e^{-kz}, \tag{5.11}$$

with $k = \sqrt{i\mu\sigma\omega}$, may be deduced from eq. 2.16, by neglecting the time term, and considering that in a homogeneous half space the field decays in vertical direction and only the first term makes physically sense. In a 4 km deep ocean with a resistivity of $0.3\,\Omega$m the amplitude of a field propagating with a period of 10 s has approximately 1% of its surface magnitude at the seafloor; the field decays dramatically – almost hundredfold. In comparison, in a $100\,\Omega$m resistivity medium, the field magnitude at a depth of 4 km suffers a loss of only about 22%, i.e the field at this depth retains approximately 78% of its surface value.

This simple relationship becomes more complicated when taking into account real conditions, where a highly conductive ocean layer is limited downward by a relatively resistive basement. Analogously to the N-layered half space (eq. 2.28), the solution has to be augmented by a further term, corresponding to the reflection from the ocean

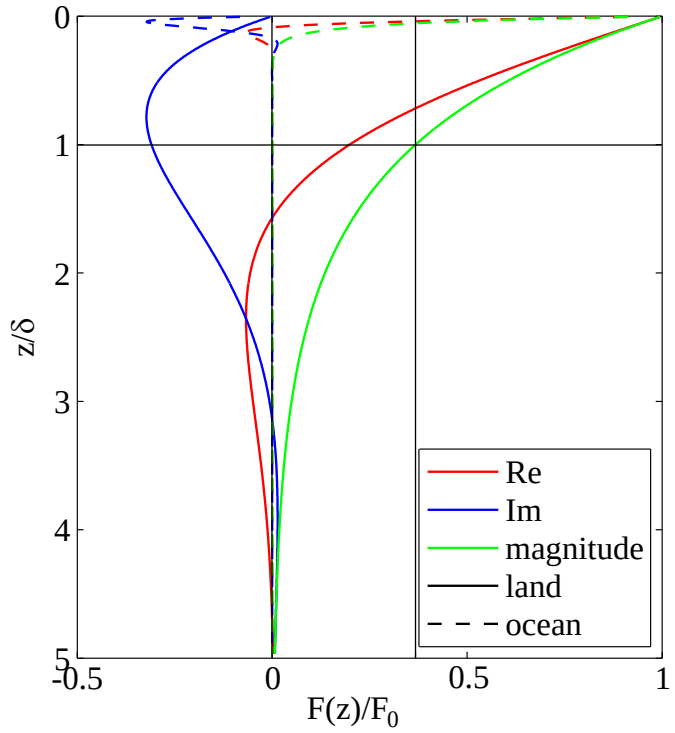

Figure 5.1.: Decay of the magnitude of an electromagnetic field $\vec{F}$ (green), and its real (red) and imaginary (blue) parts, as a function of depth in a highly conductive (0.3 Ωm) homogeneous half space, e.g. ocean water, (dashed line) and a 100 Ωm resistivity one (solid line). The decay is scaled to the surface value $\vec{F}_0$ and the z-component to the skin depth in the 100 Ωm resistivity medium.

bottom, at depth h. On the basis of eq. 2.28, if the time term is neglected, the solution for the x-component of the electric field in the first and second layers is

$$E_{1,x} = E_{11}e^{-k_1 z} + E_{12}e^{k_1 z} \tag{5.12}$$

$$E_{2,x} = E_{22}e^{-k_2 z} \tag{5.13}$$

where E_{11} is the amplitude of the downgoing and E_{12} of the upgoing wave in the first medium and E_{22} the amplitude of the downgoing wave in the second medium (Brasse, 2009; McNeill and Labson, 1987; Weaver, 1994). The $y-$component of the magnetic field in the 1-D case follows from *Faraday's law* (eq. 2.13):

$$B_{1,y} = -\frac{1}{i\omega}\frac{\partial E_{1x}}{\partial z} = \frac{k_1}{i\omega}\left(E_{11}e^{-k_1 z} - E_{12}e^{k_1 z}\right) \tag{5.14}$$

$$B_{2,y} = -\frac{1}{i\omega}\frac{\partial E_{2x}}{\partial z} = \frac{k_2}{i\omega}E_{22}e^{-k_2 z}, \tag{5.15}$$

A similar relation can be derived for the pair E_y and B_x. Using the continuity of the fields at $z = h$ as boundary conditions,

$$E_{1,x}(h) = E_{2,x}(h) \qquad B_{1,y}(h) = B_{2,y}(h), \tag{5.16}$$

equations 5.12 and 5.13 give

$$E_{11}e^{-k_1 h} + E_{12}e^{k_1 h} = E_{22}e^{-k_2 h} \tag{5.17}$$

$$E_{22} = E_{11}\left(e^{-k_1 h} + \frac{E_{12}}{E_{11}}e^{k_1 h}\right)e^{k_2 h} \tag{5.18}$$

Introducing the admittances ζ_1 and ζ_2,

$$\zeta_1 = \frac{k_1}{i\omega} = \sqrt{\frac{i\omega\mu\sigma_1}{i\omega}} = \sqrt{\frac{\mu\sigma_1}{i\omega}} \qquad \text{and} \qquad \zeta_2 = \frac{k_2}{i\omega} = \sqrt{\frac{\mu\sigma_2}{i\omega}} \tag{5.19}$$

and using equations 5.14, 5.15 and 5.18, along with the continuity conditions, gives, after a rearrangement:

$$\zeta_1\left(E_{11}e^{-k_1 h} - E_{12}e^{k_1 h}\right) = \zeta_1 E_{22}e^{-k_2 h} = \zeta_2 E_{11}\left(e^{-k_1 h} + \frac{E_{12}}{E_{11}}e^{k_1 h}\right) \tag{5.20}$$

Further rearrangements lead to the ratio of amplitudes of the downgoing and upgoing fields in the ocean:

$$\frac{E_{12}}{E_{11}} = \frac{\zeta_1 - \zeta_2}{\zeta_1 + \zeta_2}e^{-2k_1 h} = \zeta_{12}e^{-2k_1 h}, \tag{5.21}$$

where $\zeta_{12} = \frac{\zeta_1 - \zeta_2}{\zeta_1 + \zeta_2}$ is the reflection coefficient. Its value is estimated, via eq. 5.19, by the conductivity contrast at the boundary between two layers. In the case of a sharp conductivity contrast, like that between ocean water (σ_1= 3.2 S/m) and basaltic basement (σ_2= 0.001 S/m), the reflection coefficient ζ_{12}= 0.965. Note that when using the magnetic field, instead of the electric field, in eq. 5.12 and 5.13, the reflection coefficient has to be expressed by reciprocal impedances, instead of admittances, and yields: $\eta_{12} = \frac{\eta_1 - \eta_2}{\eta_1 + \eta_2}$, with $\eta_{1,2} = \frac{k_{1,2}}{\mu\sigma_{1,2}} = \sqrt{\frac{i\omega}{\mu\sigma_{1,2}}}$.
Combining eq. 5.21 and 5.12, the electric field at depths $z \leq h$ becomes

$$E_{1,x}(z) \;=\; E_{11}\left(e^{-k_1 z} + \zeta_{12}e^{-2k_1 h}e^{k_1 z}\right) \tag{5.22}$$

and at the surface ($z = 0$)

$$E_{1,x}(0) \;=\; E_{11}\left(1 + \zeta_{12}e^{-2k_1 h}\right). \tag{5.23}$$

The ratio of eq. 5.22 and 5.23 gives the attenuation of the electric field in the ocean for $0 \leq z \leq h$, normalized by the total field at the surface

$$|V_E| = \frac{E_{1,x}(z)}{E_{1,x}(0)} \;=\; \frac{E_{11}\left(e^{-k_1 z} + \zeta_{12}e^{-2k_1 h}e^{k_1 z}\right)}{E_{11}\left(1 + \zeta_{12}e^{-2k_1 h}\right)} = \frac{1 + \zeta_{12}e^{-2k_1(h-z)}}{1 + \zeta_{12}e^{-2k_1 h}}e^{-k_1 z}. \tag{5.24}$$

This applies similarly to the ratio of the magnetic fields

$$B_{1,y}(z) \;=\; B_{11}\zeta_1\left(e^{-k_1 z} - \zeta_{12}e^{-2k_1 h}e^{k_1 z}\right) \tag{5.25}$$

$$B_{1,y}(0) \;=\; B_{11}\zeta_1\left(1 - \zeta_{12}e^{-2k_1 h}\right) \tag{5.26}$$

$$|V_B| = \frac{B_{1,y}(z)}{B_{1,y}(0)} \;=\; \frac{B_{11}\left(e^{-k_1 z} - \zeta_{12}e^{-2k_1 h}e^{k_1 z}\right)}{B_{11}\left(1 - \zeta_{12}e^{-2k_1 h}\right)} = \frac{1 - \zeta_{12}e^{-2k_1(h-z)}}{1 - \zeta_{12}e^{-2k_1 h}}e^{-k_1 z}. \tag{5.27}$$

The behavior of the electric and magnetic fields as a function of depth in a 5 km deep ocean for two representative periods (100 s and 10000 s), and realistic conductivities of the ocean ($\sigma_1 = 3.2$ S/m) and a for example a basaltic basement ($\sigma_2 = 0.001$ S/m), is illustrated in Fig. 5.2. The fields are normalized to their surface magnitude as in relations

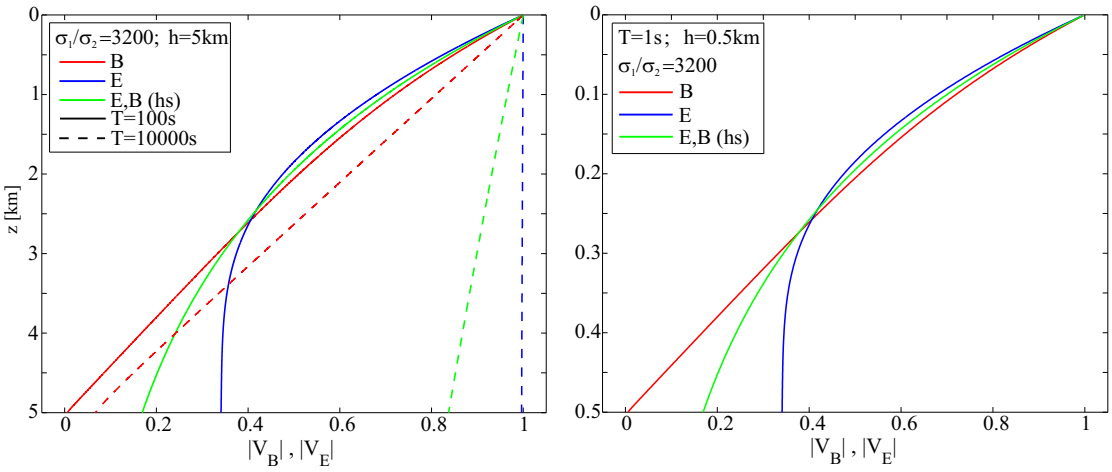

Figure 5.2.: Unlike in a homogeneous half space (green), the electric and magnetic fields decay differently in a layered structure. Left: The red and blue curves illustrate the attenuation of magnetic and electric fields for two periods T=100 s (solid line) and T=10000 s (dashed line) in a 5 km deep ocean with a sea water and seafloor conductivity of 3.2 S/m and 0.001 S/m, respectively. Right: An identical decay can be observed for all ocean depths and is determined by the ratio $\frac{h}{\sqrt{T}}$; shown here with a period of T=1 s in a 0.5 km deep ocean).

5.24 and 5.27. They show different decay, depending on period. At the shorter period both the electric (blue) and magnetic (red) fields experience strong attenuation in the form of exponential decay. Large differences in attenuation are observed at the longer period (dashed line). While the electric field penetrates the ocean layer from surface to seafloor nearly unchanged, the magnetic field is attenuated about fifteen-fold, and at the ocean bottom attains only about 7% of its surface value. However, both fields would behave identically in an infinitely extended ocean (see Fig. 5.1). The decay of the fields is determined by period T, as well as layer thickness h. This becomes evident upon expressing the exponent $e^{-2k_1 h}$ in eq. 5.22 and 5.25 in terms of skin depth (according to relations 2.24 and 2.25):

$$e^{-2k_1 h} = e^{-\frac{2h}{\delta_1}(i+1)}. \tag{5.28}$$

Thus the quantity $\frac{h}{\delta_1}$ is also, via $\delta \sim \sqrt{T}$, associated with the period length of the penetrating wave, and determines the electrical properties or the "electrical thickness" of a layer (McNeill and Labson, 1987). The fields behave identically if the exponent $\frac{h}{\delta_1}$ remains constant, regardless of whether high frequency fields (e.g. T=1 s) propagate in a shallow ocean environment (h=0.5 km), or low frequency fields (e.g. T=100 s) in a

deep ocean (h=5 km), as shown in Fig. 5.2 (solid line left and right). In a model, an identical decay of fields can be reproduced by an appropriate modifying of the exponent $\frac{h}{\delta_1}$, i.e. simultaneously increasing or decreasing the frequency and the ocean thickness and simulating either electrically thick ($\frac{h}{\delta_1} \gg 1$) or thin ($\frac{h}{\delta_1} \ll 1$) conditions. In the real world, an approximately 5 km deep ocean is for a high frequency field an electrically thick layer, with a thickness exceeding the skin depth ($h \gg \delta_1$), so that $e^{-2k_1 h}$ and $e^{-2k_1(h-z)} \to 0$. Thus, the wave reflected at the boundary is negligible, and the behavior in a thick electrical layer is governed equally, for electric and magnetic fields, by exponential decay

$$\frac{E_{1,x}(z)}{E_{1,x}(0)} \approx e^{-k_1 z} \quad \text{and} \quad \frac{B_{1,y}(z)}{B_{1,y}(0)} \approx e^{-k_1 z}. \tag{5.29}$$

The decay of both fields (blue and red solid lines in Fig. 5.2, left) becomes more alike the more the ocean depth or the frequency increases, until finally approaching the decay curve of a homogeneous half space (green solid line).

For low frequencies, or for an electrically thin ocean, where the skin depth is significantly greater than the ocean depth, $h \ll \delta_1$, the exponential terms can be linearly approximated by the first two terms of their power series

$$e^{\pm cx} \approx 1 \pm cx \qquad (c \in \mathbb{C}). \tag{5.30}$$

Additionally assuming a non-conductive basement, so that $\zeta_{12} = 1$, and substituting these approximations into eq. 5.24, the magnitude of the electric field at depth $z = h$, normalized to its surface value is

$$|V_E| = \frac{E_{1,x}(z)}{E_{1,x}(0)} = \frac{1 + e^{-2k_1(h-z)}}{1 + e^{-2k_1 h}} e^{-k_1 z} = \frac{1 - k_1(h-z)}{1 - k_1 h}(1 - k_1 z) = 1. \tag{5.31}$$

Thus, the electric field remains approximately constant throughout the ocean, as shown in Fig. 5.2 (left, blue dashed line). In this case, the current density $J_x = \sigma E_x$ is constant as well.

The magnetic field exhibits quite different behavior in an electrically thin layer. Assuming again an infinite conductivity contrast, $\zeta_{12} = 1$, equation 5.27 yields at $z = h$

$$|V_B| = \frac{B_{1,y}(z)}{B_{1,y}(0)} = \frac{1 - e^{-2k_1(h-z)}}{1 - e^{-2k_1 h}} e^{-k_1 z} \approx \frac{1 - 1 - 2k_1(h-z)}{1 - 1 - 2k_1 h}(1 - k_1 z) = 0. \tag{5.32}$$

Thus, the magnetic field would vanish at the ocean bottom not only in electrically thick layers, but also in electrically thin layers. These estimates are evaluated for a high, ($\frac{\sigma_1}{\sigma_2} = 3200$), but finite, conductivity contrast, and are presented by dashed lines in Fig. 5.2 (left). A small deviation from the calculated value can be observed for the magnetic field, which in fact roughly approaches the prediction, but is not exactly zero. This deviation becomes greater when a lower conductivity contrast between ocean and basement is exhibited, and the reflection coefficient $\zeta_{12} \ll 1$. The effect of ζ_{12} on the field decay is investigated in Fig. 5.3 for two different conductivity contrasts: $\frac{\sigma_1}{\sigma_2} = 3200$

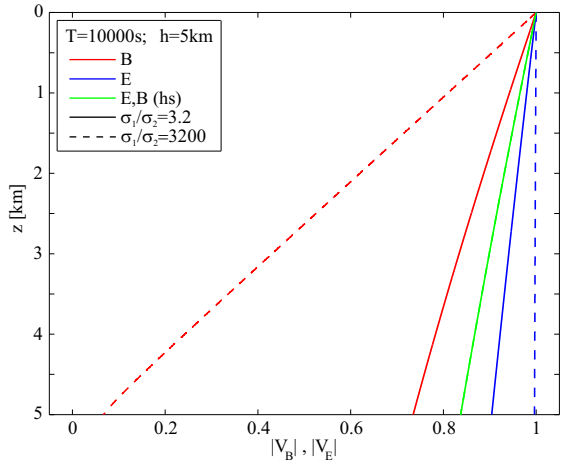

Figure 5.3.: The decay of electric and magnetic fields in the ocean depends not only on period, as shown in Fig. 5.2 but also on boundary conditions at the seafloor, i.e. the resistivity contrast between ocean water and basement. The curves show the attenuation of the electric (blue) and magnetic (red) fields at a period of 10000 s for two different basement conductivities: basaltic basement with a conductivity of 0.001 S/m (solid line) and a water saturated sediments with a conductivity of 1 S/m (dashed line).

(as presented in Fig. 5.2) and $\frac{\sigma_1}{\sigma_2} = 3.2$. In particular under the assumption of weak conductivity contrast, the magnetic field remains considerably more robust. It is clear that the attenuation is not only smaller if the wave periods are larger, and the ocean depth shallower, but also if the conductivity contrast decreases. While the first two can be directly associated with the electrical thickness of the ocean layer, and thus considered in terms of skin depth, the latter is related to the current distribution in the ocean and the seafloor. In accordance with Ohm's law, $\vec{j} = \sigma\vec{E}$, the current density is much higher in the conductive ocean than in the resistive basement. In the theoretical case of an infinitely resistive basement this would imply that the currents flow only in the ocean, inducing a secondary magnetic field which entirely negates the opposite primary field, in agreement with eq. 5.32. In real conditions, with high but not infinite basement resistivity, the currents also diffuse into the seafloor, so that the secondary magnetic field of the diminished currents in the ocean can only reduce, but not completely cancel, the primary magnetic field. That is why the curves calculated for high, but finite, conductivity contrast ($\zeta_{12} = 1$) don't approach zero, but rather approach $0 < \frac{B_{1,y}(z)}{B_{1,y}(0)} < 1$, depending on ζ_{12} and the electrical conditions of the ocean layer. In other words, the reflection coefficient regularizes the conditions for distribution of electrical currents in the sea bottom, and estimates the damping behavior of the fields (Chave et al., 1991). In the limiting case, where $\zeta_{12} = 0$, the layered half space becomes a homogeneous half space and eq. 5.24 and 5.27 become

$$\frac{E_{1,x}(z)}{E_{1,x}(0)} = e^{-k_1 z} \quad \text{and} \quad \frac{B_{1,y}(z)}{B_{1,y}(0)} = e^{-k_1 z}. \tag{5.33}$$

The manner of decay of the electric field in the ocean is contrary to intuition, and is

negligible compared to that of the magnetic field. In the theoretical case, with an infinite conductivity contrast ($\zeta_{12} = 1$) and at long periods, the ocean presents an electrically thin layer that the electric field passes almost intact. In real conditions, as mentioned above, ζ_{12} is still high, and the low frequency field decays gently, as it is still effectively an electrically thin layer. This would change if there were a layer of highly conductive sediments on the ocean bottom. The thicker such layer is present, the more strongly the electric field decays; the magnetic field, in contrast, is much less affected, since a part of the current now flows in the sediments. Thus, both fields would approximate the curve of attenuation in a homogeneous half space, which for short periods is given by an exponential decay (Fig. 5.2).

Similar effects would be observed considering the fields at a given depth z_1 within the ocean as a function of ocean depth h ($0 < z_1 < h$). As the ocean depth increases, the fields at z_1 show different trends: the electric field becomes smaller and the magnetic field larger. Again, in a deeper ocean, currents flow through a broader region, thus the density becomes smaller, in combination with the compensating effect of the secondary opposite magnetic field at depth, this causes the magnetic field to increase compared to the shallow-ocean case. On the other hand, the electric field experiences greater attenuation, due to increased electrical thickness.

It is also instructive to consider the decay of electric and magnetic fields on the seafloor for oceans of various total depth, and for different reflection coefficients, as a function of period. Fig. 5.4 shows the ratio $|V_B| = \frac{B_{1,y}(z)}{B_{1,y}(0)}$ (in red) and $|V_E| = \frac{E_{1,x}(z)}{E_{1,x}(0)}$ (in blue)

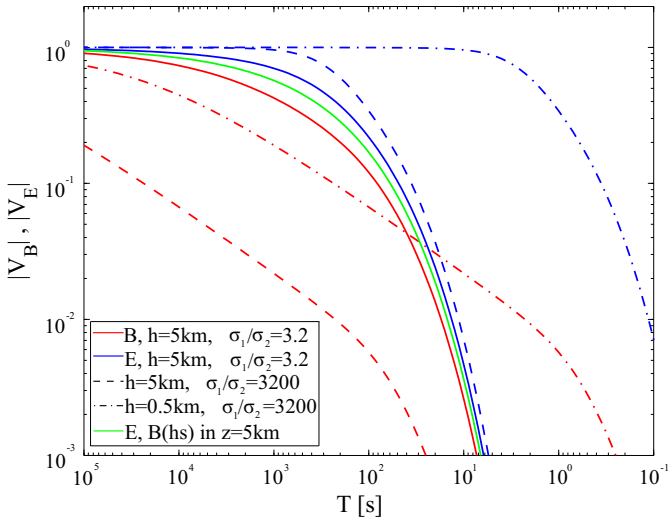

Figure 5.4.: Magnitude of magnetic and electric fields at the seafloor at 0.5 km and 5 km depth as function of period. For comparison, the green curve shows the behavior of the fields at a depth of 5 km in a downwardly unlimited ocean (homogeneous half space).

on a 1 Ωm (solid line) and 1000 Ωm (long dashed line) resistive seafloor, overlaid by a 5 km deep ocean as well as on 1000 Ωm resistive seafloor overlaid by a 0.5 km deep ocean (short dashed line). Additionally, the green curve depicts the decay of fields

in a homogeneous half space at a depth of 5 km. It is immediately evident that the attenuation of the fields differs fundamentally over the total period range. While the electric field remains nearly unchanged in the electrically thin layer ($\frac{h}{\delta_1} \ll 1$), i.e. when the skin depth exceeds the ocean thickness, the magnetic field experiences a marked attenuation over the total period range (even in a shallow ocean); up to more than hundredfold that of the electric field. As expected, the range of periods over which both fields exponentially decay increases in a deeper ocean. The range increases also for the electric field, when the resistivity of the basement diminishes; unlike the magnetic field that increases significantly due to smaller compensating effect of the secondary field in case of less resistive ocean bottom. In the limiting case, where $\zeta_{12} = 0$, the currents flow through an unboundedly broad region, and the curves approximate the decay in a homogeneous half space (green curve).

Note that in the case of reversed conditions, i.e. the upper layer is more resistive than the lower layer – as may be the case on land – the fields' behavior is reversed as well: the electric field decays quickly, while the magnetic field passes through the layer almost unchanged.

5.3. Offshore magnetotelluric and magnetic transfer functions in the presence of bathymetry

Discussions about magnetotellurics on the seafloor are often dominated by attenuation of electromagnetic fields by a highly conductive ocean, and secondary induction by sea tides. Fewer studies refer to induction in an overlaying highly conductive environment due to changes in seafloor bathymetry. Thus, unlike the terrestrial case, where this so-called ocean effect has been extensively investigated (e.g. Fischer, 1979), the distorting impact of this induction on electromagnetic fields and marine transfer functions has remained largely obscure (e.g. Key, 2003; Constable et al., 2009). In order to investigate these effects on the sea side, a model incorporating a homogeneous half space with a resistivity of 100 Ωm and a conductive ocean with bathymetry of that observed at the South Chilean continental margin was constructed, and is depicted at the top of Fig. 5.5. For this model, magnetotelluric transfer functions were calculated by the algorithm of Rodi and Mackie (2001). The images in Fig. 5.5 (middle and bottom) show that the bathymetry produces dramatic anomalous effects in the ocean, which can be observed in the phases and apparent resistivities of the TE mode. In TM mode, the phases are largely unaffected, however the apparent resistivities seem to be diminished by an order of magnitude, which is typical for galvanic distortion, and *static shift effect* in onshore magnetotellurics (Constable et al., 2009). The effects which occur only in the ocean appear clearly by plotting the apparent resistivities and phases at representative points, as shown in Fig. 5.6. In TE mode the distorting effect of bathymetric rise is more spectacular. The resistivity in TE mode rises and falls dramatically, producing cusps in the image and phases in excess of -180° and 180°. Note that phases, for reasons of clarity, are plotted in a range between 135° and -45°, with exception of station *ob7*, so that phases that attain extreme values jump to another quadrant. The coast effect on land (right

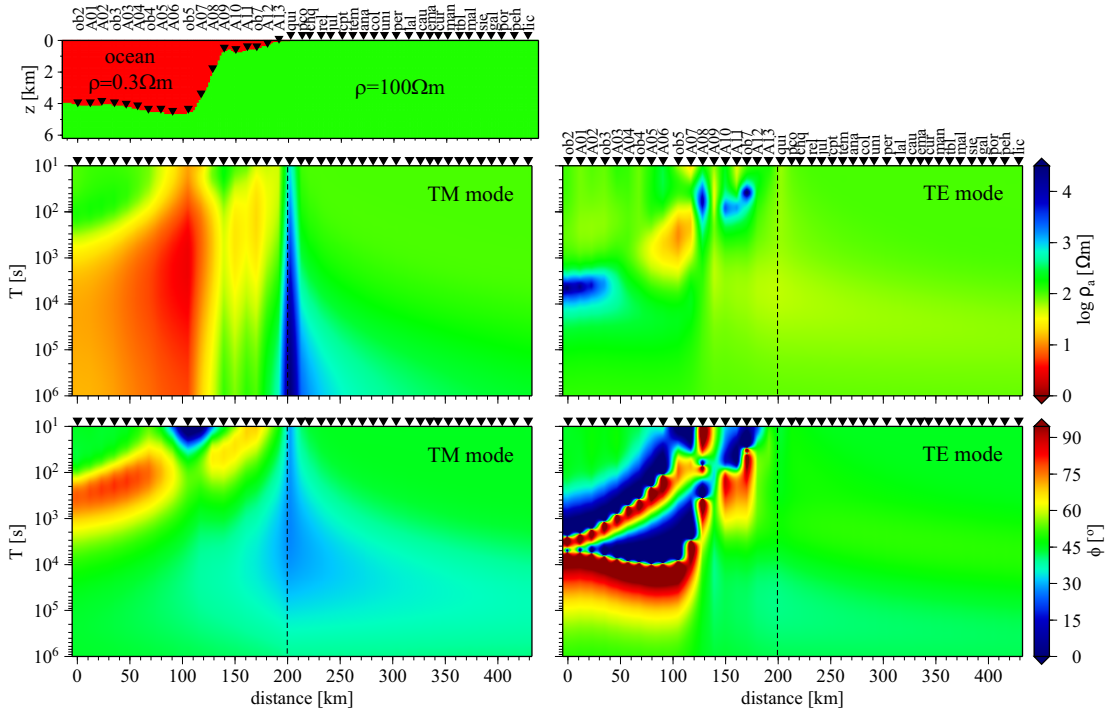

Figure 5.5.: Responses of a synthetic amphibious model shown in the upper panel. Middle panel: resistivity of TM and TE modes. Bottom panel: phases of TM and TE modes. Dashed line separates the profile into offshore and onshore parts.

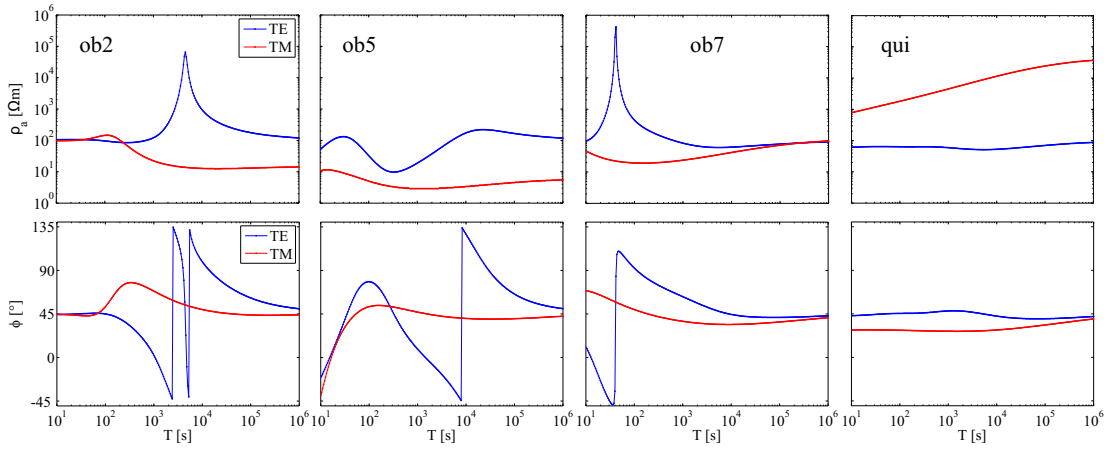

Figure 5.6.: Apparent resistivities and phases on the sea floor and at a continental margin, derived at four selected points from the model presented in Fig. 5.5. The bathymetric rise has a huge distorting effect on the electric and magnetic fields on the seafloor, which results in anomalous transfer functions in TE mode, like sharp upward peaks in apparent resistivity and phases leaving quadrants. Note that phases, for reasons of clarity, are plotted in a range between 135° and -45°.

of the dashed line) is of only marginal significance compared to the anomalous transfer functions on the ocean floor, which is consistent with the calculated pseudosections of real data presented in chapter 4.

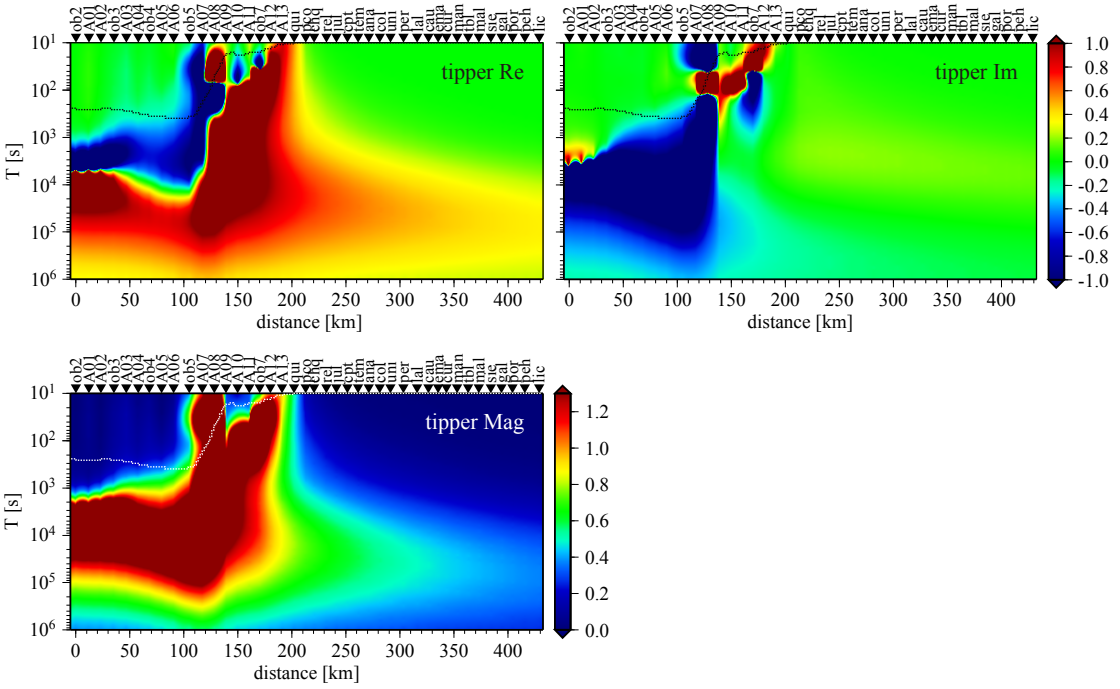

Figure 5.7.: In the upper panel: the real (left) and the imaginary (right) parts; in the lower panel: the magnitude of the tipper calculated for the synthetic amphibious model shown at the top of figure 5.5. The dotted lines indicate the model bathymetry.

Similar anomalous features can be observed in modeled magnetic transfer functions; the real and imaginary parts of which, as well as magnitude, are presented in Fig. 5.7. Jumps from very high positive to very high negative values in both real and imaginary parts dominate in the slope region. However, high values, often exceeding the color scale, in the left half of the images also show clearly that the tipper in the ocean is affected by the bathymetry, which is adumbrated by a dotted line, even far away from the slope. The unusually high imaginary values compared to what would be expected of a land survey indicate a large phase shift between the vertical and horizontal magnetic fields at the seafloor; they are, in addition to the anomalous effects in magnetotelluric responses, like peaks in apparent resistivity and phases below -180° and over 180°, a typical feature for magnetotelluric surveys at the continental margin. Note the sharp threshold from high negative to moderate values: especially in the imaginary, but also in the real part, at point *A09* which marks the beginning of a plateau on the shelf. It is obvious that strong bathymetric changes cause correspondingly strong responses in tipper. Nevertheless, even slight changes in the shape of the seafloor are reflected by dramatic variations in the magnitude of the induction arrows, as becomes evident by

inspecting the smooth bathymetric change between stations *A09* and *A13* and its large impact on the magnitude of the induction vectors. On the other hand, the ocean effect at onshore stations is limited to long periods and to near-coastal regions. This distorting effect of bathymetry seems to be confirmed by magnetic transfer functions measured at the offshore station *ob7*, the only station at the continental slope of the South Chilean margin. The real parts of the induction vectors shown in Fig. 5.8 are remarkable for their considerable amplitude, exceeding 1, and correspond roughly, at middle and long periods, with magnitude values calculated by the simple amphibious model. For short periods (up to 100 s), a comparison is impossible due to unavailable data.

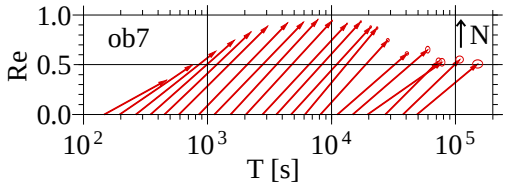

Figure 5.8.: Real parts of the observed induction vectors at station *ob7*, deployed on the continental margin off Southern Chile. Induction vectors observed land-side are presented by Brasse et al. (2009). Much larger vectors were observed at the Costa Rican margin by T. Worzewski (pers. comm.)

Considering these anomalous responses, two questions arise:

- Does exist a relation between the anomalous phases and apparent resistivites in the TE mode?
- What causes this phenomenon, and how can it be explained?

5.3.1. Kramers-Kronig dispersion relations

The first question can be addressed by the *Kramers-Kronig dispersion relations* (*K-K relations*). Derived by R. de Laer Kronig and H. A. Kramers (de Kronig R. L., 1926; Kramers, 1927) the relations connect the real and the imaginary parts of any causal response function which is analytic in the upper half of the complex plane. These relations are well known and widely used in different branches of physics, and also exists between the real and imaginary parts of a complex magnetotelluric impedance Z so long as Z satisfies the condition of causal response. The causality principle postulates that the response of a system is zero before an impulse is applied. In the context of electromagnetic induction in the Earth it implies that observed internal magnetic and electric fields at the time t cannot be the effect of external magnetic field inducing at the time $t + dt$. Weidelt (1972) also shows that the magnitude and the argument of the complex impedance function are not independent, but rather related to each other similarly to the way the real and the imaginary part are connected. For magnetotelluric applications, relations between the apparent resistivity and the phase are more interesting than relations between the real and imaginary parts. The fact that the phase $\phi_{ij}(T)$ can be derived from the resistivity $\rho_{a_{ij}}(T)$, and vice versa, can be used to study the

relationship between the anomalous apparent resistivities and phases at the continental margin. Before applying these relations to the anomalous responses of the model in Fig. 5.5, the basic principles of the Kramers-Kronig relations will first be presented.

5.3.1.1. Basic principles of the Kramers-Kronig relations

The principle of causality is the fundamental property on which the K-K relations depend. From the magnetotelluric point of view, it implies that the induced currents in the Earth are a causal consequence of the inductive activity of the source. It can be shown that the Fourier transform of a causal response function $F[c(t)] = c(z)$, with $z = \omega + i\nu$, is an analytic function in the complex, upper half z-plane, i.e. it is infinitely differentiable at every point in the upper half plane. Thus, there exists a relationship between causality and the mathematical properties of a function. A necessary and sufficient condition for a complex function $c(z) = \Re c(z) + i\Im c(z)$ to be analytic, is that $\Re c(z)$ and $\Im c(z)$ satisfy the Cauchy-Riemann equations:

$$\frac{\partial \Re c(z)}{\partial \omega} = \frac{\partial \Im c(z)}{\partial \nu}, \qquad \frac{\partial \Re c(z)}{\partial \nu} = -\frac{\partial \Im c(z)}{\partial \omega}, \tag{5.34}$$

and that their partial derivatives are continuous. From these equations, it is obvious that the real and imaginary parts of an analytic function are related to each other. These specific properties of analytic functions play a crucial role in dispersion theory and the Kramers-Kronig relations. The K-K relations separate a complex, analytic function in its real and imaginary parts, so that the full function can be reconstructed given just one of its parts. In other words, if the real part of $c(z)$ is known, the K-K relations can be used to determine the imaginary part, and vice versa. For the derivation of such relations the analyticity of $c(z)$ in the upper z-plane is utilized, which allows to express $c(z)$ in terms of *Cauchy's integral theorem*:

$$\frac{1}{2\pi i} \oint_L \frac{c(z)}{z - z_0} dz = c(z_0) \cdot \begin{cases} 1, & \text{if } z_0 \in L \\ 0, & \text{if } z_0 \notin L \\ \frac{1}{2}, & \text{if } z_0 \text{ is on } L \end{cases} \tag{5.35}$$

Cauchy's integral theorem connects values of an analytic function in a complex plane and states that

- the integral of an analytic function $c(z)$ around a closed contour L yields zero if no singularities exist on or within this contour,
- an analytic function $c(z)$ can be uniquely determined anywhere inside the closed contour L if the values on this contour are specified (Arfken and Weber, 2001; Riley et al., 1998).

Application of Cauchy's integral theorem in order to derive the K-K relations for the magnetotelluric response requires a closed contour L in the upper half plane, being a domain in which the response function is assumed to be analytic. Additionally, it is appropriate to extend the contour along the real axis, from $-\infty$ to ∞, because the

magnetotelluric responses are functions of real frequencies and the relationship between the real and imaginary parts only make physical sense at a point on the real axis. If the function $c(z)$ is analytic in each point of the closed contour L, equivalent here to the entire upper half space, the integral only yields a trivial solution. For non-trivial solution a pole $z_0 = \omega_0$ is introduced on the real axis. At this point the integral $\frac{c(z)}{z-z_0}$ is not analytic and is excluded from the interior of the contour by indentation in form of semicircles of infinitesimal radius ε as shown in Fig. 5.9. Thus the entire path in 5.35

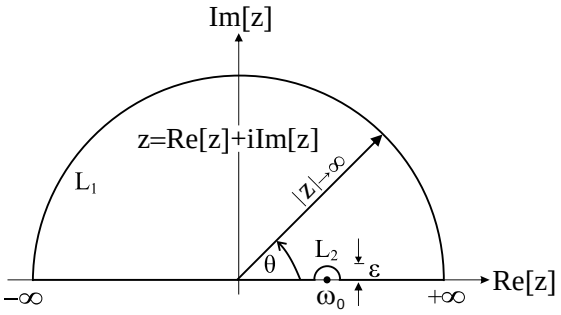

Figure 5.9.: Schematic of the path of integration for K-K derivation, to be evaluated with Cauchy's integral theorem, which states that the integration of an analytic function around a closed path yields zero. The integration path L is divided into segments. The integral along the semicircle L_1 goes to zero for large $|z|$. The integration over real ω is defined as the principal value: $\wp \int_{-\infty}^{\infty} \frac{c(\omega)}{\omega-\omega_0} d\omega$. The contribution of the small semicircle L_2 is $-\pi i c(\omega_0)$.

can be decomposed into a sum:

$$\oint_L \frac{c(z)}{z-\omega_0} dz =$$
$$\int_{L_1} \frac{c(z)}{z-\omega_0} dz + \int_{-\infty}^{\omega_0-\varepsilon} \frac{c(z)}{z-\omega_0} dz + \int_{L_2} \frac{c(z)}{z-\omega_0} dz + \int_{\omega_0+\varepsilon}^{\infty} \frac{c(z)}{z-\omega_0} dz = 0, \qquad (5.36)$$

where $\lim \varepsilon \to 0$. The contribution of the integral over the semicircle L_1 determined by $z = |z| e^{i\theta}$ and $0 \leq \theta \leq \pi$ vanishes as $|z| \to \infty$, so the first subintegral in eq. 5.36 becomes:

$$\lim_{|z|\to\infty} \int_{L_1} \frac{c(z)}{z-\omega_0} dz = 0, \qquad (5.37)$$

and the contour reduces to a path along the real ω-axis. In the vicinity of the pole ω_0 any point z on the small semicircle L_2 in the upper half plane is given by:

$$z = \omega_0 + \varepsilon e^{i\theta} \qquad \text{and} \qquad dz = i\varepsilon e^{i\theta} d\theta. \qquad (5.38)$$

Thus, the value of the integral over the ε-semicircle is

$$\lim_{\varepsilon\to 0} \int_{L_2} \frac{c(z)}{z-z_0} dz = \lim_{\varepsilon\to 0} \int_{-\pi}^{0} \frac{c(\omega_0+\varepsilon e^{i\theta})}{\omega_0+\varepsilon e^{i\theta}-\omega_0} i\varepsilon e^{i\theta} d\theta = -i\pi c(\omega_0). \qquad (5.39)$$

Finally, both integrals along the real axis ($z \to \omega$), can be recombined:

$$\lim_{\varepsilon \to 0} \int_{-\infty}^{\omega_0 - \varepsilon} \frac{c(\omega)}{\omega - \omega_0} d\omega + \int_{\omega_0 + \varepsilon}^{\infty} \frac{c(\omega)}{\omega - \omega_0} d\omega := \wp \int_{-\infty}^{\infty} \frac{c(\omega)}{\omega - \omega_0} d\omega, \tag{5.40}$$

where $\wp$ is the Cauchy principal value

$$\lim_{\varepsilon \to 0} \left[\int_{-\infty}^{\omega_0 - \varepsilon} + \int_{\omega_0 + \varepsilon}^{\infty} \right] = \wp \int_{-\infty}^{\infty}. \tag{5.41}$$

Since the upper semicircle vanishes, the integral over the entire contour L becomes the sum of an integral along the real ω-axis and the contribution from the lower semicircle, and eq. 5.36 can be, in combination with 5.37 - 5.40, rewritten as:

$$c(\omega_0) = \frac{1}{i\pi} \wp \int_{-\infty}^{\infty} \frac{c(\omega)}{\omega - \omega_0} d\omega. \tag{5.42}$$

Substituting for $c(\omega)$ and $c(\omega_0)$

$$c(\omega) = \Re\left[c(\omega)\right] + i\Im\left[c(\omega)\right] \qquad \text{and} \qquad c(\omega_0) = \Re\left[c(\omega_0)\right] + i\Im\left[c(\omega_0)\right] \tag{5.43}$$

relationship 5.42 can be decomposed as follows:

$$\Re\left[c(\omega_0)\right] + i\Im\left[c(\omega_0)\right] = \frac{1}{\pi} \wp \int_{-\infty}^{\infty} \frac{\Im\left[c(\omega)\right]}{\omega - \omega_0} d\omega + \frac{1}{i\pi} \wp \int_{-\infty}^{\infty} \frac{\Re\left[c(\omega)\right]}{\omega - \omega_0} d\omega. \tag{5.44}$$

and then separated in real and a imaginary parts, so that the real and imaginary parts are *Hilbert transforms* of each others:

$$\Re\left[c(\omega_0)\right] = \frac{1}{\pi} \wp \int_{-\infty}^{+\infty} \frac{\Im\left[c(\omega)\right]}{\omega - \omega_0} d\omega \tag{5.45}$$

$$\Im\left[c(\omega_0)\right] = -\frac{1}{\pi} \wp \int_{-\infty}^{+\infty} \frac{\Re\left[c(\omega)\right]}{\omega - \omega_0} d\omega. \tag{5.46}$$

Making use of the symmetry properties of $c(\omega_0)$ about the imaginary axis,

$$c(-\omega) = c^*(\omega), \tag{5.47}$$

by which the real part is even, i.e $\Re\left[c(-\omega)\right] = \Re\left[c(\omega)\right]$; and the imaginary part odd, i.e. $\Im\left[c(-\omega)\right] = -\Im\left[c(\omega)\right]$. The integrals in 5.45 and 5.46 can thus be reformulated for a positive, and thus physically reasonable, frequency domain:

$$\begin{aligned}
\Re\left[c(\omega_0)\right] &= \frac{1}{\pi} \wp \int_{-\infty}^{+\infty} \frac{\Im\left[c(\omega)\right]}{\omega - \omega_0} d\omega \\
&= \frac{1}{\pi} \wp \int_{-\infty}^{0} \frac{\Im\left[c(\omega)\right]}{\omega - \omega_0} d\omega + \frac{1}{\pi} \wp \int_{0}^{+\infty} \frac{\Im\left[c(\omega)\right]}{\omega - \omega_0} d\omega \\
&= \frac{1}{\pi} \wp \int_{0}^{+\infty} \frac{\Im\left[c(-\omega)\right]}{-\omega - \omega_0} d\omega + \frac{1}{\pi} \wp \int_{0}^{+\infty} \frac{\Im\left[c(\omega)\right]}{\omega - \omega_0} d\omega \\
&= \frac{1}{\pi} \wp \int_{0}^{+\infty} \Im\left[c(\omega)\right] \left(\frac{1}{\omega + \omega_0} + \frac{1}{\omega - \omega_0} \right) d\omega \\
&= \frac{2}{\pi} \wp \int_{0}^{+\infty} \frac{\omega \Im\left[c(\omega)\right]}{\omega^2 - \omega_0^2} d\omega
\end{aligned} \tag{5.48}$$

$$\begin{aligned}
\Im\left[c(\omega_0)\right] &= -\frac{1}{\pi}\wp\int_{-\infty}^{+\infty}\frac{\Re\left[c(\omega)\right]}{\omega-\omega_0}d\omega \\
&= -\frac{1}{\pi}\wp\int_{-\infty}^{0}\frac{\Re\left[c(\omega)\right]}{\omega-\omega_0}d\omega - \frac{1}{\pi}\wp\int_{0}^{+\infty}\frac{\Re\left[c(\omega)\right]}{\omega-\omega_0}d\omega \\
&= -\frac{1}{\pi}\wp\int_{0}^{+\infty}\frac{\Re\left[c(-\omega)\right]}{-\omega-\omega_0}d\omega - \frac{1}{\pi}\wp\int_{0}^{+\infty}\frac{\Re\left[c(\omega)\right]}{\omega-\omega_0}d\omega \\
&= \frac{1}{\pi}\wp\int_{0}^{+\infty}\Re\left[c(\omega)\right]\left(\frac{1}{\omega+\omega_0}-\frac{1}{\omega-\omega_0}\right)d\omega \\
&= -\frac{2}{\pi}\wp\int_{0}^{+\infty}\frac{\omega_0\Re\left[c(\omega)\right]}{\omega^2-\omega_0^2}d\omega. \qquad (5.49)
\end{aligned}$$

Weidelt (1972) shows that similar relations between the apparent resistivity and phase can be also derived. Let

$$c(\omega_0) = |c(\omega_0)|\, e^{i\phi(\omega_0)} \qquad (5.50)$$

be the exponential form of the analytic response function $c(\omega_0)$ and

$$\ln(c(\omega_0)) = \ln\left(|c(\omega_0)|\right) + i\phi(\omega_0) \qquad (5.51)$$

the natural logarithm of $c(\omega_0)$; then the function

$$\ln\left(\sqrt{i\omega_0\mu_0\sigma(0)}c(\omega_0)\right) = \ln\left(\sqrt{|\omega_0|\,\mu_0\sigma(0)}\,|c(\omega_0)|\right) + i\arg\left(\omega_0 c(\omega_0)\sqrt{i}\right) \qquad (5.52)$$

is also analytic in the complex plane, just as $c(\omega_0)$ is (Weidelt, 1972; Weaver, 1994). Thus the modulus $\ln\left(\sqrt{|\omega_0|\,\mu_0\sigma(0)}\,|c(\omega_0)|\right)$ corresponds to the real part, and the argument or the phase ϕ to the imaginary part of $\ln\left(\sqrt{i\omega_0\mu_0\sigma(0)}c(\omega_0)\right)$ and these can be connected through the Hilbert transforms 5.48 and 5.49. For example, the phase expressed in terms of amplitude yields:

$$\phi(\omega_0) = \frac{\pi}{4} + \frac{2\omega_0}{\pi}\wp\int_0^{\infty}\frac{\ln\left(\sqrt{\omega\mu_0\sigma(0)}\,|c(\omega)|\right)}{\omega^2-\omega_0^2}d\omega. \qquad (5.53)$$

Substituting the apparent resistivity $\rho_a(\omega) = \omega\mu_0\,|c(\omega)|^2$ according to 2.33, as well as the reference resistivity $\rho_0(T) = \frac{1}{\sigma(0)}$, and finally replacing the angular frequency ω by the period $T = \frac{2\pi}{\omega}$ gives

$$\phi(T_0) = \frac{\pi}{4} + \frac{T_0}{\pi}\wp\int_0^{\infty}\frac{\ln\left(\frac{\rho_a(T)}{\rho_0}\right)}{T_0^2-T^2}dT. \qquad (5.54)$$

Since the magnetotelluric transfer functions are conventionally presented on a logarithmic scale, it is appropriate to substitute a logarithmic differential, so that $\phi(T)$ in terms of $\rho_a(T)$, after integration by parts, takes the final form (Fischer and Schnegg, 1980):

$$\phi(T_0) = \frac{\pi}{4} - \frac{1}{2\pi}\wp\int_{-\infty}^{+\infty}\ln\left|\frac{T_0+T}{T_0-T}\right|\frac{d\ln\left(\frac{\rho_a(T)}{\rho_0}\right)}{d\ln T}d(\ln T). \qquad (5.55)$$

Conversely, $\rho_a(T)$ in terms of $\phi(T)$ expressed in logarithmic scale is:

$$\ln\left(\frac{\rho_a(T_0)}{\rho_0}\right) = \frac{4T_0^2}{\pi}\wp\int_{-\infty}^{+\infty}\frac{\frac{\pi}{4}-\phi(T)}{T_0^2-T^2}d(\ln T) \tag{5.56}$$

The relations 5.55 and 5.56, based on the causality principle, can be applied to calculate $\phi(T)$ using values of $\rho_a(T)$ in a causal system, and vice versa. The phase relation 5.55 can be significantly simplified to:

$$\phi(T_0) \approx \frac{\pi}{4}\left[1-\frac{d\ln\left(\frac{\rho_a(T)}{\rho_0}\right)}{d\ln T}\right] \tag{5.57}$$

by approximating the function kernel by a Dirac $\delta-$function as proposed by Weidelt (1972).

5.3.1.2. Application of the Kramers-Kronig relations to magnetotelluric 2-D models

Weidelt (1972) and Fischer and Schnegg (1980, 1993) have already presented examples which quantitatively prove the validity of these relations for 1-D and 2-D structures. Another example relating to an offshore model is presented in Fig. 5.10 (top). The model is a usual 2-D scenario and includes a conductive half layer (0.3 Ωm) embedded in a 100 Ωm resistive background. The half layer is bounded to the right by an oblique conductivity contrast, which would correspond to a slope in a offshore model; however, this is not a offshore model, but rather a 2-D onshore model with stations on the model surface.

The integral in eq. 5.55 is calculated numerically by using the trapezoid method. Although the relations 5.55 requires an integration over all periods between $T = 0$ and $T = \infty$, evaluation of the function kernel $\ln\left|\frac{T_0+T}{T_0-T}\right|$ reveals that only periods in the vicinity of T_0 contribute significantly to the integral. With increasing difference between T and T_0 the value of $\log_{10}(T/T_0)$ vanishes, so that a limited interval between $\log_{10} T_a = -3.0$ and $\log_{10} T_b = +9.0$ was chosen, and divided into N steps of length $\Delta = (\log_{10} T_b - \log_{10} T_a)/N = 0.001$, which produced adequate results. The apparent resistivities needed for the computation of the phases presented below, were initially calculated for 20 periods within each decade with the algorithm of Rodi and Mackie (2001) implemented in the software package *Winglink*, which is used within the working group. This was then interpolated with the linear spline function to obtain the desired smoothness. At the poles the function takes singular values and the areas in the neighborhood of the poles were calculated separately.

The phases' responses on the surface, computed directly from the model, and presented in Fig. 5.10 in the middle panel, correlate very well with phases in the lower panel, which are calculated from apparent resistivities via the Kramers-Kronig relations. Fig. 5.10 suggests that in 1-D (approximately station *A22* on the right edge on the model) or 2-D conditions the K-K relations is valid in TM as well as TE mode. The quality of the correlation can be more precisely evaluated by taking into account phase curves at

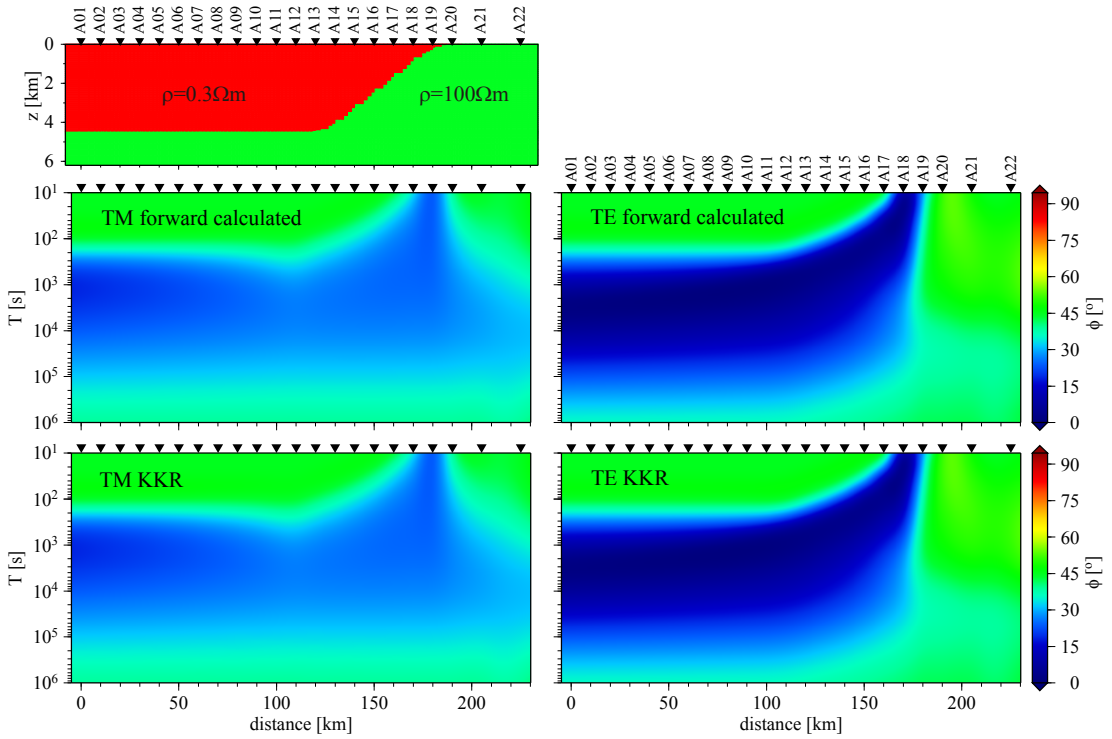

Figure 5.10.: Responses in the form of pseudo sections calculated for a 2-D onshore model that is shown in the upper panel. Middle panel: phases of TM and TE modes derived directly from this model. Bottom panel: phases of TM and TE modes calculated from the Kramers-Kronig relations via eq. 5.55.

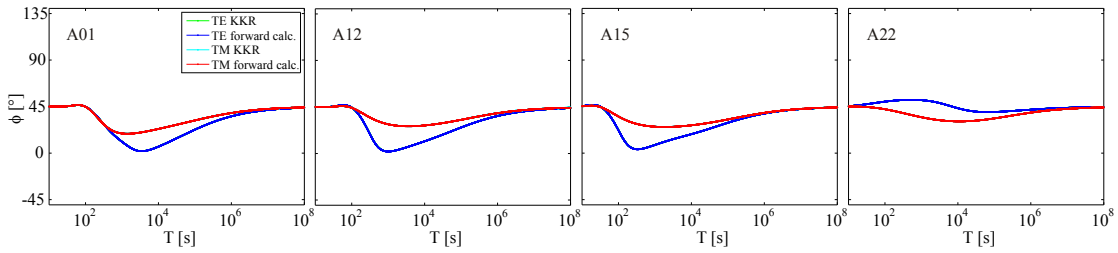

Figure 5.11.: Phase curves calculated at four representative profile points for the 2-D onshore model shown in Fig. 5.10. In blue and red: phases in TE and TM mode derived directly from the model; in green and cyan: phases in TE and TM mode calculated from the Kramers-Kronig relations via eq. 5.55.

four representative stations selected from different profile sections, as shown in Fig. 5.11. A discrepancy of less than a few tenths of one degree between phases calculated with the Kramers-Kronig relations and phases derived directly from the model is due to numerical inaccuracies and thus confirms the validity of the Kramers-Kronig relations for the presented 2-D model.

Additionally, an attempt was undertaken to evaluate the phases via eq. 5.57, in which the function kernel from eq. 5.55 is approximated by the Dirac $\delta-$ function. Although the numerical implementation of the function becomes simpler, and the computation faster, the inaccuracy increases, too. The calculated phases only fit roughly with the modeled responses. Thus, in the interest of greater accuracy and satisfactory coincidence with the modeled phases, a numerical integration should be the preferred method, and was also applied in the following.

Having verified the validity of these relations for a 2-D onshore model, we return to the anomalous magnetotelluric responses in TE mode in Fig. 5.5 prepared to address the question asked at the end of the previous section, which we here restate more precisely: Do the anomalous phases on the seafloor in the presence of bathymetry, derived directly from the model, correspond with phases calculated from anomalous offshore resistivities via the Kramers-Kronig relations? Weidelt (1994) qualitatively illustrated the induction process in the vicinity of strong bathymetry, as found at a continental margin, and suggested anomalous behavior of phases in the TE mode might occur if inhomogeneous anomalous sources control the induction.

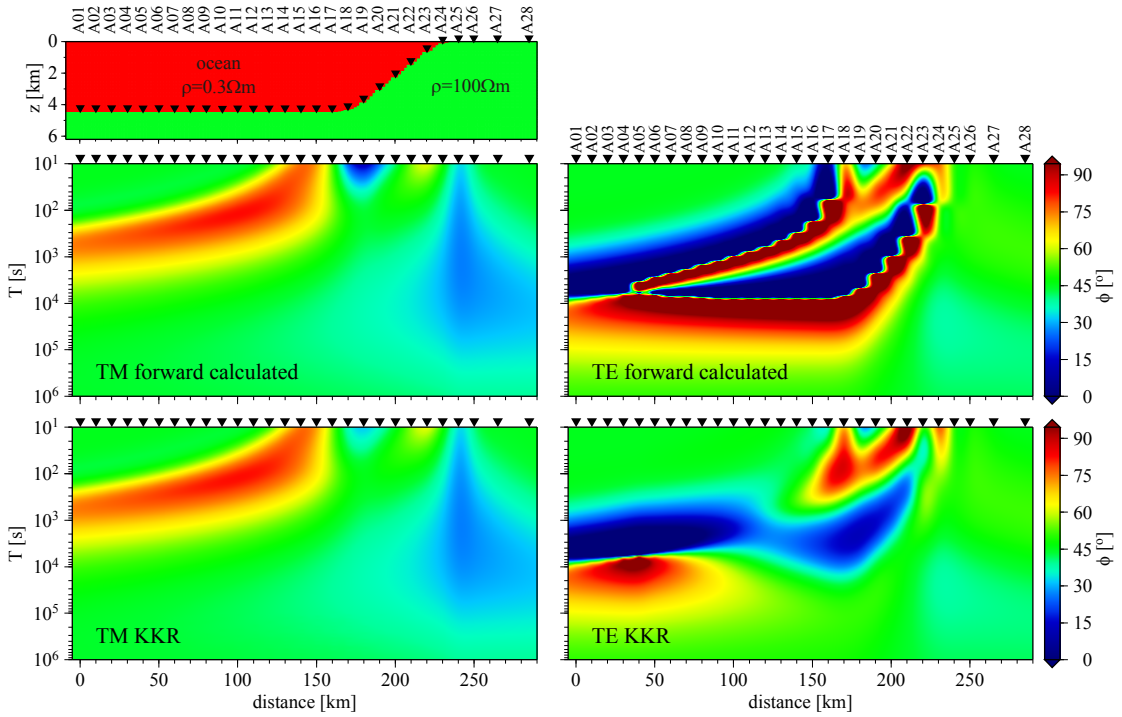

Figure 5.12.: Responses in the form of pseudosections, calculated for the 2-D amphibious model shown in the uppermost panel. The model consists of a highly conductive ocean (0.3 Ωm), and a resistive homogeneous half space (100 Ωm) with a step bathymetry. Middle panel: phases of the TM and TE modes derived directly from this model. Bottom panel: phases of TM and TE modes calculated from the Kramers-Kronig relation via eq. 5.55.

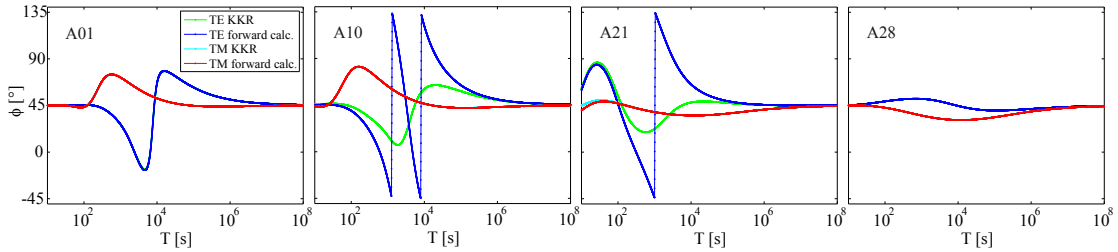

Figure 5.13.: Phase curves calculated at four representative profile points for the 2-D amphibious model shown in Fig. 5.12. While at sites located far enough from the bathymetric changes (*A01*, *A28*), the phases derived directly from model agree very well with the phases calculated from the Kramers-Kronig relations via eq. 5.55, this is not the case at sites located close to the slope (*A10*, *A21*). Note that at sites *A01* and *A28* the curves calculated via K-K relations presented in green and cyan are covered by curves obtained directly from the model and thus are difficult to recognize.

For a quantitative evaluation an amphibious model, presented in Fig. 5.12, was constructed. It incorporates a conductive ocean (0.3 Ωm) with simple bathymetry and a resistive background (100 Ωm). The model geometry is as in Fig. 5.10, but unlike the onshore model, the stations are not placed on the model surface, but on the seafloor and on the continental slope, i.e. below highly conductive sea water.

In TM mode the phases calculated via the Kramers-Kronig relations agree very well with those derived directly from the model. Some discrepancies can be observed at very short periods in the vicinity of the slope, and may be caused by numerical inaccuracies due to discontinuous TM responses across a strong conductivity gradient. More interestingly, TE mode phases derived directly from the model and those calculated via Kramers-Kronig relations yield substantially different results. The images agree only on the flanks, far away from bathymetric changes, where the induction is not affected by the shape of the seafloor. In the central part there is no correlation between phases derived from the model and by the Kramers-Kronig relation. A more detailed view of the phases in the TE and TM modes at selected single points of the profile is presented in Fig. 5.13. It is clear from these figures that the spikes in apparent resistivities and reversal phases in the TE mode cannot be reproduced via the Kramers-Kronig relations. Note that the amphibious profile has been extended by 60 km on the sea side, compared to the onshore profile, by adding 6 additional stations, in order to investigate how far from the slope the offshore impedances are affected. Fig. 5.12 reveals that at long periods, even responses more than 100 km away from the bathymetric onset are still strongly marked by heterogeneous fields induced in the vicinity of the slope.

5.3.1.3. Discussion

A thorough study verifying the validity of Kramers-Kronig relations for a typical synthetic 2-D onshore impedance tensor is given by Fischer (1992) and in Fischer and Schnegg (1993). The authors state that in 1-D case and in TM mode the external and

internal magnetic fields are practically identical at the surface, and thus conclude that a 2-D model in TM mode justifies these relations. The TE mode is more complicated, since the fields are not identical, and thus the question of whether for a 2-D model in TE mode, the application of the Kramers-Kronig relations is justified seems to be legitimate. A discussion about the necessary conditions for this is raised in Yee and Paulson (1988), who suggest adoption of the properties of Kramers-Kronig relations, valid for the 1-D case, for the general case of a 3-D impedance tensor. This assumption was seriously questioned by Egbert (1990). In a critical review, he raises doubts as to whether, for a general 3-D magnetotelluric impedance tensor, the Kramers-Kronig relations are still preserved; and shows that in a 3-D Earth, certain conductivity distributions can violate the fundamental conditions necessary to connect the modulus and phase of an impedance tensor. He argues that under certain circumstances, the linear relation between the horizontal electric and magnetic field vectors is not necessarily causal, and thus does not satisfy conditions required by the Kramers-Kronig relations. The crucial point of this argumentation is the need to distinguish between the physically obvious causality and passivity of the whole system and the causality and passivity of the impedance tensor, which is a ratio of the **total** (external and internal) magnetic and electric field at a single measurement point. While the causality is justified if the impulse arises from an external magnetic field, it is not the case if the total magnetic field is regarded. By way of example, he outlined a conductivity distribution in which the induced internal magnetic field cancels the external source field so that the causality principle at a single point fails. In a further example, Egbert (1990) contrives a conductivity distribution which causes a violation of the local passivity condition, defined here on the basis of simple energy conservation. Such failure can occur if the currents focus on a local conductor. The high concentration of current acts as an internal source, whose energy flux is larger than that of the external source, producing anomalous phases exceeding the quadrant, and not satisfying the passivity requirements of magnetotelluric impedance. This phenomenon, termed "current channelling", since currents are strongly bundled, violates the passivity conditions at a single point, and limits the usefulness of the Kramers-Kronig relations.

Although it is also generally possible to contrive a 2-D conductivity distribution leading to channelling of currents, Fischer (1992) suggests that they wouldn't result in a breakdown of the dispersion relations, and Egbert (1990) argues that for 2-D conductivities the impedance is in TM mode certainly and in TE mode almost certainly causal.

However, considering the special induction conditions in marine environment and the anomalous responses on the seafloor the questions of the validity of the Kramers-Kronig relations in the TE mode of an amphibious 2-D model (or of the validity of the assumption of causality and passivity in such special conditions), seem to be more current than ever. Berdichevsky (1999) postulated "to leave room for the possibility of violation of dispersion relations in the E-polarized 2-D models and 3-D models", and presented a model which reveals an obvious discrepancy between responses derived directly from this model and responses calculated via KK-relations. More interesting in the context of the present work is the amphibious 2-D model presented by Alekseev et al. (2009). The phases of this model leave the quadrant in the TE mode, at sites close to the continental slope, and they interpreted this behavior as indicator for the violation of the

KK-relations in the TE mode.

The answer to the question for the reason of this phenomenon may be provided by studying the induction and distribution of electric currents and magnetic fields in the ocean, or particularly on the ocean bottom, in presence of bathymetric changes.

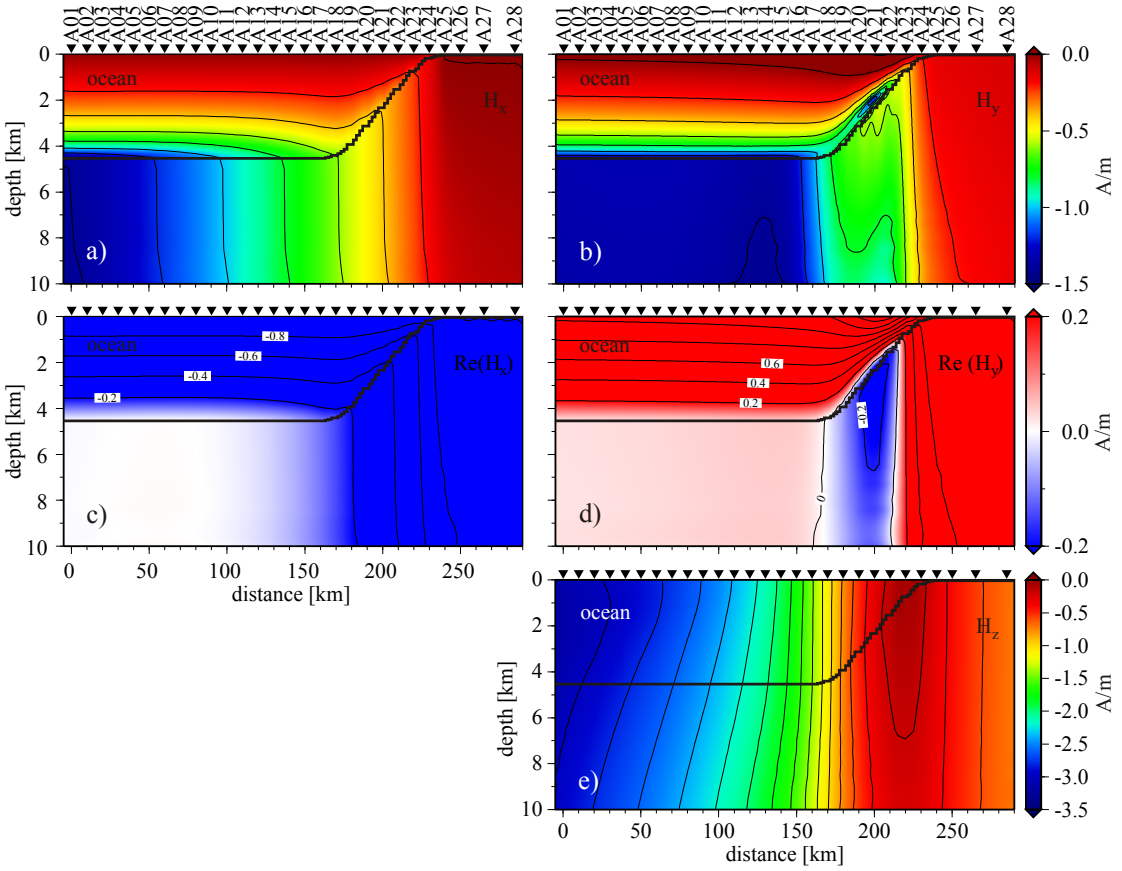

Figure 5.14.: Distribution of magnetic fields at a period of $T = 315\,\mathrm{s}$ at on- and offshore parts of the continental margin. The left column shows magnetic fields in TM mode; right column in TE mode. The input reference magnetic intensity on the surface is $1\,\mathrm{A/m}$. In a)-b) and e) the logarithm of the field and current magnitude was taken, whereas in c)-d) a linear scale is used. a) Magnitude of H_x (TM mode), b) magnitude of H_y (TE mode), c) real part of H_x, d) real part of H_y; note that, at the slope in TE mode, $\Re(H_y)$ reverses on the ocean bottom (blue color corresponds to negative values), e) magnitude of vertical magnetic field H_z.

Due to the high sea water conductivity, the induced electric currents concentrate primarily in the ocean, avoiding the more resistive subsurface and generate a secondary magnetic field. This opposes the primary field, so that the total magnetic field diminishes considerably, or even disappears completely in the case of an insulating substrate. The effect for the one dimensional case was discussed in detail in section 5.2, and depicted in Fig. 5.2. However, at continental margins, the conditions become two dimensional,

and the bathymetric changes affect the distribution of electric currents and the electromagnetic fields. To study this, fields and electric currents were calculated for the model presented in Fig. 5.12 by applying the 2-D finite-difference algorithm of Pek and Verner (1997), and plotted for a period of $T = 315\,s$ in Fig. 5.14 and 5.15. Fig. 5.14, parts a)-b), show clearly once again that far enough from any bathymetric changes the horizontal magnetic field in the ocean experiences a strong attenuation and decays on the ocean bottom, to a slight fraction of its surface value, whereas the horizontal electric field in Fig. 5.15 doesn't change significantly, in accordance with previous conclusions for one dimensional conditions. A striking feature is the different color patterns and the densities of field contours in the offshore and onshore model parts; or, respectively, in the highly conductive ocean and the less conductive background. The reason for this is higher attenuation and smaller skin depth for the fields in the highly conductive seawater on the left side (small distance between the contours) and smaller attenuation and larger skin depth in less conductive background on the right side (large space between the contours). Note that in Fig. 5.14 a)-b) and e) as well as in 5.15 the logarithm of the field and current magnitude is taken, whereas Fig. 5.14 c)-d) show the real parts of H_x and H_y using linear scale.

At a continental margin, where the seafloor shallows towards land, the density of the TE polarized electric currents j_x flowing in the ocean, i.e. above the ocean bottom and along the coast, increases as shown in Fig. 5.15 i) (brown color and higher density of contour lines). These squeezed currents induce a secondary, anomalous, and on the ocean bottom oppositely directed magnetic field, that becomes predominant in the shelf region in TE mode (Weidelt, 1994), not only below but also above the seafloor, in the deeper part of the ocean, as shown in Fig. 5.14 d) (blue color corresponds to reverse field). This effect is not seen in TM mode (Fig. 5.14 c)). According to eq. 2.1 this magnetic field curls around the electric current, so that a vertical magnetic field H_z also arises at the lateral conductivity gradient, as expected, and as shown in Fig. 5.14 e). This effect, known in terrestrial magnetotellurics as coast effect (Fischer, 1979), can also be seen in the contour pattern of the electric field in TE mode (E_x) in Fig. 5.15 g). The bending contours of constant E_x correspond to magnetic stream lines with a strong vertical component in TE mode around the slope. The contours of the magnitude of the electric field (or, equivalently, the streamlines of magnetic field) turn horizontal as the conditions becomes one dimensional.

The impact of bathymetric changes on the fields is reflected directly in the impedance relation 2.40. While the horizontal magnetic component vanishes accompanied by arising vertical magnetic field, as seen in Figs. 5.14 b) d) e), so that the denominator tends to zero, the electric field in the numerator is only marginally modified, and thus the impedance becomes singular; see Constable et al. (2009). Furthermore, the resistivities in the TE mode increase, generating upward cusps, while the phase jumps by 180°, as presented in Fig. 5.13; and the tipper gets very large. The period at which these effects occur depends on the position of the probe in relation to the slope, and corresponds to the lateral distance at which a transfer function is sensitive to bathymetry. However, at high frequencies the field is generally unaffected by the bathymetry and the results are MT-like because the fields still look like plane waves. At low frequencies, the currents

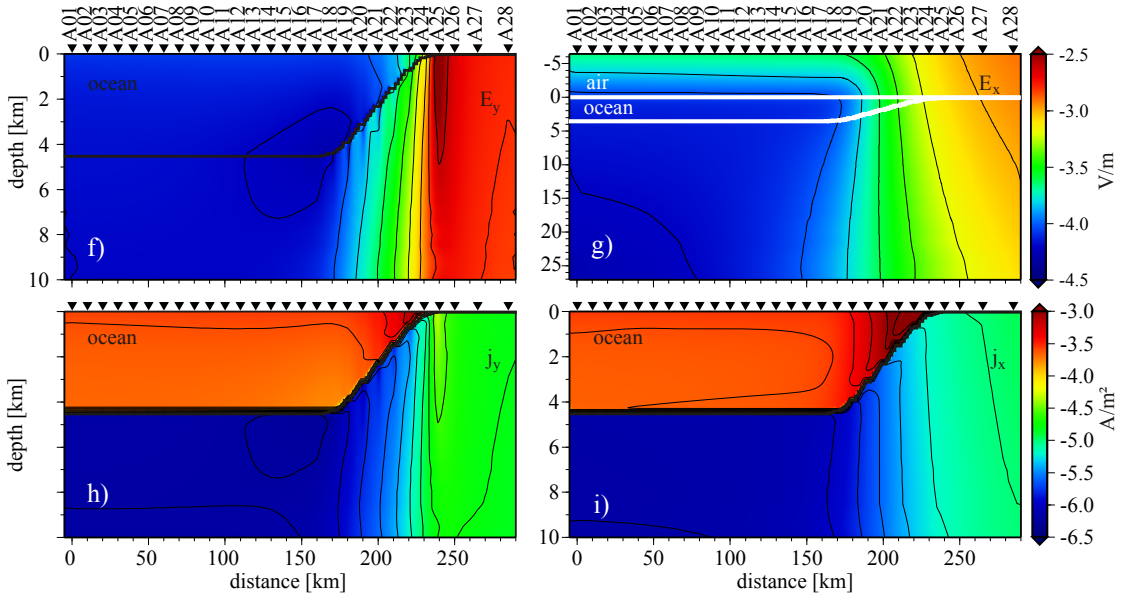

Figure 5.15.: Distribution of electric fields and currents at a period of $T = 315\,s$ at on- and offshore parts of the continental margin. The left column shows electric fields and current in TM mode; right column in TE mode. f) magnitude of E_y, g) magnitude of E_x; note the different depth scale and that the contours of E_x bend above the surface in the supplementary air layer (the contours of the magnitude correspond with stream lines of H_y in Fig. 5.14), h) magnitude of electric currents j_y in TM mode, i) magnitude of electric currents j_x in TE mode. The density of j_x increases significantly in the shallow ocean, close to the coast (brown color and higher density of contour lines). Note that the currents are continuous across the interface, but due to the large conductivity contrasts between the ocean and the ocean bottom the density vary very rapidly.

are below the ocean. At intermediate frequencies, the currents prefer to accumulate in the highly conductive ocean instead of the resistive ocean bottom, and this causes the responses to look like those due to infinite line currents right above the station. Note that if the MT responses are recorded at the top of the sea (Fig. 5.10), they behave as in a usual 2-D case, since all the currents are distributed below the sounding surface, instead of above, as is the case in the presented marine model.

The anomalous responses on ocean bottom are overcome or mitigated by introducing a very conductive layer below the seafloor, which must be at least several kilometers thick. However, the assumption of an oceanic crust being wholly conductive seems unrealistic. This is even more the case for the continental crust below the slope: every aquiclude would prohibit the intrusion of sea water into deeper layers. But another class of models makes the effect described above disappear, too: the association of the upper part of the downgoing plate with a good conductor (in accordance with standard models of subduction). Since the recorded seafloor data (see next section) behave relatively "normal", they may be interpreted as a hint of free fluids in the plate interface or its surroundings. The violation of the Kramers-Kronig relations by a strong seafloor

topography in connection with a highly conductive environment as a result of non-uniform induction has been observed in the San Diego Trough at the boundary of the Pacific and North American plates by Constable et al. (2009).

5.4. Marine measurements

5.4.1. Offshore instrumentation

The seafloor magnetotelluric measurements were performed during RV Sonne leg SO-181, in collaboration with the Woods Hole Oceanographic Institution, using the newly designed HEFMAG system. The instruments (Fig. 5.16) measured the natural temporal

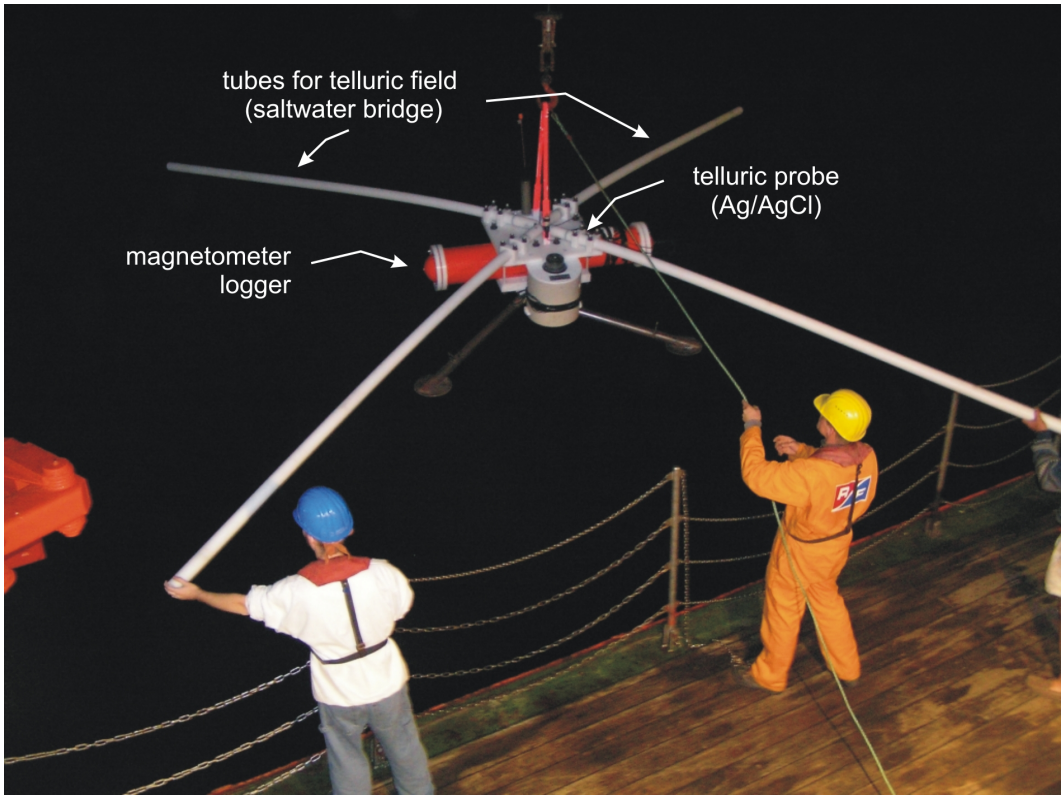

Figure 5.16.: Deployment of the HEFMAG seafloor magnetotelluric system during the RV Sonne cruise SO181. The HEFMAG system consists of a fluxgate magnetometer and a short-span telluric device based on saltwater bridges (Photo: H. Brasse).

geomagnetic and geoelectric (telluric) field variations in a period range from T = 80s - DC. While the fluxgate magnetometer is an adaptation of the terrestrial instrument, the usual terrestrial layout for probing the two components of the horizontal electric field – with an electrode spacing of 50-100 m, is on the ocean bottom, for practical and technical reasons, difficult to implement. Instead, a short-span device with approx. 6.50 m long dipole arms, incorporating unpolarizable Ag/AgCl electrodes at the inner

end, was deployed. Such salt water bridges enable the probing of the electric field at the ocean bottom without direct contact with the seafloor (Filloux, 1973, 1974; Chave et al., 1991).

Seven instruments were deployed at intervals of 30-35 km along a track that extends the onshore profile across the trench, towards the Pacific plate, as shown in Fig. 3.4. The stations recorded the variation of electromagnetic fields on the ocean floor at depths from 512 m up to 4568 m between December 2004 and February 2005. The significantly longer recording times are essential for obtaining high-quality transfer functions, since the magnetic field on the sea floor is substantially damped by the overlying, high-conductivity seawater layer, as described in section 5.2. Water motions, like sea movements and ocean currents, induce not only secondary magnetic fields which overlay the source field, as described in section 5.1, but can also cause instrument motion, and change instrument orientation. Furthermore, the shortened electrode spacing leads to less potential difference in the electric field; this results in lower signal-to-noise ratio, but this can be compensated for by longer recording time. On the other hand, noise sources like temperature drift, poor contact between the electrodes and subsurface and cultural or anthropogenic effects, which are typical for land measurements don't exist on the ocean floor, so that robust transfer functions can be expected (Chave et al., 1991). The movement and the absolute orientation of the sensors, i.e. the deviation from the azimuth and from the horizontal position, is measured by integrated compasses and inclinometers, and can be reconstructed by matrix rotations. The electromagnetic fields $\vec{E}, \vec{B}$, recorded in an arbitrarily orientated system can be transformed into the geomagnetic frame, denoted with $'$, via rotation by three angles: heading α, pitch β and roll γ. In matrix notation the operation can be written as:

$$\vec{E}' = \overleftrightarrow{R}_\alpha \overleftrightarrow{R}_\beta \overleftrightarrow{R}_\gamma \vec{E} \qquad \vec{B}' = \overleftrightarrow{R}_\alpha \overleftrightarrow{R}_\beta \overleftrightarrow{R}_\gamma \vec{B}. \tag{5.58}$$

where

$$\overleftrightarrow{R}_\alpha = \begin{pmatrix} \cos\alpha & -\sin\alpha & 0 \\ \sin\alpha & \cos\alpha & 0 \\ 0 & 0 & 1 \end{pmatrix} \overleftrightarrow{R}_\beta = \begin{pmatrix} \cos\beta & 0 & \sin\beta \\ 0 & 1 & 0 \\ -\sin\beta & 0 & \cos\beta \end{pmatrix} \overleftrightarrow{R}_\gamma = \begin{pmatrix} 1 & 0 & 0 \\ 0 & \cos\gamma & -\sin\gamma \\ 0 & \sin\gamma & \cos\gamma \end{pmatrix}. \tag{5.59}$$

The matrix multiplication yields a total rotation matrix, $\overleftrightarrow{R}$, and the three magnetic and two electric field components measured in the reference system of the instruments are calculated as follows:

$$\begin{pmatrix} B_x' \\ B_y' \\ B_z' \end{pmatrix} = \begin{pmatrix} \cos\alpha\cos\beta & -\sin\alpha\cos\gamma + \cos\alpha\sin\beta\sin\gamma & \sin\alpha\sin\gamma + \cos\alpha\sin\beta\cos\gamma \\ \sin\alpha\cos\beta & \cos\alpha\cos\gamma + \sin\alpha\sin\beta\sin\gamma & -\cos\alpha\sin\gamma + \sin\alpha\sin\beta\cos\gamma \\ -\sin\beta & \cos\beta\sin\gamma & \cos\beta\cos\gamma \end{pmatrix} \begin{pmatrix} B_x \\ B_y \\ B_z \end{pmatrix},$$

$$\begin{pmatrix} E_x' \\ E_y' \end{pmatrix} = \begin{pmatrix} \cos\alpha\cos\beta & -\sin\alpha\cos\gamma + \cos\alpha\sin\beta\sin\gamma \\ \sin\alpha\cos\beta & \cos\alpha\cos\gamma + \sin\alpha\sin\beta\sin\gamma \\ -\sin\beta & \cos\beta\sin\gamma \end{pmatrix} \begin{pmatrix} E_x \\ E_y \end{pmatrix}. \tag{5.60}$$

Note that if pitch β and roll γ are negligible, which is here true for all sites except ob5, the rotation matrix $\overleftrightarrow{R}$ can be simplified to

$$\overleftrightarrow{R} = \begin{pmatrix} \cos\alpha & -\sin\alpha & 0 \\ \sin\alpha & \cos\alpha & 0 \\ 0 & 0 & 1 \end{pmatrix} \tag{5.61}$$

and only the horizontal fields have to be rotated around the fixed z-axis.

5.4.2. Marine data

During the RV Sonne leg SO-181 a CTD log at depths of up to 4000 m was performed, and is shown in Fig. 5.17. The knowledge of sea water resistivity is essential for subse-

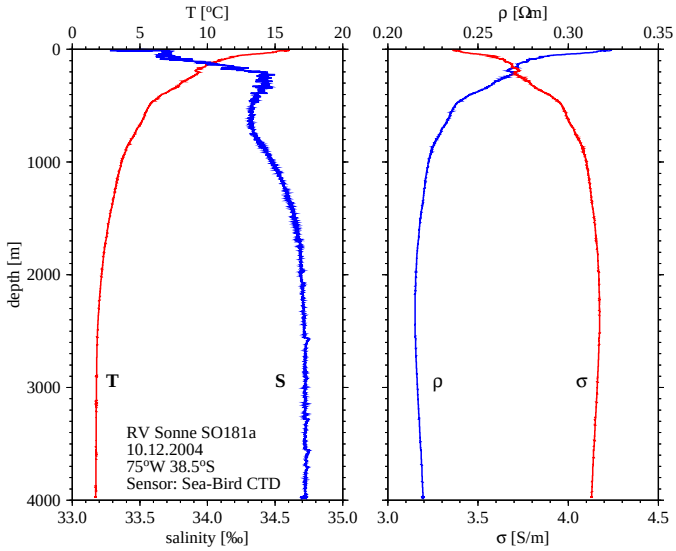

Figure 5.17.: Logs of temperature and salinity (left); and electrical conductivity and resistivity (right), measured during RV Sonne leg SO-181.

quent modeling, since the ocean layer exercises a large influence over the offshore study, as well as the onshore, and has to be incorporated as an a priori structure in the starting model. The conductivity of seawater depends on pressure, salinity, and temperature, and has been investigated by Horne and Frysinger (1963). While the effects of pressure and salinity variations are typically in the range of approximately 5% and 2.5% respectively have only a negligible effect on the sea water conductivity, the strongly varying water temperature in the ocean results in resistivity variations between 0.16 Ωm at 30°C and 0.33 Ωm at 1.0°C. Thus, temperature is the dominant factor controlling electrical conductivity (Filloux, 1987). The estimated salinity values, presented in Fig. 5.17 agree very well with the literature data (Filloux, 1987).

A short section of time series data recorded during a magnetic storm on Jan 8, 2005 at the seafloor by all offshore stations (top) and on land by the station *jul* (bottom) is

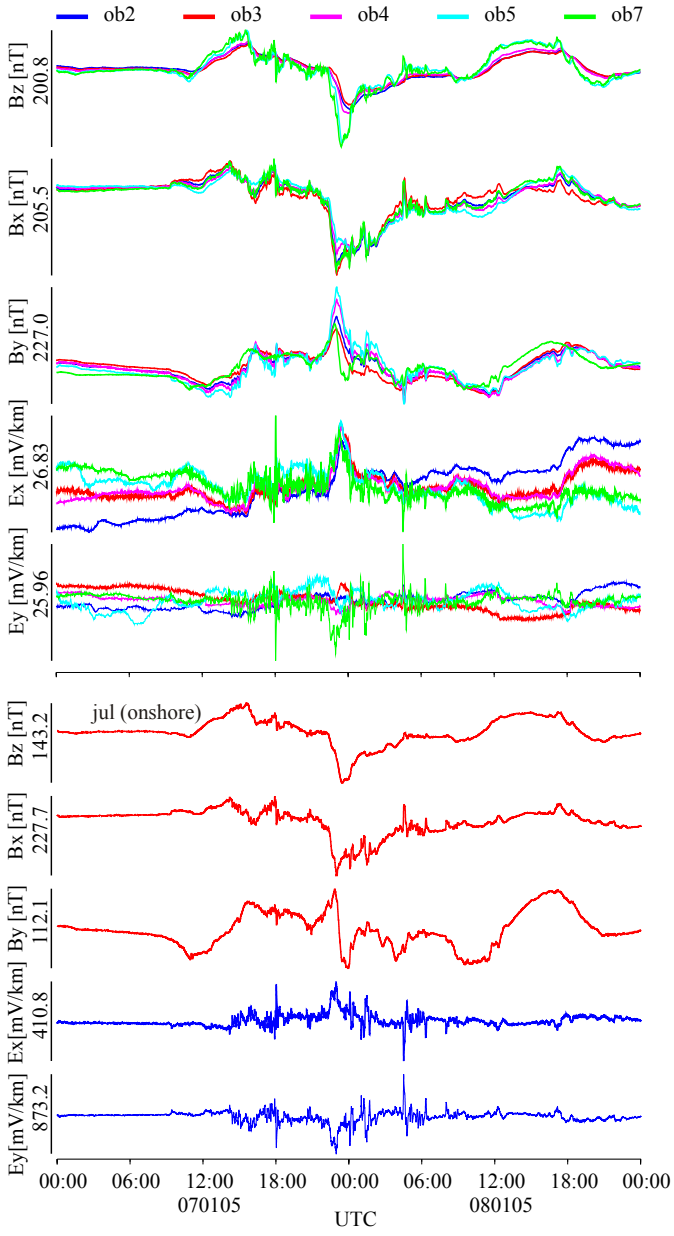

Figure 5.18.: Comparison of the time series recorded at the ocean bottom (top) and the land station *jul* (bottom). Note the high correlation between the magnetic components between the sites.

shown in Fig. 5.18. The offshore data were preliminarily interpolated and resampled by a spline function, and then rotated to geomagnetic north according to eq. 5.60. Besides an obvious correlation between the on- and offshore magnetic fields apparent in this short section, all offshore records clearly reveal regular diurnal variations of the Earth's magnetic field, commonly known as *Sq variations*; especially in B_y and B_z. In the B_x

component, Sq variations are slightly attenuated, though still recognizable. This indicates that Sq electric currents flow predominantly in the x-direction (N-S) and generate Sq magnetic variations primarily in y-direction. The strength of variation as a function of frequency is presented as power spectra in Fig. 5.19. The Power Spectrum Density (PSD) is a measure of power per unit of frequency and reveals useful information as to at which frequencies the variations are strong and at which weak. The spectra of observed electromagnetic fields and tilts can reveal whether the electromagnetic signals arise from natural sources, or are induced by motions of the instruments. The power and cross spectral densities are estimated by Welch's method. This method divides the time series $x(t)$ into n_d overlapping segments $x_i(t)$ of length T, and averages their Fourier transforms. A two sided autospectral density function S_{xx} described by Bendat and Piersol (1971) is given by:

$$S_{xx}(f) = \frac{1}{n_d T} \sum_{m=1}^{n_d} \left| \int_0^T x_m(t) e^{-i2\pi f t} dt \right|^2 \tag{5.62}$$

For numerical computation of the PSD, each record segment $x_i(t)$ is discretized into N data values, equally spaced on time intervals Δt. The Fourier transform for each segment calculated at discrete frequencies $f_k = \frac{k}{T} = \frac{k}{N\Delta t}$ with $k = 0, 1, ..., N-1$ yields:

$$X_m(f_k) = \Delta t X_{mk} = \Delta t \sum_{n=0}^{N-1} x_{in} e^{\frac{-i2\pi kn}{N}} \tag{5.63}$$

and thus eq. 5.62 becomes, in digital terms:

$$S_{xx}(f_k) = \frac{1}{n_d N \Delta t} \sum_{m=1}^{n_d} |X_m(f_k)|^2 . \tag{5.64}$$

The power spectra calculated from the recorded magnetic and electric fields and the tilts are presented in Fig. 5.19. In the y, the z, and to a lesser extent, in the x component of the magnetic field, as well as in the x component of the electric field, three prominent spectral lines rise clearly from the ground or noise level, and can be identified as the first three harmonics of the periodical solar daily variations designated here as S_1, S_2, S_3 (see the enlarged views). This plot corresponds with the well-marked pattern of the daily variations observed in the time series, and the prominent peaks in E_x, B_y and B_z are attributed to N-S flowing Sq electric currents. In the E_y component, which is not affected by the N-S currents, and also in the tilts, the principal lunar variation M_2, at period $T = 1.93$ cpd, becomes dominant over the Sq fluctuations. Note the significantly lower spectral magnitude in E_y. Daily variations generated by ocean tides were already observed in the seafloor data by Larsen (1968), and are listed in the following table: "Solar and lunar cycles", taken from Chave and Filloux (1984).

For the processing of the offshore time series, Egbert's code has been modified to conform with the format of the offshore data. Since the magnetic field is strongly attenuated by the ocean layer, and the sampling period of 30 s is much lower than for land surveys

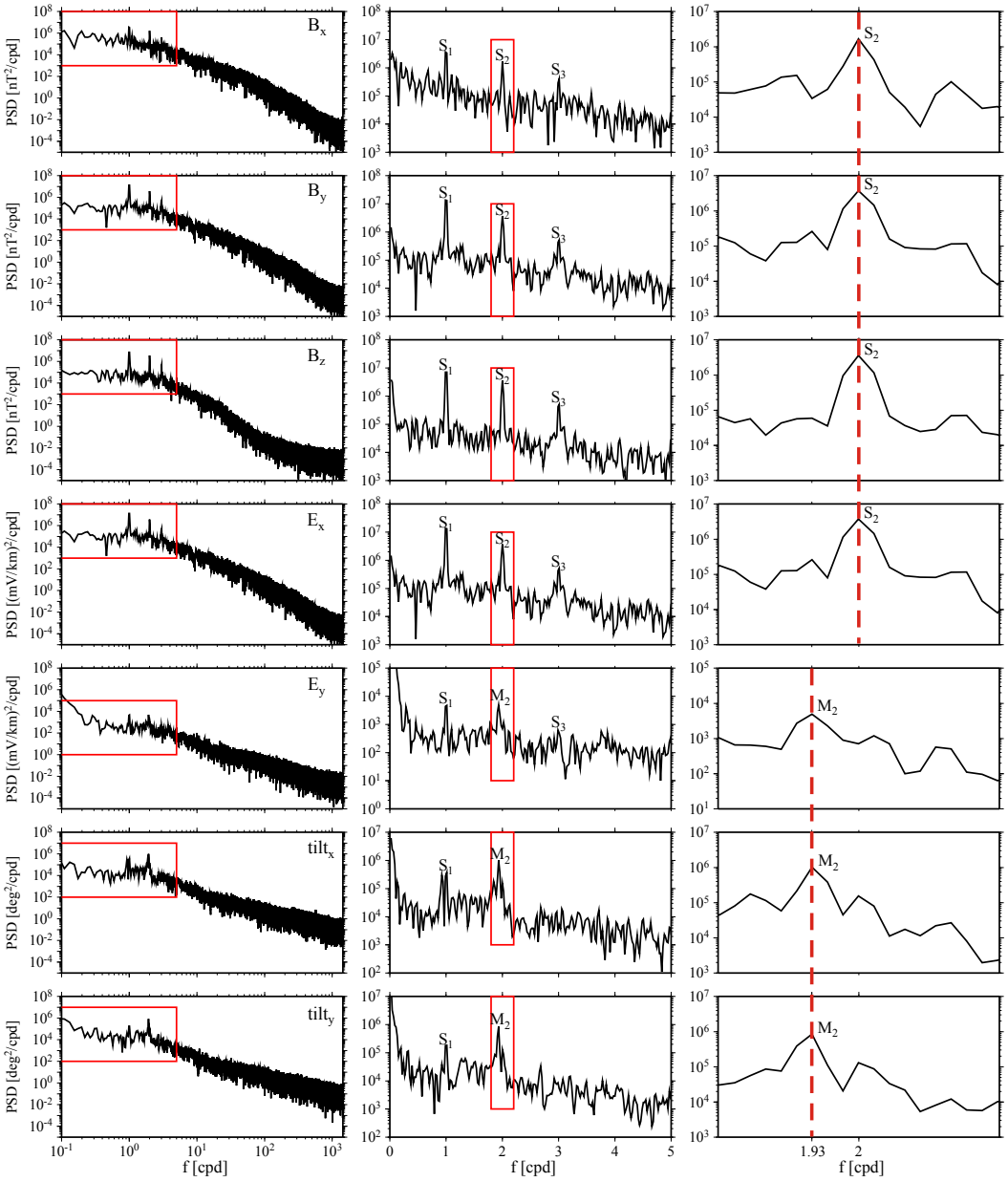

Figure 5.19.: Spectra of magnetic and electric fields and tilts recorded at the seafloor site *ob2*. The harmonics, designated S_1, S_2, S_3, occurring at frequencies of 1, 2, 3 cpd (cycles per day), correspond to Sq variations. Harmonics denoted as M_2 correspond to the principal lunar tide. The entire spectrum is presented on the left side. The red windows encompass intervals of 5 cpd, which are presented in the middle column. In a further enlargement, in the right column tides associated with the principal lunar tide M_2 can be clearly distinguished from Sq peaks.

Solar and lunar cycles

	Tidal mode	Frequency (cpd)	Frequency (cph)	Period (hours)
S_1	solar diurnal	1	0.04166667	24
N_2	elliptical lunar	1.89598605	0.07899942	12.658321
M_2	principal lunar	1.932275048	0.08051146	12.420592
S_2	solar semidiurnal	2	0.08333333	12
S_3	solar third harmonic	3	0.12500000	8
S_4	solar fourth harmonic	4	0.16666667	6
S_5	solar fifth harmonic	5	0.20833333	4.8

the transfer function were calculated for a period range of 100 - 60 000 s. The quality of the magnetotelluric transfer functions shown in Fig. 5.20 is significantly worse than on land, with exception from the data of the closest station to the coast, *ob7*. Jumping values in both the apparent resistivity and phase, particularly in Z_{yx}, dominate the image over a large period range, and the phases of both modes cover two quadrants. Smooth curves similar to that observed onshore are only exhibited at station *ob7*. This may, in part, be due to the employment of the newly-designed HEFMAG instruments, for which insufficient opportunity for prior testing was available. The quality couldnt't also be improved using the remote-reference technique, which utilizes remotely recorded magnetic fields at the local station. The underlaying idea is based on the assumption that the natural and uncontaminated part of induced fields are coherent over a large spatial range, whereas the noise is only a local effect, and does not correlate with the induced signal; and thus can be removed from the data. However, at a continental margin, where the fields in the ocean are strongly disturbed by bathymetric effects, as described in the previous section, the fields of one station can not be replaced by fields recorded at another place, even at the modest distance between the stations.

In contrast to this, the geomagnetic transfer functions, presented here in the form of induction arrows, yield a consistent image and show a smooth behavior over the recorded period range. The magnitude of their real part is small in the deep ocean beyond the trench, and doesn't show any special orientation contrary to the data from the stations at the onshore profile. This is a clear indication of the different geological and tectonic properties of the Nazca and South American plates. The arrows become significantly larger at stations close to the trench (*ob5*), and on the continental shelf (*ob7*). The unusually large imaginary arrows (compared to land surveys) at station *ob5*, are caused by anomalous magnetic fields generated by bathymetry, and can only be qualitatively explained by forward modeling with detailed reconstructed bathymetry, as shown in Fig. 5.7. They can be interpreted as a hint of a large phase shift between the vertical and horizontal magnetic fields at the seafloor, and are, in addition to the anomalous effects in the magnetotelluric responses, like peaks in apparent resistivity and phases exceeding the "normal" quadrant, a typical feature for magnetotelluric surveys at the continental margin. Although in general the magnitude of the modeled induction vectors on the

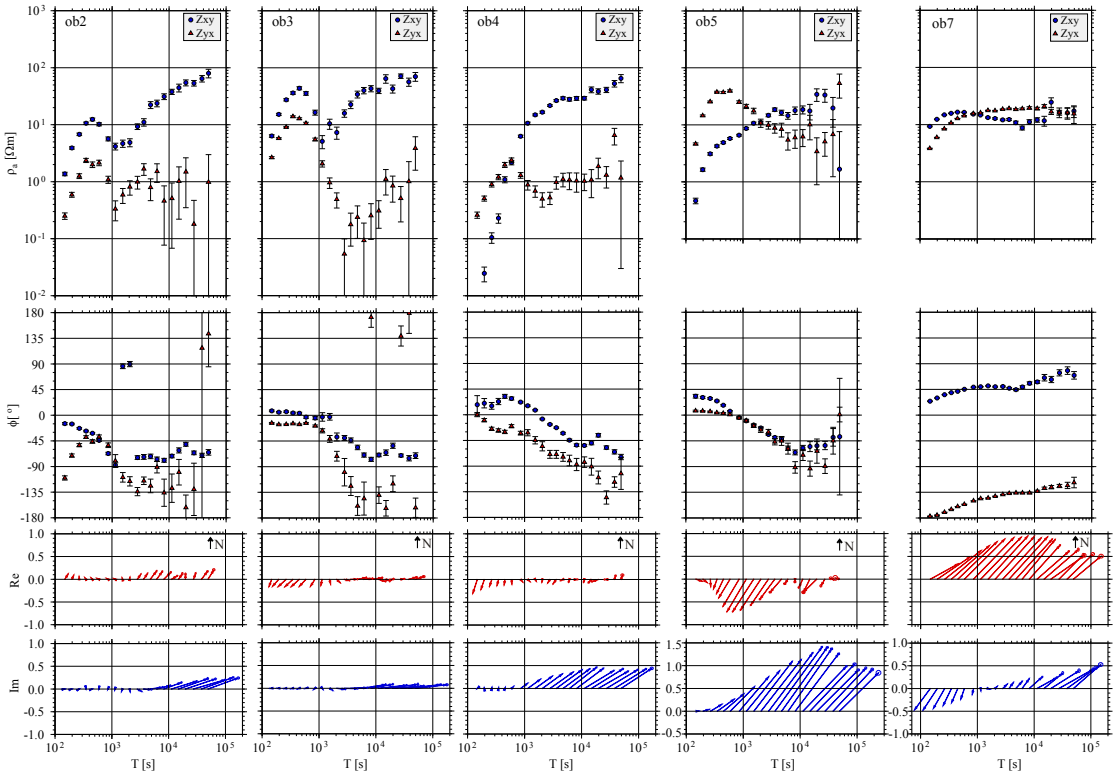

Figure 5.20.: Apparent resistivities and phases, and real and imaginary induction arrows calculated at the offshore sites.

ocean bottom can be very large, its exact value depends strongly on the position and the distance to the slope, because the fields, and consequently the geomagnetic transfer function, are sensitive to bathymetric changes. Thus, a nearly exact image of the true bathymetry is required in order to evaluate the data fit. This is, however, difficult to realize without excessive grid refinement. Note also that the responses in Fig. 5.7 are generated from a model that consists only of an ocean and a homogeneous half space, so that it is not surprising that this very simple model does not completely explain the observed induction vectors. For this purpose a more complex model, probably including 3-D bathymetry, is required. Also remarkable is the huge magnitude and the orientation of the real arrows at station *ob7*, which also point systematically NE, similar to the unique pattern observed at all onshore stations on the South American Plate.

In search of the appropriate strike direction, the profile was divided into segments, paying regard to different geologic units and tectonic settings within the measurement area. A separate strike analysis for the offshore profile presented in the rose diagrams in Fig. 5.21 reveals a unique and realistic strike angle of about N6°E, that corresponds with the strike onshore, and with the trench axis. Note that this value can only be obtained if the offshore site *ob7*, deployed on the continental shelf, is taken into account. Omitting

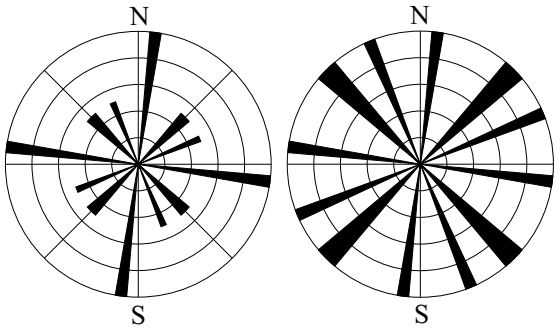

Figure 5.21.: Electrical strike of the offshore side of the TIPTEQ profile for a period range of 150 - 38 000 s. A strike of N6°E can be resolved if all offshore stations are included (left side). Omitting the offshore station ob7 on the continental shelf, a strike direction cannot be determined; probably due to poor data quality (right side).

the data from this station, and regarding only the poor quality impedances of the deep ocean stations on the Nazca Plate, a preferred strike direction cannot be identified any more.

6. The standard isotropic modeling

The dimensionality analyses of the data acquired at the South-Central Chilean continental margin, performed by Brasse and Soyer (2001) for the central and southern profile, and in chapter 4 of this work for the northern profile, reveal that 2-D modeling and interpretation of the conductivity distribution is adequate and justified. This chapter concentrates on isotropic 2-D inversions of the transfer functions along these three profiles, and 3-D forward modeling at the volcano Villarrica. The 2-D inversion was performed with the non-linear conjugate gradient (NLCG) algorithm from Rodi and Mackie (2001); and the 3-D forward modeling with the MT3DFWD algorithm from Mackie and Madden (1993) and Mackie et al. (1994) which solves the attendant second order partial differential equations using the finite-difference (FD) method. Both algorithms are implemented in the *WinGLink* software package.

First, the chapter provides an overview of the basics of the theoretical principles of the inversion problem, followed by the practical application of the isotropic 2-D inversion and 3-D forward approaches and the presentation of the resultant models.

6.1. Basics of inverse problem

6.1.1. Formulation of the nonlinear inverse problem

The ultimate goal of the modeling of magnetotelluric data is to find a model of conductivity distribution in the Earth's interior which corresponds to the electromagnetic fields observed on the Earth's surface. The relation between predicted or synthetic data $\vec{d}^{syn}$ comprising N elements in the data space $(d_1, d_2 ... d_N)$ and model parameters $\vec{m}$ comprising M elements in the model space $(m_1, m_2 ... m_M)$ can be written in the form of a simple mathematical equation:

$$\vec{d}^{syn} = \vec{f}(\vec{m}), \tag{6.1}$$

where $\vec{f}$ is a forward functional. In order to obtain model parameters from synthetic data the relationship must be formulated inversely:

$$\vec{m} = \vec{f}^{-1}(\vec{d}^{syn}). \tag{6.2}$$

Both the forward and inverse problem are solved numerically, which requires a fragmentation or discretization of the model space:

$$\vec{m}(\vec{r}) = \vec{\sigma}(\vec{r}) = \sum_{i=1}^{N} \sum_{j=1}^{L} \sigma_{i,j} \phi_{i,j}(\vec{r}) \tag{6.3}$$

where $\vec{\sigma}(\vec{r})$ is a conductivity distribution and $\phi_{i,j}$ is a basis function which attributes a conductivity value $\sigma_{i,j}$ at the location of the (i,j)th node in a grid with $N \times L$ cells in horizontal and vertical direction (McGillivray and Oldenburg, 1990; Schwalenberg, 1997). The discretization of the model space generates a system of algebraic equations at each grid node, so a large set of equations must be solved numerically. In a nonlinear case, or if a large number of parameters exist, the problem is solved by iterative techniques that attempt to approximate a solution by successively improving an initial guess until a convergence criterion is satisfied.

In the case of a linear relation between model parameters and data the functional $\vec{f}$ can be replaced by a matrix $\overleftrightarrow{G}$, and eq. 6.1 is rewritten as a linear system of equations:

$$\vec{d}^{syn} = \overleftrightarrow{G}\vec{m}. \tag{6.4}$$

6.1.2. The Gauss-Newton algorithm

6.1.2.1. Linearization of a nonlinear problem – the sensitivity matrix

If the relation between the data and the model is nonlinear, as is usually the case, then the forward operator (in vector notation $\vec{f} = \{f_i\}$) can be linearly approximated by the first two terms of the Taylor series, provided that $\vec{f}$ is a continuously differentiable function:

$$\begin{aligned}
\vec{d}^{syn} = \vec{f}(\vec{m}) = \vec{f}(\vec{m}_0 + \Delta\vec{m}) &= \sum_{i=1}^{N} f_i(\vec{m}_0) + \sum_{i=1}^{N} \frac{\partial f_i(\vec{m}_0)}{\partial m_1}\delta m_1 + \sum_{i=1}^{N} \frac{\partial f_i(\vec{m}_0)}{\partial m_2}\delta m_2 + \dots \\
&+ \sum_{i=1}^{N} \frac{\partial f_i(\vec{m}_0)}{\partial m_k}\delta m_k + \dots + \mathcal{O}(\|\delta m\|) \\
&\approx \sum_{i=1}^{N} f_i(\vec{m}_0) + \sum_{i=1}^{N}\sum_{k=1}^{M} \frac{\partial f_i(\vec{m}_0)}{\partial m_k}\delta m_k \\
&= \vec{f}(\vec{m}_0) + \frac{\partial \vec{f}(\vec{m}_0)}{\partial \vec{m}}\Delta\vec{m} \\
&= \vec{f}(\vec{m}_0) + \nabla\vec{f}(\vec{m}_0)\Delta\vec{m} \\
&= \vec{f}(\vec{m}_0) + \overleftrightarrow{S}\Delta\vec{m},
\end{aligned} \tag{6.5}$$

where $\Delta\vec{m}$ is a small perturbation about the starting model $\vec{m}_0$, and

$$\overleftrightarrow{S}(\vec{m}_0) = \nabla\vec{f}(\vec{m}_0) = \begin{pmatrix} \nabla f_1(\vec{m}_0)^T \\ \vdots \\ \nabla f_N(\vec{m}_0)^T \end{pmatrix} = \begin{pmatrix} \frac{\partial f_1(\vec{m}_0)}{\partial m_1} & \dots & \frac{\partial f_1(\vec{m}_0)}{\partial m_M} \\ \vdots & \ddots & \vdots \\ \frac{\partial f_N(\vec{m}_0)}{\partial m_1} & \dots & \frac{\partial f_N(\vec{m}_0)}{\partial m_M} \end{pmatrix} \tag{6.6}$$

denotes the *Jacobian-Matrix* or *sensitivity matrix*. The *Jacobian*, composed of partial derivatives of the nonlinear operators f_i with respect to each of the model parameters m_k, is a linear approximation of a function $\vec{f}$, and depicts how sensitive the function is

to changes of the model parameters. The contribution of each grid element to the model modification is determined by

$$s_k = \sum_{i=1}^{N} \frac{\partial f_i(\vec{m}_0)}{\partial m_k} \delta m_k. \tag{6.7}$$

Due to equality of the relationships:

$$\vec{f}(\vec{m}) - \vec{f}(\vec{m}_0) = \vec{f}(\vec{m}_0 + \Delta\vec{m}) - \vec{f}(\vec{m}_0) = \vec{d}^{syn} - \vec{d}_0^{syn} = \Delta\vec{d}^{syn} = \frac{\partial \vec{f}(\vec{m}_0)}{\partial \vec{m}} \Delta\vec{m} \tag{6.8}$$

the linearized forward problem can be expressed as:

$$\Delta\vec{d}^{syn} = \overleftrightarrow{S}\Delta\vec{m}. \tag{6.9}$$

6.1.2.2. Iterative solution of the linearized unconstrained inverse problem

Because the observed data $\vec{d}^{obs}$ are afflicted with errors $\vec{e}$, they differ from the synthetic data $\vec{d}^{syn}$ calculated by the forward operator $\vec{f}$, so that it is impossible to find a model which satisfies every d_i^{obs} exactly; therefore, the relationship in eq. 6.1 must be modified to account for this

$$\vec{f}(\vec{m}) = \vec{f}(\vec{m}_0 + \Delta\vec{m}) = \vec{d}^{obs} - \vec{e} = \vec{d}^{syn}. \tag{6.10}$$

In this case, the solution can only be approximated, and the strategy is to find a model parameter $\vec{m}$ which produces the smallest residual

$$\vec{e} = \vec{d}^{obs} - \vec{d}^{syn} = \vec{d}^{obs} - \vec{f}(\vec{m}) \tag{6.11}$$

between observed data $\vec{d}^{obs}$ and synthetic data $\vec{d}^{syn} = \vec{f}(\vec{m})$. This problem is equivalent to minimization of the so called *penalty*, *misfit* or *objective function* $\psi_1(\vec{m})$, defined as the sum of the squares of the residuals e_i:

$$\psi_1(\vec{m}) = \psi_1(\vec{m}_0 + \Delta\vec{m}) = \sum_{i=1}^{N} e_i^2 = \vec{e}^T\vec{e}. \tag{6.12}$$

Substitution of eq. 6.11 in eq. 6.12 and application of eq. 6.5 yields:

$$\begin{aligned}
\psi_1(\vec{m}) = \psi_1(\vec{m}_0 + \Delta\vec{m}) &= \|\vec{d}^{obs} - \vec{f}(\vec{m}_0 + \Delta\vec{m})\|^2 \\
&= \left[\vec{d}^{obs} - \vec{f}(\vec{m}_0) - \overleftrightarrow{S}\Delta\vec{m}\right]^T \left[\vec{d}^{obs} - \vec{f}(\vec{m}_0) - \overleftrightarrow{S}\Delta\vec{m}\right] \\
&= \Delta\vec{d}^T\Delta\vec{d} - \Delta\vec{d}^T\overleftrightarrow{S}\Delta\vec{m} - \Delta\vec{m}^T\overleftrightarrow{S}^T\Delta\vec{d} + \Delta\vec{m}^T\overleftrightarrow{S}^T\overleftrightarrow{S}\Delta\vec{m} \\
&= \Delta\vec{d}^T\Delta\vec{d} - 2\Delta\vec{m}^T\overleftrightarrow{S}^T\Delta\vec{d} + \Delta\vec{m}^T\overleftrightarrow{S}^T\overleftrightarrow{S}\Delta\vec{m},
\end{aligned} \tag{6.13}$$

where $\Delta\vec{d} = \vec{d}^{obs} - \vec{f}(\vec{m}_0)$ describes the misfit between observed and predicted data on the basis of the starting model $\vec{m}_0$. The minimization of the penalty function is

accomplished by applying the *least squares method*, i.e. taking the derivatives of ψ_1 with respect to $\Delta\vec{m}$ and setting them equal to zero:

$$\nabla\psi_1(\vec{m}) = \frac{\partial\psi_1(\vec{m})}{\partial\Delta\vec{m}} = \begin{pmatrix} \frac{\partial\psi_1(\vec{m})}{\partial\Delta m_1} \\ \vdots \\ \frac{\partial\psi_1(\vec{m})}{\partial\Delta m_M} \end{pmatrix} = -2\overleftrightarrow{S}^T\Delta\vec{d} + 2\overleftrightarrow{S}^T\overleftrightarrow{S}\Delta\vec{m} \stackrel{!}{=} 0 \tag{6.14}$$

From the resulting so-called *normal equation*:

$$\overleftrightarrow{S}^T\overleftrightarrow{S}\Delta\vec{m} = \overleftrightarrow{S}^T\Delta\vec{d} \tag{6.15}$$

a linearized inverse relation can be formulated:

$$\Delta\vec{m} = (\overleftrightarrow{S}^T\overleftrightarrow{S})^{-1}\overleftrightarrow{S}^T\Delta\vec{d}. \tag{6.16}$$

Note that relation 6.16 is equivalent to the linear problem in eq. 6.2, with the quantity $(\overleftrightarrow{S}^T\overleftrightarrow{S})^{-1}\overleftrightarrow{S}^T$ corresponding to the inverse operator $\vec{f}^{-1}$. In contrast to eq. 6.2, the operator $(\overleftrightarrow{S}^T\overleftrightarrow{S})^{-1}\overleftrightarrow{S}^T$ doesn't act on the perfect data but on the residual between the observed and predicted data $\Delta\vec{d}$, and thus it doesn't recover $\vec{m}$ but rather a perturbation update $\Delta\vec{m}$ with respect to a starting model $\vec{m}_0$. In order to yield the searched-for model $\vec{m}$ fitting the observed data, $\Delta\vec{m}$ must be applied to $\vec{m}_0$:

$$\vec{m}_1 = \vec{m}_0 + \left(\overleftrightarrow{S}(\vec{m}_0)^T\overleftrightarrow{S}(\vec{m}_0)\right)^{-1}\overleftrightarrow{S}(\vec{m}_0)^T\Delta\vec{d}. \tag{6.17}$$

Repeating this process, by adding the latest model increment $\Delta\vec{m}_{n+1}$ to the prior model $\vec{m}_n$, where the former is estimated by partial differentiation with respect to the modified starting model $\vec{m}_n$, will result in an improved model $\vec{m}_{n+1}$:

$$\vec{m}_{n+1} = \vec{m}_n + \left(\overleftrightarrow{S}(\vec{m}_n)^T\overleftrightarrow{S}(\vec{m}_n)\right)^{-1}\overleftrightarrow{S}(\vec{m}_n)^T\left(\vec{d}^{obs} - \vec{f}(\vec{m}_n)\right). \tag{6.18}$$

An iterative application of this procedure by successively refining the model parameters is implemented by the *Gauss-Newton algorithm* used to solve nonlinear least squares problems. The algorithm updates and approximates the solution of the nonlinear inversion problem until a stable solution of desired accuracy is obtained.

6.1.2.3. Levenberg-Marquardt approach

Difficulties arise if the dimension of the model space exceeds the dimension of the data space, i.e. the number of equations is not as great as the number unknowns, which is the case in most geophysical modeling. The problem is then underdetermined and the matrix $\overleftrightarrow{S}^T\overleftrightarrow{S}$ becomes singular, i.e., $\det(\overleftrightarrow{S}^T\overleftrightarrow{S})$ is zero and its eigenvalues vanish so that the inverse of $\overleftrightarrow{S}^T\overleftrightarrow{S}$ doesn't exist. As soon as $\overleftrightarrow{S}^T\overleftrightarrow{S}$ becomes nearly singular, the perturbation vector $\Delta\vec{m}$ tends to oscillate unboundedly, and the Gauss-Newton algorithm will in turn become extremely unstable. Thus, small changes in the data can drive large changes in the estimated models and the algorithm may diverge (e.g., Lines and Treitel, 1984). To

stabilize the diverging solution and to damp the parameter perturbation during iterative applications of Taylor's approximations, the *Gauss-Newton algorithm* is modified by introducing the term $\beta\overleftrightarrow{I}$ in the normal equation

$$\left(\overleftrightarrow{S}^T\overleftrightarrow{S} + \beta\overleftrightarrow{I}\right)\Delta\vec{m} = \overleftrightarrow{S}^T\left(\vec{d}^{obs} - \vec{f}(\vec{m}_0)\right), \tag{6.19}$$

so that

$$\vec{m}_{n+1} = \vec{m}_n + \left(\overleftrightarrow{S}(\vec{m}_n)^T\overleftrightarrow{S}(\vec{m}_n) + \beta\overleftrightarrow{I}\right)^{-1}\overleftrightarrow{S}(\vec{m}_n)^T\left(\vec{d}^{obs} - \vec{f}(\vec{m}_n)\right). \tag{6.20}$$

The parameter β is successively adjusted during the inversion and, via the identity matrix $\overleftrightarrow{I}$, added to the main diagonal of $\overleftrightarrow{S}^T\overleftrightarrow{S}$, preventing the eigenvalues thereof from vanishing, and the matrix becoming singular. If β attains to very large values, the algorithm approaches the *steepest descent method*, providing slow but certain convergence, whereas as β gets small the least squares method from eq. 6.18 becomes dominant. This technique, called the *Levenberg-Marquardt method*, is thus a hybrid technique capable of alternating between the *steepest descent* and *Gauss-Newton* algorithms, offering the good performance of the *Gauss-Newton* algorithm where possible, as well as very good convergence properties (Levenberg, 1944; Marquardt, 1963, 1970; Aster et al., 2005).

6.1.2.4. Constrained solution of nonlinear problems by including a priori information

The solution of an inversion problem is usually non-unique, and a range of different models that adequately satisfy the experimental data can be found. Inverse problems where these situations arise, or small perturbations of the data have large effects on the solution, as described above, are referred to as ill-conditioned problems (Hansen, 1998). The conventional way to deal with an ill-conditioned problem is to impose an additional constraint (ψ_2) in order to bias the solution. Such constraints can be, for instance, external information about the size and smoothness of the desired solution. This so-called *a priori information* can be inferred from geological sources or previous geological surveys. The process referred to as *regularization* constraints the model space, stabilizes the inversion, and helps to select a unique solution among infinitely equivalent solutions that explains the data and satisfies the requirements on the model. Mathematically, such conditions are realized by introducing an expression in the penalty function of the form:

$$\overleftrightarrow{R}\vec{m} = \vec{h}, \tag{6.21}$$

that maps the model parameter $\vec{m}$ onto the a priori vector $\vec{h}$, where $\overleftrightarrow{R}$ is a diagonal matrix with values of 1 if the corresponding model parameter should be considered or 0 if not. In matrix notation it can be generally written as:

$$\overleftrightarrow{R}\vec{m} = \vec{h} = \begin{pmatrix} 1 \text{ or } 0 & & 0 \\ & \ddots & \\ 0 & & 1 \text{ or } 0 \end{pmatrix} \cdot \begin{pmatrix} m_1 \\ \vdots \\ m_k \end{pmatrix} = \begin{pmatrix} h_1 \\ \vdots \\ h_k \end{pmatrix}. \tag{6.22}$$

One possible way to constrain the solution, amongst many others, is to invert inexact data by damping the variability of the inverted model parameter $\vec{m}$ (i.e. normalizing the length of the solution vector). A preferable and effective constraint is to impose a condition that ensures that the model parameters vary slowly with position, giving a smooth or flat solution. Generally this is realized by minimizing the difference

$$\sum_{j=1}^{N}(m_j - m_{j+1})^2, \tag{6.23}$$

between physically adjacent parameters, and setting $\vec{h} = [0, ..., 0]^T$. In matrix notation this choice of constraint yields

$$\overleftrightarrow{R}\vec{m} = \vec{h} = \begin{pmatrix} 1 & -1 & 0 \\ & \ddots & \\ 0 & 1 & -1 \end{pmatrix} \cdot \begin{pmatrix} m_1 \\ \vdots \\ m_k \end{pmatrix} = \begin{pmatrix} 0 \\ \vdots \\ 0 \end{pmatrix}, \tag{6.24}$$

where the difference operator $\overleftrightarrow{R}$ is the $(k-1) \times k$ dimensional smoothness matrix (see e.g., Constable et al., 1987; Meju, 1994).

As mentioned above, a reasonable strategy for finding the "best" approximate solution to an ill-conditioned and regularized system is to find an $\vec{m}$ that produces not only a minimum misfit or residual between the data and the theoretical predictions of the forward problem ($\|\vec{d}^{obs} - \vec{f}(\vec{m})\|$) but also biases the model parameter $\vec{m}$ towards the *a priori* vector $\vec{h}$. Thus, the penalty function must be extended by a constraining term ψ_2, which can be expressed by

$$\psi_2(\vec{m}) = \sum_{i=1}^{N}(R_{ij}m_j - h_i)^2 = \left[\overleftrightarrow{R}\vec{m} - \vec{h}\right]^T \left[\overleftrightarrow{R}\vec{m} - \vec{h}\right] \tag{6.25}$$

and the entire (modified) penalty function is a sum of the misfit and regularization terms:

$$\begin{aligned} \psi(\vec{m}) &= \psi_1(\vec{m}) + \overleftrightarrow{\Lambda}\psi_2(\vec{m}) \\ &= \left[\Delta\vec{d} - \overleftrightarrow{S}\Delta\vec{m}\right]^T \left[\Delta\vec{d} - \overleftrightarrow{S}\Delta\vec{m}\right] + \left[\overleftrightarrow{\lambda}\left(\overleftrightarrow{R}\vec{m} - \vec{h}\right)\right]^T \left[\overleftrightarrow{\lambda}\left(\overleftrightarrow{R}\vec{m} - \vec{h}\right)\right], \end{aligned} \tag{6.26}$$

where $\overleftrightarrow{\Lambda} = \overleftrightarrow{\lambda}^T\overleftrightarrow{\lambda}$ is a matrix whose elements are regularization parameters. $\overleftrightarrow{\lambda}^T\overleftrightarrow{\lambda}$ becomes a scalar quantity λ^2 if the parameters are equally weighted. λ adjusts and controls the relation between data fit $\psi_1(\vec{m})$ and model smoothness $\psi_2(\vec{m})$ in the penalty function. The optimal regularization parameter is determined empirically, usually by plotting on a log-log scale the data fit $\|\vec{d}^{obs} - \vec{f}(\vec{m})\|$ versus the model roughness $\|\Delta\vec{m}\|$ for various values of λ. In a desirable case, this trade-off curve takes an L shape ("L curve"), since for increasing λ, $\|\vec{d}^{obs} - \vec{f}(\vec{m})\|$ increases as well, and $\|\Delta\vec{m}\|$ decreases.

In order to reduce the effect of measurement errors and limit the influence of poorly estimated (i.e. noisy) data, the data and model parameters can additionally be selectively

weighted by applying a diagonal weighting matrix $\overleftrightarrow{W}$

$$\overleftrightarrow{W} = \begin{pmatrix} \frac{1}{\sigma_1^2} & & & 0 \\ & \frac{1}{\sigma_2^2} & & \\ & & \ddots & \\ 0 & & & \frac{1}{\sigma_j^2} \end{pmatrix}, \tag{6.27}$$

where the weighting elements are related to the reciprocal of the variance of the measurements: $W_{jj} = \frac{1}{\sigma_j^2}$ (see Meju, 1994; Schwalenberg, 1997). After accounting for the weighting matrix, the penalty function ψ of an ill-conditioned and regularized problem is extended to:

$$\begin{aligned} \psi(\vec{m}) &= \left[\overleftrightarrow{W}\Delta\vec{d} - \overleftrightarrow{W}\overleftrightarrow{S}\Delta\vec{m}\right]^T \left[\overleftrightarrow{W}\Delta\vec{d} - \overleftrightarrow{W}\overleftrightarrow{S}\Delta\vec{m}\right] \\ &+ \lambda^2 \left[\overleftrightarrow{R}(\vec{m}_0 + \Delta\vec{m}) - \vec{h}\right]^T \left[\overleftrightarrow{R}(\vec{m}_0 + \Delta\vec{m}) - \vec{h}\right] \\ &= \Delta\vec{d}^T\overleftrightarrow{W}^T\overleftrightarrow{W}\Delta\vec{d} - \Delta\vec{d}^T\overleftrightarrow{W}^T\overleftrightarrow{W}\overleftrightarrow{S}\Delta\vec{m} \\ &- \Delta\vec{m}^T\overleftrightarrow{S}^T\overleftrightarrow{W}^T\overleftrightarrow{W}\Delta\vec{d} + \Delta\vec{m}^T\overleftrightarrow{S}^T\overleftrightarrow{W}^T\overleftrightarrow{W}\overleftrightarrow{S}\Delta\vec{m} \\ &+ \lambda^2 \left[\vec{m}_0^T\overleftrightarrow{R}^T\overleftrightarrow{R}\vec{m}_0 + \vec{m}_0^T\overleftrightarrow{R}^T\overleftrightarrow{R}\Delta\vec{m} - \vec{m}_0^T\overleftrightarrow{R}^T\vec{h}\right. \\ &+ \Delta\vec{m}^T\overleftrightarrow{R}^T\overleftrightarrow{R}\vec{m}_0 + \Delta\vec{m}^T\overleftrightarrow{R}^T\overleftrightarrow{R}\Delta\vec{m} - \Delta\vec{m}^T\overleftrightarrow{R}^T\vec{h} \\ &- \left.\vec{h}^T\overleftrightarrow{R}\vec{m}_0 - \vec{h}^T\overleftrightarrow{R}\Delta\vec{m} + \vec{h}^T\vec{h}\right]. \end{aligned} \tag{6.28}$$

After the minimization of ψ

$$\begin{aligned} &\frac{\partial\psi(\vec{m})}{\partial\Delta\vec{m}} = \\ &-2\overleftrightarrow{S}^T\overleftrightarrow{W}^T\overleftrightarrow{W}\Delta\vec{d} + 2\overleftrightarrow{S}^T\overleftrightarrow{W}^T\overleftrightarrow{W}\overleftrightarrow{S}\Delta\vec{m} + 2\lambda^2\overleftrightarrow{R}^T\overleftrightarrow{R}\vec{m}_0 + 2\lambda^2\overleftrightarrow{R}^T\overleftrightarrow{R}\Delta\vec{m} - 2\lambda^2\overleftrightarrow{R}^T\vec{h} = 0 \end{aligned} \tag{6.29}$$

and, introducing the *Levenberg-Marquardt* term, the normal equation yields

$$\left[\overleftrightarrow{S}^T\overleftrightarrow{W}^T\overleftrightarrow{W}\overleftrightarrow{S} + \lambda^2\overleftrightarrow{R}^T\overleftrightarrow{R} + \beta\overleftrightarrow{I}\right]\Delta\vec{m} = \left[\overleftrightarrow{S}^T\overleftrightarrow{W}^T\overleftrightarrow{W}\left(\vec{d}^{obs} - \vec{f}(\vec{m}_0)\right) + \lambda^2\left(\overleftrightarrow{R}^T\vec{h} - \overleftrightarrow{R}^T\overleftrightarrow{R}\vec{m}_0\right)\right]. \tag{6.30}$$

The corresponding iterative formula can now be derived:

$$\begin{aligned} &\vec{m}_{n+1} = \vec{m}_n + \\ &\left[\overleftrightarrow{S}^T\overleftrightarrow{W}^T\overleftrightarrow{W}\overleftrightarrow{S} + \lambda^2\overleftrightarrow{R}^T\overleftrightarrow{R} + \beta\overleftrightarrow{I}\right]^{-1} \left[\overleftrightarrow{S}^T\overleftrightarrow{W}^T\overleftrightarrow{W}\left(\vec{d}^{obs} - \vec{f}(\vec{m}_n)\right) + \lambda^2\left(\overleftrightarrow{R}^T\vec{h} - \overleftrightarrow{R}^T\overleftrightarrow{R}\vec{m}_n\right)\right]. \end{aligned} \tag{6.31}$$

The normal equation is adjusted depending upon the *a priori* information and constraints; for example, if the a priori information is unreliable, the *a priori* vector is set to zero, $\vec{h} = [0, ..., 0]^T$, and $\overleftrightarrow{R}$ is an identity matrix $\overleftrightarrow{I}$; so eq. 6.31 simplifies to

$$\vec{m}_{n+1} = \vec{m}_n + \left[\overleftrightarrow{S}^T\overleftrightarrow{W}^T\overleftrightarrow{W}\overleftrightarrow{S} + \lambda^2\overleftrightarrow{I} + \beta\overleftrightarrow{I}\right]^{-1} \left[\overleftrightarrow{S}^T\overleftrightarrow{W}^T\overleftrightarrow{W}\left(\vec{d}^{obs} - \vec{f}(\vec{m}_n)\right) - \lambda^2\vec{m}_n\right]. \tag{6.32}$$

For a smooth model, conditions as described by eq. 6.24 are required, and thus the iteration formula in eq. 6.31 will be modified to

$$\vec{m}_{n+1}=\vec{m}_n+\left[\overleftrightarrow{S}^T\overleftrightarrow{W}^T\overleftrightarrow{W}\overleftrightarrow{S}+\lambda^2\overleftrightarrow{R}^T\overleftrightarrow{R}+\beta\overleftrightarrow{I}\right]^{-1}\left[\overleftrightarrow{S}^T\overleftrightarrow{W}^T\overleftrightarrow{W}\left(\vec{d}^{obs}-\vec{f}(\vec{m}_n)\right)-\lambda^2\overleftrightarrow{R}^T\overleftrightarrow{R}\vec{m}_n\right]. \quad (6.33)$$

While the term $\beta\overleftrightarrow{I}$ in the above equations, with the Marquardt's damping factor β stabilizes the solution and ensures the convergence of the algorithm, the regularization parameter $\lambda\overleftrightarrow{I}$ in the minimized penalty function constrains the solution of the least squares problem.

A criterion to assess the quality of the data fit by the responses of the calculated model is the ***R**oot-**M**ean-**S**quare-* or **RMS**-error:

$$\mathbf{RMS}=\sqrt{\frac{(\vec{d}-\vec{f}(\vec{m}))^T\overleftrightarrow{W}(\vec{d}-\vec{f}(\vec{m}))}{N}}, \quad (6.34)$$

where N is the number of data points. An RMS $\gg 1$ implies that the standard deviation of the residuals is much larger than that of the measurement error, whereas the unreliable RMS < 1 exceeds the measurement accuracy, and can occur if the data are assigned with too high error floor.

6.1.3. Steepest descent and conjugate gradient methods

The quasi-Newton methods converge very fast if the initial guess is close to the minimum, but may converge very slowly, or even fail altogether, if the initial appraisal is far from the solution. On the other hand, there are methods known as descent methods, which are guaranteed to find the solution, but are not fast. Often, both types of method are combined, i.e., the descent method is applied initially, and is followed by a quasi-Newton method as convergence is approached. The method of *Conjugate Gradients* (CG) can be considered as an improved version of the *Steepest Descent* (SD) method that approaches the minimum searching in a direction which is orthogonal to the previous search direction (Hestenes and Stiefel, 1952; Golub and Van Loan, 1989; Aster et al., 2005). Both methods enable one to find the solution $\vec{m}$ or $\Delta\vec{m}$ of the normal equation in 6.15.

The minimum of the penalty function in eq. 6.13, expressed here as

$$\psi_1(\vec{m})=\left\|\Delta\vec{d}-\overleftrightarrow{S}\Delta\vec{m}\right\|^2, \quad (6.35)$$

can be obtained when the gradient is set to zero, as shown in eq. 6.14

$$\nabla\psi_1(\vec{m})\stackrel{!}{=}0 \quad (6.36)$$

which yields the basic normal equation without any regularization terms:

$$\overleftrightarrow{S}^T\overleftrightarrow{S}\Delta\vec{m}=\overleftrightarrow{S}^T\Delta\vec{d}. \quad (6.37)$$

Eq. 6.37 can be summarized as

$$\overleftrightarrow{A}\vec{m}=\vec{b} \quad (6.38)$$

with $\overleftrightarrow{A} = \overleftrightarrow{S}^T \overleftrightarrow{S}$ as a positive definite matrix, i.e., $\overleftrightarrow{A}$ is symmetric and its eigenvalues are positive, $\vec{m} = \Delta\vec{m}$ and $\vec{b} = \overleftrightarrow{S}^T \Delta\vec{d}$. Solving the system 6.38 is equivalent to finding the minimum of

$$\phi(\vec{m}) = \frac{1}{2}\vec{m}^T \overleftrightarrow{A}\vec{m} - \vec{b}^T\vec{m}, \tag{6.39}$$

which can be thought of as a surface in a hyperspace. A plausible way to find the minimum of ϕ is the method of *steepest descent*. The function ϕ is a surface in a hyperspace, and the initial guess a point on this surface. The minimization is performed by an iterative procedure, in which k is an iteration counter. The steepest downward path at this point is opposite to the gradient of the function ϕ

$$-\nabla\phi(\vec{m}_k) = \vec{g}_k = \vec{b} - \overleftrightarrow{A}\vec{m}_k \tag{6.40}$$

where $\vec{g}_k$ as the residual of $\vec{b} - \overleftrightarrow{A}\vec{m}_k$ has the same direction as $-\nabla\phi(\vec{m}_k)$, i.e., the direction of the steepest descent. If $k = 0$ and $\vec{g}_k \neq 0$ then there is a point

$$\vec{m}_1 = \vec{m}_0 + \alpha\vec{g}_0 \tag{6.41}$$

on this path, that is lower than the initial guess $\vec{m}_0$, i.e., $\phi(\vec{m}_k + \alpha\vec{g}_k) < \phi(\vec{m}_k)$ and in this sense closer to the solution. α is a positive value that minimizes ϕ along the direction of $-\nabla\phi(\vec{m}_k)$ if $\frac{\partial}{\partial\alpha}\phi(\vec{m}_1)$ is set to zero

$$\frac{\partial}{\partial\alpha}\phi(\vec{m}_1) = \nabla\phi(\vec{m}_1)^T \frac{\partial}{\partial\alpha}(\vec{m}_1) = \nabla\phi(\vec{m}_1)^T\vec{g}_0 = 0 \tag{6.42}$$

and can be determined by combining eqs. 6.40, 6.41, and 6.42 as

$$\alpha = \frac{\vec{g}_0^T\vec{g}_0}{\vec{g}_0^T\overleftrightarrow{A}\vec{g}_0}. \tag{6.43}$$

The new value $\vec{m}_1$ is now the starting point for the next iteration, and the process is continued until the global minimum is found. At each step the residual g_k is computed and the value of the step α should be chosen, so that $\nabla\phi(\vec{m}_{k+1})$ and $\vec{g}_k$ are orthogonal in accordance with 6.42. After small modifications, the algorithm can be written as:

$$\begin{aligned} \vec{g}_k &= \vec{b} - \overleftrightarrow{A}\vec{m}_k & (6.44)\\ \alpha_k &= \frac{\vec{g}_k^T\vec{g}_k}{\vec{g}_k^T\overleftrightarrow{A}\vec{g}_k} & (6.45)\\ \vec{g}_{k+1} &= \vec{g}_k - \alpha_k\overleftrightarrow{A}\vec{g}_k. & (6.46) \end{aligned}$$

Although the steepest descent method is guaranteed to converge, it does so very slowly, since it always uses the same search direction. Improvement is offered by the *conjugate gradient method*, (CG) which is based on the idea of minimizing a function along several directions, which do not necessarily correspond to the residuals $\{g_0, g_1, ...\}$, instead of over just a single line. The minimization procedure becomes more efficient, and its convergence significantly faster, since CG selects and minimizes along search directions $\{p_1, p_2, ...\}$ which are orthogonal with respect to the matrix $\overleftrightarrow{A}$ instead of minimizing along a orthogonal direction, in usual sense. Any pair of vectors which satisfies the condition

$$\vec{p}_i^T \overleftrightarrow{A} \vec{p}_j = 0 \qquad \text{for} \qquad i \neq j. \tag{6.47}$$

is referred to as *A-orthogonal* or *mutually conjugate*. This condition states that $\vec{p}_i^T$ and $\vec{p}_j$ mus be orthogonal or perpendicular to each other in a new subspace $\mathbb{R}^n$ by a transformation via matrix $\overleftrightarrow{A}$ (Hestenes and Stiefel, 1952; Golub and Van Loan, 1989; Aster et al., 2005). The search directions $\{p_1, p_2, ...p_k\}$ form a basis for a subspace of $\mathbb{R}^n$, and the solution $\vec{m}$ of the minimization problem in that basis can be expressed in terms of the linearly independent *conjugate vectors* as

$$\vec{m} = \sum_{i=0}^{n-1} \alpha_i \vec{p}_i, \tag{6.48}$$

so that the function ϕ of eq. 6.39 can be rewritten as

$$\phi(\vec{\alpha}) = \frac{1}{2} \left(\sum_{i=0}^{n-1} \alpha_i \vec{p}_i \right)^T \overleftrightarrow{A} \left(\sum_{i=0}^{n-1} \alpha_i \vec{p}_i \right) - \vec{b}^T \left(\sum_{i=0}^{n-1} \alpha_i \vec{p}_i \right). \tag{6.49}$$

After some rearrangements by using the *A-orthogonality* of the vectors eq. 6.49 simplifies to

$$\phi(\vec{\alpha}) = \frac{1}{2} \sum_{i=0}^{n-1} \left(\alpha_i^2 \vec{p}_i^T \overleftrightarrow{A} \vec{p}_i - 2\alpha_i \vec{b}^T \vec{p}_i \right), \tag{6.50}$$

and shows that $\phi(\vec{\alpha})$ consists of n terms, which are independent of each other (Aster et al., 2005).

The CG algorithm can be sketched as follows:

- The input for the minimum search of the quadratic function is the staring point $\vec{m}_0$.
- The first minimization runs along the direction of the local gradient $\vec{g}_0 = -\nabla\phi(\vec{m}_0) = \vec{b} - \overleftrightarrow{A}\vec{m}_0 = \vec{p}_0$, and searches for the local minimizer at $\vec{m}_1$

for k=0,1,...n-1 **do**

1. The minimization of $\phi(\alpha)$ can be accomplished in $\mathbb{R}^n$ by setting the derivative of eq. 6.50 equal to zero and determining the optimal step size α_k

$$\alpha_k = \frac{\vec{g}_k^T \vec{g}_k}{\vec{p}_k^T \overleftrightarrow{A} \vec{p}_k}. \tag{6.51}$$

   Note that by replacing the search vectors $\vec{p}_k$ by gradients $\vec{g}_k$ the step size α_k would be identical to the α used by SD (eq. 6.46).

2. The minimum at point $\vec{m}_{k+1}$ is

$$\vec{m}_{k+1} = \vec{m}_k + \alpha_k \vec{p}_k. \tag{6.52}$$

   For k=0, the initial iteration is completed. Note that the first minimum at point $\vec{m}_1$ was determined searching along the gradients, i.e., the same way as in the SD method. The result $\vec{m}_1$ is closer to the solution than the initial guess $\vec{m}_0$.

3. Now, the next residual vector $\vec{g}_{k+1}$ can be calculated

$$\vec{g}_{k+1} = \vec{g}_k - \alpha_k \overleftrightarrow{A} \vec{p}_k. \tag{6.53}$$

4. To ensure that the next search direction $\vec{p}_{k+1}$ is orthogonal to the previous direction $\vec{p}_k$, a scalar quantity β_k has to be calculated as follows (Golub and Van Loan, 1989)

$$\beta_k = \frac{\vec{g}_{k+1}^T \overleftrightarrow{A} \vec{p}_k}{\vec{p}_k^T \overleftrightarrow{A} \vec{p}_k} = \frac{\vec{g}_{k+1}^T \vec{g}_{k+1}}{\vec{g}_k^T \vec{g}_k}. \tag{6.54}$$

5. While SD minimizes along the residual vector, i.e., in the same direction as earlier steps, CG minimizes along "search vectors" $\vec{p}_k$ which are not perpendicular to the previous direction but *A-orthogonal* with respect to the underlying matrix, i.e, perpendicular to the contours in the new transformed space. The next search direction $\vec{p}_{k+1}$ is a linear relation of the opposite of the current gradient $\vec{g}_{k+1} = -\nabla\phi(\vec{m}_{k+1})$ and the previous search direction $\vec{p}_k$ scaled by the factor β_k:

$$\vec{p}_{k+1} = \vec{g}_{k+1} + \beta_k \vec{p}_k. \tag{6.55}$$

   The iteration is completed.

return

This procedure will be repeated until a convergence criterion is satisfied. After each loop the algorithm moves along the new search direction $\vec{p}_{k+1}$ and the new step length

α_{k+1} reaches the point $\vec{m}_{k+2}$

$$\vec{m}_{k+2} = \vec{m}_{k+1} + \alpha_{k+1}\vec{p}_{k+1} \tag{6.56}$$

which is a better approximation to the solution than the initial model $\vec{m}_0$ and the previous solution $\vec{m}_k$.

The efficiency and convergence properties of the algorithm can be significantly improved by introducing a preconditioned matrix $\overleftrightarrow{C}$ with the goal of improving the condition number of $\overleftrightarrow{A}$ (Golub and Van Loan, 1989). Thus the system in eq. 6.38, and, accordingly, the search direction will be modified to

$$\overleftrightarrow{C}^{-1}\overleftrightarrow{A}\vec{x} = \overleftrightarrow{C}^{-1}\vec{b} \tag{6.57}$$

$$\vec{p}_0 = \overleftrightarrow{C}^{-1}\vec{g}_0 \tag{6.58}$$

To solve the minimization problem of a non-quadratic objective function a modified form of the scalar β is used. The nonlinear conjugate gradients algorithm of Rodi and Mackie (2001), used for the following modeling, employs the Polak-Ribiere variant of eq. 6.54

$$\vec{\beta}_k = \frac{(\vec{g}_{k+1} - \vec{g}_k)^T \vec{g}_{k+1}}{\vec{g}_k^T \vec{g}_k}. \tag{6.59}$$

6.2. 2-D isotropic inversion and conductivity distribution below the South-Central Chilean continental margin

All presented 2-D inversion models for the three profiles at the South-Central Chilean continental margin were calculated with the nonlinear conjugate gradient inversion algorithm of Rodi and Mackie (2001). To minimize the penalty function $\psi(\vec{m})$ derived in the previous section, the algorithm offers diverse settings and parameters. Furthermore, the effect of the model discretization on the results must be investigated, and the existing a priori information taken into account and verified, as far as possible, in order to find an optimal model. Such a model must both be able to reproduce the data satisfactorily, i.e., its responses fit the observed transfer function within an acceptable RMS error, and be geologically reasonable.

6.2.1. Inversion settings

In accordance with Rodi and Mackie (2001), $\psi(\vec{m})$ can be rewritten as

$$\psi(\vec{m}) \;=\; \left[\vec{d}^{obs} - \vec{f}(\vec{m})\right]^T \overleftrightarrow{W}_{jj} \left[\vec{d}^{obs} - \vec{f}(\vec{m})\right] + \tau \left\| \overleftrightarrow{R}(\vec{m} - \vec{m}_0) \right\|^2 \tag{6.60}$$

where $\overleftrightarrow{W}_{jj}$ is the data weight matrix, or error covariance matrix, τ the regularization parameter and $\overleftrightarrow{R}$ the regularization operator.

The regularization parameter τ in eq. 6.60 is a trade-off between data misfits and model smoothness, and was determined after running several inversions using different

values. After several tests, $\tau = 10$ was set for the following inversions as a value that gives the best compromise between the smoothest model and the target misfit, and also corresponds to the optimum point of the *L-curve* presented in Fig. 6.1.

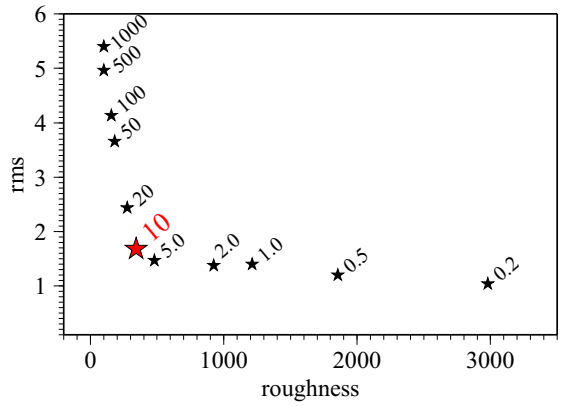

Figure 6.1.: Estimation of regularization parameter τ. Several inversion runs for different τ values show that best trade-off between the smoothness and RMS error is given for $\tau = 10$.

The regularization term in eq. 6.60 can be written as $\tau \vec{m}^T \overleftrightarrow{R}^T \overleftrightarrow{R} \vec{m}$, and its remainder is specified by a weighting function $w(y, z)$; the Laplacian of the model is integrated over the model area A:

$$\vec{m} \overleftrightarrow{R}^T \overleftrightarrow{R} \vec{m} \approx \int w(y,z)(\nabla^2 \vec{m})^2 dA. \tag{6.61}$$

In the following, the derivatives specified in $\overleftrightarrow{R}$ are computed using the uniform model mesh (uniform grid Laplacian operator) so that the weighting function $w(y, z)$, defined by

$$\begin{aligned} w(z) &= (z(k)/z_0)^\beta, \quad z(k) > z_0 \\ w(z) &= 1.0, \quad z(k) \leq z_0, \end{aligned} \tag{6.62}$$

penalizes the horizontal roughness, and avoids vertical stretching of the model structures. The weighting magnitude is determined by the parameter β, $z(k)$ is the thickness of k-th row, and z_0 fixes the minimal block thickness, under which the cells experience no weighting. It was found that the effect of β depends on the discretization of the mesh. The influence of β is investigated in more detail and discussed in section 6.2.2.1, appendix A.1 and also by Brasse (2011).

In accordance with the results of the dimensionality analysis presented in chapter 4, and in agreement with the previous models at the South-Central Chilean margin, no rotation of the impedance tensor for 2-D modeling was deemed necessary. Error floors were set to 5% for phases and 20% for apparent resistivities, so that phases are more heavily weighted in the inversion than the static-shift-affected apparent resistivities. On the other hand, a relatively high absolute value of 0.1 set for the real and imaginary parts

of the tipper reduces the influence of tipper on the results of the isotropic inversion. This underweighting of the tipper is motivated by an anomalous behavior of the induction vectors, which is caused by an anisotropic layer in the upper crust, and thus is impossible to handle by an isotropic 2-D inversion algorithm, as described in chapters 4 and 7.

6.2.2. Starting models

An early modeling approach, inverting only impedance data was carried out by Brasse and Soyer (2001) for the central profile at 38.9°S, and is depicted in Fig. 3.4, which corresponds to the seismic ISSA line (Lueth and Wigger, 2003). The current modeling study extends this by incorporating tipper transfer functions and a priori information like ETOPO2 and highly accurate swath bathymetry data, obtained during several cruises of RV Sonne (Scherwath et al., 2006).

6.2.2.1. A priori information and model discretization

The average apparent resistivity of ocean water (0.3 Ωm) was obtained from a CTD log, which was performed close to the measuring area during RV Sonne leg SO-181 at depths up to 4000 m, and is presented in Fig. 5.17 of chapter 5. The code allows one to force this solid a priori information to remain fixed through the inversion. Although the data enable to generate a very detailed image of the seafloor shape and the west margin of the a priori model in principle, practically a compromise between bathymetric accuracy and mesh size has to be made. A disadvantage of a grid applied in the FD method is that it is inflexible and does not allow to reconstruct bathymetric changes in detail without also refining the mesh for other parts of model. So a crude bathymetry must be adopted, in order to avoid bias in conductivity distribution due to over-exaggerated weighting of the peripheral regions, if too high refinements, required for a detailed reconstruction of bathymetry, would be performed on the mesh. This results in an equidistant mesh in the central part of the model with a horizontal spacing of 4 km on the sea side; 2 km on the land side; and approximately exponentially increasing column widths towards the periphery, in accordance with the exponential decay of the fields. In the vertical direction, an equidistant mesh in the upper layers, with layer thickness of 150 m, and additional refinements close to the surface and on the ocean bottom, is used due to bathymetric changes at the continental slope.

Another feature included in the starting model is a highly-resistive slab (1000 Ωm) of the subducted Nazca Plate – an assumption justified by EM measurements on the seafloor (Chave et al., 1991) – which is embedded in a half space of moderate resistivity (100 Ωm). The dip angle of the slab is determined by seismological studies (Bohm et al., 2002; Yuan et al., 2006) and the TIPTEQ seismic transect along the northern MT profile (Groß et al., 2008; Haberland et al., 2009; Micksch, 2008). Introducing such a priori data into the starting model may, in fact, be helpful to constrain the range of mathematically possible solutions, and overcome the non-uniqueness problem, but also carries the risk of producing undesirable effects and to critically bias crucially the solution towards geologically doubtful or controversial models, if the available a priori estimates

are insufficient or not solid. While the subducted oceanic crust, and thus the topmost part of the slab, is well-resolved by seismic and seismologic data down to great depths, the thickness of the oceanic crust, and thus the lower boundary of the slab, are not likewise resolved, and its position below the eastern part of the MT profile is unknown. Similarly, the high resistivity of the downgoing Nazca Plate should be regarded as an approximate value. In contrast to the slope bathymetry and sea water resistivity, which can be quite exactly measured, the electrical properties of the slab are rather a matter of dispute than firmed and reliable informations.

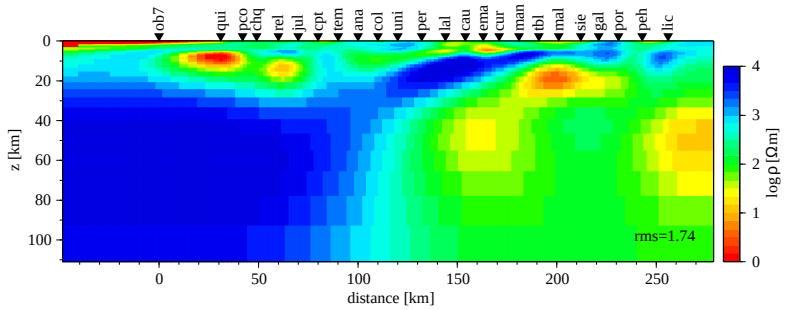

Figure 6.2.: The influence of discretization and the weighting parameter β on the inversion result. The inversion was started from a homogeneous half space including the Pacific Ocean as the only a priori information, and with a logarithmically discretized mesh, except for the upper model part containing the ocean. The parameter β in the weighting function was set to 3.0.

Given these uncertainties, the dependence of the solution on a priori information included in the starting model must be investigated. In particular the dependence of the data fit and the robustness of modeled structures on the underlying starting model must be inspected. However, the inclusion of a priori features like the top of the downgoing lithosphere, derived from from active and passive seismic observations, requires a refined mesh. On the other hand such a mesh may bias the inversion, as mentioned above. So it is instructive to see how the mesh refinement affects the solution, before studying the influence of a priori constraints on the modeling. The models presented in Figs. 6.2 and 6.3 are obtained from a joint inversion of TE, TM mode, and the tipper, using different grids, but identical inversion settings and starting models. The latter consist of a homogeneous half space and the ocean (without a downgoing slab). In the upper image a logarithmic mesh is used, except for the upper part of the model at the slope, where the grid is equidistant. In the lower image, the fine and predominantly equidistant mesh, at depths between 5 and 80 km, with a vertical cell dimension of 2 km, represents a grid which would be used if a downgoing lithosphere were to be incorporated in the starting model. Below this depth, the cell dimension increases exponentially, in accordance with the exponential field decay. However, note that in both images the starting model is a homogeneous half space without a slab.

At first sight the models look quite different. The deviations are not surprising and have a plausible explanation: differently discretized model parts experience unequal

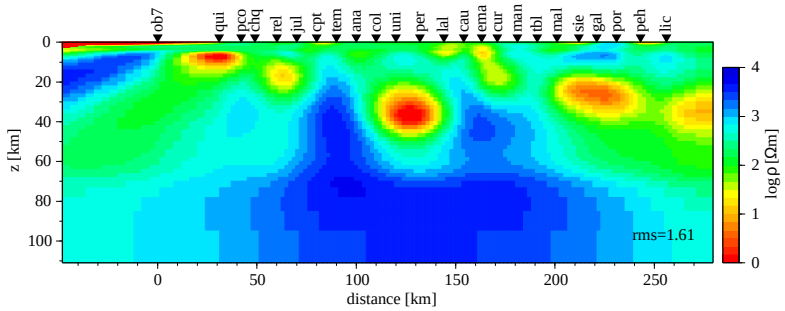

Figure 6.3.: Inversion result for the same starting model and weighting parameter (β=3.0) as in Fig. 6.2, but different mesh. The model uses a predominantly equidistant mesh up to the depth of 80 km. Note that the differences between this model and the model in Fig. 6.2 arise not so much due to the different meshes, but rather due to the interaction between the mesh and the weighting function $w(y, z)$, or weighting parameter β, equivalently. For more see the text and appendix A.1.

weighting. On the one hand, the algorithm pays more attention to the part of the model with the refined mesh, but on the other hand the weighting parameter β penalizes finely discretized model parts less strongly than roughly discretized regions in the model with logarithmic mesh. Thus, the differences are not only caused by a higher attention of the code to the model parts with a finer grid, but also by an unequal penalization in differently discretized meshes by the weighting parameter β which here was set to relatively high value: 3.0. This becomes especially obvious when β is set to zero, and is investigated in appendix A.1.

Besides these obvious differences, equal features are observed in the western and eastern parts of the models. The prominent conductive anomalies at the west flank of the profile beneath the slope and the Coastal Cordillera recur in all models, independent of the starting model, likewise the superficial conductors in the center of the model, which can be associated with sediments of the Longitudinal Valley. The resistive superficial structures beneath the Main Cordillera and the conductor east of the profile occur in all models as well.

The most prominent structures also remain largely unaffected if the starting model is extended by an a priori feature like a downgoing slab. The inversion result using this starting model is the final model presented in Fig. 6.6 (upper panel). Generally the images in Fig. 6.3 and the upper pannel of 6.6 look quite similar, except for the western part of the models, which is related to the slab. While in Fig. 6.6 the contour of the incorporated slab remains largely preserved, the inversion of a starting model without a slab can not reproduce such a continuous feature. Although some indications of a slab-like structure can be observed towards the model periphery, it seems to be not required by the data beneath the slope, where the initial intermediate resistivity is instead maintained. To investigate this, the resistivity in that part of the model was increased to 1000 Ωm, so that a slab-like connection between the resistive feature on the left of the profile and the huge resistive structure in the middle of the profile was established, and the resulting model was forward calculated. The responses from

the inverted and the modified model at stations *ob7* and *qui* differ in the TM mode only marginally, as shown in Fig. 6.4, and thus corroborate the assumption that a slab may not be required, but is at least compatible with the data. In TE mode slab-like resistive structures are principally difficult or impossible to resolve (see section 6.2.2.3), and any deviations in the model responses are barely recognizable. However, this part of the model has poor data coverage, and cannot be adequately resolved, so that any conclusion must be drawn tentatively.

A possible slab-like structure also arises in the western part of the model in Fig. 6.2, but without the inclusion of any a priori data about a downgoing slab it terminates in the eastern Coastal Cordillera. Instead, a highly resistive, E-W extending, concave feature arises in the upper crust from the slab-like structure to the Main Cordillera. Apparently, a resistive slab at large depth cannot be resolved without any a priori information, and disappears in favor of a resistive feature in the crust, or, rather is shifted into the crust. In other words, without any constraints on the model conditions, and due to the non-uniqueness of the solution of the inversion problem, a downgoing continuous slab is not the unique option that agrees with the data. Either, a resistive slab in the mantle or a resistive feature in the crust are able to explain the data; but these are only two of a number of mathematically possible solutions. The crustal resistive feature shifts the good conductor beneath the station *uni*, and *per* in Fig. 6.3, approximately 30 km to the east and deeper into the mantle, where it appears larger, perhaps because it is difficult to resolve.

Although such a resistive feature in the crust is also apparent in Fig. 6.6 and 6.3, it is less pronounced; less resistive, and discontinuous, due to crustal conductors beneath the stations *uni* and *cur*. However, a downgoing resistive Nazca Plate as a priori information seems to satisfy the data better, if taking into account the lower RMS as a criterion for the quality of the model.

6.2.2.2. Static shift

A strong frequency-independent offset of apparent resistivities along the vertical axis accompanied by unaffected phases (Fig. 4.1) is a clear indication of a non-inductive effect caused by small scale heterogeneities. Ignoring this effect during the inversion can result in models with unfounded and unreliable structures, and lead to misinterpretation of models (Spitzer, 2001). Although techniques have been developed that can be helpful to obtain a reliable estimate of the static shift factor and remedy this problem, the task is non-trivial, and none of these methods can absolutely guarantee control of this problem (Bahr, 1988; Groom and Bailey, 1989, 1991; Weaver et al., 2000; Spitzer, 2001). A technique that is implemented in *WinGLink* relies on the assumption that the electric fields arose due to charges at conductivity boundaries, and cancel out along an infinitely extended profile, so that the static shift factors, defined as the difference between the logarithm of the corrected and measured apparent resistivities, sum up to one. This assumption is justified for datasets with a large number of sites, where the high probability is that conductive small-scale anomalies balance the resistive ones, but it can produce bias if conductive heterogenities exceed the resistive ones, or vice versa. To investigate

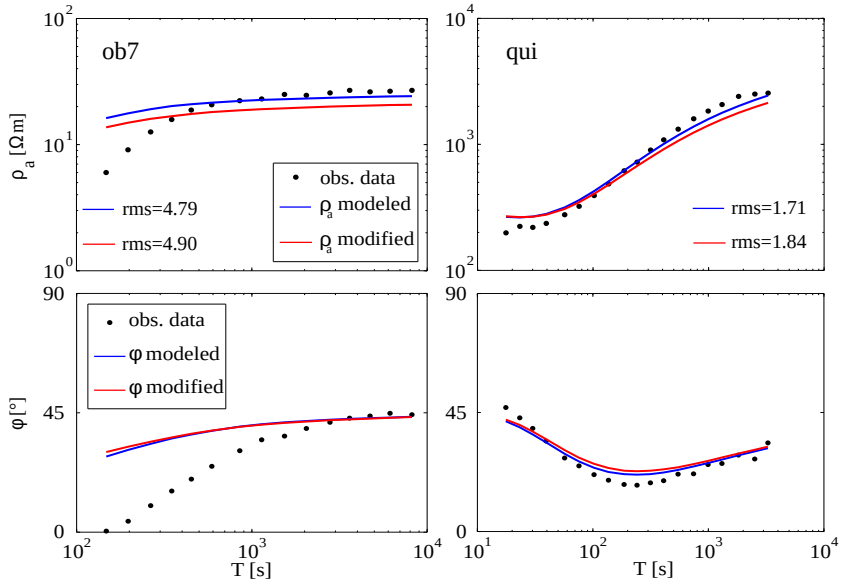

Figure 6.4.: Sensitivity test of the downgoing slab beneath the slope. To test if the data are able to resolve a resistive slab at the western flank of the profile, the resistivity in this region, in Fig. 6.3, was increased to 1000 Ωm; so that a slab-like connection between the resistive feature left of the profile and the huge resistive structure in the middle of the profile was established. The TM responses (apparent resistivity and phase) at sites *ob7* and *qui* of the forward calculation of this modified model (red line) diverge only marginally from the responses obtained from the original (inverted) model (blue line). Points: measured transfer function in TM mode. Note the large RMS value at site *ob7*.

how effectively the used algorithm can handle static shift, a 3-D model containing several near-surface, small-scale anomalies embedded in a homogeneous half space with a large-scale conductor 20 km below the surface was constructed. These model responses, affected by static shift, were then 2-D inverted as synthetic data, first by omitting and then by using the algorithm's internal static shift correction. Without going into details, the algorithm reproduced the conductor quite properly and fit the synthetic data very well when the static shift correction was used. If the inversion for static shift is not selected, the data fit gets significantly worse and the algorithm generates large surficial structures which compensate for the static effect. These results, along with further tests with real data, revealed that the inversions for static shift also provide geologically more reliable models. Thus an inversion for static shift seems justified, and was chosen for the following inversion runs.

6.2.2.3. Single inversion

Useful information for the interpretation of the conductivity distribution in the South-Central Chilean subduction zone can be obtained by separately inverting the data for TM modes, TE modes, and the magnetic transfer functions. The modes differ in sensitivity to electrical targets, because of their distinct properties associated with the current flow

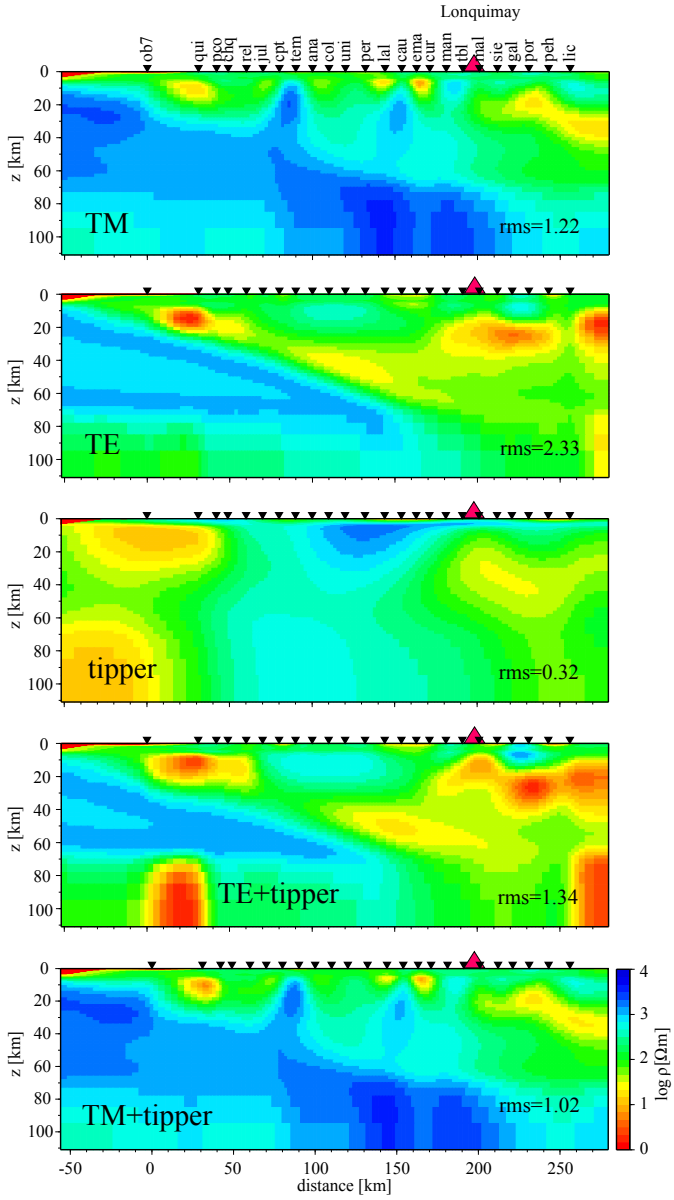

Figure 6.5.: Single inversion for TM and TE mode, tipper as well as TE mode together with tipper and TM together with tipper. While TM mode is able to resolve superficial structures and the resistive slab due to discontinuity of E_y across a vertical contact, TE mode is more sensitive to small-scale and deep conductive structures that are embedded in a resistive host. The tipper can be used to image more detailed lateral conductivity contrasts.

direction. Therefore structures that are obscured for TE mode or tipper are generally resolved by TM mode, and vice versa. Knowing which mode, and with which structures it contributes to the final model, reveals more about the nature of the modes, and can

be helpful in model interpretation. The resolving capability of the modes can be derived from Fig. 6.5, which presents the conductivity distribution obtained by inverting the data separately for TM mode, TE mode, and the tipper as well as for TE mode and the tipper together.

In TM mode, which is sensitive to surficial resistive structures (Berdichevsky et al., 1998) and to vertical conductivity boundaries, due to discontinuity of E_y across a vertical contact, several anomalies can be resolved in the upper crust in the western part of the profile and in the Longitudinal Valley, as well as in the lower crust in the backarc and beyond the profile. Besides the moderate resistivity of the underground, with several anomalies in the crust, a prominent resistive feature appears in the deeper parts of the image. The subducted Nazca Plate, included as a priori information in the starting model, may be modified in the course of the inversion process but remains, along with further vertical structures that rise into the crust, as slab-like resistive features in the final model. Such a low-conductivity slab seems to be not only justified, but even required by the TM data, and will eventually be modeled in a similar form and as a resistive zone, even if the starting model does not include a slab. Furthermore, the choice of a starting model and inclusion of a priori information like a slab have only a marginal effect on the remaining structures. Particularly, the crustal conductors seem to remain unaffected regardless of whether the starting model includes a slab or not.

The inversion of TE mode produces a quite different image of the conductivity distribution. The TE mode impedance is more sensitive to deep conductive structures which are embedded in a resistive host (Berdichevsky et al., 1998), and is, unlike the TM mode, less suitable to resolve resistive structures like a subducted slab. Although a resistive slab included in the starting model does not disappear and remains nearly unaffected in the course of inversion, such a feature is not required by the TE data, and there is no indication of a slab-like structure arising if one is not introduced in the starting model, as inversions with a starting model without slab revealed (not shown here). Moreover, the RMS becomes even lower. The most prominent features in the TE mode are crustal conductors beneath the slope, the Main Cordillera (offset east of the volcanic arc), the backarc beyond the profile, as well as a huge outlying mantle anomaly, whose dimension can probably not be resolved. Note that the conductor beneath the slope also appears in TM mode. Similarly to TM mode, the crustal anomalies are only slightly affected by the employment of a starting model without a slab (e.g. a homogeneous half space with the Pacific Ocean included).

The anomalies can also be expected in the models of neighboring profiles if 2-D conditions – the electrical currents flow parallel to strike in TE mode and the conductivity remains constant along an infinitely extended geological strike – are truly justified. Indeed, inspecting the joint inversions of all models, as shown in Fig. 6.6, the conductive structures in the crust continue, in both southern models, yielding a consistent image of the conductivity distribution.

Auxiliary information can be obtained from the inversion of the tipper. As a relationship of horizontal and vertical magnetic fields, the tipper is more sensitive to lateral conductivity contrasts. A joint inversion with TE mode can be useful to image more detailed a conductivity structure. Several structures, already evident in the separate in-

versions of TE mode and tipper, become more prominent. On the other hand, a resistive feature, like a slab remains hidden for the tipper, or at least cannot be resolved with the same clarity as in TM mode.

A conductivity image derived by a joint inversion of the tipper and TM mode, as suggested by Wannamaker (1999) in order to limit effects produced in TE mode by a finite strike, is here predominantly characterized by features observed in the model derived by inversion of TM mode. Structures resolved by tipper such as the the good conductor below the shelf and the coast contribute only marginally to the overall image, or are suppressed completely, like the conductive anomaly in the mantle observed in TM mode, west of the profile. This is probably because a large error floor is assigned to the tipper data. For the same reason the RMS-error of the tipper is only 0.32, which implies overfitting of the data, i.e, the data are fitted below the measurement accuracy. A high error floor of 0.1 of the tipper data was chosen to underweight the influence of the anomalous geomagnetic transfer function in the isotropic 2-D inversion because the observed uniform deflection of induction vectors cannot be explained by an isotropic 2-D approach (see chapters 4 and 7).

6.2.2.4. Joint inversion - model discussion

The conductivity distribution below the South-Central Chilean continental margin along three profiles is presented in Fig. 6.6. The middle and bottom panels show models of newly inverted data, acquired during the campaign of 2000 (see chapter 3.1). The starting models incorporate the Pacific Ocean with bathymetry, and a resistive slab (1000 Ωm) encompassed by a homogeneous background with a resistivity of 100 Ωm. The main conductors, although differing in prominence, are present in all models, and provide a uniform conductivity image of the South-Chilean subduction zone. As in Brasse and Soyer (2001), nearly all conductors, apart from the anomaly labeled **A** below the Central Valley, are located in the crust.

The subducting Nazca Plate was modified in the course of the inversion process. Particularly, a few resistive features arise in the continental crust or mantle and merge seamlessly with the slab, leading to a much more heterogeneous image of the slab.

A very conductive anomaly at **D** is modeled in the crust beneath the continental shelf in the central as well as in the northern profile, where an additional offshore station was incorporated, whereas in the southern profile just a zone of slightly enhanced conductivity (<100 Ωm) appears. However, this structure is not seen when only crude bathymetry is taken into account (Brasse and Soyer, 2001) – this underlines the importance of exact bathymetry for near-coastal data. Although this anomaly may at first glance seem like an inversion artifact, comparable anomalies can also be observed in the Cascadian and Costa Rican subduction zones (Soyer and Unsworth, 2006; Worzewski et al., 2011). The edge of the anomaly also coincides with a zone of strong seismic reflectivity beneath the northern profile (Groß et al., 2008). Furthermore, a seismic tomography has revealed that the frontal part of the forearc is characterized by a low seismic P wave velocity (ν_p), and a high ratio of P and S wave velocities (ν_p/ν_s), which indicates a fluid-saturated accretionary wedge (Haberland et al., 2009), perhaps fed by faults originating at the

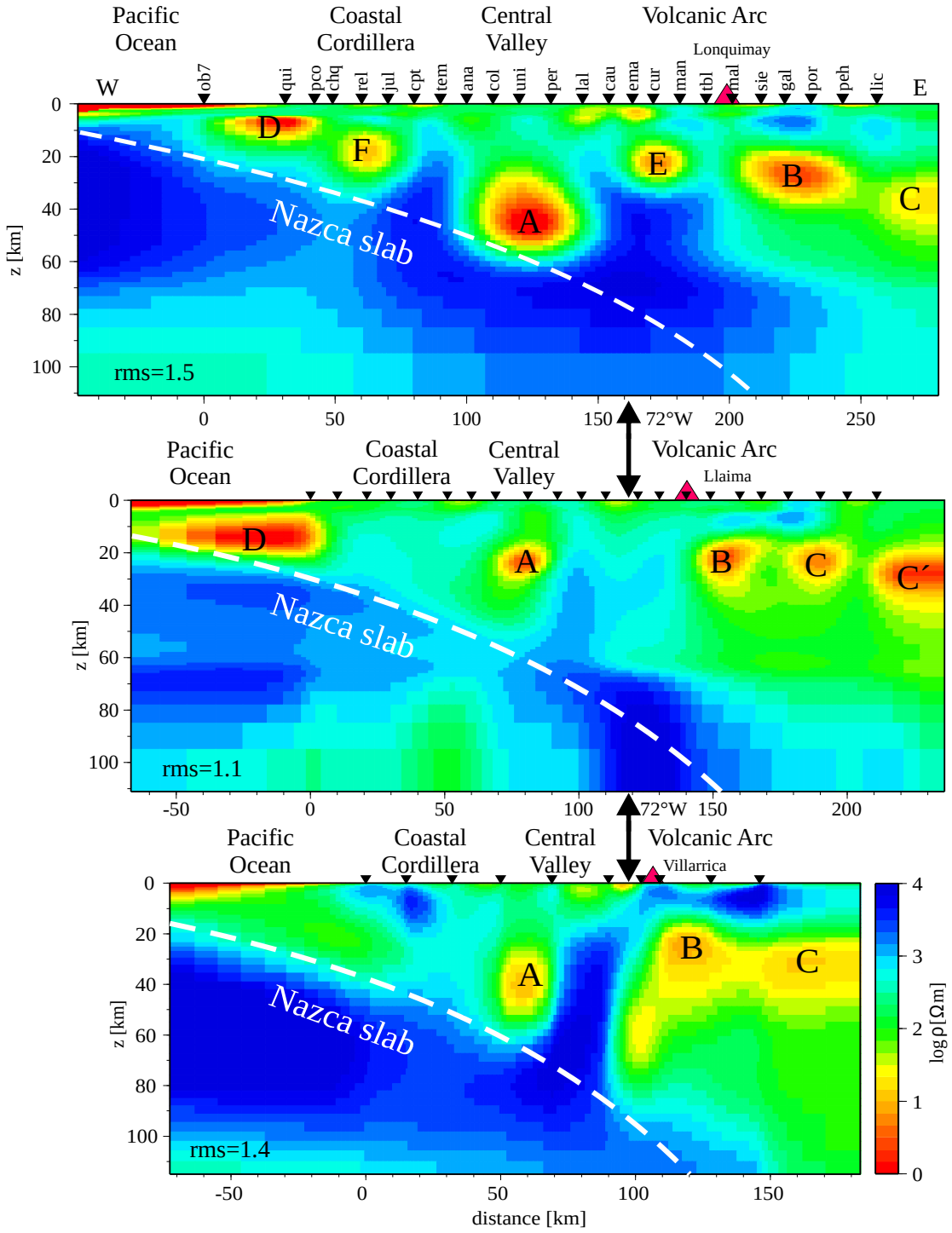

Figure 6.6.: 2-D conductivity distribution below the South Chilean Continental Margin. The models of the three profiles are obtained by inversion of the impedances and the tipper. They show a consistent image of the South Andean subduction zone with several crustal conductors. While higher conductivities beneath the volcanic arc were expected, the anomalies below the ocean and Coastal Cordillera are rather surprising. Note a high conductivity zone in the backarc of all models.

downgoing plate.

A prominent structure is anomaly at **A**, below the Central Valley. In the center profile, it coincides with the NW-SE running, seismically active Lanalhue Fault, obliquely traversing the northern Patagonian Andes in a SE-NW direction. Since this conductor is also modeled and firmly established in the other profiles at the same lateral position, it cannot be associated with Lanalhue Fault alone. Anomaly **A** is an instance of rather a general phenomenon, related to subduction zones worldwide, and must be seen as an important feature which plays a key role in the fluid balance during the subduction process. Such a conductor is also observed at other subduction zones, like the northern Cascadia (British Columbia) or the Costa Rican subduction zone (Soyer and Unsworth, 2006; Worzewski et al., 2011).

All models resolve the highly-conductive zone **B**, which is at mid-crustal depths beneath the volcanic arc. This anomaly is not surprising, and can be associated with the active volcanoes Lonquimay, Villarrica and Llaima. The conductor **B** may simply be regarded as a large magma deposit beneath the volcanoes, but offset by ∼10 km to the east. However, 3-D forward studies at Villarrica, motivated by the orientation of induction vectors provided by a small network around the volcano, revealed a conductive anomaly beneath the caldera (see next section), i.e not in the exact position as the anomaly at **B**. Note that Llaima erupted violently on 1 January 2008, and the effect of this eruption on the conductor by removing or relocating a significant part of the magma depositis is unknown, because these data were collected in 2000.

A consistent feature is the conductor at **C** or **C'**, east of the eastern margin of the profile (in Argentina) – although not truly resolved with respect to location and resistivity due to the lack of nearby stations, it appears in all inversion runs. A preliminary explanation may lie in a root zone for the Holocene backarc volcanism in the Loncopué Trough. However, only a future extension of the profile to Argentina could unambiguously answer this question. The prominent anomalies are discussed in detail in chapter 8.

Apart from the main features, minor and superficial structures are also modeled, particularly in the Central Valley and and the Bío-Bío Valley. These anomalies can be associated with accumulation of well-conducting (10 Ωm) and shallow (about 2 km) Pliocene-Quaternary sediments, in accordance with tectonic assumptions (H. Echtler, pers. comm.).

In terms of a RMS error, the obtained data fit is remarkably good, with RMS = 1.5, 1.1 and 1.4 for the northern, central and southern profiles; but note that this is mainly due to the relatively high error floor assigned to the tipper data. Full details are presented in appendix A.2.

In the modeling of the northern profile the offshore transfer functions of sites beyond the trench couldn't be incorporated. Any attempts to fit satisfactorily these data failed due to the poor quality of the impedances (see section 5.4), and the offshore data, with exception of the site closest to the coast (*ob7* on the slope), had to be omitted in the inversion.

6.2.2.5. Sensitivities

The key task of an inversion procedure and one of the most time-consuming parts is the evaluation of the Jacobian matrix (eq. 6.6). Its elements, defined as the partial derivatives of the predicted data with respect to the current model parameters, are a measure of the sensitivity of the model responses to perturbations of model parameters (eq. 6.7). In other words, the Jacobian matrix reflects the effect of small changes in conductivity on the model responses. Inspection of the Jacobian is absolutely essential before interpreting the model structures, because it indicates which of them are reliable, and necessary to fit the data, and conversely, which are unstable or redundant. In Fig. 6.7 the sensitivity of the model is imaged as a map. The map reveals which features in the model are robust and reliable, and which may only be artifacts. Here it is clear that the upper part of the model and the highly conductive structures are particularly sensitive to the data, whereas poor conductors may be rather difficult to resolve, and may remain obscure.

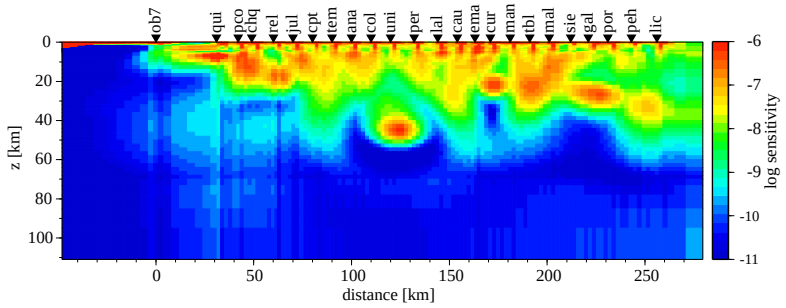

Figure 6.7.: Sensitivity map calculated for the northern profile. The image shows that the high conductivity structures in the upper part of the model are robust, whereas poor conductors below may be rather difficult to resolve.

Regardless of the map's validation of the conductive features, a constrained inversion was additionally used to ensure that they are required by the input data. For this, all prominent conductive structures were successively removed, the modified models forward recalculated, and finally the data fit and RMS reevaluated. The overall RMS became higher, if the conductivity in regarded cells was perturbed, suggesting that these structures are required to fit the data. Moreover, further inversion runs recovered the previously removed structures, slightly modifying the model and conductivity values, and further decreasing RMS, i.e., below the value before the sensitivity test.

Although the 2-D inversion model may fit the observed magnetotelluric transfer functions quite well, and the resolved structures are indeed geologically interpretable, it does not represent a "complete" or "final" model. The inability to explain, via a 2-D model, the induction vectors that at long periods point NE throughout the study area, irrespective of the most important known geological features, and the conductivity strike, as described in section 4.3, indicates that a 2-D approach does not exploit the whole of the information content inherent in the data. A further discussion of the data fit and sensitivities is here omitted and the model interpretation deferred, until a model is found

which can also explain the vertical magnetic field. The modeling of the the anomalous magnetic transfer function is the topic of the next chapter.

6.3. Isotropic 3-D forward modeling at Villarrica volcano

The attempt to model the conductivity distribution beneath active Villarrica volcano was motivated by the orientation of the induction vectors, which at short periods point away from the volcano's center (Fig. 6.8). Such behavior suggests a conductivity anomaly, but can also be caused by elevated topography, since in a homogeneous underground the electrical current lines and their equipotential surfaces diverge beneath a hill, leading to less potential difference and lower apparent resistivity, as shown by Fox et al. (1980). However, modeling by Brasse and Eydam (2008) and Eydam (2008) with synthetic topographic data showed that the topographic gradient of Villarrica and Llaima volcanoes would produce a static shift problem in TM mode but does not affect the vertical magnetic field for periods above 10 s. This result is indirectly supported by the fact that at Llaima the induction vectors are orientated independently of the topography of the volcanic edifice, as shown in Fig. 6.9. On the other hand, this disagreement is a further indication that the orientation of the induction vectors at Villarrica is caused by a conductive anomaly rather than by topography.

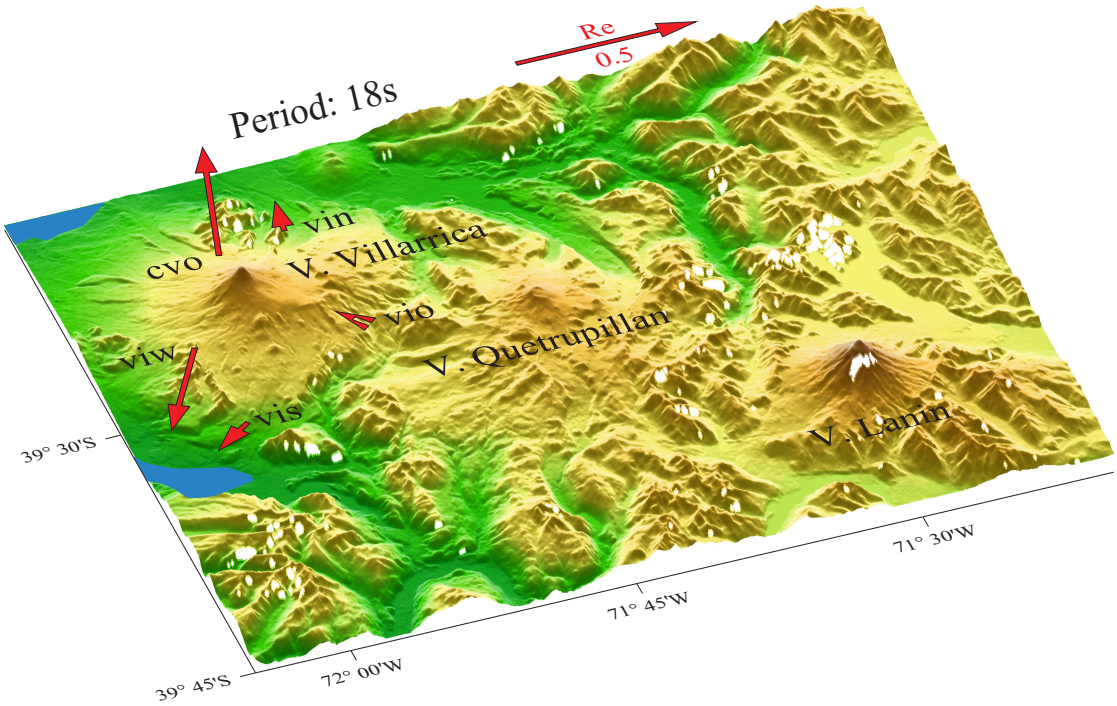

Figure 6.8.: Topography around the volcano chain comprising Villarrica, Quetrupillan, Lanin; observed real part of induction arrows at Villarrica at a period of 18 s.

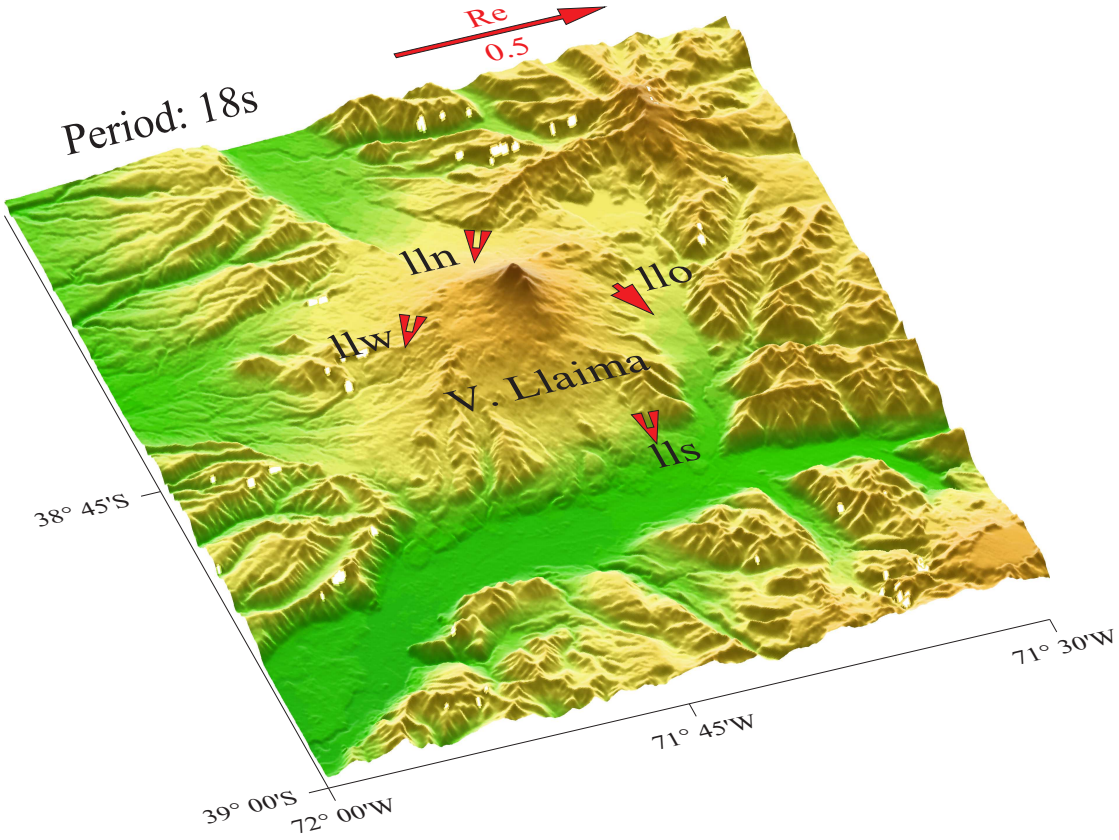

Figure 6.9.: Topography around Llaima volcano; observed real part of induction arrows at a period of 18 s.

6.3.1. Measurements and data

The surveys at Villarrica and Llaima volcanoes were intended as auxiliary to the main 2-D profiles across the subduction zone, so the survey layout is not typical for magnetotelluric investigations at volcanoes. The data recorded at two networks of four long-period magnetotelluric sites, which were deployed around the volcano edifices during the campaign of 2004/2005 (the site *cvo* at Villarrica belongs to the profile of 2000), yielded magnetic and, with few exceptions, also magnetotelluric transfer functions in the period range between 10 – 10000 s. Responses in this period range only permit inferences about the deeper crust; to assess a possible magma deposit just beneath the volcanic edifices, measurements at shorter periods (in the AMT range) and on a denser network are usually required. Additionally, the apparent resistivities are probably affected by static shift. Also, the quality of magnetotelluric transfer functions at periods above 1000 s is worse than that of the magnetic responses. At site *vio*, where the electric field could not be recorded due to bad coupling between electrodes and a volcanic ash-covered subsurface, the magnetotelluric transfer functions are not available.

Since, in contrast to Villarrica, the data recorded at Llaima do not reveal any direct hints of a possible magma deposit beneath Llaima volcano will not be further considered. From a survey layout consisting of five sites, which provides only four magnetotelluric transfer functions, is impossible to derive a complete and reliable 3-D image of the conductivity distribution. Thus the aim of this supplementary study is rather to provide a simple and realistic model that explains the effects observable at induction vectors of periods below 1000 s, paying attention primarily to fitting the magnetic transfer functions.

The most remarkable induction effects at periods >100 s are observed at sites *cvo* and *viw*, which are the closest to the caldera. Especially, the large induction arrows at site *cvo* pointing radially from the volcano center, to north, over the period range from 10-100 s, indicate a highly conductive anomaly below the volcano. On the other hand, the arrows at site *viw* southwest of the volcano point nearly in the opposite direction, suggesting that the extent of the anomaly must be limited to the central area beneath the volcano. While at site *cvo* the real induction vectors remain large in the period range between 100-1000 s, pointing systematically north without differing significantly in magnitude, and only slightly in direction, at *viw* the arrows turn north (and at periods over 1000 s to northeast) and their length becomes smaller with increasing period and approaches zero at 1000 s. At the remote sites, the small induction vectors at short periods become larger between 100-1000 s and rotate clockwise to north, and, at periods above 1000 s, to the northeast.

6.3.2. Model discretization

To investigate the behavior of induction vectors in more detail a 3-D approach, the code MT3DFWD from Mackie and Madden (1993) and Mackie et al. (1994), implemented in *WinGLink*, was applied. The algorithm allows inclusion of the topography, and thus estimation of its effect on the responses, provided that the shape of the volcano cone is reconstructed correctly. The effect of the topography on the induction vectors is presented in Fig. 6.10. The presented arrows in the period range between 0.01-100 s are produced by a model with a homogeneous resistivity of 400 Ωm, and as accurate as possible, but unavoidably simplified, topography. The plots confirm the assumption that the topographic effect is limited to the AMT period range, and is thus negligible at regarded periods (>10 s). Although high accuracy in the topography reconstruction can be obtained using the SRTM data set, a fine mesh that exactly reflects the topography therefrom exceeds computational feasibility. An appropriate compromise between accuracy and computational cost is provided by a grid with an equidistant mesh size of 100 m in vertical direction and 500 m in horizontal direction above sea level and within the central area, and an exponentially increasing cell dimension below sea level and beyond the central model area.

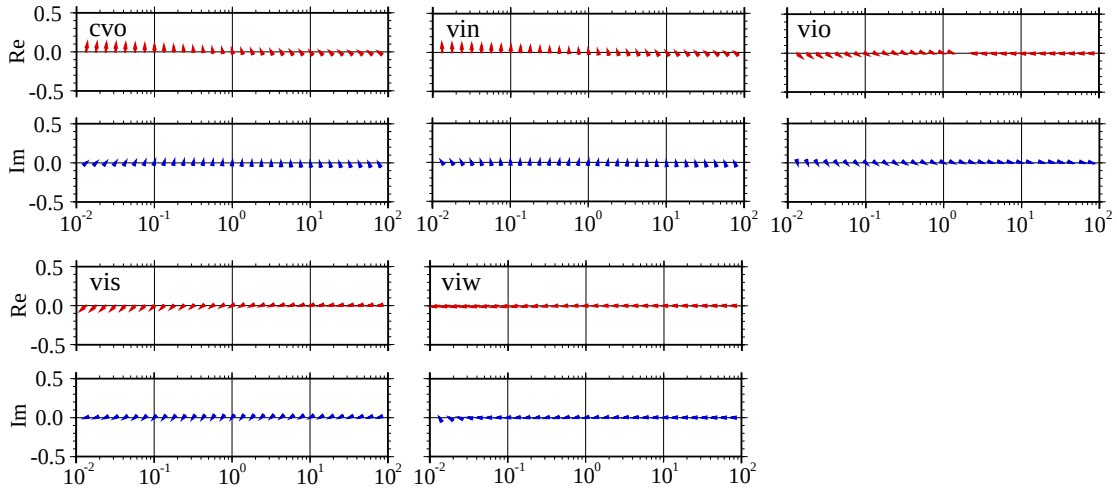

Figure 6.10.: Effect of the topography on the induction vectors. The model for which the induction vectors are calculated has a homogeneous resistivity of 400Ωm and exactly identical topography which is used for the later calculations. The topography of Villarrica affects only responses at periods <1 s and is negligible at recorded periods (>10 s).

6.3.3. Results from 3-D forward modeling

It is a time consuming issue to find a 3-D model by forward modeling that explains the observed responses and is, as far as possible, pertinent from a geological point of view. The model search followed the principle of simplicity, and concentrated on fitting the induction vectors. Such a simple model, which none the less satisfactorily explains the main features of the magnetic transfer functions, is presented in Figs. 6.11 and 6.12 (for a comparison with the conductivity distribution close to Villarrica derived from 2-D inversion of the southern profile see the bottom panel of Fig. 6.6.

The model consists of a moderately resistive background (400 Ωm) and

- (**A**) a high conductivity anomaly (0.1-0.5 Ωm) directly below the volcano edifice at depths between 250 m above sea level, and extending into the deeper crust,
- (**B**) a regional conductor (0.5-4 Ωm) southeast from Villarrica at depths between 50 m and 35 km,
- (**C**) a crustal NE-SW running highly conductive layer (1 Ωm) at depths between 20 and 35 km.

The model also incorporates the Pacific Ocean which does not affect the induction vectors at short periods (<1000 s), however.

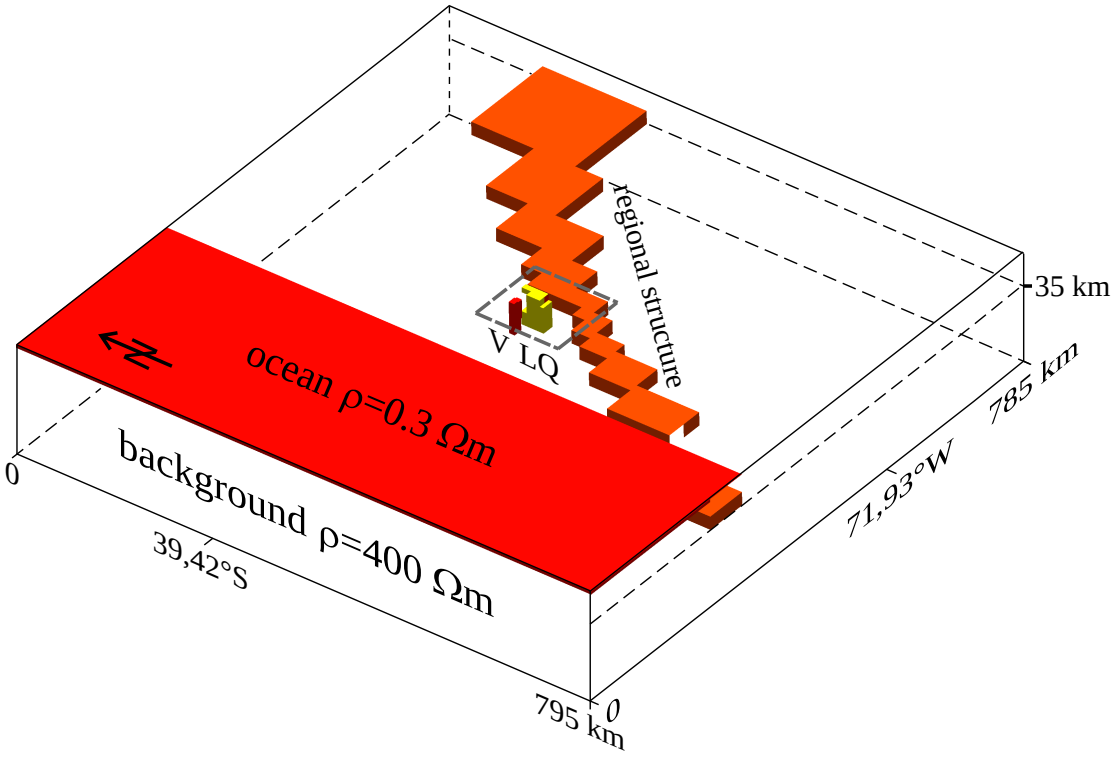

Figure 6.11.: A 3-D overview of the conductive structures used to explain the observed induction vectors at the volcano Villarrica. The magnetic responses are affected primarily by: (**A**) a good conductor (0.5 and 0.1 Ωm) beneath the volcano Villarrica, denoted by V in the image; (**B**) a conductive anomaly (0.5-4 Ωm) beneath the volcanoes Lanin and Quetrupillan (LQ); and (**C**) a regional, NE-SW striking, conductive (1 Ωm) structure. The background resistivity is set to 400 Ωm. The ocean does not affect the induction vectors below 1000 s. The area in the dashed box is presented in Fig. 6.12.

6.3.3.1. (A) Anomaly below the volcano edifice

The highly conductive anomaly (**A**) beneath the volcano cone is required by the large induction vectors at sites *cvo* and *viw* that occur at short periods. Its vertical extent cannot be exactly resolved, since the vertical magnetic field is primarily sensitive to a lateral conductivity contrast. Sensitivity tests show that the anomaly can be allowed to reach depths of 10 km, or 20 km, or even more without affecting the arrows significantly, i.e. producing very similar responses, or providing at some sites marginally better, at others again worse data fit. The lateral extent of the anomaly may be estimated more precisely. The orientation of the observed arrows was reproduced quite accurately at all sites (Fig. 6.13) by positioning the anomaly at the western flank of the volcano, directly below the present position of the lava filled crater. Its conductivity was set to 0.5 Ωm and, around site *cvo*, as low as 0.1 Ωm, to provide a high conductivity contrast to the surroundings. Such a large conductivity gradient can be guessed by viewing the

large arrows at short periods. Nevertheless, even these high conductivity values seem to be insufficient to fit the observed large arrow length. Probably the resistivity of the surrounding must also be made larger to approximate the measured arrow length of ∼0.8 at a period of 13 s. The location and the high conductivity of this anomaly tempt one to interpret them as a volcanic vent.

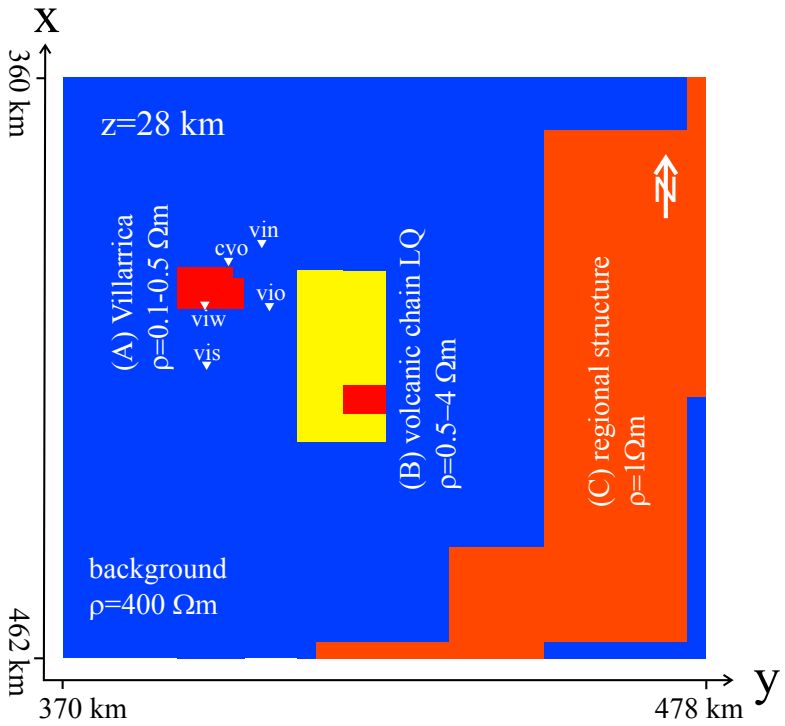

Figure 6.12.: Plan view of the central part of the model (dashed box in Fig. 6.11) at a depth of z=28 km. The conductive anomaly **A**, beneath Villarrica volcano, **B**, beneath the neighboring volcanoes Quetrupillan and Lanin, as well as the regional structure **C** provide a good fit to the induction vectors measured at sites around Villarrica below 1000 s.

6.3.3.2. (B) Conductive structure below the volcanoes Quetrupillan and Lanin

The conductive and local structure (**B**) southeast of Villarrica is required by the data to reproduce the arrows at middle periods, particularly at site *vio*. This feature is motivated by the volcanic chain with the active volcanoes Villarrica, Quetrupillan and Lanin. Such a conductor induces a NW orientation of the arrow that compensates for the effect of the anomaly below Villarrica, and further cause a deflection of the arrows at most sites more or less to the west. The effect is most obvious at site *vio*, whose observed induction arrows point away from the structure and towards Villarrica, in opposition to the prevalent pattern. Sensitivity tests for the presented configuration revealed that without this neighboring conductive feature, the arrows at periods of up to approximately 60 s would be orientated at the site *vio*, as expected, away from Villarrica. The westward

range of this anomaly may approach or even exceed site *vio*, as can be inferred from the fact that the arrows at the shortest periods (∼10 s) of *vio* point to the NW, away from the volcanoes Quetrupillan and Lanin. However, the effects of the anomaly are related to field attenuation and penetration depth, and thus depend strongly on the background resistivity. Its vertical extent cannot be resolved due to insufficient resolution capacity of the tipper, and its extent to the north, east and south can in turn not be determined due to unavailable data. The resistivity of the anomaly, set to 4 Ωm and partly to 0.5 Ωm provides an adequate fit for the observed induction vectors.

In order to evaluate whether any common structure exists beneath the volcanic chain, such as a magma deposit which feeds and connects the individual volcanoes, the conductive structure at depths of 20-35 km below the volcanoes Quetrupillan and Lanin was extended to Villarrica. However, such a conductive root structure in the lower crust has a negligible effect on the induction vectors of interest. Thus, a connection between the single volcanoes is absolutely conceivable, or at least cannot be ruled out.

6.3.3.3. (C) NE-SW running regional feature

The NE-SW running highly conductive (1 Ωm) regional crustal structure (**C**) at depths between 20 and 35 km is required by the data to fit the induction vectors at periods >100 s. This feature, motivated by anisotropic modeling, corresponds to the concept of a structural anisotropy in the continental crust, and provides, together with the ocean layer, a uniform NE pattern of induction vectors at long periods (>1000 s), at all stations throughout the survey area, as described in section 4.3. In contrast to an intrinsic anisotropy, which is a property existing at a smaller scale, a structural anisotropy is an emergent property generated by a sequence of conductive and microscale-isotropic lamellae, which in the macroscale produce a preferred conductivity orientation (Weidelt, 1999). Such a NE-SW running, regional and an isotropic feature simulates a single lamella, and has a contrary effect to that of the conductive anomalies beneath the volcanoes, thus providing the final north orientation of the arrows at longer periods. This orientation grossly corresponds to the observed induction vectors at all sites except at *viw*, where responses deviate from the consistent pattern observed at other sites. It is obvious that the regional structure affects the responses at all sites, and its modification will not improve the fit at site *viw* without also degrading the fit at the neighboring sites. Additional structures and a more heterogeneous model are likely necessary to more precisely match the data at single sites.

Although the assumption of a uniform background resistivity provides a reasonable fit of the observed induction vectors (Fig. 6.13) and the resolved structures appear to be plausible results (Fig. 6.11 and 6.12), it must be pointed out that the model is an oversimplification which doesn't reflect the complete conductivity distribution beneath Villarrica volcano. The inability to fit the magnetotelluric impedances implies that other structures and resistivities cannot be ruled out, and in some cases may even be required by the data. However, given the limited nature of data from the few sites around Villarrica, it is obvious that the aim of this supplementary study cannot be to provide a complete 3-D conductivity distribution, but must be limited rather to the derivation of

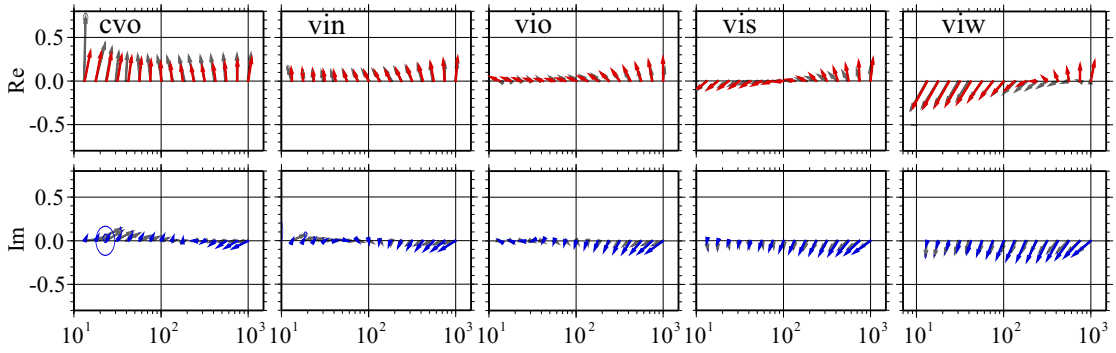

Figure 6.13.: Comparison of the observed real and imaginary parts of the induction vectors (grey) at Villarrica with the real (red) and imaginary (blue) responses of the model presented in Figs. 6.11 and 6.12

a simple and realistic model that adequately explains the effects observable at induction vectors below 1000 s.

7. Anisotropic 2-D forward modelling

Although the 2-D inversion model presented in section 6.2 is a plausible result, and the resolved conductive features beneath the profile seem to be geologically reasonable, the image does not reflect the complete conductivity distribution in the South-Central Chilean subduction zone. As mentioned in the previous chapter, the model can only reproduce the observed magnetotelluric transfer functions, but fails to explain the observed magnetic transfer functions. At long periods, all real induction vectors point systematically NE at all sites in the measurement area, as described in section 4.3, instead of directly E as would be expected, considering the most important geological features and the conductivity strike. Attempts to model this pattern with a 3-D approach failed to provide satisfactory solutions. The inability to explain the unique pattern of induction vectors via a standard 2-D approach and the fact that the 2-D isotropic models (Fig. 6.6), inferred by a joint inversion of magnetotelluric and magnetic data, reveal a number of conductors, is diagnostic of anisotropic properties of the underground. Although the anomalies can be grossly interpretable as a result of a conjunction of dehydration processes and partial melting in the subduction zone (see chapter 8), such conductive "blobs" can also arise when attempting to model anisotropic data by an isotropic 2-D approach. Given these facts, an auxiliary anisotropic approach was applied to derive a complete conductivity model for the South-Central Chilean subduction zone. Such anisotropic modeling and interpretation of the data has already been subject of a study by Brasse et al. (2009).

7.1. 3-D modeling attempts to explain induction vectors

The previous 2-D modeling of the data has been justified by the results of dimensionality analysis, which reveals a skew value below 0.3 for most of the impedances and an electrical strike coinciding with the expected geological strike, as presented by Brasse and Soyer (2001) for the central and southern profiles, and in chapter 4 of this work for the northern profile. However, considering the large-scale pattern of uniform to NE-SW deflected long-period induction vectors, as described in section 4.3 and shown in Fig. 4.5, it is obvious that a 2-D approach disregards some information inherent in the magnetic transfer function; particularly, no isotropic 2-D model exists which is able to explain this effect. It is imaginable that instead, a 3-D approach is more appropriate to provide a solution. The challenge is then to fit the real and imaginary parts of the tipper over a large area, in particular a N-S extent of at least 350 km, and from forearc

up to backarc in E-W direction[1]. Such a 3-D model must incorporate structures which reflect the geographical conditions in the region, i.e. the South American continent, whose resistivity was set to 500 Ωm with a very roughly N-S running coastline, a highly conductive (0.3 Ωm) and 4.5 km deep Pacific Ocean, and some other features of large, regional extent which may be essential for the observed pattern.

Attempts to model the observed induction vectors are presented below. The modeling was performed by D. Eydam with the 3-D algorithm of Mackie and Madden (1993) and Mackie et al. (1994).

- It is possible to generate a 3-D model which roughly reproduces the observed deflection of induction vectors at long periods. The most crucial feature in this model is a simple N-S striking unbounded layer in the crust or mantle with a conductance (conductivity-thickness product) that increases southwards, which in turn constrains the induction vectors to point northwards. The resulting NE orientation is obtained as a combination of this layer and the ocean effect, which provides an eastwards deflection. However, such a model, although theoretically possible, is geologically unreasonable. The given pattern of induction vectors over the whole study area exhibits a large positive conductance gradient from south to north, and this in turn presupposes that either the layer thickness or the layer conductivity increases continuously, up to unrealistic values. As a layer with such a conductance gradient is not indicated, much less evidenced, so that the idea was not pursued further.

- The coastline in South Chile becomes irregular, and, south of the southernmost site, where the Central Depression is submerged and the Coastal Cordillera becomes a chain of islands, with Isla de Chiloé being the largest, the trend of the coastline even changes to W-E. Thus, it is imaginable that the water masses of the Gulf of Ancud generate a N-S component in the induction vectors, and crucially contribute to the observed NE deflection. Indeed, considering the known water depths, such an effect can be modeled for the southernmost sites at latitude 41°S, but does not reach far enough to the north, and cannot serve as the only explanation for the deflection.

- At 45-46°S, on the southern coast of Chile, the Chile Rise, which forms the plate boundary between the diverging Antarctic and Nazca Plates, is subducted beneath the South American Plate, forming a triple junction between Nazca, South American and Antarctic plates. Such special locations are associated by some authors with deep-seated plume structures of enhanced conductivity. Because this hypothetic good conductor (∼1 Ωm), occurring 450-550 km south of the study area would have a regional inductive effect, it must be taken into account, and incorporated into the 3-D model as a possible cause for the observed deflection. However inspecting the model responses in Fig. 7.1, it is evident that such a plume at the

[1] On the basis of the previous measurements it is not possible to state how far beyond the study area the deflection of induction vectors continues. This can only be resolved by sounding further northward, eastward and southward.

triple junction is only able to deflect the induction vectors NE at the southernmost sites, whereas in the north the vectors, pointing strictly WE, are beyond its influence and are incompatible with the data, which suggests that a plume cannot satisfy the observed uniform pattern of induction vectors in the measured area on its own.

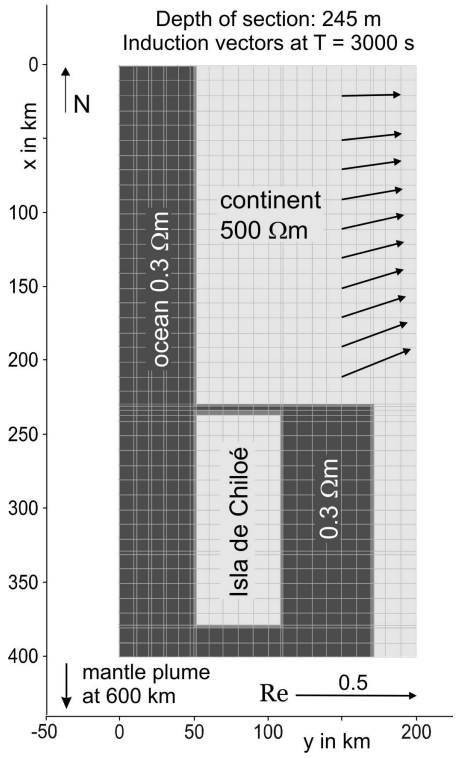

Figure 7.1.: Plan view of a 3-D test model (last item in text) at a depth of 245 m. The model is taken from Brasse et al. (2009). Real induction vectors at a period of 3000 s are simulated for a N-S profile in the Longitudinal Valley. The model comprises the ocean, the island of Chiloé, the Gulf of Ancud, and a deep mantle anomaly in the area of the triple junction, 200 km to the south of the plot margin. This class of 3-D models does not explain the uniform pattern of induction vectors in the northern study area.

This study shows that none of these simple and (geologically) realistic 3-D models, including giant isotropic anomalies in the form of seawater masses, or a plume south of the survey, is able to reproduce at large scale the observed pattern of induction vectors at the South Chilean continental margin. Therefore, in the next step, another scenario was tested – a 2-D model with an anisotropic conductivity distribution, motivated by a deeply fractured continental crust.

7.2. 2-D models with anisotropy: some principal considerations

The electrical anisotropy can be modeled either as a micro- or macroscale feature. Whereas the first possibility, also called intrinsic anisotropy, is attributed to an inherent rock property, the second is a pseudo-anisotropy generated by a sequence of conductive and resistive dikes, which are isotropic on the microscale, but exhibit anisotropic properties on the macroscale. This dichotomy shows that the electrical anisotropy is basically a question of scale, i.e, anisotropic properties observed at large scale can be generated by small-scale isotropic structures if a preferred conductivity orientation exists. Because the inductive scale length ("wave length") of fields in the earth is larger than the width of the individual isotropic units (Kellett et al., 1992; Weidelt, 1999), magnetotellurics is unable to resolve the isotropic single lamellae or dikes, and thus fails to distinguish between intrinsic and structural anisotropy.

In an anisotropic medium the conductivity σ becomes a second rank 3-D tensor $\overleftrightarrow{\sigma}$. Because $\overleftrightarrow{\sigma}$ is symmetric and positive definite, it can be transformed to a diagonal form with three principle conductivities via successive Euler rotations through three angles: strike ξ, dip ψ, and slant ζ. In matrix notation the operation can be expressed as

$$\overleftrightarrow{\sigma} = \begin{pmatrix} \sigma_{xx} & \sigma_{xy} & \sigma_{xz} \\ \sigma_{yx} & \sigma_{yy} & \sigma_{yz} \\ \sigma_{zx} & \sigma_{zy} & \sigma_{zz} \end{pmatrix} = \overleftrightarrow{R}_z^T(\xi)\overleftrightarrow{R}_x^T(\psi)\overleftrightarrow{R}_{z'}^T(\zeta) \begin{pmatrix} \sigma_1 & 0 & 0 \\ 0 & \sigma_2 & 0 \\ 0 & 0 & \sigma_3 \end{pmatrix} \overleftrightarrow{R}_{z'}(\zeta)\overleftrightarrow{R}_x(\psi)\overleftrightarrow{R}_z(\xi). \quad (7.1)$$

Thus an anisotropic structure can be fully described by six variables: three resistivities along the principal axes, and three angles (strike, dip, slant) which determine the orientation of the principal resistivities with respect to the reference frame.

Before applying the anisotropic approach to the real data, several basic models were experimented in order to evaluate the effects of some basic anisotropic structures on the magnetic transfer function. The calculations were performed by Brasse et al. (2009) using the algorithms of Pek and Verner (1997) and also of Li (2002); both yielded comparable results. As outlined in Fig. 7.2, the models generally consist of two basic components: a homogeneous half space with a resistivity of 300 Ωm, and an anisotropic layer. In the course of this study, a further structure, representing the Pacific Ocean, modeled as a 5 km thick layer, was included, and the properties of the anisotropic layer, like the location and lateral extent, varied. For reasons of simplicity, and because dip and slant (if not too large) have a much smaller influence on transfer functions than the other parameters, the investigation focused on the crucial horizontal parameters, leaving dip and slant constant at 90° and 0°, respectively. Further simplification can be made with respect to ρ_z, which was fixed to the value of ρ_x, which is possible because the tipper is less sensitive to the vertical conductivity variations. So, the principal resistivities $\rho_x = \rho_z$ were set to 1 Ωm, ρ_y to 300 Ωm, and the anisotropy strike α to 45°. A ratio of $\gg$100 between the directions of low and high conductivity seems justified, assuming that in the damage zone conductive, fluid-rich fault planes cross resistive host rock.

The model responses calculated for 102 s and 3277 s correspond, respectively, to relatively small and large penetration depths. Contrary to the magnetotelluric transfer functions, the tipper becomes zero if the anisotropic layer extends in lateral direction to

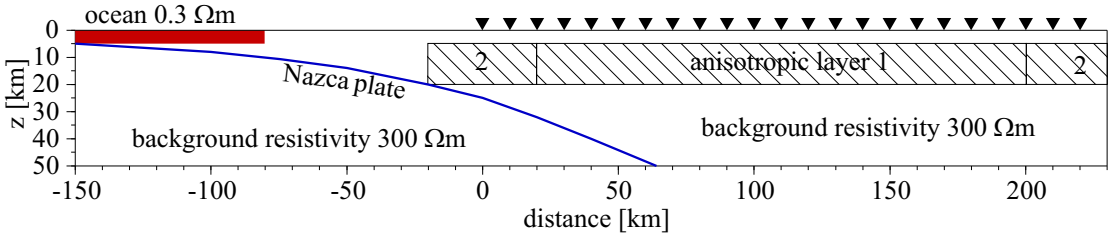

Figure 7.2.: Principle 2-D models incorporating the Pacific Ocean and an anisotropic layer in the upper crust. The anisotropy (1) is bounded on both sides in the E-W direction. Layer (2) is extended to the W and unbounded to the E. The top of the downgoing Nazca plate is outlined by a blue line; positions of receivers, where responses are calculated, are indicated by inverted triangles. For parameters see text.

infinity. This is because the vertical secondary fields induced by currents in the parallel conductive planes cancel out each other out. A vertical field only arises if the anisotropic layer is bounded, or if, in an isotropic background, some other lateral inhomogeneity is present. While in a pure, isotropic, 2-D Earth one component of tipper is identically zero, in a structure including an anisotropic feature with a preferred conductivity direction, that differs from the structural strike, both components of the tipper exist, $\vec{T} = (T_x, T_y)$.

1. If the anisotropic layer located between z=5 km and 20 km is bounded on both sides at y=20 and 200 km, induction vectors arise at both margins of the block, pointing N-W in the west an S-E in the east, as presented in Fig. 7.3 (1a) and (1b). Because the vertical magnetic fields superpose destructively, and cancel each other out in the block's center, the induction vectors decrease towards the center and even vanish completely in the middle of the block. The decreasing length of induction vectors at long periods can be explained in terms of penetration depths, i.e., the shallow anisotropic block has an inductive effect primarily for the magnetic field at short periods (102 s) and is inductively inefficient for a longer periodic field (3277 s).

2. This changes if the anisotropic layer is only bounded in the west at y=-20 km and extends to infinity in the east. Such a layer geometry is motivated by the tectonic conditions, and the data in which significant T_x component is present, namely at all sites on the continental plate; which suggests that the anisotropy persists eastwards beyond the profile. Since no data exist in Argentina at this latitude, the eastern lateral extent of the anisotropy can not be resolved, and an eastwards infinitely extending layer is simply assumed for this study. On the western margin, the subducted oceanic lithosphere is apparently a natural border for a continental crustal anisotropy. A large T_x component is present at coastal sites, and even at sea-bottom site *ob7*, located 20 km offshore on the northern profile (Kapinos and Brasse, 2006), as well as on Isla Mocha (O. Ritter, pers. comm.), but does not occur at the sites on the Nazca Plate, beyond the trench, where "normally" behaving,

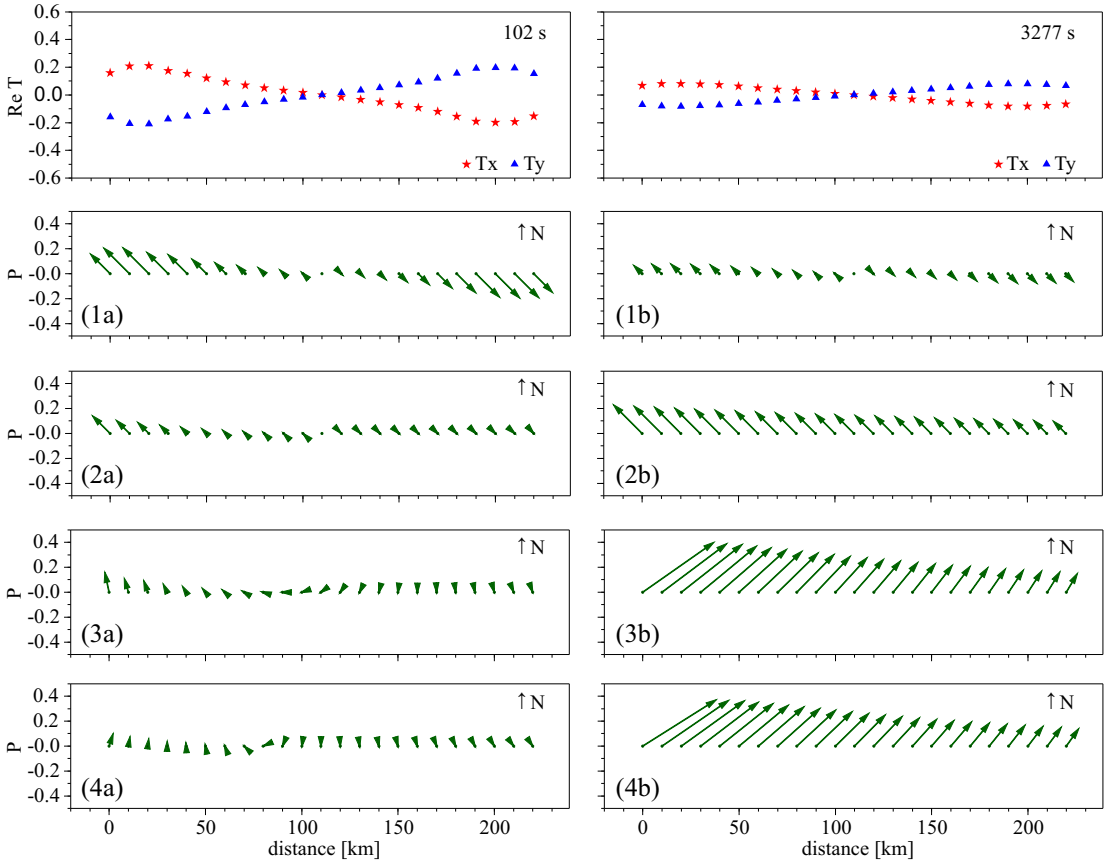

Figure 7.3.: Response (tipper) of the models from Fig. 7.2; at left 102 s, at right 3277 s. Re T is the real part of tipper transfer function, P denotes the real-valued induction vector. (1) Bounded anisotropic layer with T_x and T_y on top, (2) layer unbounded to the E, (3) unbounded layer, now with ocean, and (4) as (3), but with the layer in the lower crust. For further explanation see text.

i.e. non-deflected, induction vectors are observed. Therefore, the western margin has to be extended below the ocean, but not beyond the slab; here it is arbitrarily set to y=-20 km. The induction vectors of this model are shown in Fig. 7.3 (2a) and (2b). As expected, the anisotropy bounded at the western margin deflects the induction vectors to the west, with the largest effect at long periods, which display the induction process over a larger volume, being sensitive to the limitation of the anisotropic layer in the west, and its infinite extent towards the east.

3. The Pacific Ocean is introduced as a simple 5 km thick half layer with a resistivity of 3 Ωm at y=-80 km, i.e. 60 km away from the anisotropy. Although this simple model completely neglects the bathymetry and any geological structures in assuming uniform resistivity for the oceanic lithosphere (sediments deposits, crust and mantel) and the continental crust and mantel, its responses at long periods repro-

duce the observed pattern of induction vectors quite well (Fig. 7.3 (3a) and (3b)). The NE deflection of the vectors over the whole profile, accompanied by a slow and continuous decrease in length with increasing distance from the ocean can be reproduced by a simple vector addition of the "ocean" vector pointing eastwards and the "anisotropy" vector oriented NW, i.e. perpendicular to the preferred conductivity direction of the anisotropy, as presented in Fig. 7.4. The vectors become smaller eastwards because with increasing distance, the effects of both the ocean and the anisotropic margin decrease.

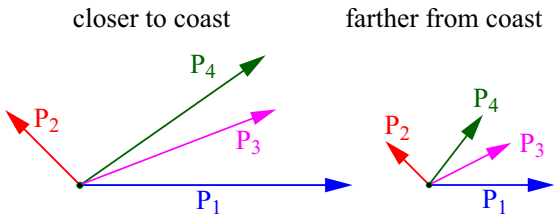

Figure 7.4.: Induction vectors near (left) and farther (right) from the coast. P1: vector originating from the coast effect above an otherwise homogeneous and isotropic half space, P2: from the anisotropic layer, P3: vector addition of P1 and P2, P4: correct vector with modeled anisotropy.

Such simple superposition of induction vectors can only be applied if the ocean and the anisotropic layer are sufficiently separated from one another. If, however, the anisotropic layer extends below the ocean, the anomalous fields of both structures would be coupled, and the resultant induction vectors are not determined by simple vector addition. Pek and Verner (1997) and Weidelt (1999) show that if an anisotropic structure overlies a conductive isotropic block, or vice versa, the real induction vectors are not perpendicular to the predominant induced currents, as is expected, but are deflected in the preferred conductivity direction of the anisotropy. This rather surprising observation could be explained by the fact that the currents in the isotropic ocean, perpendicular to the structural strike, enter into the anisotropic layer when they encounter the margin of the isotropic ocean. The currents flow in the anisotropic layer along the anisotropic strike, and induce "secondary secondary" currents in the isotropic ocean, which are opposite to the inducing currents in the anisotropy, and thus no longer perpendicular to the structural strike, but rather obliquely oriented with respect to the coast. The vertical magnetic field of the coast-parallel component of these currents is now coupled with B_x and causes the deflection of real induction vectors towards the anisotropy strike.

However, considering the significant distance between the isotropic ocean and the anisotropic half layer, as argued previously, a coupling between the fields can be ruled out, and the observed induction vectors must be a result of vector addition of the "ocean" and "anisotropy" vectors. These arguments imply, in turn, that the anisotropy strike does **not** reflect the NW-SE oriented fault pattern as displayed in Fig. 3.4. Highly conductive planes in that direction would produce, together with

the ocean effect, NW-SE oriented induction vectors; thus the information from tipper reveals other, less obvious structures (see discussion below).

4. Motivated by the fact that the induction vectors at short periods are affected by more localized anomalies, and that the uniform pattern of deflection is only observed at periods >1000 s, the anisotropic layer was shifted into the lower crust. This produces only minor differences in the responses (Fig. 7.3(4a) and (4b)) with respect to the previous model, and indicates that by taking into account only one period, the vertical extent of the half layer cannot be satisfactorily resolved by the vertical magnetic field.

7.3. Anisotropic models for the Chilean margin

Given the large number of parameters, the search for a geologically reliable model that explains the observed real and imaginary induction vectors at all sites for all frequencies is a time consuming process. However, following the principle of simplicity, the number of options can be significantly reduced by setting the slant and dip to constant values, and ρ_z equal to ρ_x. Constraints of this nature are justified, and even required, by the fact that no geological evidence for a dipping or a slanting layer within the crust exists. Moreover, this ensures that the model remains simple and comprehensible.

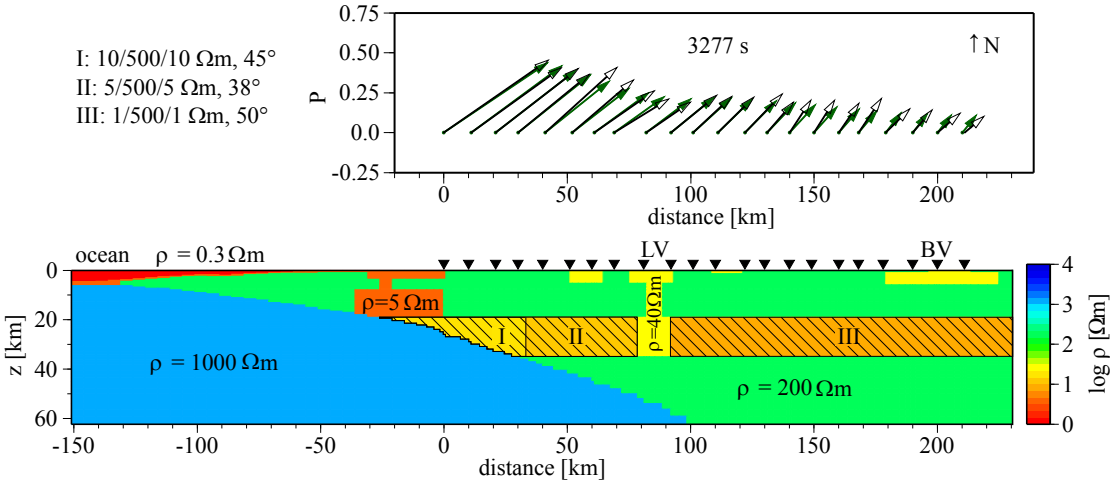

Figure 7.5.: The 2-D anisotropic model of the central profile which yields the best-fitting response. The anisotropic layer is broken by an isotropic block; in addition the sediments of the Longitudinal Valley (LV), and the Valley of Bío-Bío river (BV), are introduced as good conductors. The upper left corner shows resistivities of anisotropic blocks, with principal directions and strike angles. Upper right: Comparison of model responses (green, filled arrows) with data (black, open arrows) for the real part of the induction vectors at 3277 s along the profile.

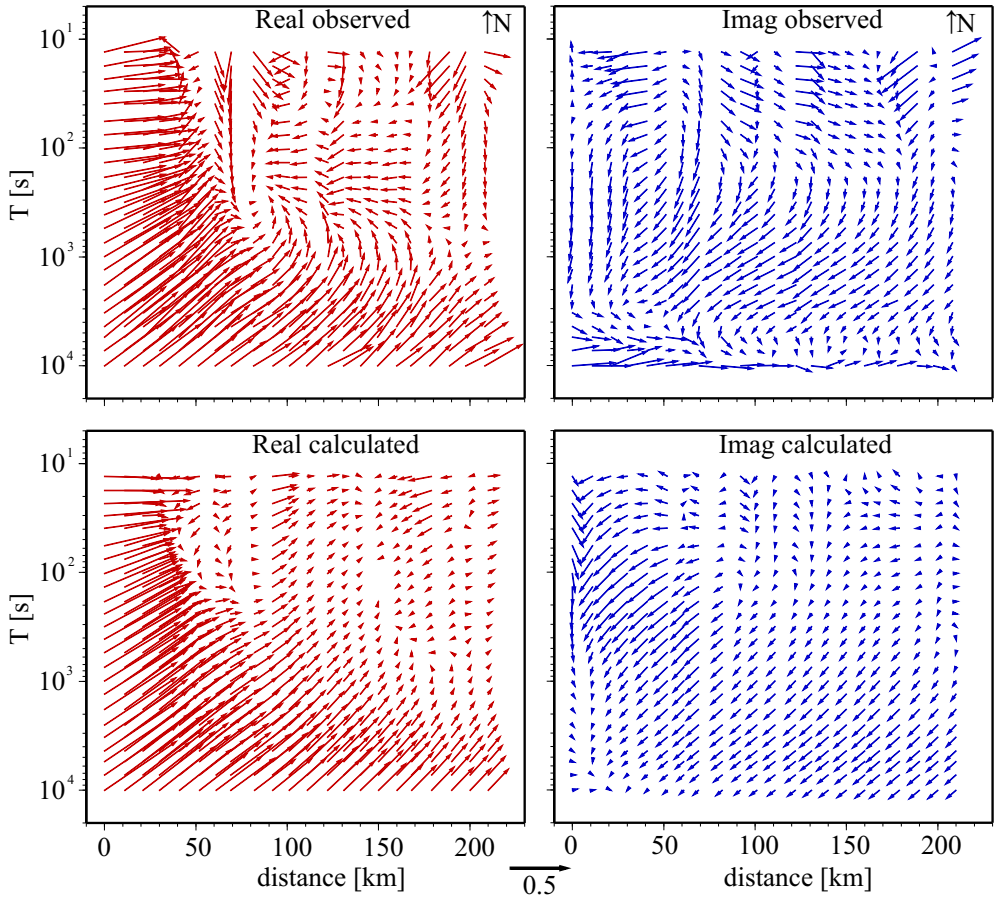

Figure 7.6.: Comparison of model response (bottom) with data (top) for all periods along the central profile (left: real, right: imaginary parts). The model reproduces the main tendency of the real and imaginary tipper components, with the exception of short-period data, which are distorted by local, probably 3-D effects.

Such simple models designed for the central and northern profiles by varying only ρ_x, ρ_y, the anisotropy strike ξ, and the layer thickness are presented in Fig. 7.5 and in Fig. 7.7. The models basically consist of the Pacific Ocean, a resistive, and up to 150 km thick, subducted oceanic lithosphere, already introduced as an a priori constraint in the isotropic model, and an anisotropic layer located at depths corresponding to the lower crust which is surrounded by a moderate background resistivity of 200 Ωm. The bathymetry was designed according to ETOPO2 data and swath bathymetry obtained during several cruises of RV Sonne (Scherwath et al., 2006). The resistivity of the ocean layer (0.3 Ωm) was derived from a CTD log presented in Fig. 5.17, and the resistivity of the slab (1000 Ωm) is postulated by Chave et al. (1991). The topmost part, and the dip angle of the slab is located by seismological studies (Bohm et al., 2002; Yuan et al., 2006) and a seismic transect approximately corresponding with the northern MT profile (Groß et al., 2008; Haberland et al., 2009; Micksch, 2008). Marginal effects on the

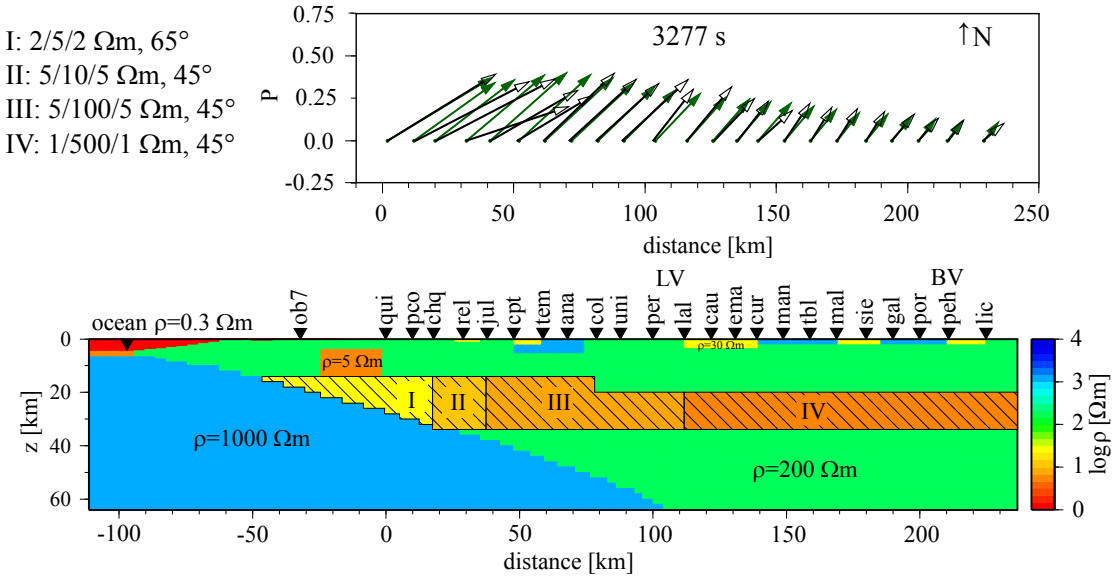

Figure 7.7.: The 2-D anisotropic model of the northern profile which yields the best-fitting response. The model includes the Pacific ocean, a crude bathymetry, the subducting slab and an anisotropic layer embedded in a moderately resistive background. In addition, superficial features like sediments of the Longitudinal Valley (LV) and the Valley of Bío-Bío river (BV) are introduced in order to fit, at least roughly, the induction vectors at short periods. The top of the anisotropic layer varies from ≈14 km below the continental shelf and Coastal Cordillera down to ≈20 km below the eastern part of the profile. Significant differences are also exhibited in the ratio between the directions of high and low conductivity in the western and eastern part of the anisotropic layer. The resistivities in principal directions and strike angle are shown in the upper left corner. Upper right: Comparison of model response (green, filled arrows) with data (black, open arrows) for the real part of the induction vectors at 3277 s along the profile.

onshore magnetic transfer functions may be due to sediments covering the oceanic plate and the continental shelf, suggested by several authors (Völker et al., 2006; Melnick and Echtler, 2006a,b; Bangs and Cande, 1997; Blumberg et al., 2008; Glodny et al., 2006), and are included in the model as a highly conductive (5 Ωm) feature. Their geometry and thickness (up to several hundred meters on the ocean bottom and continental shelf) and the increasing accumulation towards the trench, with a thickness of about 2 km in the trench basin, is obtained from offshore reflection seismics (e.g., Sick et al., 2006; Scherwath et al., 2006; Contreras-Reyes et al., 2008b). Other model details are motivated by the results of isotropic inversion. Thus the highly conductive (5 Ωm) features in the west flanks of the central and northern profiles (anomaly **D** in Fig. 6.6) affect the induction vectors (primarily their length) at long periods up to the Longitudinal Valley. Without this conductive isotropic feature the modeled arrows are smaller than the observed and might only be fitted with difficulties. The homogeneous and isotropic block beneath the Longitudinal Valley, in the central profile (Fig. 7.5), required by the geomagnetic trans-

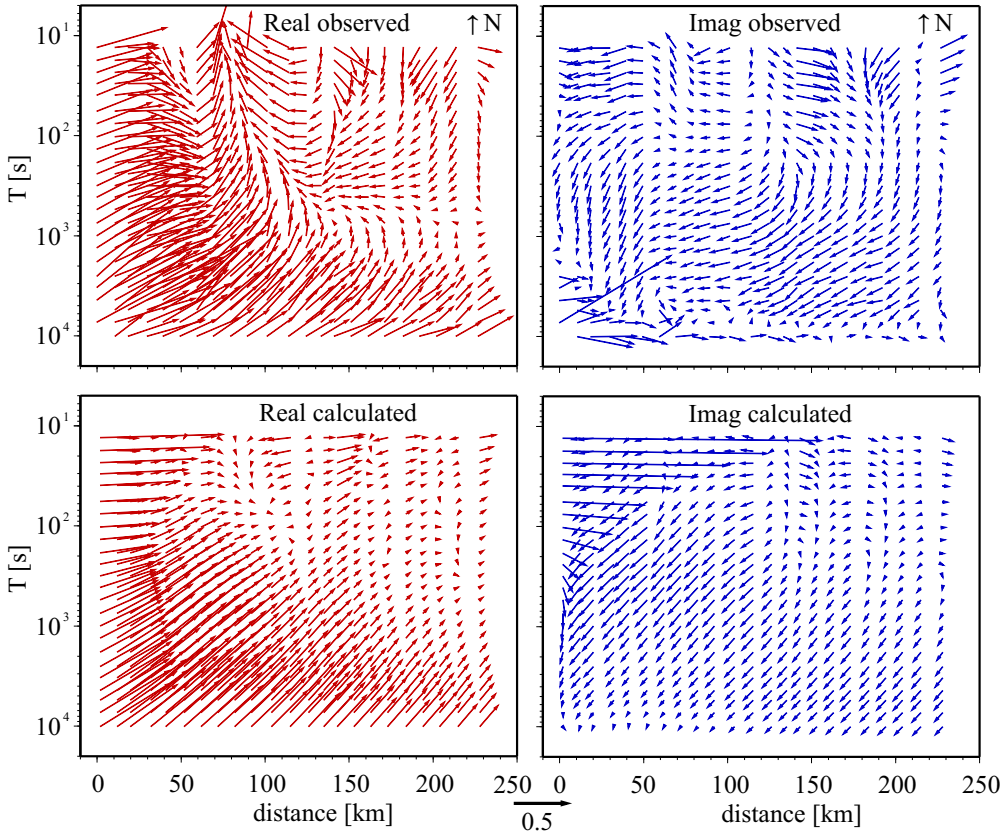

Figure 7.8.: Comparison of model responses (bottom) with data (top) for all periods along the northern profile (left: real parts, right: imaginary parts). Similarly to the central profile, the model reproduces the main tendency of the real and imaginary tipper components, with the exception of short-period data, which are distorted by local, probably 3-D effects.

fer function to explain the minimum of arrows lengths at ≈75 km, corresponds with the conductive anomaly **A** in the isotropic model at the location where the profile crosses the Lanalhue Fault. Equally important are the superficial features, such as the conductive sediments in the Longitudinal and the Bío-Bío Valleys; their thickness was here set to between 2 and 4 km, and their resistivities arbitrarily to 10–40 Ωm. These superficial structures, motivated by isotropic models were incorporated and adjusted where necessary in order to fit, at least approximately, the short-period induction vectors. On the other hand, the fact that the structures revealed by isotropic inversion complement the anisotropic model point to a compatibility between the isotropic and anisotropic models.

The location and the vertical extent of the anisotropic layer can only be roughly estimated, since the vertical magnetic fields are induced by lateral conductivity contrasts, and are not sensitive enough against variations in vertical conductivity. Thus, similar responses can be generated by a layer occurring in the mantle as well as one in the crust. Nevertheless, only the second possibility seems likely since the deflection of induction

vectors also persists at sites on the shelf, which requires a layer extending below the shelf, up to the slab. Taking into account the path and the dip angle of the subducted plate, such a westwards-elongated layer may only be realistic as a crustal feature, whereas a layer at mantle depth would be cut by the downgoing slab. The lower and upper limit of the layer can only be roughly estimated. While the crustal Moho, which has been resolved by seismological surveys in South Chile at a depth of between 25-40 km (e.g., Bohm et al., 2002; Krawczyk et al., 2006; Yuan et al., 2006; Asch et al., 2006), serves as a benchmark for the lower limit, the upper boundary was arbitrarily set to 20 km for the central profile and to between 14 and 20 km for the northern profile (see Fig. 7.5 and 7.7). Of course, the possibility that a certain degree of anisotropy persists in the uppermost continental mantle as well as in the upper crust cannot be ruled out. It also is certainly conceivable that in the upper crust the discrepancy between ρ_x and ρ_y decreases, so that a clear upper bound of the anisotropic layer cannot be exactly determined. Additionally, at short periods, effects of local (also 3-D) features become more significant, and make it difficult to fit the observed induction vectors.

The lateral extent of the anisotropy towards north, east and south cannot be resolved because in the whole study area no single station exists at which the observed real induction vectors diverge from this current pattern of uniformly deflected arrows observed at long periods. Nevertheless this allows to draw the conclusion that anisotropy persists in the whole region, and extends eastwards below the volcanic arc (where induction vectors are small but still deflected), and even into Argentina, east of the easternmost site location. The best fit was obtained by dividing the anomalous layers into segments with minor variations in the anisotropic parameters. Such a fragmented layer is in accordance with the idea of a fractured crust caused by tectonically-related stress field. Moreover, it is indicated, at least qualitatively, by the observed system of oblique faults traversing the entire study area. It would also be rather unrealistic to assume that a layer in a extensively fractured crust remains homogeneous at large scale and maintains a constant strike direction. Although the anisotropy strike – i.e., the conductive axis – runs predominantly NE-SW, the anisotropy resistivity and strike direction change slightly along the profile, which is directly reflected in the induction vectors. This basic NE-SW direction is also motivated by lineaments of minor eruptive centers along the Liquiñe-Ofqui lineament, which can be used to determine the horizontal stress field as discussed later (López-Escobar et al., 1995). The values of the resistivities in the x-, y- and z-directions and the strikes are shown in Fig. 7.5 and in Fig. 7.7.

The models for both profiles look very similar which is not surprising considering the approximately uniform deflection of induction vectors at long periods. They both also reproduce the observed data, at least at periods above 1000 s, quite well. While the ocean accounts primarily for the length of the induction vectors near the coast, the strike of the anisotropy is responsible for the deflection from W-E. Nevertheless, a few deviations from this pattern occur in both profiles. The most prominent of these appear in the Central Depression in the central profile, and in the Coastal Cordillera in the northern profile. In the central profile (Fig. 7.5), the minimum of vector lengths at $\approx$75 km may be accounted for by introducing a homogeneous and isotropic block at the location where the profile crosses the Lanalhue Fault, in accordance with the

isotropic inversion results. In the northern profile (Fig. 7.7) the arrows in the Coastal Cordillera behave more turbulently and change their orientation significantly over small scales which indicates a more heterogeneous conductivity distribution. The strongly varying tilt couldn't be satisfactory fitted by adoption of either small-scale isotropic or anisotropic structures with differing resistivities and strike directions, without also affecting the adjoining sites; more complicated structures, perhaps a 3-D anomaly, which cannot be modeled here, must be taken into account in order to explain this outlier. Nevertheless, the best fit was obtained when the layer in the coastal region is only gently anisotropic, i.e., if the ratio between the highly conductive axis to the poorly conductive is of about 2, which is very small compared the ratio of $\gg$100 in the eastern part of the layer. The thickness of the anisotropic layer in the model varies along the profile, and its top extends in the western part of the model up to the upper crust ($\approx$14 km), and in the eastern part up to the lower crust ($\approx$20 km), whereas the bottom layer may extend up to the crust-mantle boundary at $\approx$34 km. Of course an anisotropic model with differing parameters that provides similar quality of fit can not be ruled out.

Note that MT and GDS data are usually measured in geomagnetic coordinates, so the magnetic declination of the main geomagnetic field in this area and during the survey time must be taken into account. For this purpose, a declination angle of approximately N9°E, which roughly corresponds to the declination in the year 2000 on the central profile, and a value of N7°E for the survey along the northern profile in the years 2004-2005, must be added to the estimated geomagnetic strike directions of the anisotropy in order to express the direction in a geographic coordinate system.

Of course, there may also exist an anisotropic feature in the oceanic crust arising from fracturing of the oceanic crust due to bending-related faulting on the outer rise, or due to lattice preferred orientation of minerals such as alignment of olivine grains (Evans et al., 1999; Baba, 2005; Baba et al., 2006a,b). However, the vertical magnetic field recorded on the seafloor doesn't show any evidence of this. Additionally, model studies showed that a possible anisotropy in the oceanic crust would not be able to affect the vertical magnetic field over the entire survey area. Thus, an anisotropic oceanic crust may be discarded as the cause for the observed pattern of induction vectors.

A multi-site and multi-frequency overview of the observed and modeled transfer functions for the real and imaginary parts for both profiles is presented in summary in Fig. 7.6 for the southern, and in Fig. 7.8 for the northern, profile. Apart from the responses at short periods (and at long periods for the imaginary part) the data fit is reasonable.

8. Discussion and outlook

In processing the data and inspecting the magnetotelluric and magnetic transfer functions a degree of ambiguity became apparent. Although the dimensionality analysis determined a unique strike direction that corresponds well with the expected structural strike, and skew values below 0.3 justify a 2-D interpretation of most impedances, the uniformly deflected real induction vectors at all sites in the survey area, suggest, that a pure, 2-D isotropic modeling is insufficient to satisfy all of the data. To explain the geomagnetic transfer functions and to complete the conductivity image, an anisotropic approach had to be applied. The aim of this chapter is a joint interpretation of the most prominent electrical features – which were revealed by isotropic and anisotropic approaches – in the context of results from the active and passive seismic studies as well as results from the conductivity distribution at other subduction zones.

8.1. Isotropic models

Isotropic inversion along three profiles traversing the main geological and tectonic structures in the South-Central Chilean continental margin reveals a consistent conductivity distribution with several good conductors, particularly in the crust (Fig. 6.6). The most plausible cause of the enhanced conductivity in the subduction zone are fluids which play a key role in the subduction process; firstly, as a controlling factor of the rupture and earthquake nucleation; secondly, as a driving force of the melting process and volcanic activity.

Water is carried into the continental lithosphere, particularly by water saturated marine sediments, but also by the oceanic lithosphere. The latter is hydrated due to bending of the downgoing plate at the plate boundary. This so-called bending-related faulting mechanism generates new cracks and fissures in the oceanic crust, or reactivates pre-existing ones, increasing its porosity and permeability, providing pathways for water infiltration through the crust down to the mantle, and promoting its hydration (Contreras-Reyes et al., 2007, 2008a,b; Ranero et al., 2003). The conductivity increment of the oceanic lithosphere due to hydration process in a subduction zone was presented recently by Worzewski et al. (2011). Fissure formations and hydration are already incipient at the middle oceanic ridge, where the oceanic crust is produced. On the landward side of the trench, the hydration process is, due to subsidence of the oceanic plate beneath the overriding continental plate as well as the increase in pressure and temperature, replaced by the dehydration mechanism, and free water is squeezed from the marine sediments.

Hydrous phases are associated with an enhanced conductivity and can therefore be detected by geoelectric methods like magnetotellurics. Such a conductor, associated

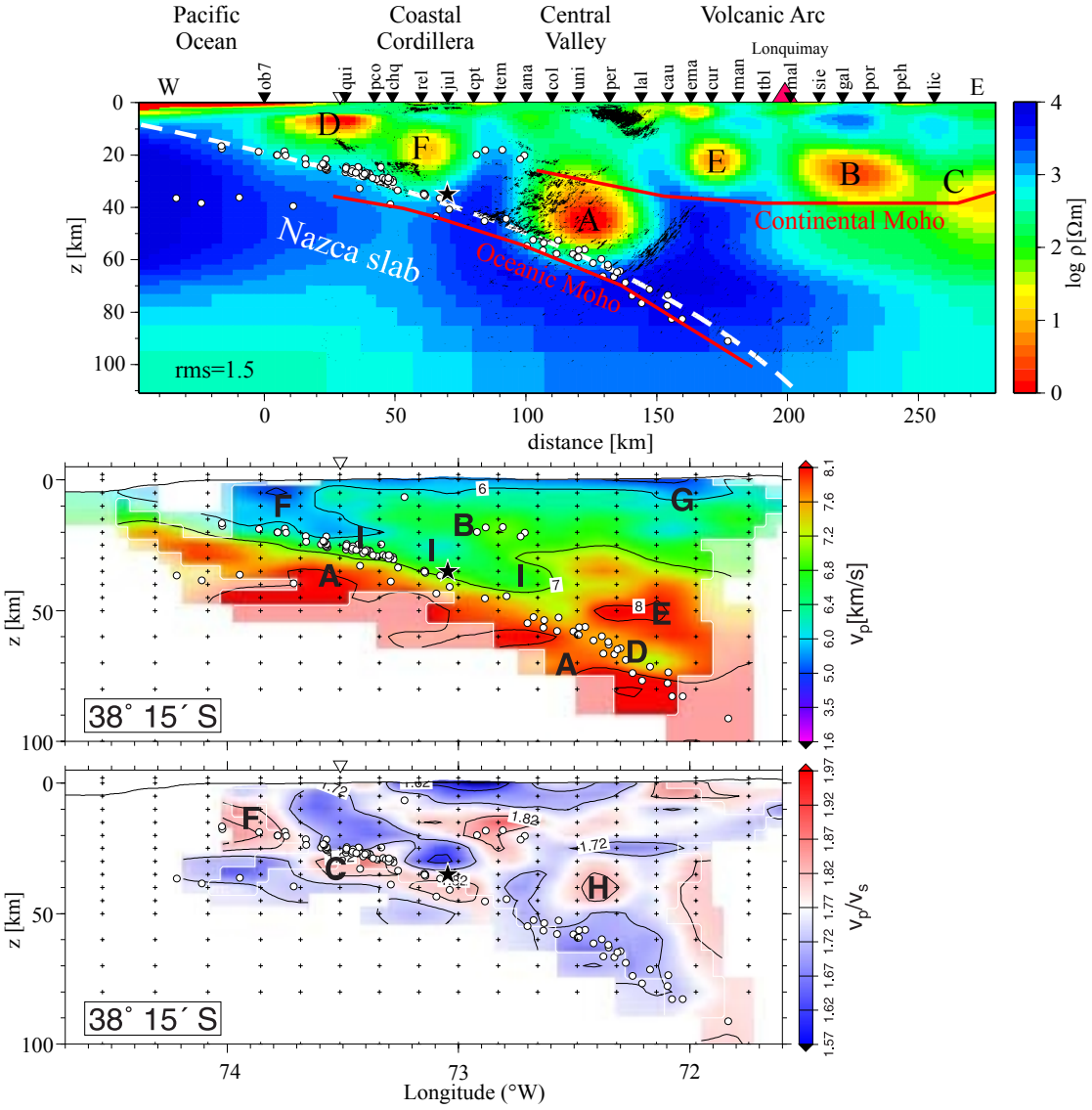

Figure 8.1.: Comparison between the results of magnetotellurics and active and passive seismics for the TIPTEQ transect. Upper panel: conductivity distribution below the South-Central Chilean continental margin along the northern profile, and Kirchhoff Prestack Depth Migration (in black) from Groß et al. (2008), and seismic events (white circles); the hypocenter of the 1960 earthquake is marked by a star; The Oceanic and Continental Moho is sketched after Yuan et al. (2006). Middle panel: ν_p velocity model; lower pannel: ν_p/ν_s ratio from Haberland et al. (2009).

with an accumulation of water released from the downgoing plate, may be anomaly **D** in the accretionary wedge situated underneath the continental shelf depicted in Fig. 6.6. This assumption is supported by active and passive seismic observations. The edge of

anomaly **D** correlates with a zone of strong seismic reflectivity observed in both prestack (Fig. 8.1) and postack (Fig. 8.2) seismic sections at the northern profile (Groß et al., 2008; Micksch, 2008). Such enhanced reflectivity may be caused by the presence of trapped fluids: a fluid-saturated material in the forearc is corroborated by local earthquake traveltime tomography, which reveals low seismic P wave velocity (ν_p) and a high ratio of P to S wave velocity (ν_p/ν_s) in the accretionary wedge. The source of the fluids may be water-saturated sediments overlaying the downgoing lithosphere, as well as water infiltration of the crust and the upper part of the oceanic mantle. At shallow depth (<40 km), a considerable amount of pore fluid is expelled due to compaction and lithification processes that occur as the oceanic lithosphere submerges beneath the continental plate. The released fluids drain from the plate interface, migrate upward through the fractured overlaid plate, and accumulate there (Haberland et al., 2009; Peacock, 1990).

The oceanic lithosphere, included in the starting model as a resistive a priori constraint, and modified in the course of the inversion, is marked on its topmost part, at depths between 20 and 40 km, by a patch of seismicity. This patch overlies a region of increased ν_p/ν_s ratio beneath the coast (labeled **C** in the lower panel of Fig. 8.1) and extends to a depth of 50 km; it may be attributed to the hydration of the oceanic crust and parts of the mantle (Haberland et al., 2009) due to bending-related faulting at the outer rise (Contreras-Reyes et al., 2007). The upper edge of the region is characterized by an increase in reflectivity, observed in both prestack and poststack sections, and caused by a porosity collapse in the basalt of the oceanic crust and release of trapped fluids (Micksch, 2008). This would also explain the high conductivity anomaly **F**, which can be associated with an accumulation of fluids in the forearc. The anomaly occurs at depths (∼15 km) at which water bound to the structures of hydrous minerals starts to release. The authenticity of this fluid-related conductor can be corroborated by a decrease in seismicity at depths of 40-55 km, which indicates the transition of a seismogenic zone to an aseismic creep.

Such accumulations of fluids in the forearc, resulting from dewatering of the subducting slab, are also observed in other subduction zones in the world. Magnetotelluric experiments in Cascadia (British Columbia, Canada) and Costa Rica revealed enhanced conductivity in the forearc, and support the assumption that such anomalies are a global phenomenon (Soyer and Unsworth, 2006; Worzewski et al., 2011). Fluid seeps in the slope of the Costa Rican subduction system are an unambiguous indicator for fluid presence in the accretionary prism (Worzewski et al., 2011); at the South Chilean margin, the existence of such seeps has not yet been observed, but cannot be ruled out, either.

While at shallow depths (10-40 km) and low pressures, compaction, lithification and diagenesis drive the dewatering of the subducting slab and account for the majority of expulsion of pore fluids, further downwards, low metamorphic devolatilization reactions primarily cause the dehydration due to increases in temperature and pressure. Further fluid release through the metamorphic dehydration mechanism reduces the effective stress and may trigger seismicity in the brittle material (Haberland et al., 2009; Peacock, 1990). These released fluids are widely supposed to account for hydration of the mantle wedge. The prominent anomaly **A** may be indication for a hydrated mantle wedge below the Longitudinal Valley, observed in all transects in South Chile at depths between 20

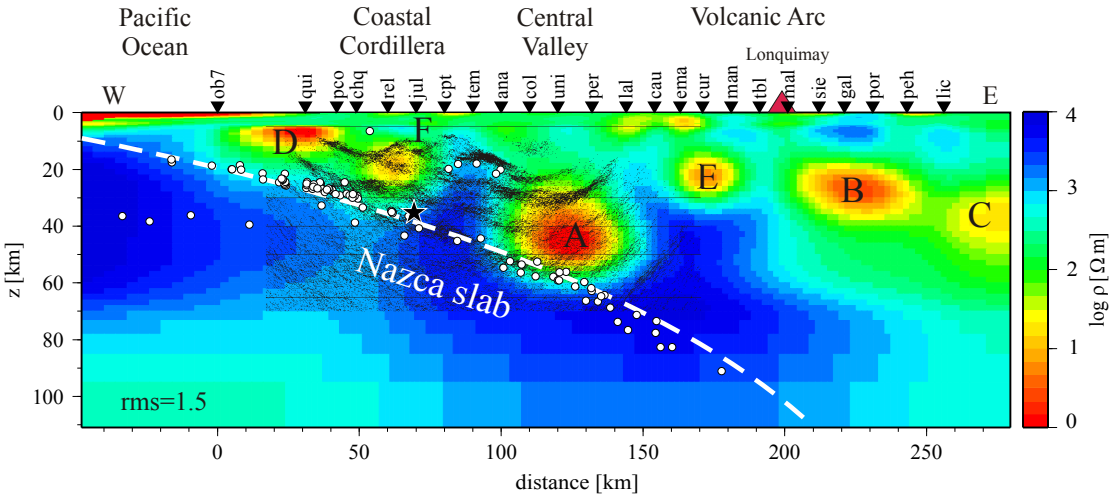

Figure 8.2.: Poststack reflection seismic section overlain on conductivity distribution revealed by isotropic inversion along the northern profile. The poststack section was kindly provided by Micksch (2008). Hypocenter of earthquakes are marked as white circles and the hypocenter of the 1960 earthquake as star.

and 50 km. Such a conductive feature is also observed at other subduction zones, including the North Andes (Brasse et al., 2002), Mexico (Jödicke et al., 2006), the northern Cascadia (Soyer and Unsworth, 2006) and the Costa Rican subduction zone (Worzewski et al., 2011), and thus may be regarded as a general phenomenon, related to subduction zones worldwide. The anomaly corresponds to the proposed hydrated mantle wedge (Micksch, 2008), and is characterized by an enhanced surrounding reflectivity, as shown in Figs. 8.1 and 8.2. Isolated structures, which can be associated with a serpentinized mantle, are also revealed by tomographic inversion, but a large-scale hydrated mantle wedge is missing (Haberland et al., 2009). According to Seno (2005), this might be explained by the particular conditions of the compressional regime, in which the released fluids flow through the fractured material along the plate interface, without serpentinization of the mantle wedge; unlike a tensional regime, in which the fluids rise to the mantle wedge and drive the serpentinization. Considering the temperature conditions in the (relatively cold) forearc, caused by the fact that the hydrated cold subducting slab cools the surrounding warm mantle, the high conductivity at depths between 20-50 km, close to the slab, is unlikely to be attributable to partial melts. Worzewski et al. (2011) associated the anomaly with fluids released from the hydrated oceanic crust, or with heating and dewatering of the serpentinized mantle wedge, and interpreted it as an important feature which plays a key role in the fluid balance during the subduction process.

Elevated electrical conductivity can also be observed at mid-crustal depths beneath the volcanic arc and backarc. These anomalies are, in general, unsurprising, and can be associated with accumulations of partial melts, which feed the active volcanoes Lon-

quimay, Villarrica and Llaima. The resistivity of 3-4 Ωm corresponds to a partial melt rate of approx. 5 vol. % according to mixing laws (Hashin-Shtrikman upper bound). Quite surprisingly however, is the fact that none of these magma deposits, thought to be feeders of the active volcanoes, are modeled directly beneath the volcanoes, but are offset by approximately 20 km to the east. This can be explained by considering that the melts do not necessarily rise to the surface through the shortest and most vertical path, but rather follow the path of the least resistance, i.e. they use fractures, ruptures, cracks of the brittle continental crust as a conduit to reach the surface. Thus, the pathway of the melts depends on the geometry of the fractures, and this may account for an offset between the magma deposit in the crust and the volcanic crater on the surface. Even though the anomaly is located at shallow depths of ≈30 km, temperatures of about 600°, derived from a thermal model of a subduction zone, can be anticipated for this region, if a young, warm, oceanic slab is considered (Schmidt and Poli, 1998; Hyndman and Peacock, 2003). These temperatures can be be sufficient to enable partial melting in the wet middle and lower crust if a considerable amount of water is transported within the subducting slab. Water, whether stored as a distinct volatile phase, or bound in the crystal structure of minerals and released during dehydration reactions, not only triggers the melting processes, but also reduces the melting point (Peacock, 1990).

The conductor at **C** or **C'** is a consistent feature, east of the eastern margin of the profile (in Argentina) – although not truly resolved in either location or resistivity, due to the lack of nearby stations, it appears in all inversion runs. A preliminary explanation may lie in a root zone for the Holocene backarc volcanism in the Loncopué Trough. However, only a future extension of the profile to Argentina could unambiguously answer this question.

8.2. Anisotropic models

Structural anisotropy in a subduction zone should not be surprising, considering the presence of a stress field due to the plate collision, in conjunction with the fact that rocks under stress become anisotropic. The anisotropic investigations result in models with a large-scale anisotropic layer predominantly in the lower, and partially in the upper, continental crust. Taking into account the offshore data, it can be quite safely assumed that the structural anisotropy in the west reaches the plate interface, or at least significantly beneath the Pacific Ocean. Nevertheless, without further sites beyond the current survey area, the lateral extent can not be resolved, because no onshore site yet exists at which the induction vectors oppose the observed uniform pattern. It would be useful to extend the profile at least several tens of kilometers eastwards to Argentina in order to clarify whether the anisotropy reaches to the backarc volcanic centers of the Loncopué Trough. Further sites south of 41°S and north of the Bío-Bío Fault could resolve and clarify the N-S extent of the anisotropy.

The NE-SW modeled anisotropy strike is motivated by an early observation of Nakamura (1977); he concluded that the distribution of parasitic vents, minor eruptive centers, and flank craters at latitudes between 37° and 41.5°S is oblique to the overall trend

of the volcanic arc. Here this is associated with the ≈N10°E running lineaments of the Liquiñe-Ofqui Fault (LOF), and is regarded as the main feature controlling the volcanic activity in South Chile.

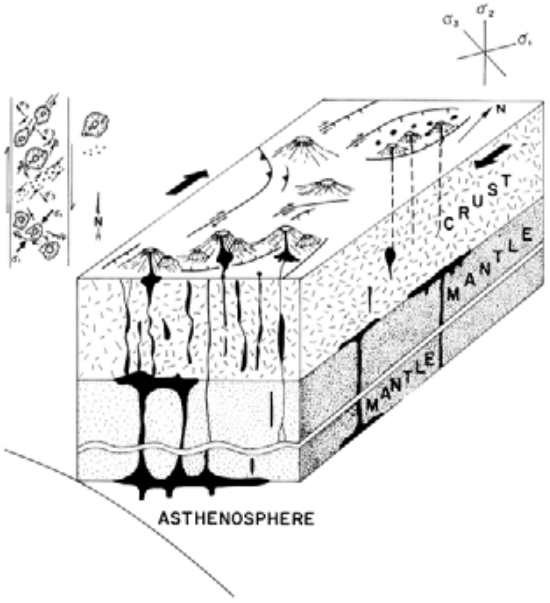

Figure 8.3.: Distribution of minor volcanic centers and alignment of feeder dikes in relation to the maximum horizontal stress and crust fracturing. Model taken from López-Escobar et al. (1995). The magma ascents through feeder dikes to the surface through a system of fractures, which is controlled by the maximum horizontal stress S_H.

Because the minor volcanic centers on the surface are supposed to be fed by vertical dikes underneath, the overall trend of these dikes can be approximately deduced from the alignment of the volcanic centers. The dikes' extent is closely related to the controlling tectonic regime, and depends on the direction of the principal axis of the stress field in the lithospheric plates (Assumpcão, 1992). The model relies on the supposition that the magma ascends to the surface as feeder dikes through a pattern of tensional and shear crustal fractures that are determined by the maximum horizontal stress S_H, and serve as pathways for the rising melt (Fig. 8.3). Nakamura (1977) proposed to use this pattern of radial dikes as an indicator for tectonic stress orientation and attributed the NE-SW aligned minor volcanic centers in the Central Southern Volcanic Zone to the maximum horizontal stress S_H. According this hypothesis, for a compressional regime with a strike-slip fault, like that in South Chile, an oblique trend of the flank crater zones orientated at around 45° to the fault is expected. This corresponds to ≈N55°E, if the ≈N10°E orientation of the main lineament is considered and matches the observed trend.

It follows from this model that an angular relation should arise between the trend of the South Chilean volcanic belt, which extends in a compressional regime parallel to the converging plate boundaries, and the zone of flank craters, which are aligned parallel to

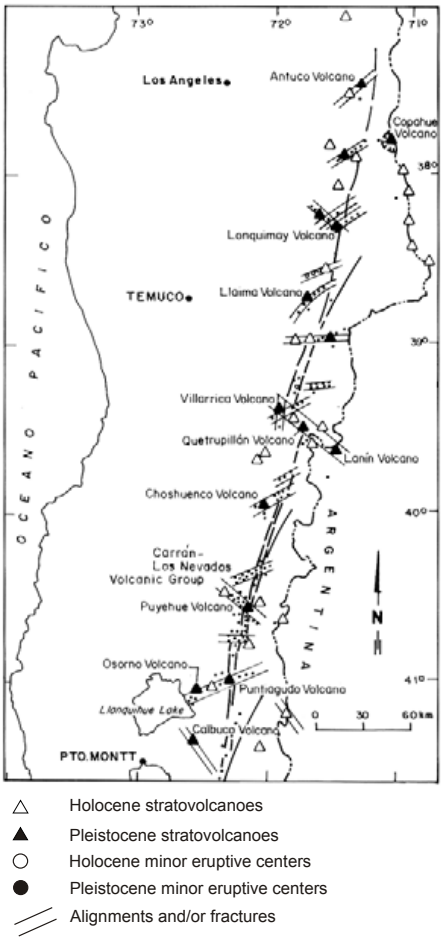

Figure 8.4.: Spatial distribution of stratovolcanoes and of minor eruptive centers in the South Andes, between 37° and 41°S. Stratovolcanoes are aligned northeast or northwest. Minor eruptive centers are aligned along lineaments of the ≈N10°E-striking Liquiñe-Ofqui Fault, but predominantly form clusters which are elongated along N50-70°E. Map taken from López-Escobar et al. (1995).

the maximum compressional stress and to the convergence direction. Although most of the composite Quaternary and active volcanoes are aligned along the main trace of the ≈N10°E-striking Liquiñe-Ofqui Fault, regarded as the main structural feature controlling the volcanism in South Chile (e.g., Cembrano et al., 1996; Melnick et al., 2006b), or along arc-parallel lineaments, the N50-70°E arc-oblique oriented alignments of parasitic vents and minor eruptive centers map the more likely pathways through crustal fractures for the low viscosity magma (Fig. 8.4).

The observed N50-70°E alignment of the flank volcanoes, which are supplied with magma by a similarly oriented system of feeder dikes indicates, according to the model proposed by Nakamura (1977), the direction of S_H, and corresponds roughly with the modeled conductivity strike of the structural anisotropy, as presented in section 7.3.

Thus, this strike seems not to be related to the NW-SE striking fault system in the South Central Andes postulated by Melnick et al. (2006a), as might be suspected.

In the central profile, the strike direction is overall perpendicular to the forearc fault pattern, apart from few divergences, such as the isotropic feature beneath the forearc, and corresponds satisfactorily with the arc-oblique alignment of the flank craters in the volcanic arc. In the northern profile, the relatively small, modeled anisotropy strike at around NW45°SE is below the N50-70°E angle of the arc-oblique distribution of flank eruptions. A possible explanation for this deviation may be provided by pre-existing crustal fractures, probably formed during past subduction under divergent conditions and under a different convergence angle and stress regime. López-Escobar et al. (1995) suggested that such pre-existing structures serve as channels for magma ascent in the volcanic arc, regardless of the present stress orientation. Pre-existing structures and a deeply fractured crust may also account for the structural anisotropy modeled along the whole profile, from the volcanic arc up to the Pacific Ocean. While in the volcanic arc, partial melts, ascending through a quite uniform pattern of fractures, conventionally account for the modeled conductivity values, the presence of molten material in the forearc can be excluded because the temperatures in the crust are insufficient to trigger melting. Here instead, fluids, released from the subducted plate during dehydration, and infiltrating the pre-existing fracture system, widely account for the modeled conductivities. Alternatively, solidified magma intrusions, enriched with metallic phases, can also account for the enhanced conductivities, at least in part.

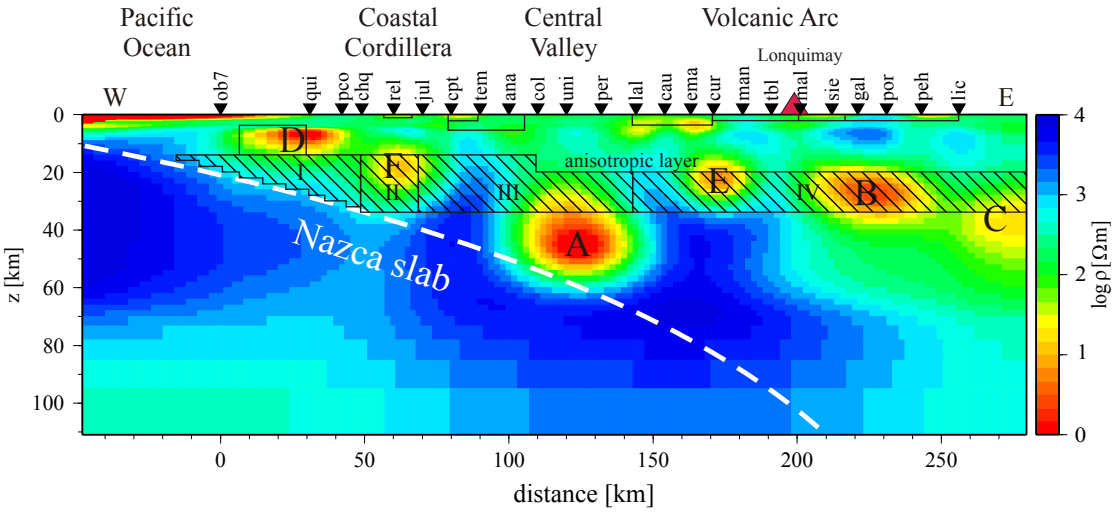

Figure 8.5.: Comparison of the the conductivity distribution, revealed by the isotropic inversion for the northern profile (upper panel in Fig. 6.6), and the anisotropic model (Fig. 7.7), which is presented here as contour. Letters label isotropic conductors, roman numerals mark anisotropic segments.

Although the origin and the exact alignment of pre-existing structures may be difficult to determine and resolve, the marks left in the geologic past by changing subduction

geometry can be observed, even if indirectly, even today, and allow reconstruction of the evolution and broadening of magmatic activity in the Andes. Westwards expansion of magmatic activity into the present Longitudinal Valley and Coastal Cordillera, and the formation of Eocene-Miocene Longitudinal Depression Volcanic Belt and Coastal Magmatic Belt in the mid-Tertiary has been suggested by several authors (e.g., Muñoz et al., 2000; Parada et al., 2007; López-Escobar et al., 1997), and is discussed in detail in chapter 3.1. Such a migration of the volcanic front was induced by changes of convergence conditions – probably by variation in the plate convergence rate and subduction angle – and must be associated with changes in the stress field, and thus also in crust fracturing. Accordingly, the modified subduction regime, accompanied by the broadening of the mid-Tertiary volcanism to the Pacific coast and the propagation of dikes into areas of the present Coastal Cordillera and Central Depression, would explain the extension of structural anisotropy into the forearc, as well as the slightly varying anisotropy strike. Ancient dikes, and/or possibly water-filled interconnected patterns of fractures beneath the forearc, as well as dikes filled with molten or partially molten material beneath the volcanic arc, would behave as lineaments of preferred conductivity and explain the observed pattern of the induction vectors in the survey area.

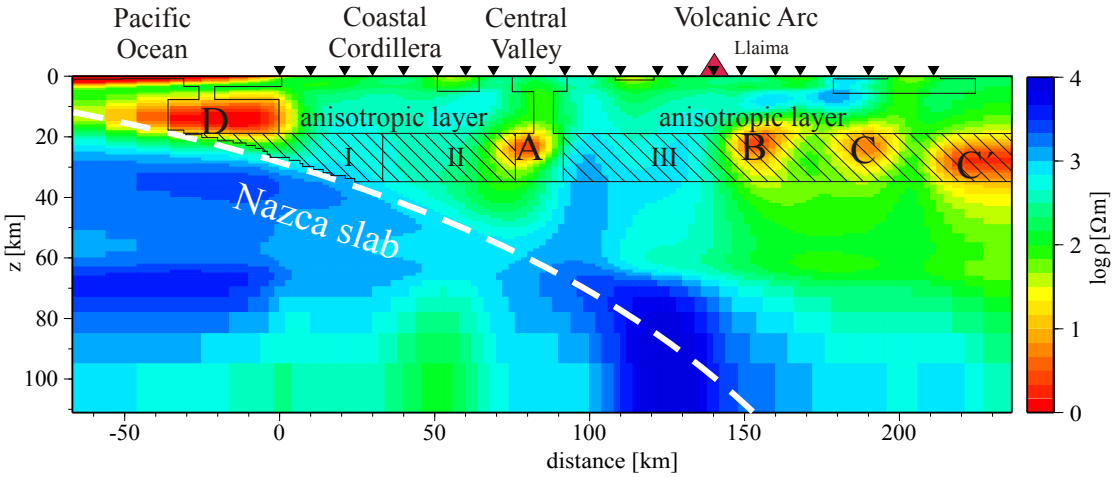

Figure 8.6.: Comparison of the conductivity distribution, revealed by isotropic inversion for the central profile (middle panel in Fig. 6.6), and the anisotropic model (Fig. 7.5), which is presented here as contour. Letters label isotropic conductors, roman numerals mark anisotropic segments.

This model explains not only the geomagnetic transfer functions, but is also in accordance with models derived from isotropic 2-D inversion. It corresponds to the concept of fluid migration from the dehydrated slab into the continental crust in the forearc, and magma ascent in the volcanic arc, and provides a plausible explanation for the zones of enhanced conductivity in the isotropic models. A joint presentation of the contours of the anisotropic model together with the isotropic image in Figs. 8.5 and 8.6 shows that most features of both approaches are compatible, and completes the entire conductivity

image of the subduction zone. The highly conductive blocks (5 Ωm), in the west flanks of the central and northern profiles in Figs. 7.5 and 7.7 correspond with anomaly **D** in the isotropic models. In both models, the structures affect the induction vectors at longer periods up to the Longitudinal Valley. Without these conductive isotropic features, the length of the modeled induction vectors in this area is clearly less than the observed magnitudes, and cannot readily be fit by other means. In the northern profile, the anisotropic segments **I** and **II** in the forearc are only "lightly anisotropic", i.e. without any clearly preferred conductivity direction (for the conductivity values in the particular directions see Fig. 7.7). This, and the low resistivity values suggest a conductive, and perhaps quite isotropic, front part of forearc region. Note that the "lightly anisotropic" segment **II** coincides with the conductor **F**.

The isotropic block beneath the Longitudinal Valley, introduced in the anisotropic layer in the central profile, was motivated by the conductivity anomaly revealed by the isotropic inversion, and is required by the geomagnetic transfer functions to fit the locally decreasing induction vectors at ≈75 km. In the central profile, the block matches anomaly **A**, which is also interpreted as a fluid accumulation in the lower crust.

In the northern profile, anomaly **A** is modeled mainly in the mantle wedge, and thus below the anisotropic layer. A conductive and isotropic block, included in the anisotropic model in the place of anomaly **A**, may primarily influence on the length of the induction vectors, and have less effect on their orientation. Thus, the attempts to improve the fit of the turbulent induction vectors in the Coastal Cordillera, on the northern profile, by introducing such isotropic block in the anisotropic model, have failed.

Although the anisotropic models appear to complement the conductivity distributions revealed by isotropic inversions, they explain the impedances only crudely. At the present time it has not been possible to construct a model which satisfactorily fits both magnetotelluric and vertical magnetic field observations; this constitutes the next task for the evaluation of the data set.

9. Summary

In the austral summer of 2004-2005, the South-Central Chilean continental margin became the subject of an amphibious magnetotelluric experiment to image the conductivity distribution of the subduction zone, performed within the multidisciplinary TIPTEQ project (from **T**he **I**ncoming **P**late to mega-**T**hrust **E**arth**Q**uake processes). The enhanced conductivity is diagnostic of the presence of fluids, i.e. water or partial melts. Magnetotellurics enables to assess qualitatively and quantitatively fluid volumes in the Earth's interior, and thus applies as an appropriate approach for investigating subductions zones, in which fluids play a key role, as a trigger and a controlling factor of rupture evolution, and earthquake nucleation, as well as partial melting reactions and volcanic activity.

The magnetotelluric data were collected at several on- and offshore sites predominantly aligned along a transect, running over 400 km across the main geological and morphotectonic units. It extended from the backarc up to the Pacific coast on the land side, and beyond the trench on the sea side, and complemented previous measurements from 2000 in this area in South Chile.

A complete image of the conductivity distribution associated with dehydration and melting processes can only be provided if the data are acquired on both the sea and land side of the trench. This is because the fluids in the continental plate are electrically coupled with the ocean through the subduction zone via connecting pathways which can only be resolved by measurements in the sea.

Whilst the terrestrial magnetotelluric approach is well established for imaging electrical conductivity structures deep in the Earth's interior, electromagnetic investigation in marine environments does not permit a direct application of the terrestrial approach to offshore measurements with respect to acquisition, analysis, and interpretation of offshore data, due to the special conditions at the ocean bottom.

The highly conductive sea water acts like a low pass filter, and causes, at short periods, strong attenuation of the electric, and even more, of the magnetic field. Towards long periods the decay of the electric and magnetic fields is significantly different. The electric field penetrates the ocean layer from surface to the seafloor nearly unchanged, while the magnetic field experiences a strong decay, and reaches the ocean bottom with just a fraction of its surface value. However, the field decay depends strongly on the resistivity contrast between the ocean and the seafloor, and both fields approximate the decay that would be observed in a homogeneous half space if the resistivity of the basement decreases.

The induction process on the seabed is significantly affected by the seafloor relief. Even a gently changing bathymetry generates preferentially in the overlaying highly conductive ocean layer an enhanced concentration of electric currents flowing along the slope, and

above instead of below the sensing points. At a continental margin, where the seafloor shallows towards land, the accumulated currents in TE mode induce an anomalous, and on the seafloor, oppositely directed magnetic field, that becomes predominant over the attenuated normal field. The effect of the secondary field on the impedances is manifested in TE mode by cusps in the apparent resistivities, accompanied by phases exceeding the "normal" quadrant. Unlike TM mode, the offshore apparent resistivities and phases are disturbed by strongly changing bathymetry, and the resulting concentration of electric currents, and cannot be linked together via Kramers-Kronig dispersion relations as can be the causal (analytical) responses at the surface.

The dimensionality analysis of the onshore impedances revealed predominantly a regional skew value below 0.3, which suggests a two-dimensional conductivity distribution, and justifies a 2-D approach and interpretation of the data. The estimated conductivity strike direction matches the roughly N-S striking land-sea boundary and is nearly perpendicular to the MT profile.

The isotropic 2-D modeling along the new, northern (TIPTEQ) profile, and renewed modeling along the central and southern profiles reveals a consistent conductivity image, with several zones of enhanced conductivity above the subducted Nazca Plate in the region of the volcanic arc, as well as in the forearc and backarc.

Although the resolved structures appear geologically plausible, and the model responses fit the magnetotelluric impedances quite well, inspection of the geomagnetic transfer function indicates that the 2-D approach does not exploit the whole information content inherent in the data. Neither 2-D nor 3-D isotropic approaches could explain the behavior of the real induction vectors, which point, at long periods (>1000 s), at all sites throughout the study area systematically NE, irrespective of the nearly N-S direction of the conductivity strike as determined by the impedances. It is thus obvious that the isotropic images do not express the "complete" conductivity distribution at the South-Central Chilean subduction zone. On the other hand, such a pattern of uniformly deflected induction arrows coupled with the fact that conductors can also arise in a model when if attempting to model anisotropic data by an isotropic approach, may be diagnostic of anisotropic properties of subsurface.

Indeed, geologically realistic models, which satisfactorily reproduce this behavior, are provided by the anisotropic approach, and are compatible with the conductivity distribution derived from the isotropic approach. They consist mainly of two crucial structures: the Pacific Ocean, and a structural anisotropy in the lower continental crust. This structural anisotropy might be associated with a deeply fractured crust, caused by subduction-related stress. The NE-SW anisotropic strike direction coincides with the distribution of the minor volcanic centers in the volcanic arc, and with the alignment of the feeder dikes underneath. While in the volcanic arc, partial melts, ascending through a pattern of fractures, might account for the preferred conductivity along the anisotropic strike, as well as for zones of enhanced conductivity revealed by the isotropic approach, in the forearc, water, released from the subducted plate and migrating upward through the fractured upper plate, might better explain the modeled isotropic and anisotropic features. Alternatively, solidified magma intrusions in pre-existing structures, enriched with metallic phases, can also explain, at least partly, the modeled enhanced conductiv-

ities.

Further zones of high conductivity are suggested by the behavior of induction vectors derived from a supplementary 3-D study around the active Villarrica volcano. The model derived from 3-D forward consists of the Pacific Ocean, a conductive anomaly directly beneath Villarrica, a conductive structure below the volcanoes Quetrupillan and Lanin, and a regional feature running NE-SW in accordance with conductive lineaments, which provide the strike direction in the anisotropic models. The modeling fits the geomagnetic transfer functions quite well at periods >10 s, but might be too simple to satisfactorily explain the apparent resistivities and phases. A more complex conductivity distribution can be provided by a denser network of sites measuring at short periods (in the AMT range) and by a 3-D inversion approach.

10. Zusammenfassung

Im südlichen Sommer 2004/2005 wurde im Rahmen des multidiziplinären Projekts TIPTEQ (abgeleitet von **T**he **I**ncoming **P**late to mega-**T**hrust **E**arth**Q**uake processes) der zentrale Teil des südchilenischen Kontinentalrandes mit einem amphibischen magnetotellurischen Experiment untersucht, um die Leitfähigkeitsverteilung dieser Subduktionszone abzubilden. Die erhöhte Leitfähigkeit ist kennzeichnend für das Vorhandensein von Fluiden, wie Wasser oder partiellen Schmelzen. Magnetotellurik ermöglicht eine qualitative und quantitative Abschätzung von Fluidvorkommen im Erdinnern. Sie ist somit eine geeignete Methode, Subduktionszonen zu untersuchen, in welchen Fluide eine Schlüsselrolle spielen als Auslöser und kontrollierender Faktor von Bruchentwicklungen und Erdbeben, aber auch bei der Produktion von partiellen Schmelzen und damit vulkanischer Aktivität.

Die magnetotellurischen Daten wurden sowohl on- wie offshore an mehreren Punkten aufgezeichnet, vorwiegend entlang eines Profils, das über 400 km quer zu den geologischen und morphotektonischen Haupteinheiten verläuft. Es erstreckt sich landseitig vom Backarc bis zur Pazifikküste und auf der Seeseite über den Trench hinaus und vervollständigt bisherige Messungen entlang zwei Profile in diesem Teil Südchiles aus dem Jahr 2000.

Für eine komplette Abbildung der Leitfähigkeitsverteilung, die eng mit Dehydration und Schmelzprozessen zusammenhängt, ist eine Datenerhebung sowohl auf der Land- wie auf der Seeseite des Trench notwendig, da insbesondere Messungen im Ozean sensitiv auf elektrisch wirksame, verbindende Strukturen zwischen den Fluiden in der Kontinentalplatte und dem Ozean und vorwiegend längs der abtauchenden Platte, sind.

Magnetotellurik an Land ist eine erprobte Methode zur Erkundung elektrischer Leitfähigkeitsstrukturen im Erdinnern; eine direkte Übertragbarkeit des terrestrischen Ansatzes bei elektromagnetischen Untersuchungen in mariner Umgebung ist jedoch hinsichtlich der Erhebung, Analyse und Interpretation der Offshoredaten aufgrund der besonderen Bedingungen am Meeresboden eingeschränkt.

Das hochleitfähige Seewasser wirkt wie ein Tiefpassfilter und verursacht bei kurzen Perioden eine starke Abschwächung des elektrischen und vor allem des magnetischen Feldes. Hin zu langen Perioden wird jedoch der Abfall für beide Felder deutlich unterschiedlich. Das elektrische Feld dringt durch den Ozean nahezu unverändert hindurch, während das magnetische Feld einen starken Abfall erfährt und den Meeresboden lediglich mit einem Bruchteil seines Oberflächenwertes erreicht. Die Feldabschwächung hängt stark von dem Widerstandskontrast zwischen Ozean und Meeresboden ab. Mit abnehmendem Widerstand des Untergrundes, d.h. abnehmendem Widerstandskontrast zwischen Ozean und Untergrund, ähnelt der Abfall der Feldabschwächung dem in einem homogenen Halbraum.

Der Induktionsprozess am Meeresboden wird erheblich durch dessen Relief beeinflusst. Bereits eine leicht veränderte Bathymetrie generiert vorzugsweise in der hoch leitfähigen Ozeanschicht eine erhöhte Konzentration von elektrischen Strömen, die entlang des kontinentalen Hangs und oberhalb anstatt unterhalb der Messpunkte fließen. Am Kontinentalrand, wo der Meeresboden zum Land hin abflacht, induzieren die akkumulierten Ströme in der TE-Mode ein anomales, sekundäres und am Meeresgrund ein dem primären Feld entgegengerichtetes magnetisches Feld, das über das abgeschwächte normale Feld dominiert. Der Effekt dieses sekundären Feldes auf die Impedanzen zeigt sich in der TE-Mode durch Auftreten von Spitzen in den scheinbaren spezifischen Widerständen, begleitet von Phasen die den normalen Quadranten verlassen. Anders als in der TM-Mode werden die Widerstände und Phasen am Ozeanboden von stark wechselnder Bathymetrie und einer daraus resultierenden Konzentration elektrischer Ströme gestört und können nicht via Kramers-Kronig Dispersionsrelation miteinander in Beziehung gebracht werden, wie das bei kausalen (analytischen) Antwortfunktionen an der Landoberfläche der Fall ist.

Die Dimensionalitätsanalyse der Onshoreimpedanzen zeigt vorwiegend einen regionalen Wert der Skewness unter 0.3, was eine zweidimensionale Leitfähigkeitsverteilung nahelegt und somit einen 2D-Ansatz und eine entsprechende Interpretation der Daten rechtfertigt. Die Streichrichtung der Leitfähigkeit stimmt mit der annähernd nord-süd verlaufenden Land-Ozean-Grenze überein und ist nahezu senkrecht zum MT-Profil.

Das isotrope 2D-Modell entlang des neuen, nördlichen (TIPTEQ) Profils und erneute Modellierung entlang des zentralen und südlichen Profils zeigen ein konsistentes Leitfähigkeitsbild mit Zonen erhöhter Leitfähigkeit oberhalb der subduzierenden Nazca-Platte in der Region des vulkanischen Bogens, ebenso wie im Forearc und im Backarc.

Obwohl die aufgelösten Strukturen geologisch plausibel erscheinen und die Anpassung der Impedanzen durch die Modellantworten gut ist, deuten die geomagnetischen Übertragungsfunktionen darauf hin, dass der 2D-Ansatz nicht den gesamten Informationsgehalt der Daten ausschöpft. Weder isotrope 2D- noch 3D-Ansätze können das Verhalten der realen Induktionsvektoren erklären, die bei langen Perioden (>1000 s) und an allen Messpunkten des gesamten Studiengebiets systematisch nord-östlich weisen, ungeachtet der nahezu nord-südlichen Ausrichtung der aus den Impedanzen abgeleiteten Leitfähigkeitsstrukturen. Es ist offensichtlich, dass das isotrope Modell nicht die vollständige Leitfähigkeitsverteilung des zentralen Teils der südchilenischen Subduktionszone offenbart.

Solche einheitlich abgelenkten Induktionsvektoren sind jedoch charakteristisch für anisotrope Eigenschaften des Untergrundes. Unter Anisotropie wird hierbei strukturelle Anisotropie verstanden, d.h. eine Abfolge oder Serie von Leitern, die nicht individuell aufgelöst werden können, wie sie auch im isotropen 2D-Modell zum Ausdruck kommen.

Geologisch plausible Modelle, die dieses Verhalten der Induktionsvektoren zufriedenstellend wiedergeben, können in der Tat aus einem anisotropen Ansatz gewonnen werden und ergänzen die Leitfähigkeitsverteilung, die durch einen isotropen Ansatz hergeleitet wird. Die Modelle bestehen hauptsächlich aus zwei grundlegenden Strukturen: dem Pazifik und einer strukturellen Ansiotropie in der unteren Kontinentalkruste. Die strukturelle Anisotropie entspricht der Idee einer zerklüfteten Kruste in Folge tektonischer

Spannungen und Kräfte, die durch das Subduktionsprozess hervorgerufen werden. Die nordost-südwestlich verlaufende, bevorzugte Leitfähigkeitsrichtung der Anisotropie deckt sich mit der Verteilung von Flankenvulkanen, Nebenschloten und kleinen Eruptionszentren und ihren darunter liegenden Förderkanälen im vulkanischen Bogen. Partielle Schmelzen im vulkanischen Bogen, die durch ein System von Klüften aufsteigen, können sowohl die Ursache für die bevorzugte Leitfähigkeit entlang der anisotropen Streichrichtung als auch für die mit einem isotropen Ansatz aufgelösten Zonen erhöhter Leitfähigkeit sein. Im Forearc hingegen kann Wasser, freigesetzt von der subduzierten Platte und durch die zerklüftete obere Platte aufsteigend, die modellierten isotropen und anisoptropen leitfähigen Strukturen erklären. Auch mit metallischen Phasen angereicherte und erstarrte Magmaintrusionen in pre-existierenden Strukturen bieten zumindest teilweise eine alternative Erklärung für die modellierte erhöhte Leitfähigkeit.

Weitere Zonen erhöhter Leitfähigkeit können aus der Ausrichtung der Induktionsvektoren, ermittelt im Rahmen einer ergänzenden 3D-Studie am aktiven Vulkan Villarrica, gefolgert werden. Das durch 3D-Vorwärtsmodellierung erhaltene Modell besteht aus dem Pazifik, einer leitfähigen Anomalie direkt unter dem Villarrica, einer leitfähigen Struktur unter den Vulkanen Quetrupillan und Lanin und einer leitfähigen regionalen Struktur, deren nordöstlich-südwestlicher Verlauf mit der Streichrichtung der anisotropen Schicht übereinstimmt. Dieses einfaches Modell reproduziert zwar recht gut die geomagnetischen Übertragungsfunktionen bei Perioden >10 s, ist aber unzureichend um die scheinbaren Widerstände und Phasen zufriedenstellend anzupassen. Eine komplexere Leitfähigkeitsverteilung könnte durch ein dichteres Netzwerk von kurzperiodischen Stationen (AMT) sowie durch einen 3D-Inversionsansatz erhalten werden.

Bibliography

Alekseev, D. A., Palshin, N. A. and Varentsov, I. M.(2009). *Magnetotelluric dispersion relations in a two-dimensional model of the coastal effect.* Izvestiya, Physics of the Solid Earth, 45(2), 167–170.

Arfken, G. B. and Weber, H. J.(2001). *Mathematical Methods for Physicists.* Elsevier Academic Press, San Diego.

Asch, G., Schurr, B., Bohm, M., Yuan, X., Haberland, C., Heit, B., Kind, R., Woelbern, I., Bataille, K., Comte, D., Pardo, M., Viramonte, J., Rietbrock, A. and Giese, P.(2006). *Seismological Studies of the Central and Southern Andes.* In: O. Oncken et al. (Eds), *The Andes: Active Subduction Orogeny*, 443–458. Springer, Berlin.

Assumpcão, M.(1992). *The regional intraplate stress field in South America.* J. Geophys. Res., 97, 11889–11903.

Aster, R. C., Borchers, B. and Thurber, C.(2005). *Parameter Estimation and Inverse Problems.* Elsevier Academic Press, Burlington.

Baba, K.(2005). *Electrical structure in marine tectonic settings.* Surv. Geophys., 26, 701–731, doi: 10.1007/s10712–005–1831–2.

Baba, K., Tarits, P., Chave, A. D., Evans, R. L., Hirth, G. and Mackie, R. L.(2006a). *Electrical structure beneath the northern MELT line on the East Pacific Rise at 15°45'S.* Geophys. Res. Lett., 33, L22301, doi:10.1029/2006GL027528.

Baba, K., Chave, A. D., Evans, R. L., Hirth, G. and Mackie, R. L.(2006b). *Mantle dynamics beneath the East Pacific Rise at 17°S: Insights from the Mantle Electromagnetic and Tomography (MELT) experiment.* J. Geophys. Res., 111, B02101, doi:10.1029/2004JB003598.

Bahr, K.(1988). *Interpretation of the magnetotelluric impedance tensor: regional induction and local telluric distortion.* J. Geophys., 62, 119–127.

Bangs, N. and Cande, S.(1997). *Episodic development of a convergent margin inferred from structures and processes along the southern Chile margin.* Tectonics, 16, 489–503.

Bendat, J. S. and Piersol, A.(1971). *Random Data: Analysis and Measurement Procedures.* Wiley-Interscience, New York.

Berdichevsky, M. N.(1999). *Marginal notes on magnetotellurics.* Surv. Geophys., 20, 341–375.

Berdichevsky, M. N., Dimitriev, V. I. and Pozdnjakova, E.(1998). *On two-dimensional interpretation of magnetotelluric soundings.* Geophys. J. Int., 133, 585–606.

Bibby, H. M.(1986). *Analysis of multiple-source bipole-quadripole resistivity surveys using the apparent resistivity tensor.* Geophysics, 51, 972–983.

Bibby, H. M., Caldwell, T. G. and Brown, C.(2005). *Determination and non-determinable parameters of galvanic distortion in magnetotellurics.* Geophys. J. Int., 163, 915–930.

Blumberg, S., Lamy, F., Arz, H., Echtler, H., Wiedicke, M., Haug, G. and Oncken, O.(2008). *Turbiditic trench deposits at the South-Chilean active margin: A Pleistocene-Holocene record of climate and tectonics.* Earth Planet. Sci. Lett., 268, 526–539.

Bohm, M., Lüth, S., Echtler, H., Asch, G., Bataille, K., Bruhn, C., Rietbrock, A. and Wigger, P.(2002). *The Southern Andes between 36° and 40° S latitude: seismicity and average seismic velocities.* Tectonophysics, 356, 275–289.

Brasse, H.(2009). *Methods of geoelectric and electromagnetic deep sounding.* Lecture notes (unpublished), Free University, Berlin, Germany.

Brasse, H.(2011). *Electromagnetic Images of the South and Central American Subduction Zones.* In: E. Petrovský, E. Herrero-Bervera, T. Harinarayana and T. Ivers (Eds), *The Earth's Magnetic Interior*, 43–81. IAGA Special Sopron Book Series, Berlin.

Brasse, H. and Eydam, D.(2008). *Electrical conductivity beneath the Bolivian Orocline and its relation to subduction processes at the South American continental margin.* J. Geophys. Res., 113, B07109, doi:10.1029/2007JB005142.

Brasse, H. and Soyer, W.(2001). *A magnetotelluric study in the southern Chilean Andes.* Geophys. Res. Lett., 28, 3 757–3 760.

Brasse, H., Lezaeta, P., Rath, V., Schwalenberg, K., f, W. and Haak, V.(2002). *The Bolivian Altiplano conductivity anomaly.* J. Geophys. Res., 107(B5), doi:10.1029/2001JB000391.

Brasse, H., Kapinos, G., Li, Y., Mütschard, L., Soyer, W. and Eydam, D.(2009). *Structural electrical anisotropy in the crust at the South-Central Chilean continental margin as inferred from geomagnetic transfer functions.* Phys. Earth Planet. In., 173, 7–16.

Cagniard, L.(1953). *Basic theory of the magneto-telluric method of geophysical prospecting.* Geophysics, 18, 605–635.

Calder, E., Harris, A., Peña, P., Pilger, E., Flynn, L., Fuentealba, G. and Moreno, H.(2004). *Combined thermal and seismic analysis of the Villarrica volcano lava lake, Chile.* Rev. Geol. Chile, 31, 259–272.

Caldwell, T. G., Bibby, H. M. and Brown, C.(2004). *The magnetotelluric phase tensor.* Geophys. J. Int., 158, 457–469.

Cantwell, T.(1960). *Detection and analysis of low frequency magnetotelluric signals.* Dissertation, Dep. of Geology and Geophysics, M.I.T, Cambridge (Mass.).

Cembrano, J., Hervé, F. and Lavenu, A.(1996). *The Liquiñe Ofqui fault zone: a long-lived intra-arc fault system in southern Chile.* Tectonophysics, 259, 55–66.

Cembrano, J., Schermer, E., Lavenu, A. and Sanhueza, A.(2000). *Contrasting nature of deformation along an intra-arc shear zone, the Liquiñe Ofqui fault zone, southern Chilean Andes.* Tectonophysics, 319, 129–149.

Cembrano, J., Lavenu, A., Yañez, G., Riquelme, R., García, M., González, G. and Hérail, G.(2007). *Neotectonics.* In: T. Moreno and W. Gibbons (Eds), *The Geology of Chile*, 231–261. Geological Society, London.

Chave, A. D.(1984). *On the electromagnetic fields induced by oceanic internal waves.* J. Geophys. Res., 89(C6), 10519–10528.

Chave, A. D. and Filloux, J. H.(1984). *Electromagnetic induction fields in the deep ocean off California: oceanic and ionospheric sources.* Geophys. J. R. Astron. Soc., 77, 143–171.

Chave, A. D. and Smith, J. T.(1994). *On electric and magnetic galvanic distortion tensor decompositions.* J. Geophys. Res., 99(B3), 4669–4682.

Chave, A. D., Constable, S. C. and Edwards, R. N.(1991). *Electrical exploration methods for the seafloor.* In: M. N. Nabighian (Ed.), *Electromagnetic Methods in Applied Geophysics - Volume 2, Application*, 931–966. Society of Exploration Geophysicists, Tulsa, Oklahoma.

Cifuentes, I.(1989). *The 1960 Chilean earthquakes.* J. Geophys. Res., 94, 665–680.

Constable, S. C., Parker, R. L. and Constable, C. G.(1987). *Occam's inversion: A practical algorithm for generating smooth models from electromagnetic sounding data.* Geophysics, 52, 289–300.

Constable, S. C., Key, K. and Lewis, L.(2009). *Mapping offshore sedimentary structure using electromagnetic methods and terrain effects in marine magnetotelluric data.* Geophys. J. Int., 176, 431–442.

Contreras-Reyes, E., Grevemeyer, I., Flueh, E. R., Scherwath, M. and Heesemann, M.(2007). *Alteration of the subducting oceanic lithosphere at the southern*

central Chile trench-outer rise. Geochemistry Geophysics Geosystems, 8, Q07003, doi:10.1029/2007GC001632.

Contreras-Reyes, E., Grevemeyer, I., Flueh, E. R., Scherwath, M. and Bialas, J.(2008a). *Effect of trench-outer rise bending-related faulting on seismic Poisson's ratio and mantle anisotropy: a case study offshore of Southern Central Chile.* Geophys. J. Int., 173, 142–156, doi: 10.1111/j.1365–246X.2008.03716.x.

Contreras-Reyes, E., Grevemeyer, I., Flueh, R. and Reichert, C.(2008b). *Upper lithospheric structure of the subduction zone offshore of southern Arauco peninsula, Chile, at ∼38° S.* J. Geophys. Res., 113, B07303, doi:10.1029/2007JB005569.

de Kronig R. L.(1926). *On the theory of dispersion of X-rays.* J. Opt. Soc. Am., 12, 547–556.

Egbert, G. D.(1990). *Comments on 'Concerning dispersion relations for the magnetotelluric impedance tensor' by E. Yee and K.V. Paulson.* Geophys. J. Int., 102, 1–8.

Egbert, G. D.(1997). *Robust multiple-station magnetotelluric data processing.* Geophys. J. Int., 130, 475–496.

Evans, R. L., Tarits, P., Chave, A. D., White, A., Heinson, G., Filloux, J. H., Toh, H., Seama, N., Utada, H., Booker, J. R. and Unsworth, M. J.(1999). *Asymmetric Electrical Structure in the Mantle Beneath the East Pacific Rise at 17° S.* Science, 286, 752–756.

Evans, R. L., Chave, A. D. and Booker, J. R.(2002). *On the importance of offshore data for magnetotelluric studies of ocean-continent subduction systems.* Geophys. Res. Lett., 29(0), doi:10.1029/2001GL013960.

Eydam, D.(2008). *Magnetotellurisches Abbild von Fluid- und Schmelzprozessen in Kruste und Mantel der zentralen Anden.* Diplomarbeit, Fachrichtung Geophysik, Freie Universität Berlin, Germany.

Filloux, J. H.(1973). *Techniques and instrumentation for study of natural electromagnetic induction at sea.* Phys. Earth Planet. In., 7, 323–338.

Filloux, J. H.(1974). *Electric field recording on the sea floor with short span instruments.* J. Geomagn. Geoelectr., 26, 269–279.

Filloux, J. H.(1987). *Instrumentation and experimental methods for oceanic studies.* In: J. A. Jacob (Ed.), *Geomagnetism*, 143–246. Academic Press, London.

Fischer, G.(1979). *Electromagnetic induction effects on the ocean coast.* Proc. IEEE, 67, 1050–1060.

Fischer, G.(1992). *Die kausalen Dispersions-Relationen in der Magnetotellurik.* In: V. Haak and H. Rodemann (Eds.), *Protokoll über das Kolloquium "Erdmagnetische Tiefensondierung" in Borkheide bei Berlin vom 25.-29. Mai 1992*, 31–41.

Fischer, G. and Schnegg, P. A.(1980). *The dispersion relations of the magnetotelluric response and their incidence on the inversion problem.* Geophys. J. R. astr. Soc., 62, 661–673.

Fischer, G. and Schnegg, P.-A.(1993). *The magnetotelluric dispersion relations over 2-D structures.* Geophys. J. Int., 115, 1119–1123.

Folguera, A., Zapata, T. and Ramos, V. A.(2006). *Late Cenozoic extension and the evolution of the Neuquén Andes.* In: S. M. Kay and V. A. Ramos (Eds.), *Evolution of an Andean Margin: A Tectonic and Magmatic View from the Andes to the Neuquén Basin (35-39° S lat)*, 267–285. Geol. Soc. Am. Spec. Paper 407, doi:10.1130/2006.2407(12).

Folguera, A., Introcaso, A., Giménez, M., Ruiz, F., Martinez, P., Tunstall, C., García Morabito, E. and Ramos, V.(2007). *Crustal attenuation in the Southern Andean retroarc (38°-39° 30' S) determined from tectonic and gravimetric studies: The Lonco-Luán astenospheric anomaly.* Tectonophysics, 439, 129–147.

Fox, R., Hohmann, G., Killpack, T. and Rijo, L.(1980). *Topographic effects in resistivity and induced-polarisation surveys.* Geophysics, 45(1), 75–93.

Glodny, J., Echtler, H., Figueroa, O., Franz, G., Gräfe, K., Kemnitz, H., Kramer, W., Krawczyk, C., Lohrmann, J., Lucassen, F., Melnick, D., Rosenau, M. and Seifert, W.(2006). *Long-Term Geological Evolution and Mass-Flow Balance of the South-Central Andes.* In: O. Oncken et al. (Eds.), *The Andes: Active Subduction Orogeny*, 401–428. Springer, Berlin.

Glodny, J., Echtler, H., Collau, S., Ardiles, M., Burón, P. and Figueroa, O.(2008). *Differential Late Paleozoic active margin evolution in South-Central Chile (37° S-40° S) - the Lanalhue Fault Zone.* J. S. Am. Earth Sci., 26, 397–411.

Golub, G. H. and Van Loan, C. F.(1989). *Matrix Computations, 2nd edition.* John Hopkins University, Baltimore.

Gonzáles-Ferrán, O.(1994). *Volcanes de Chile.* Instituto Geográfico Militar, Santiago de Chile.

Groom, R. and Bailey, R.(1991). *Analytic investigation of the effects of near-surface three-dimensional galvanic scatterers on MT tensor decompositions.* Geophysics, 56, 496–518.

Groom, R. W. and Bahr, K.(1992). *Corrections for near surface effects: Decomposition of the magnetotelluric impedance tensor and scaling corrections for regional resistivities: A tutorial.* Surv. Geophys., 13, 341–379.

Groom, R. W. and Bailey, R. C.(1989). *Decomposition of magnetotelluric impedance tensors in presence of local three-dimensional galvanic distortion.* J. Geophys. Res., 94, 1913–1925.

Groß, K., Micksch, U. and TIPTEQ Research Group, S. T.(2008). *The reflection seismic survey of project TIPTEQ – the inventory of the Chilean subduction zone at 38.2°S.* Geophys. J. Int., 172, 565–571.

Haberland, C., Rietbrock, A., Lange, D., Bataille, K. and Hofmann, S.(2006). *Interaction between forearc and oceanic plate at the south-central Chilean margin as seen in local seismic data.* Geophys. Res. Lett., 33, doi:10.1029/2006GL028189.

Haberland, C., Rietbrock, A., Lange, D., Bataille, K. and Dahm, T.(2009). *Structure of the seismogenic zone of the southcentral Chilean margin revealed by local earthquake traveltime tomography.* J. Geophys. Res., 114, doi:10.1029/2008JB005802.

Hackney, R., Echtler, H., Franz, G., Götze, H., Lucassen, F., Marchenko, D., Melnick, D., Meyer, U., Schmidt, S., Tašárová, S., Tassara, A. and Wienecke, S.(2006). *The Segmented Overriding Plate and Coupling at the South-Central Chilean Margin (36-42°S).* In: O. Oncken et al. (Eds.), *The Andes: Active Subduction Orogeny*, 355–374. Springer, Berlin.

Hansen, P. C.(1998). *Rank-Deficient and Discrete Ill-Posed Problems. Numerical Aspects of Linear Inversion.* SIAM, Philadelphia.

Heise, W., Caldwell, T. G., Bibby, H. M. and Brown, C.(2006). *Anisotropy and phase splits in magnetotellurics.* Phys. Earth Planet. In., 158, 107–121.

Hervé, F.(1988). *Late Paleozoic subduction and accretion in southern Chile.* Episodes, 11, 183–188.

Hervé, F., Munizaga, F., Parada, M., Brook, M., Pankhurst, R., Snelling, N. and Drake, R.(1988). *Granitoids of the Coast Range of central Chile: Geochronology and geologic setting.* J. S. Am. Earth Sci., 1, 185–194.

Hervé, F., Faundez, V., Calderón, M., Massonne, H. and Willner, A.(2007). *Metamorphic and plutonic basement complex.* In: T. Moreno and W. Gibbons (Eds.)), *The Geology of Chile*, 5–19. Geological Society, London.

Hestenes, M. R. and Stiefel, E.(1952). *Methods of conjugate gradients for solving linear systems.* J. Res. Nat. Bur. Stand., 49, 409–436.

Horne, R. and Frysinger, G.(1963). *The Effect of Pressure on the Electrical Conductivity of Sea Water.* J. Geophys. Res., 68(7), 1967–1973.

Hyndman, R. D. and Peacock, S. M.(2003). *Serpentinization of the forearc mantle.* Earth Planet. Sci. Lett., 212, 417–432.

Isacks, B. L.(1988). *Uplift of the Central Andean Plateau and Bending of the Bolivian Orocline.* J. Geophys. Res., 93(B4), 3211–3231.

Jiracek, G. R.(1990). *Near-Surface and Topographic Distortions in Electromagnetic Induction.* Surv. Geophys., 11 (2-3), 163–203.

Jödicke, H., Jording, A., Ferrari, L., Arzate, J., Mezger, K. and Rüpke, L.(2006). *Fluid release from the subducted Cocos plate and partial melting of the crust deduced from magnetotelluric studies in southern Mexico: Implications for the generation of volcanism and subduction dynamics.* J. Geophys. Res., 111, B08102.

Kapinos, G. and Brasse, H.(2006). *An Amphibious Magnetotelluric Experiment at the South Chilean Continental Margin.* In: O. Ritter and H. Brasse (Eds.), *Prot. 21. Koll. Elektromagnetische Tiefenforschung*, 307–314, Haus Wohldenberg, Holle, 3.-7. 10. 2005. ISSN 0946-7467.

Keller, G. and Frischknecht, F.(1966). *Electrical Methods in Geophysical Prospecting.* Pergamon Press, Oxford.

Kellett, R. L., Mareschal, M. and Kurtz, R. D.(1992). *A model of lower crustal electrical anisotropy for the Pontiac subprovince of the Canadian Shield.* Geophys. J. Int., 111, 141–150.

Key, K. W.(2003). *Application of Broadband Marine Magnetotelluric Exploration to a 3D Salt Structure and a Fast-Spreading Ridge.* Dissertation, University of California, San Diego.

Klotz, J., Abolghasem, A., Khazaradze, G., Heinze, B., Vietor, T., Hackney, R., Bataille, K., Maturana, R., Viramonte, J. and Perdomo, R.(2006). *Long-Term Signals in the Present-Day Deformation Field of the Central and Southern Andes and Constraints on the Viscosity of the Earth's Upper Mantle.* In: O. Oncken et al. (Eds.), *The Andes: Active Subduction Orogeny*, 65–89. Springer, Berlin.

Kramers, H. A.(1927). *La diffusion de la lumière par les atomes.* Atti Cong. Intern. Fisica, 2, 545–557.

Krawczyk, C. and the SPOC Team(2003). *Amphibious seismic survey images plate interface at 1960 Chile earthquake.* EOS Trans. Am. Geophys. Union, 84(32), 301, 304–305.

Krawczyk, C., Mechie, J., Tašárová, Z., Lüth, S., Stiller, M., Brasse, H., Echtler, H., Bataille, K., Wigger, P. and Araneda, M.(2006). *Geophysical Signatures and Active Tectonics at the South-Central Chilean Margin.* In: O. Oncken et al. (Eds.), *The Andes: Active Subduction Orogeny*, 171–192. Springer, Berlin.

Lara, L. E. and Folguera, A.(2006). *The Pliocene to Quaternary narrowing of the Southern Andean volcanic arc between 37° and 41°S latitude.* In: S. M. Kay and V. A. Ramos (Eds.), *Evolution of an Andean Margin: A Tectonic and Magmatic View*

from the Andes to the Neuquén Basin (35-39° S lat), doi:10.1130/2006.2407(14). Geol. Soc. Am. Spec. Paper 407.

Lara, L. E., Naranjo, J. A. and Moreno, H.(2004). *Rhyodacitic fissure eruption in Southern Andes (Cordón Caulle; 40.5° S) after the 1960 (Mw:9.5) Chilean earthquake: a structural interpretation.* J. Volcan. Geotherm. Res., 138, 127–138.

Larsen, J.(1968). *Electric and Magnetic Fields Inducted by Deep Sea Tides.* Geophys. J. R. astr. Soc., 16, 47–70.

Lavenu, A. and Cembrano, J.(1999). *Compressional- and transpressional-stress pattern for Pliocene and Quaternary brittle deformation in fore arc and intra-arc zones (Andes of Central and Southern Chile).* J. Struct. Geol., 21, 1669–1691.

Levenberg, K.(1944). *A method for the solution of certain nonlinear problems in least squares.* Quat. Appl. Math., 2, 164–168.

Li, Y.(2002). *A finite-element algorithm for electromagnetic induction in two-dimensional anisotropic conductivity structures.* Geophys. J. Int., 148, 389–401.

Lines, L. R. and Treitel, S.(1984). *Tutorial: A review of least-squares inversion and its application to geophysical problems.* Geophys. Prosp., 32, 159–186.

López-Escobar, L., Cembrano, J. and Moreno, H.(1995). *Geochemistry and tectonics of the Chilean Southern Andes basaltic Quaternary volcanism (37-46° S).* Rev. Geol. Chile, 22, 219–234.

López-Escobar, L., Cembrano, J. and Moreno, H.(1997). *Eocene-Miocene longitudinal depression and Quaternary volcanism in the Southern Andes, Chile (33-42.5° S).* Rev. Geol. Chile, 24, 227–244.

Lueth, S. and Wigger, P.(2003). *A crustal model along 39° S from a seismic refraction profile-ISSA 2000.* Rev. Geol. Chile, 30, 83–101.

Mackie, R. L. and Madden, T. R.(1993). *Three-dimensional magnetotelluric inversion using conjugate gradients.* Geophys. J. Int., 115, 215–229.

Mackie, R. L., Smith, J. T. and Madden, T.(1994). *Three-dimensional electromagnetic modeling using finite difference equations: The magnetotelluric example.* Radio Science, 29, 923–935.

Marquardt, G. W.(1963). *An algorithm for least-squares estimation of nonlinear parameters.* J. Soc. Indust. Appl. Math., 11(2), 431–441.

Marquardt, G. W.(1970). *Generalized inverses, ridge regression, biased linear estimation, and nonlinear estimation.* Technometrics, 12, 591–612.

Maus, S.(2007). *Electromagnetic ocean effects.* In: D. Gubbins and E. Herrero-Bervera (Eds.), *Encyclopedia of Geomagnetism and Paleomagnetism*, 739–742. Springer, The Netherlands.

McGillivray, P. R. and Oldenburg, D. W.(1990). *Methods for calculating Fréchet derivatives and sensitivities for the non-linear inverse problem: a comparative study.* Geophys. Prosp., 38, 499–524.

McNeill, J. D. and Labson, V.(1987). *Geological Mapping Using VLF Radio Fields.* In: M. N. Nabighian (Ed.), *Electromagnetic Methods in Applied Geophysics - Volume 2, Appliction*, 521–639. SEG, Tulsa.

Meju, M.(1994). *Geophysical Data Analysis: Understanding Inverse Problem Theory and Practice.* SEG, Tulsa.

Melnick, D.(2007). *Neogene seismotectonics of the south-central Chile margin: Subduction-related processes over various temporal and spatial scales.* Dissertation, Universität Potsdam, Germany.

Melnick, D. and Echtler, H.(2006a). *Inversion of forearc basins in south-central Chile caused by rapid glacial age trench fill.* Geology, 34(9), 709–712.

Melnick, D. and Echtler, H.(2006b). *Morphotectonic and geologic digital maps compilations of the south-central Andes (36°-42°S).* In: O. Oncken et al. (Eds.), *The Andes: Active Subduction Orogeny*, 565–568. Springer, Berlin.

Melnick, D., Rosenau, M., Folguera, A. and Echtler, H. P.(2006a). *Neogene tectonic evolution of the Neuquén Andes western flank (37-39°S).* In: S. M. Kay and V. A. Ramos (Eds.), *Evolution of an Andean Margin: A Tectonic and Magmatic View from the Andes to the Neuquén Basin (35-39°S lat)*, 73–95. Geol. Soc. Am. Spec. Paper 407, doi:10.1130/2006.2407(04).

Melnick, D., Folguera, A. and Ramos, V. A.(2006b). *Structural control on arc volcanism: The Caviahue-Copahue complex, Central to Patagonian Andes transition (38°S).* J. S. Am. Earth Sci., 22, 66–88.

Micksch, U.(2008). *The Chilean subduction zone at 38,2°S: New geophysical images derived from seismic reflection data of project TIPTEQ – Implications for the subduction channel and the seismogenic coupling zone.* Dissertation, Freie Universität Berlin, Germany.

Muñoz, J., Troncoso, R., Duhart, P., Crignola, P., Farmer, L. and Stern, C.(2000). *The relation of the mid-Tertiary coastal magmatic belt in south-central Chile to the late Oligocene increase in plate convergence rate.* Rev. geol. Chile, 27, 177–203.

Muñoz, M., Fournier, H., Mamani, J., Febrer, P., Borzotta, E. and Maidana, A.(1990). *A comparative study of results obtanined in magnetotelluric deep soundings in Villarrica active volcano zone (Chile) with gravity investigations, distributions of earthquake foci, heat flow empirical relationship, isotopic geochemistry $^{87}Sr/^{86}Sr$ and SB systematics.* Phys. Earth Planet. In., 60, 195–211.

Nakamura, K.(1977). *Volcanoes as possible indicators of tectonic stress orientation - principle and proposal*. J. Volcan. Geotherm. Res., 2, 1–16.

Onwumechili, C. A.(1997). *The Equatorial Electrojet*. Gordon and Breach Science Publishers, Netherlands.

Pankhurst, R. J.(1990). *The Paleozoic and Andean magmatic arcs of West Antarctica and southern South America*. In: S. M. Kay and C. W. Rapela (Eds.), *Plutonism from Antarctica to Alaska*, 1–7. Geol. Soc. Am. Spec. Paper 241.

Parada, M. A., López-Escobar, L., Oliveros, V., Fuentes, F., Morata, D., Calderón, M., Aguirre, L., Féraud, G., Espinoza, F., Moreno, H., Figueroa, O., Muñoz Bravo, J., Troncoso Vásquez, R. and Stern, C.(2007). *Andean magmatism*. In: T. Moreno and W. Gibbons (Eds.), *The Geology of Chile*, 115–146. The Geological Society, London.

Parker, E. N.(1958). *Dynamics of the Interplanetary Gas and Magnetic Fields*. Astrophys. J., 128, 664–676.

Peacock, S. M.(1990). *Fluid Processes in Subduction Zones*. Science, 248, 329–337.

Pek, J. and Verner, T.(1997). *Finite-difference modelling of magnetotelluric fields in two-dimensional anisotropic media*. Geophys. J. Int., 128, 505–521.

Ramos, V. A. and Kay, S. M.(2006). *Overview of the tectonic evolution of the southern Central Andes of Mendoza and Neuquén (*$35° - 39° S$ *latitude)*. In: S. M. Kay and V. A. Ramos (Eds.), *Evolution of an Andean Margin: A Tectonic and Magmatic View from the Andes to the Neuquén Basin (35-39° S lat)*, 1–17. Geol. Soc. Am. Spec. Paper 407, doi:10.1130/2006.2407(01).

Ranero, C., Morgan, J. P., McIntosh, K. and Reichert, C.(2003). *Bending-related faulting and mantle serpentinization at the Middle American Trench*. Nature, 425, 367–373.

Rietbrock, A., Haberland, C., Bataille, K., Dahm, T. and Oncken, O.(2005). *Studying the Seismogenic Coupling Zone with a Passive Seismic Array*. EOS Trans. Am. Geophys. Union, 86(32), 293–297.

Riley, K. F., Hobson, M. P. and Bence, S. J.(1998). *Mathematical Methods for Physics and Engineering: A Comprehensive Guide*. Cambridge University Press, Cambridge.

Rodi, W. and Mackie, R. L.(2001). *Nonlinear conjugate gradients algorithm for 2-D magnetotelluric inversion*. Geophysics, 66, 174–187.

Rokityansky, I. I.(1982). *Geoelectromagnetic Investigation of the Earth's Crust and Mantle*. Springer, Berlin.

Rosenau, M., Melnick, D. and Echtler, H.(2006). *Kinematic constraints on intra-arc shear and strain partitioning in the southern Andes between 38° S and 42° S latitude.* Tectonics, 25, doi:10.1029/2005TC001943.

Rosenau, M. R.(2004). *Tectonics of the Southern Andean Intra-arc Zone (38°-42° S).* Dissertation, Fachbereich Geowissenschaften, Freie Universität Berlin, Germany.

Scherwath, M., Flueh, E., Grevemeyer, I., Tilmann, F., Contreras-Reyes, E. and Weinrebe, W.(2006). *Investigating Subduction Zone Processes in Chile.* EOS Trans. Am. Geophys. Union, 87(27), 265–272.

Schmidt, M. and Poli, S.(1998). *Experimentally based water budgets for dehydrating slabs and consequences for arc magmatic generation.* Earth Planet. Sci. Lett., 163, 361–379.

Schmucker, U.(1973). *Regional induction studies: A review of methods and results.* Phys. Earth Planet. In., 7, 365–378.

Schwalenberg, K.(1997). *Zweidimensionale Modellrechnung und Inversion audio-magnetotellurischer Daten aus der Oberpfalz.* Diplomarbeit, Institut für Angewandte Geophysik, Technische Universität Berlin, Gemany.

Seno, T.(2005). *Variation of downdip limit of the seismogenic zone near the Japanese islands: Implications for the serpentinization mechanism of the forearc mantle wedge.* Earth Planet. Sci. Lett., 231(3-4), 249–262.

Sick, C., Yoon, M.-K., Rauch, K., Buske, S., Lüth, S., Araneda, M., Bataille, K., Chong, G., Giese, P., Krawczyk, C., Mechie, J., Meyer, H., Oncken, O., Reichert, C., Schmitz, M., Shapiro, S., Stiller, M. and Wigger, P.(2006). *Seismic Images of Accretive and Erosive Subduction Zones from the Chilean Margin.* In: O. Oncken et al. (Eds.), *The Andes: Active Subduction Orogeny*, 147–170. Springer, Berlin.

Siemon, B.(1997). *An interpretation technique for superimposed induction anomalies.* Geophys. J. Int., 130, 73–88.

Singer, B. S.(1992). *Corrections for distortions of magnetotelluric fields: Limits of validity of the static approach.* Surv. Geophys., 13, 309–340.

Smith, J. T.(1997). *Estimating galvanic-distortion magnetic fields in magnetotellurics.* Geophys. J. Int., 130, 65–72.

Soyer, W.(2002). *Analysis of geomagnetic variations in the Central and Southern Andes.* Dissertation, Fachbereich Geowissenschaften, Freie Universität Berlin.

Soyer, W. and Unsworth, M.(2006). *Deep electrical structure of the northern Cascadia (British Columbia, Canada) subduction zone: Implications for the distribution of the distribution of fluids.* Geology, 34, 53–56.

Spitzer, K.(2001). *Magnetotelluric static shift and direct current sensitivity.* Geophys. J. Int., 144, 289–299.

Stern, C. R., Frey, F. A., Futa, K., Zartman, R. E., Peng, Z. and Kyser, T. K.(1990). *Trace-element and Sr, Nd, Pb and O isotopic composition of Pliocene and Quaternary alkali basalts of the Patagonian Plateau lavas of southernmost South America.* Contrib. Mineral. Petrol., 104, 294–308.

Steveling, E.(1996). *Erweiterung des aus MAGSON-Magnetometer und RAP-Datenlogger bestehenden Meßsystems.* In: K. Bahr and A. Junge (Eds.), *EMTF-Kolloquiumsprotokoll*, 173–178, Burg Ludwigstein, Holle, 9.-12. 04. 1996. ISSN 0946-7467.

Swift, C. M.(1967). *A magnetotelluric investigation of an electrical conductivity anomaly in the southwestern United States.* Dissertation, Dept. of Geology and Geophyics, MIT, Cambridge, Mass.

Szarka, L. and Menvielle, M.(1997). *Analysis of rotational invariants of the magnetotelluric impedance tensor.* Geophys. J. Int., 129, 133–142.

Tikhonov, A. N.(1950). *On determining electrical characteristics of the deep layers of the Earth's crust.* Dokl. Akad. Nauk SSSR, 73, 295–297.

Völker, D., Wiedicke, M., Ladage, S., Gaedicke, C., Reichert, C., Rauch, K., Kramer, W. and Heubeck, C.(2006). *Latitudinal Variation in Sedimentary Processes in the Peru-Chile Trench off Central Chile.* In: O. Oncken et al. (Eds.), *The Andes: Active Subduction Orogeny*, 193–216. Springer, Berlin.

Vozoff, K.(1987). *The magnetotelluric method.* M. N. Nabighian, *Electromagnetic Methods in Applied Geophysics. Volume 2, Appliction*, 641–711. SEG, Tulsa.

Wait, J. R.(1954). *On the Relation Between Telluric Currents and the Earth's Magnetic Field.* Geophysics, 19, 281–289.

Wannamaker, P. E.(1999). *Affordable magnetotellurics: Interpretation in natural environments.* In: M. Oristaglio and B. Spies (Eds.), *Three-Dimensional Electromagnetics*, 349–374. SEG, Tulsa.

Ward, S. and Hohmann, G.(1988). *Electromagnetic Theory for Geophysical Applications.* In: M. N. Nabighian (Ed.), *Electromagnetic Methods in Applied Geophysics*, 131–311. Society of Exploration Geophysicists, Tulsa, Oklahoma.

Weaver, J.(1994). *Mathematical Methods for Geo-electromagnetic Induction.* Wiley, New York.

Weaver, J. T., Agarwal, A. K. and Lilley, F. E. M.(2000). *Characterisation of the magnetotelluric tensor in terms of its invariants.* Geophys. J. Int., 141, 321–336.

Weidelt, P.(1972). *The inverse problem of geomagnetic induction.* Z. f. Geophys., 38, 257–289.

Weidelt, P.(1994). *Phasenbeziehungen für die B-Polaristation.* In: Bahr, K. and Junge, A. (Eds.), *Protokoll über das Kolloquium "Erdmagnetische Tiefensondierung" in Höchst in Odenwald vom 28.-31. März 1994*, 60–65.

Weidelt, P.(1999). *3-D conductivity models: Implications of electrical anisotropy.* In: M. Oristaglio and B. Spies (Eds.), *Three-Dimensional Electromagnetics*, 119–137. SEG, Tulsa.

Wiese, H.(1962). *Geomagnetische Tiefentellurik Teil II: Die Streichrichtung der Untergrundstrukturen des elektrischen Widerstandes, erschlossen aus geomagnetischen Variationen.* Geofis. Pura e Appl., 52, 83–103.

Worzewski, T., Jegen, M., Kopp, H., Brasse, H. and Taylor Castillo, W.(2011). *Magnetotelluric image of the fluid cycle in the Costa Rican subduction zone.* nature geoscience, 4, 108–111, doi:10.1038/ngeo1041.

Yee, E. and Paulson, K. V.(1988). *Concerning dispersion relations for the magnetotelluric impedance tensor.* Geophysical Journal, 95, 549–559.

Yuan, X., Asch, G., Bataille, K., Bock, G., Bohm, M., Echtler, H., Kind, R., Oncken, O. and Wölbern, I.(2006). *Deep seismic images of the Southern Andes.* In: S. M. Kay and V. A. Ramos (Eds.), *Evolution of an Andean Margin: A Tectonic and Magmatic View from the Andes to the Neuquén Basin (35-39° S lat)*, 61–72. Geol. Soc. Am. Spec. Paper, 407, doi:10.1130/2006.2407(03).

Zhdanov, M. S. and Keller, G. V.(1994). *The geoelectrical methods in geophysical exploration.* Elsevier, Amsterdam.

A. Appendix

A.1. Influence of the inversion parameters, model discretization and a priori informations on the model

The influence of the inversion parameters, model discretization and a priori informations[1]on the model is presented in Fig. A.1.

The models show a quite similar conductivity distribution (models **A**, **B**, **C**), independently if the chosen mesh is logarithmic or equidistant and independently of a priori information are used (slab is included), or not (homogeneous half space) if the weighting parameter β is set to 0. However, this changes if $\beta > 0$. For $\beta > 0$ (here $\beta = 3$) the model discretization has a significant effect on the inversion result, as can be seen by comparing the model **D**, in which a logarithmic grid is used, and the model **E**, which was calculated for an equidistant grid. That is because differently discretized model parts experience unequal weighting. On the one hand, the algorithm pays more attention to the part of the model with the refined mesh, but on the other hand the weighting parameter β penalizes finely discretized model parts less strongly than roughly discretized regions in the model with the logarithmic mesh. Thus, the differences are not only caused by a higher attention of the code to the model parts with a finer grid, but also by an unequal penalization in differently discretized meshes by the weighting parameter β.

Accordingly less differences between the models arise for a different β (β=0 and β=3), if an equidistant mesh underlies the starting model (model **B** and **C** vs. model **E**). If however a logarithmic mesh is applied, the differences between the models calculated for β=0 and β=3 become considerably larger (model **A** vs. model **D**).

[1]Descriptions used in Fig. A.1: **homogeneous half space**= the start model consists of the ocean included in a homogeneous half space. **slab**= the start model consists of the ocean and a slab included in a homogeneous half space. **logarithmic grid**= a logarithmic mesh is used, i.e. the cell dimension increases exponentially, except for the upper layers of the model at the slope, where the grid is equidistant, with a layer thickness of 150 m. **equidistant grid**= a fine and predominantly equidistant mesh, at depths between 5 and 80 km, with a vertical cell dimension of 2 km (used if the slab is incorporated in the starting model). Below this depth, the cell dimension increases exponentially (see logarithmic grid).

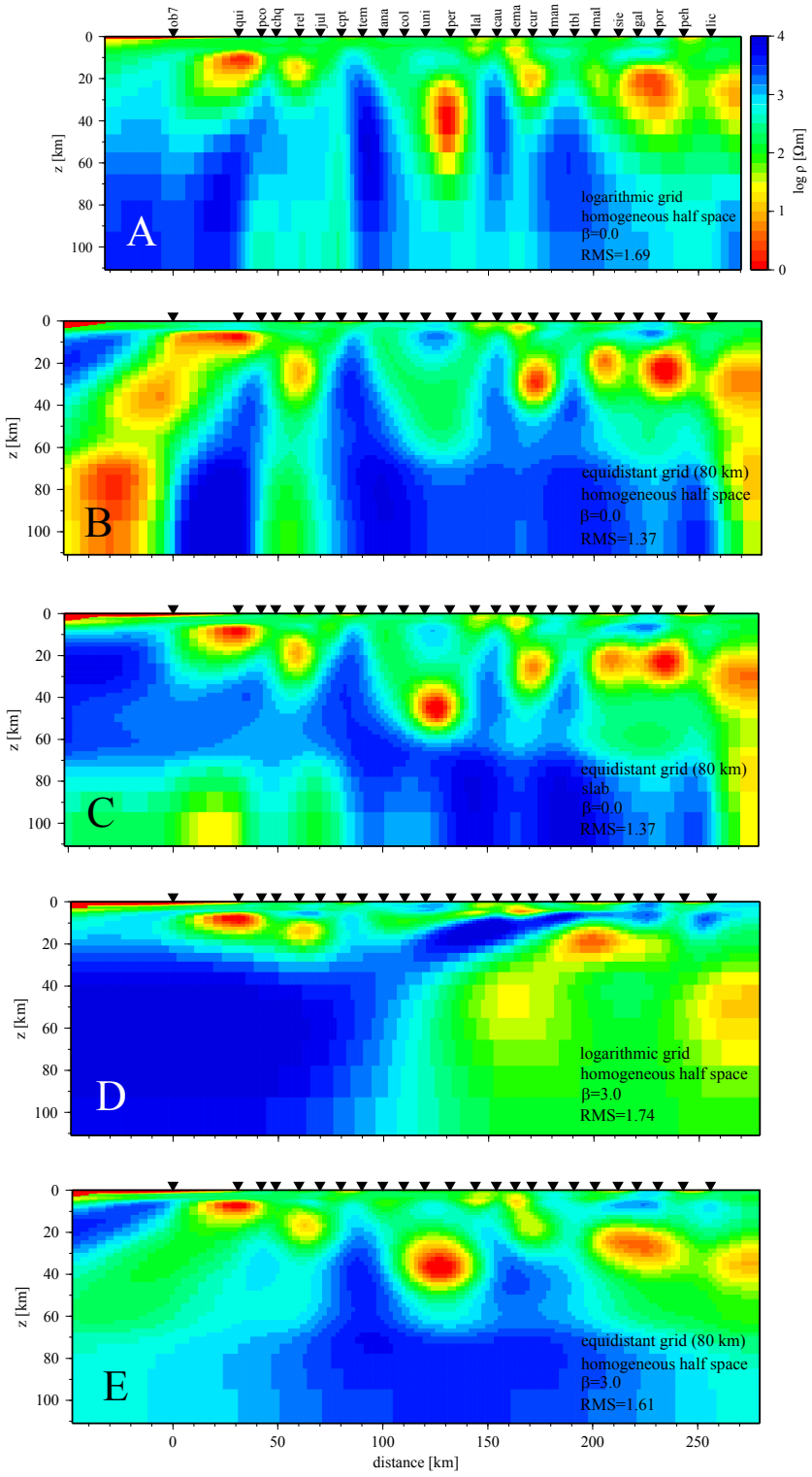

Figure A.1.: Evolution of a model depending on used a priori information, discretization mesh and constraining parameter β.

A.2. Data and inversion responses

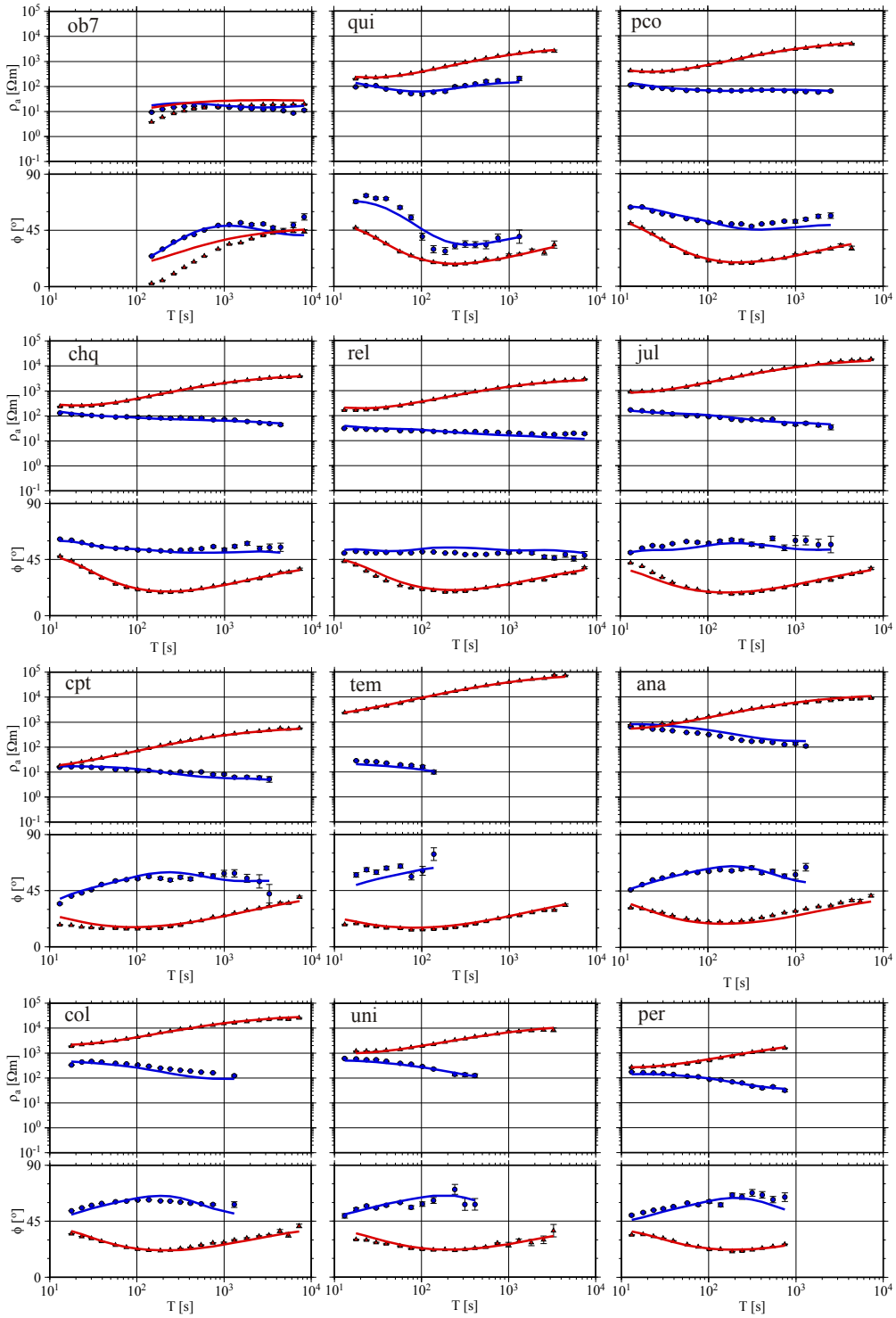

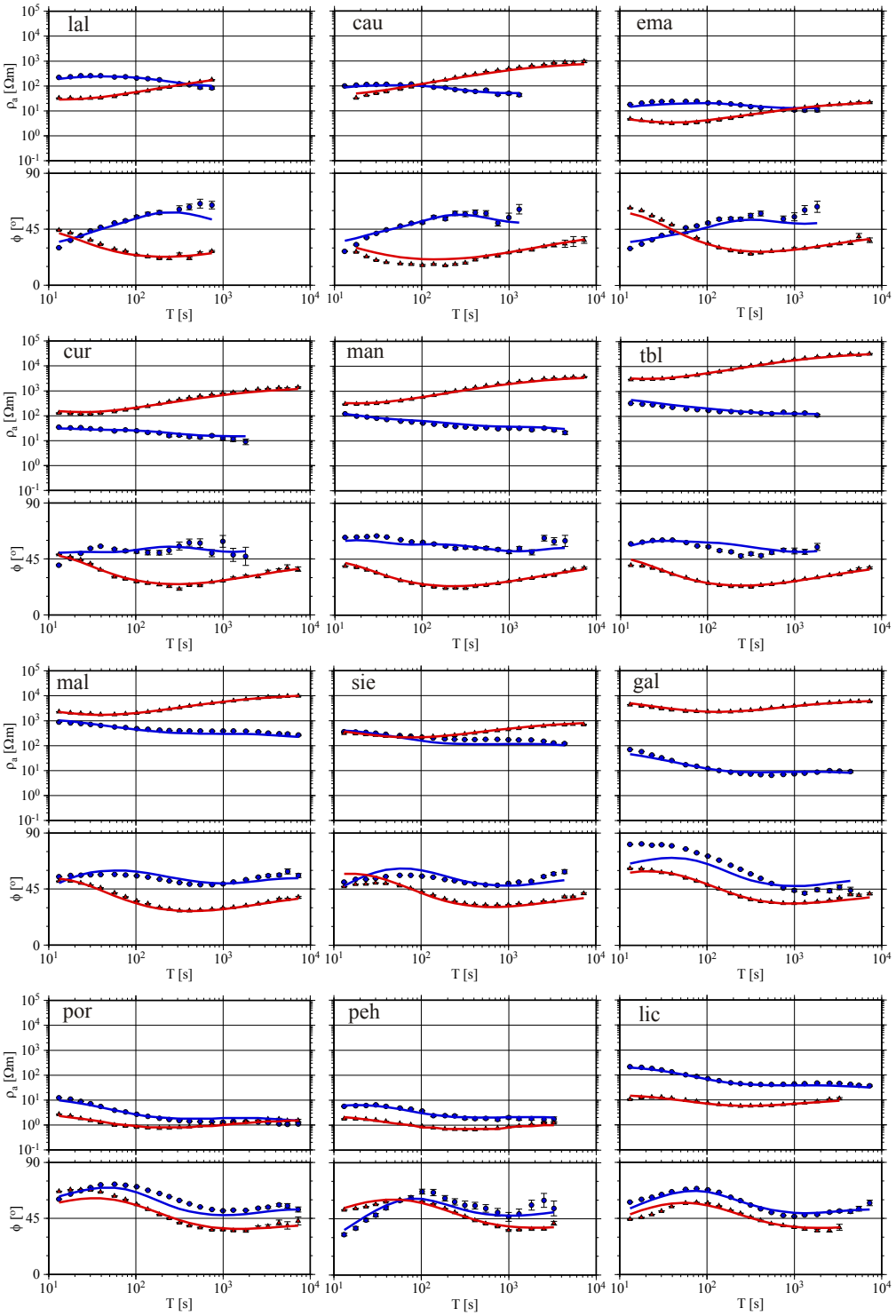

Figure A.2.: Data fit for sites of the northern profile in Fig. 6.6 (upper panel). Red triangles and blue circles represent the data of Z_{xy} or Z_{yx} respectively, red and blue lines are the model responses.

Acknowledgements

This is publication GEOTECH-213 of the R&D-Programme GEOTECHNOLOGIEN funded by the German Ministry of Education and Research (BMBF) and German Research Foundation (DFG). This work would not have been possible without the support of many people. There are many people who contributed to this work providing me with an interesting research topic. First I would like to thank Dr. Heinrich Brasse, who gave me the possibility to write this PhD thesis and for his guidance and support throughout the work. Special thanks to Prof. Dr. Serge Shapiro and Prof. Dr. Georg Kaufmann for their time and the review of this thesis. Thanks to the MT group at the FU and the MT AG for all the helpful suggestions and the interesting meetings during all the years. Dr. Josef Pek provided me with the anisotropy code and he invested a lot of time to advance it. My sincere thanks for this and for the discussion we had. Tamara for the time spent together in the office, the support during the field campaign and the useful comments concerning offshore MT. I am deeply grateful for all the time Anja Schäfer and Daniel Díaz spend reading my thesis, eating together at the Mensa and interesting and relaxing discussion about geophysics and thousand other topics. I profited a lot by the discussion with Kolja Groß and Uli Micksch about the interpretation of the data. Thanks a lot to both of them. I am greatly indebted to Diane Eydam, Andreas Gerner and Lutz Mütschard for their assistance in the fieldwork and especially to Amerika Manzanares and Fabian Sepúlveda for the mediation work with the authorities and local people during the field campaign in Chile. I thank PD Dr. Oliver Ritter and GIPP for loan of instruments. The Woods Hole Oceanographic Institution managed the offshore measurements and without the support of J. Beyli, A. Gardner, H. Moeller the experiment could not have been done. Many thanks to Prof. Dr. E. Flüh and the crew on the RV Sonne for an essential support on the ship and in carrying out the marine campaign. Many thanks to my friends and colleagues at the Institute, particularly to Lars, Dana, Julio, Mansoure, Banafshe and Jeremie who shared with me for a longer or shorter time the same office and made me enjoy even long days at the office. Jörg Graefe always had a sympathetic ear for questions concerning the software at the office. I am deeply grateful to Tarn for his critical proofreading of this work and for several useful notes in respect to the content. Special thanks go to Martin Koll for his professional assistance with computer problems. I thank Nicole for the support, patience and understanding during the last years and particularly in the final stages of this work. *Without your help the last hours would be much more tiring. Thank you so much for everything!* Not least I am very grateful to my family, especially my parents, since they supported me during the entire period of my studies and have encouraged me the whole time.